Faculty of Physics and Astronomy
University of Heidelberg

Star Formation in the Galactic Center

Master thesis carried out by

Nico Krieger

at the Max Planck Institute for Astronomy

under the supervision of Dr. Fabian Walter

examined by
Prof. Dr. Henrik Beuther and Prof. Dr. Ralf Klessen

submitted May 18, 2016

Master Thesis

Star Formation in the Galactic Center

Nico Krieger

Max Planck Institute for Astronomy

Supervisor: Dr. Fabian Walter
Examiners: Prof. Dr. Henrik Beuther, Prof. Dr. Ralf Klessen

submitted May 18, 2016
to the Department of Physics and Astronomy
at the University of Heidelberg

Abstract

The Central Molecular Zone (CMZ) in the Galactic Center (GC) contains large amounts of dense molecular gas and exhibits high star formation rate densities. Such high densities are not frequently encountered in the local universe, but appear to be more common at high redshift. Recent work by Longmore et al. (2013) and Kruijssen et al. (2015) suggest a star formation sequence (SFS) in gas streams that is triggered by a close passage to the Galactic Center, Sgr A*. This thesis describes the data reduction and imaging of the radio interferometric Survey of Water and Ammonia in The Galactic Center (SWAG), especially the targeted metastable ammonia hyperfine structure lines, which are used to test the SFS hypothesis.
SWAG is currently mapping the central 500 pc of the Milky Way at 1 pc resolution with the Australia Telescope Compact Array (ATCA) in 42 spectral lines at $21-25$ GHz. The range $-1.3° < l < 2.0°$, $-0.6° < b < 0.4°$ in Galactic longitude and latitude is observed in ~ 6500 pointings over 525 hours in three parts in $2014-2016$. This thesis covers observation and reduction of data taken in 2014 and 2015 that targeted the inner ~ 200 pc. In this context a pipeline was developed as part of this work that will be applied to the full survey after its completion in mid 2016. This survey results in maps and spectra of all 42 lines at unprecedented resolution (both spectrally and spatially), sensitivity, and areal coverage. Using ammonia hyperfine structure line fits, maps of line-of-sight velocity, line width, column density, opacity and four gas temperature measures were calculated.
Based on this data and the kinematic model of Kruijssen et al. (2015), the absolute time dependence of kinematic gas temperature is inferred along the molecular clouds' orbit. It was found that gas temperatures increase as a function of time in both regimes before and after the corresponding cloud passes pericenter where its collapse is triggered. Other investigated quantities (line width, column density, opacity) show no strong sign of time dependence but dominating cloud-to-cloud variations. The results are discussed in the framework of tidal triggering of cloud collapse and orbital kinematics and found to generally match the predictions, i.e. the existence of a tidally triggered star formation sequence in the Galactic center can be confirmed. It must now be tested if the model fulfills, or needs adaptions to, these new constraints regarding temperature evolution of molecular clouds during collapse and star formation.

Abstract

Die Central Molecular Zone (CMZ) im galaktischen Zentrum enthält große Mengen dichtes, molekulares Gas und weißt hohe Dichten der Sternentstehungsrate auf. Solch hohe Dichten treten nur selten im lokalen Universum auf, aber scheinen bei hohen Rotverschiebungen häufiger zu sein. Neue Arbeiten von Longmore et al. (2013) und Kruijssen et al. (2015) schlagen eine Sternentstehungssequenz (SFS) in Gasströmen vor, die durch eine nahe Passage des galaktischen Zentrums bei Sgr A* ausgelößt wird. Diese Arbeit beschreibt Datenreduktion und Imaging der radiointerferometrischen Studie Survey of Water and Ammonia in The Galactic Center (SWAG), speziell der metastabilen Ammoniakhyperfeinstrukturlinien, und deren Verwendung als Test der SFS-Hypothese.
Im Rahmen von SWAG werden zurzeit die zentralen 500 pc der Milchstraße mit 1 pc Auflösung mithilfe des Australia Telescope Compact Array (ATCA) in 42 Spektrallinien im Bereich $21 - 25$ GHz kartiert. Der Bereich $-1.3° < l < 2.0°$, $-0.6° < b < 0.4°$ in galaktischer Länge und Breite wird dabei in ~ 6500 pointings über 525 Stunden in den Jahren $2014 - 2016$ beobachtet. Diese Arbeit behandelt Beobachtung und Reduktion der Daten, die 2014 und 2015 aufgenommen wurden und die innersten 200 pc abdecken. Anhand dieser Daten wurde eine pipeline entwickelt, die auf die gesamte Studie nach ihrem Abschluss Mitte 2016 angewendet werden wird. Diese Studie resultiert in Karten und Spektren aller 42 Spektrallinien in bisher unerreichter Auflößung (spektral und räumlich), Sensitivität and räumlicher Abdeckung. Auf Basis von Fits der Ammoniak Hyperfeinstruktur wurden Karten von Geschwindigkeit entlang der Sichtlinie, Linienbreite, Säluendichte, Opazität und vier Maßen der Gastemperatur berechnet.
Aus diesen Daten und dem kinematischen Modell von Kruijssen et al. (2015) wird die zeitliche Abhängigkeit der kinematischen Gastemperatur in absoluten Einheiten entlang des Orbits der molekularen Wolken hergeleitet. Es stellt sich heraus, dass die Gastemperaturen im zeitlichen Verlauf ansteigen und zwar in beiden Phasen, vor und nach Passieren des Perizentrums, wo ihr Kollaps ausgelöst wird. Weitere untersuchte Größen (Linienbreite, Säulendichte, Opazität) weisen keine Anzeichen einer Zeitabhängigkeit auf, sondern variieren zwischen den einzelnen Wolken. Die Ergebnisse werden im Rahmen des Modells eines durch Gezeitenkräfte induzierten Kollaps der Wolken diskutiert, zu dessen Vorhersagen sie passen, das heißt die Existenz einer durch Gezeitenkräfte ausgelösten Sternentstehungssequenz im galaktischen Zentrum kann bestätigt werden. Es muss nun getestet werden, ob das Modell die neuen Bedingungen bezüglich Temperaturentwicklung molekularer Wolken während Kollaps und Sternentstehung erfüllen oder Anpassungen nötig sind.

Contents

Introduction

1.1 Motivation

For thousands of years, humans looked up to the stars and planets and tried to understand their place in this world. The quest solving the questions who we are and where we came from is certainly older than human records and likely older than humankind itself, probably arising when the first hominids became intelligent enough to gain self-consciousness. Today, another great question falls into line: Is there other intelligent life in the universe?
The aim of understanding these fundamental mysteries traces a long trail to the questions of how our Earth formed, how the Sun formed, which connects to the evolution of the Milky Way and other galaxies and requires understanding star formation in general. Stars are a basic ingredient of the universe and control many physical processes of the evolution of baryonic matter in the universe across redshift: reionization, galaxy evolution, metal production and enrichment follow from the life and death of stars. Star formation connects the vastly different length scales over several orders of magnitude from galactic influences (kpc) on molecular clouds (pc) down to stars (millions of km or 10^{-8} pc) which makes it an inherently complex process. Many fundamental questions are still open today like the mass distribution of newly formed stars (initial mass function, IMF) or the puzzlingly low efficiencies of gas mass to stellar mass conversion. Another unsolved problem concerns the time scales that collapsing clouds and protostars spend in a certain state before becoming an actual star. Compared to human time spans of less than 10^2 years, even fast[1] astrophysical processes like star formation proceeding over several 10^6 years appear (quasi-) static[2] and no direct time infor-

The Australia Telescope Compact Array (image from `http://www.csiro.au/en/Research/Facilities/ATNF/Australia-Telescope-Compact-Array`)

[1]Processes on small scales can be extremely fast, even for human measures like milli-second pulsars for example. In the context of this thesis, however, fast must be understand relative to galaxy evolution or cosmic timescales which means durations of tens of thousand to a few million years (Myr) are referred to as very fast and fast, respectively.

[2]Quasi-static means in this context that movement can be measured spectroscopically but

mation can be gained from observations. Luckily, the huge amount of gas clouds and galaxies come to our rescue by presenting all stages of star formation ready to be observed and interpreted. Arranging the observations in continuous, logical order and counting their relative abundances, allows the reconstruction of the star formation process and their relative durations.
A new kinematic model of molecular gas in the Galactic center now offers the possibility to derive absolute time scales for star formation processes by constructing a star formation sequence. The Galactic Center is a local analogue to the conditions at redshift $z \sim 2-3$ (Longmore et al., 2016) where the peak of the cosmic star formation history is located (Madau & Dickinson, 2014), and thus helps to understand star formation in general but also galaxy evolution.

very little or no change in appearance can be observed in an astronomers lifetime.

1.2 Theory of Interferometric Imaging in Radio Astronomy

Earth's atmosphere is opaque to electromagnetic radiation of most wavelengths, with only three spectral windows that can be observed by ground based instruments without distortion or absorption. Beside optical and infrared window, radiation in the radio at regime wavelengths of about 1 cm to 1 m can pass the atmosphere almost unaffected, while shorter mm and sub-mm wavelengths are partially absorbed. It is therefore possible to build cheap radio telescopes on earth instead of costly satellite missions for ultraviolet or infrared light. Luckily, many atomic and molecular species emit radio radiation (frequency ν) because the corresponding low energy differences ΔE between two states given by $\Delta \mathrm{E} = h\nu$ (Planck constant h) matches atomic hyperfine transitions as in HI, very high atomic excitation states (e.g. $\mathrm{H}_{64\alpha}$) and typical rotational energies of molecules like ammonia or carbon-monoxide. Hence, radio astronomy is especially suited to gain insights into molecular gas which is correlated to star formation.
Obtaining images in radio and sub-mm/mm astronomy is a complex process that involves complicated instruments and many computational steps. Radio frequencies of hundreds of GHz cannot be processed with today's digital hardware where typical clock speeds are a few GHz. It is therefore necessary introduce intermediate frequencies by interfering the sky signal with a local oscillator. All these frontend processes are already highly complicated before reaching the backend where visibilities, the final raw data, are generated by interfering signals of several antennas. Before these data can be used, several calibration steps and a deconvolution algorithm need to be applied. Hence, the following sections on theory are shortened and simplified to present a basic understanding of imaging in radio interferometry following Taylor et al. (1999) and Wilson et al. (2013).

1.2.1 Radio astronomy

In astronomy, the term radio covers the long wavelength end of the electromagnetic spectrum including radio wavelengths but also microwaves down to mm/sub-mm ranges. Photons at radio frequencies cannot be measured individually as in optical CCDs but the electrical field is detected with simple receivers like crossed dipole antennas. This design offers the advantage that signals at several frequencies can be measured at once which relate to velocity information by the Doppler effect. Data sets in radio astronomy therefore are three dimensional, two positional dimensions of projected position on the plane of the sky and a frequency or velocity dimension. These file are called cubes in reference to two dimensional image planes.

1.2.2 Radio Telescopes and Single Dish Measurements

Radio telescopes can be built in a variety of appearances, with different advantages and disadvantages depending on the requested frequency range. So called feeds guide emission with horns or dishes or omit it and use simple dipole antennas (wires) to transmit the signal through the front end system to the receiver where it is linearly amplified while adding as little noise as possible in cryogenically cooled systems and then converted to an intermediate frequency (IF) of a few GHz via mixing with a local oscillator (LO). This step of signal processing is needed to avoid damping that increases with frequency and to be manipulated with modern electronics with clock speeds of a few GHz. Wave guidance between instruments is realised with coax cables or metal wave guides (that are in principle hollow pipes) in older telescopes, until the signal is digitized and all further processing is done electronically.

Received Power and Brightness Temperature

The power transmitted to the receiver can be related to temperature under the assumption of black body radiation, which means all power is assumed to be emitted by a source characterized by a single temperature. Although this assumption is never satisfied when operating in science mode, a conversion is done anyway and it must be kept in mind that the derived temperature is not a physical quantity but a measure for power. According to Planck's law in the Rayleigh-Jeans limit, spectral radiance B_ν at frequency ν and therefore power is linearly proportional to temperature T:

$$B_\nu = \frac{2\nu^2 k_B T}{c^2} \tag{1.1}$$

with speed of light c and Boltzmann constant k_B. Due to that very simple relation, brightness temperatures are often used in radio astronomy.

Antenna Efficiency and Gain

An antenna is not uniformly sensitive to signals but has a characteristic antenna reception pattern which is the Fourier transform of the aperture, including effects like shadowing by feed legs or imperfect dish reflection. Outside a strong main lobe, weak side lobes also pick up signals as shown in fig. 1.1. Effects of beam structure on images are explained in §1.2.5.
The ratio between a theoretical, perfectly isotropically detecting antenna and the true reception is called complex gain G and must be corrected for during calibration. It accumulates all frequency independent effects of antenna hardware and electronics on amplitude and phase of the signal. Very similar to gain is the bandpass that describes the frequency dependence of the whole observation system from atmosphere to correlator. A perfect bandpass would allow signals to pass at 100% efficiency in a certain bandwidth $\Delta\nu$ and filter all other frequencies, hence have a box shape. In reality, it is not flat and square but shows ripples and rounded edges that need to be taken into account when calibrating the data.
Power collected in the feed system is always less than incident power due to various effects like imperfect surface reflection or aperture blockage resulting in a net antenna efficiency of typically $\eta \sim 0.4$.

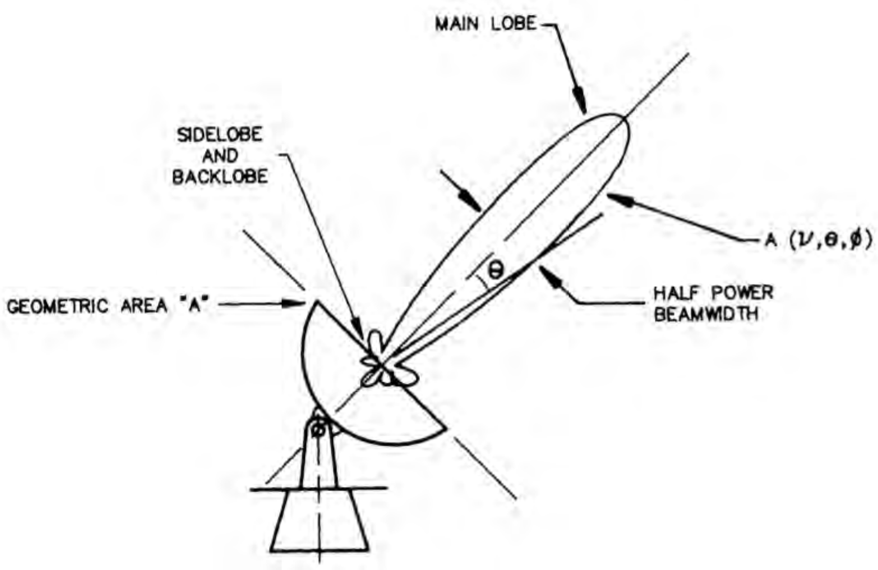

Figure 1.1: Antenna reception pattern (fig. 3-2 of Taylor et al., 1999) with strong main lobe whose size Θ is defined by the half power beam width (HPBW) and weaker side lobes. The length of the beam pattern in a certain azimuthal direction corresponds to the power detected in this direction. In the example of azimuthal angle Θ, the length is exactly half the maximum length, i.e. half the central power.

System Temperature and Noise (Radiometer Equation)

Noise is introduced in many steps in the receiver system and also expressed in terms of brightness temperature T_{RX}. System temperature T_{sys} is the sum of received power and all noise sources; hence, it can be split into antenna temperature T_A and T_{RX}, which in turn is the sum of many individual noise temperatures. For a given antenna and environment, T_A quantifies how much noise the antenna produces and not the actual temperature of the receiver.

$$T_{sys} = T_A + T_{RX} \tag{1.2}$$
$$= T_{sky} + T_{atm} + T_{loss} + T_{spill} + T_{RX} + ... \tag{1.3}$$

T_{sys} includes all noise power received from sky and earth (CMB, astronomical sources, ground around antenna) and as such depends on atmospheric properties. Atmospheric radiative transfer considerations are necessary to correct for opacity effects on gain G at frequencies $\nu > 5\,\text{GHz}$.
As the system noise level is given by T_{sys}, it defines the achievable root mean square (RMS) noise of an observation of integration time τ over bandwidth $\Delta\nu$ by the radiometer equation (1.4).

$$T_{RMS} = \frac{T_{sys}}{\sqrt{\Delta\nu\ \tau}} \tag{1.4}$$

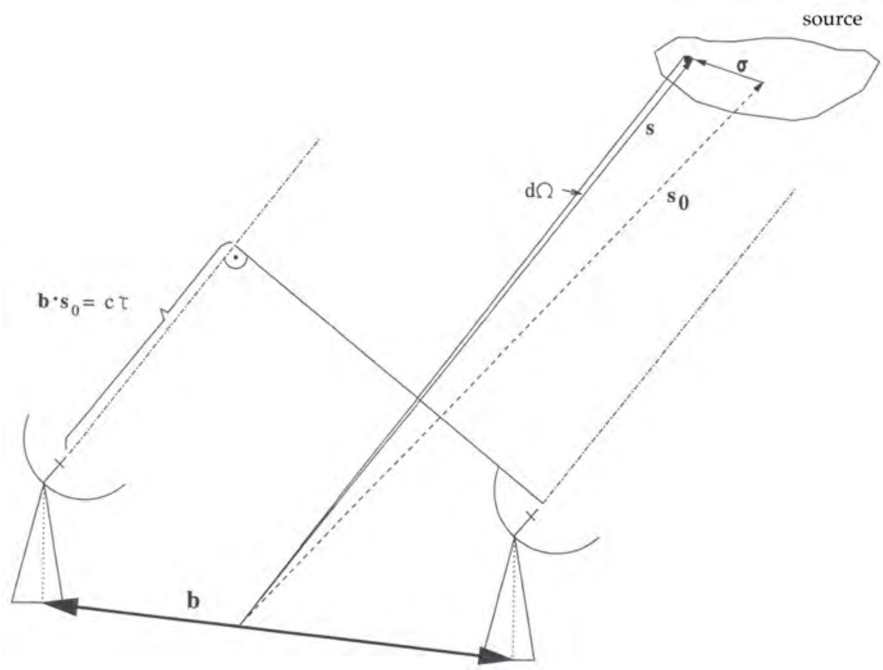

Figure 1.2: Sketch of a simple interferometric layout with two antennas (fig. 3 of Ott, 1999).

1.2.3 Interferometry

According to the Rayleigh criterion, the angular resolution of a telescope is given by wavelength and aperture as λ/D. Low frequency radio waves with wavelengths at the order of centimeters to meters inevitably result in low resolution even for very large telescopes like the 300 m Arecibo[3] dish. It is therefore necessary to use arrays of several antennas as individual detectors that are interconnected to behave as one instrument.

Interferometric array setups can be described easily for the minimum number of two antennas and then generalized towards more complex setups, such as the Australia Telescope Compact Array (ATCA)[4] with six antennas.

Figure 1.2 shows the basic principle of an interferometer: Two antennas that are separated by the distance **b**, the so-called baseline. The dishes point towards source s illustrated by the unit vector **s** and receive a signal at slightly different times denoted by the geometrical delay

$$\tau = \frac{\mathbf{b} \cdot \mathbf{s}}{c} \tag{1.5}$$

After correlating the signals and filtering out the high frequency part the result is quantified by an interferometer output R.

[3]www.naic.edu/index_scientific.php

[4]https://www.narrabri.atnf.csiro.au/

$$R \propto \cos(2\pi\nu\tau) \tag{1.6}$$

So far, a monochromatic point source is assumed. For astrophysical sources the radio brightness (intensity) $I(\mathbf{s})$ in the direction of $\mathbf{s}$ at frequency ν is introduced. The power received in bandwidth $\Delta\nu$ from a solid angle element $d\Omega$ is then given by $A(\mathbf{s})I(\mathbf{s})\Delta\nu d\Omega$ with $A(\mathbf{s})$ being the effective collecting area in direction $\mathbf{s}$. When taking the correlator into account the result using (1.5) and (1.6) is

$$R = \int_S dr = \int_S 2\pi A(\mathbf{s})I(\mathbf{s})\Delta\nu \cos\left(\frac{\mathbf{b}\cdot\mathbf{s}}{c}\right) d\Omega \tag{1.7}$$

The S specifying the integral's domain stands for the whole surface of the celestial sphere, but in practice, the primary beam as a single dish's reception pattern and the dimension of the source restrict the field of view.
The center of the field of view is referred to as phase tracking center or phase reference position $\mathbf{s_0}$, so that any point of the source can be mapped by $\mathbf{s} = \mathbf{s_0} + \sigma$ inside the primary beam.

1.2.3.1 Visibilities and the u, v Plane

Signals in the form of induced voltages in the receivers need to be converted into complex visibilities of amplitude and phase for storage and further computation. The visibility $\mathcal{V}$ is "a measure of the coherence. [...] It can be regarded as an unnormalized measure of the coherence of the electric field, modified to some extend by the characteristics of the interferometer" (Taylor et al., 1999). It is defined as

$$\mathcal{V} = |\mathcal{V}|\ e^{i\Phi_\mathcal{V}} = \int_S \mathcal{A}(\sigma)I(\sigma)e^{-2\pi\nu\mathbf{b}\cdot\sigma/c}\, d\Omega \tag{1.8}$$

where the normalized antenna reception pattern (primary beam) $\mathcal{A}(\sigma) = A(\sigma)/A(\mathbf{s_0})$ is used. It is the basis of all further analysis and is related to the correlator output R by

$$R = A(\mathbf{s_0})\Delta\nu\, |\mathcal{V}| \cos\left(\frac{2\pi\nu\mathbf{b}\cdot\mathbf{s_0}}{c} - \Phi_\mathcal{V}\right) \tag{1.9}$$

In order to obtain the desired quantity $I(\sigma)$, definition (1.8) that is nothing but a Fourier transform of $\mathcal{A}(\sigma)I(\sigma)$, must be inverted.
The inverse transformation is done on coordinates l, m, n in image space that correspond to Fourier space coordinates u, v, w (fig. 1.3). The u, v, w system can be understood as the projected baselines as seen from the source. This means a set of visibilities maps the intensity distribution on the u, v plane where u is

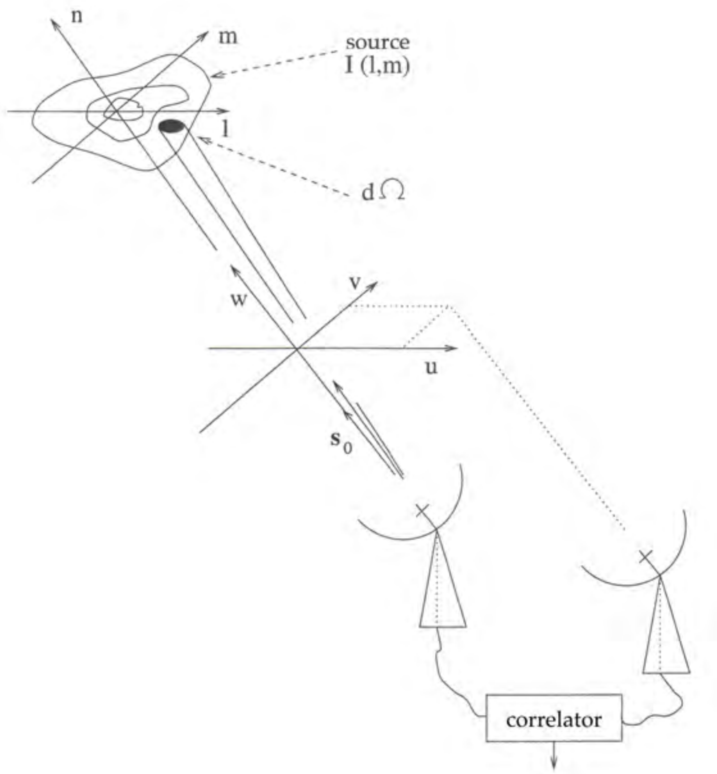

Figure 1.3: Coordinate systems used in interferometry. u points east, v to the east and w to the phase tracking center (fig. 4 of Ott, 1999).

defined to point north, v to the east (along right ascension α) and w towards the source and measured in multiples of wavelength λ. Image coordinates l, m are measured in a tangent plane to the celestial sphere and therefore are direction cosines with respect to the u, v axes. n keeps the direction of w, but measures the image coordinate.
The inverse Fourier transform is then given by

$$\mathcal{A}(l,m)I(l,m) = \int_{-\infty}^{\infty}\int_{-\infty}^{\infty} \mathcal{V}(u,v)e^{2\pi i(ul+vm)}dl\ dm \tag{1.10}$$

$$= \hat{\mathbf{F}}^{-1}[\mathcal{V}] \tag{1.11}$$

A visibility data set consists of many points in the u, v plane each measured with amplitude and phase. The Fourier transformation converts this collection into its spectrum whereas each point is transformed to a single wave pattern. The image of an astrophysical object is then build up by superimposing thousands of waves that constructively interfere where the source is located and cancel each other on empty patches of the sky.
As in other physical cases, quantities in the two spaces connected by a Fourier transform correspond to each other. The position of a visibility point determines the wave in the image plane such that angle Ψ and length $|\mathcal{V}|$ of the position vector

of a visibility defines direction of the wave vector k and frequency. Amplitude and phase $\Phi_{\mathcal{V}}$ of a visibility transform to amplitude and phase of its spatial wave in the image domain.

1.2.3.2 Sampling of the u, v Plane

Due to the position - frequency relation, it is necessary to have visibility measures over the whole u, v plane to recover structures of all sizes in the image plane. Hence, the number of baselines should be maximized by using more than just two telescopes. In aperture synthesis, n antennas provide $\frac{n(n-1)}{2}$ baselines to cover some more u, v points. An optimum is achieved by using non-redundant setups that do not cover a baseline several times, but only once.
The by far largest contribution on covering the plane is caused by the inevitable rotation of the earth. While other observation techniques require much effort to correct for this effect, synthesis interferometry would have a poor resolution without it. As earth rotation constantly changes the u, v positions of the telescopes[5], it provides a better u, v coverage. Two fundamental reasons prevent total coverage: The baselines have lower and upper limits as two telescopes cannot be placed side by side with an infinitesimal small distance, and even with telescopes on earth and in space the longest baseline is still finite. A so-called short spacing correction can be applied by combination of interferometric and single dish data to reduce the problem of missing short baselines that corresponds to missing flux by large scale emission.
If each measured visibility is given the weight 1 while all other unknown points on the plane are set to 0, the principal solution I can be obtained. The true values of the uncovered areas of the u, v plane are not known and therefore all functions with different assumptions of these points offer correct solutions, too.
The mathematical expression of gaining a first so-called dirty image I^D then is

$$
\begin{aligned}
I^D(l,m) =& \hat{\mathbf{F}}^{-1}[S(u,v)\mathcal{V}(u,v)] && (1.12)\\
=& \hat{\mathbf{F}}^{-1}[S] * \hat{\mathbf{F}}^{-1}[\mathcal{V}] && (1.13)\\
=& B * I && (1.14)
\end{aligned}
$$

According to the Convolution Theorem (Bracewell, 1978) the Fourier transform of a multiplication of functions is equal to the convolution of the Fourier transformed functions. Therefore the calculation can be simplified to the dirty image I^D being the convolution of dirty beam B and true sky brightness I (Cornwell, 2008).
The dirty beam B is the reaction of the interferometer to a hypothetical centered point source and therefore determines the achievable resolution.

$$B = I^D(point\ source) = \hat{\mathbf{F}}^{-1}[S] * \delta(0,0) = \hat{\mathbf{F}}^{-1}[S] \tag{1.15}$$

[5]An antenna moves on the u, v plane due to earth's rotation when seen from the source.

Its shape is not Gaussian as one would want it to be, nor are all the values positive. In fact, the total spatial integral over the dirty beam is zero which results in zero integrated flux in the dirty image as well. This is due to the incompletely sampled u, v plane and the ability of Fourier transforms to generate alternating functions with negative values. As the large primary beam is sampled by the smaller dirty beam, the convolution of dirty beam and true image is the dirty image. To correct the interferometer effect of vanishing flux integral, a cleaning procedure is necessary as described in §1.2.5.1. Cleaning removes the structure outside the main maximum that is caused by missing short baselines. A perfectly sampled u, v plane would result in a Gaussian beam which is why a Gaussian without any sidelobes is used as clean beam.

1.2.3.3 Weighting

The easiest possible sampling function gives covered u, v points the weight 1 and sets the rest of the plane to 0. This, however, ignores additional information about data acquisition like reliability and lacks an option to qualitatively control the image.
Visibilities are only known at certain points of the u, v plane which is mathematically expressed by a two-dimensional Dirac delta function. Three weight terms R_i, T_i and D_i are set by the telescope system, mathematical needs and the user.

$$\mathcal{V}^W = \sum_i R_i T_i D_i \delta(u - u_i, v - v_i) \mathcal{V}(u_i, v_i) \tag{1.16}$$

The reliability function R_i weights the visibility data points according to given system parameters, such as integration time, temperature and bandwidth. A tapering function T_i downweights data in the outskirts of the covered u, v plane. This is needed because the cut-off in coverage due to limited baseline length is Fourier transformed to $sinc(x) = sin(x)/x$ with strong sidelobes that deteriorate image quality. D_i is the density weighting function that corrects varying density of u, v coverage. In this thesis, only natural weighting $D_i = 1$ is used which results in the best possible signal-to-noise ratio (SNR) at the drawback of decreased resolution by putting relative emphasis on the more common short baselines which produces a larger beam. Another weighting scheme is uniform weighting $D_i = [N_s(i)]^{-1}$ that sets the weights as inverse density N in a radius s around visibility i which results in increased spatial resolution and noise. A compromise offering a trade-off between SNR and noise is robust weighting (Briggs, 1995) that allows interpolation between natural and uniform by a robustness parameter.

1.2.4 Calibration

Before the actual imaging process can take place, it is necessary to perform a number of calibration steps to reconstruct a signal as it would have been taken by a perfect telescope unaffected by atmosphere and instrument electronics.

First, bad visibilities need to be flagged, i.e. set to be excluded in all further data reduction steps. Visibility measurements are dubbed bad when they do not exclusively contain the raw science or calibration data such as satellite communication signals, internal array setup measurements or unphysically strong signals by resonant modes in the correlator.
As described in §1.2.2, a gain factor is introduced for practical reasons and must be corrected again to determine correct source intensities. Gain effects on amplitude and phase can be calculated from observations of a strong, point-like source of known flux that is located near the science source and targeted often enough to track temporal variations.
The bandpass as frequency-dependent response of antenna electronics must be determined once in a while, typically once per observation night, as it can change slowly over time. It is reconstructed from the observed spectrum of a source with known spectral behavior that needs to be integrated long enough to reach sufficient per-channel SNR.
Gain and Bandpass corrections are then applied to all other data before a flux density calibration can be performed to determine the absolute flux level. Absolute flux measurements are in principle possible but prone to errors which is why a source of assumed constant flux density is observed and the data rescaled to match the known value. There are very few standard flux density calibrators and only a single one on the southern sky, PKS 1934-638.

1.2.5 Imaging

1.2.5.1 Deconvolution

In order to recover the true image I from the convolved dirty image $I^D = B * I$, a deconvolution algorithm is needed. The easiest solution to this problem is decomposing the dirty image into a model and replacing its dirty beam with a clean beam without any sidelobes - suitably named cleaning. Högbom (1974) describes an surprisingly simple algorithm based on a point source model for all imaged emission. It starts by locating the pixel with maximum flux in the dirty image, writes the found value (clean component) multiplied by a loop gain factor in a model table and finishes an iteration by subtracting a loop gain factor scaled dirty beam. These steps are repeated on the residual image until a stopping criterion in terms of number of iterations or maximum residual value is reached. Image reconstruction is done by fitting a Gaussian clean beam to the dirty beam, convolving every clean component with this clean beam and adding them to the residual image. This way, all processed flux is now based on a clean beam of $\int B_{clean} \neq 0$ and the spatial integral over the restored image is non-zero as well. Despite its simplicity, clean and its variants[6] are robust and recover most of the true flux density of the source. However, the point source assumption is not justified for extended emission like resolved galaxies or molecular clouds and therefore performs poorly

[6] Clark clean, Cotton-Schwab clean and others are still based on point source models but differ in treating the dirty beam and computational cost by introducing major and minor cycles.

on such data. A significant pedestal of uncleaned emission remains in the residual and restored images, together with a negative valued bowl that originates in the dirty image's vanishing integral. Noise analyses of cleaned images are difficult because the restored image can contain in the same pixel both clean (clean beam) and residual (dirty beam) emission which are defined through beams of different sizes. Better suited algorithms inherently consider extended features and point sources as do multi-scale and maximum entropy clean. MIRIAD, the program used in chapter 2 offers the use of `mosmem`, an implementation of maximum entropy clean.

1.2.5.2 Maximum Entropy clean

The maximum entropy method (MEM, Jaynes, 1957) describes a general approach used in other fields of image processing as well as in radio interferometry. It selects an image that fits the sampled points in the u, v plane within the noise level and has maximum entropy. The term entropy does not correspond to its use in statistical physics but possible expressions for entropy $\mathcal{H}$ are similar to the Boltzmann H-function.

$$\mathcal{H} = -\sum_i I_i \ln \frac{I_i}{M_i} \qquad or \qquad \mathcal{H} = -\sum_i I_i \left[\ln \frac{I_i}{M_i} - 1\right] \tag{1.17}$$

I_i denotes the deconvolved image and M_i is a reference image containing all a priori knowledge. An empty field $M_i = const > 0$ is used if no knowledge of the source distribution is available or a low resolution image (e.g. from single dish observations) can be given as a prior. Maximization of $\mathcal{H}$ forces a positive image (corresponding to removal of sidelobes) with a compressed range in pixel values that results in smoothness by coupling pixels through minimization of pixel value spread.
The constraints of positive image and exactly fitting each measured visibility are practically incompatible due to noise and a small deviation χ^2 between measured visibility $\mathcal{V}_i$ and modelled visibility $\mathcal{V}'_i$ scaled by measurement error σ_i must be allowed.

$$\chi^2 = \sum_i \frac{|\mathcal{V}_i - \mathcal{V}'_i|}{\sigma_i^2} \tag{1.18}$$

The resulting problem of maximizing $\mathcal{H}$ under the constraint of χ^2 is solved by various algorithms (Cornwell & Evans, 1985; Gull & Daniell, 1978; Skilling & Bryan, 1984; Wernecke & D'Addario, 1977). For such an algorithm to work correctly it needs to know noise σ_i and total flux density which are estimated theoretically or set to a default value. As for most optimization algorithms, a threshold of iterations until a solution is found can be set. In contrast to clean, no other parameters can be tweaked to control the deconvolved image.

1.2.5.3 Image Moments

Image cubes contain a wealth of information that cannot easily be perceived by an investigator. Calculating weighted averages over the frequency/velocity axes isolates certain features of the data in a simple 2D image.
Generally, the n-th moment is defined as an integral over intensity $I(v)$ depending on velocity v.

$$M_n = \int I(v) v^n dv \tag{1.19}$$

Commonly used are moments $n = 0$, 1, 2 and rarely -2. A moment 0 map is the result of integrating the cube over velocity, which corresponds to a summation of channels for the discrete channel structure with channel width Δv_{chan}. The result is an intensity distribution map for the given tracer. The physical quantities normalized velocity distribution and normalized velocity dispersion distribution can be derived from $n = 1$ and $n = 2$, respectively. It is also possible to calculate higher (skewness $n = 3$, kurtosis $n = 4$, ...) and even negative moments (mean $n = -1$, peak intensity $n = -2$). However, these maps are becoming increasingly more difficult to interpret.

$$M_0 = \int I(v) dv = \sum_i I_i \Delta v_{chan} \tag{1.20}$$

$$M_1 = \frac{\int I(v) v dv}{\int I(v) dv} = \langle v \rangle \tag{1.21}$$

$$M_2 = \sqrt{\frac{\int I(v)(v - M_1)^2 dv}{\int I(v) dv}} = \langle \sigma \rangle \tag{1.22}$$

Moment 0 Error Map

When deriving ammonia temperatures in the optically thin limit (§1.3.2.3) from moment 0 maps, an error estimate is needed to derive temperature errors. Instead of intensity I as above, the error in terms of brightness temperature T_b (§1.2.6) can be calculated as

$$\Delta \left(\int_{v_1}^{v_2} T_b \, dv \right) = \Delta \left(\sum_{v_1}^{v_2} T_{b,i} \Delta v_{chan} \right) \tag{1.23}$$

$$= \Delta v_{chan} \sqrt{\sum_{v_1}^{v_2} \Delta T_{b,i}^2} \tag{1.24}$$

$$= \Delta v_{chan} \sqrt{\frac{v_2 - v_1}{\Delta v_{chan}} \cdot T_{RMS}^2} \tag{1.25}$$

for a data cube with fixed channel width Δv_{chan} and RMS noise T_{RMS}. This translates to an error in flux F according to eqs. (1.39) and (1.40).

1.2.6 Brightness Temperature, Flux Density and Flux

According to eq. (1.1), brightness temperature T_b is proportional to spectral radiance B_ν (also called specific intensity I_ν in astronomy). Flux density S is defined as the spectral power received from a spatially resolved source subtending solid angle Ω in a detector of projected area $d\sigma$.

$$S = \frac{dP}{d\sigma d\nu} = \int_{source} I_\nu \cos\Theta d\Omega \approx \int_{source} I_\nu d\Omega \tag{1.26}$$

Θ is the angle between source direction and normal to the detector surface. Typical astronomical sources do not extend over such large areas that the deviation from $\cos\Theta \approx \Theta$ must be considered. Brightness temperature is then related to intensity and flux density as

$$T_b = \frac{c^2}{2\nu^2 k_B} I_\nu = \frac{c^2}{2\nu^2 k_B}\frac{dS}{d\Omega} \tag{1.27}$$

The very low fluxes and flux densities in astronomy are reflected by the choice of unit. Jansky is named after the radio astronomy pioneer Karl G. Jansky and expressed in SI units by

$$1\,\mathrm{Jy} = 10^{-26}\,\frac{\mathrm{W}}{\mathrm{Hz\,m^2}} \tag{1.28}$$

The beam solid angle in steradians subtended by a Gaussian clean beam (beam area) can be calculated by integrating the area of a two dimensional Gaussian with standard deviation σ_x, σ_y and the corresponding $FWHM_x$, $FWHM_y$ in arcseconds.

$$\begin{aligned}
\Omega\,[\mathrm{sr}] &= \int_{-\infty}^{\infty}\int_{-\infty}^{\infty} \exp\left(-\frac{x^2}{2\sigma_x^2} - \frac{y^2}{2\sigma_y^2}\right) \mathrm{d}x\mathrm{d}y && (1.29)\\
&= \int_{-\infty}^{\infty} \exp\left(-\frac{x^2}{2\sigma_x^2}\right) dx \int_{-\infty}^{\infty} \exp\left(-\frac{y^2}{2\sigma_y^2}\right) dy && (1.30)\\
&= \sqrt{\pi}\sqrt{2\sigma_x}\cdot\sqrt{\pi}\sqrt{2\sigma_y} && (1.31)\\
&= 2\pi\sigma_x\,[\mathrm{rad}]\sigma_y\,[\mathrm{rad}] && (1.32)
\end{aligned}$$

The relation between σ and full width at half maximum (FWHM) is

$$\frac{1}{2} = \exp\left(-\frac{\mathrm{FWHM}^2}{2\sigma^2}\right) \tag{1.33}$$

$$\Rightarrow \sigma = \frac{\mathrm{FWHM}}{2\sqrt{2\ln 2}} \tag{1.34}$$

Therefore, Ω is given by

$$\Omega = \frac{\pi \cdot \mathrm{FWHM_x}\ \mathrm{FWHM_y}}{4\ln 2} \tag{1.35}$$

$$= 1.13309\ \mathrm{FWHM}_x\ \mathrm{FWHM}_y \tag{1.36}$$

Converting to arcseconds introduces another conversion factor.

$$1" = \frac{2\pi}{360}\frac{1}{3600}\,\mathrm{rad} = 4.848 \cdot 10^{-6}\,\mathrm{rad} \tag{1.37}$$

In total, the conversion of flux density to brightness temperature depends on frequency and beam size.

$$T_b = \frac{(c\,[\mathrm{m/s}])^2}{2(\nu\,[\mathrm{GHz}])^2 k}\frac{S\,[\mathrm{Jy/beam}]}{\Omega\,[\mathrm{sr}]} \tag{1.38}$$

$$= 1.226 \cdot 10^6 \frac{S\,[\mathrm{Jy/beam}]}{(\nu\,[\mathrm{GHz}])^2 \cdot \Theta_x\,["]\ \Theta_y\,["]} \tag{1.39}$$

Intensity maps contain the flux density per beam in Jy/beam for each pixel and it is necessary to know how many beams fit in the region of interest. This is calculated from pixelsize in arcseconds and the beam area (1.29) as $\frac{(\text{pixel size})^2}{\text{beam area}}$. Flux F and flux density S are tightly related by integration over velocity and often used interchangeably. Due to the discrete channel structure of constant width Δv_{chan}, the conversion is limited to a simple multiplication, $F = S \cdot \Delta v_{chan}$.

$$F = \frac{1\mathrm{Jy}}{beam} \cdot \frac{\text{pixel size}^2}{1.13309\ \mathrm{FWHM}_x \mathrm{FWHM}_y} \cdot \Delta v_{chan} \tag{1.40}$$

1.3 Interstellar Medium

Humans cannot directly see the enormous amount of gas between the visible stars, however, it is crucial for evolution from cosmic scales down to the formation of life on the little rocky planet we live on. Gas fuels the formation of stars and is affected by a variety of physical processes and forces from basic gravity to molecular chemistry. The space between stars is filled not only with gas but also contains dust grains, cosmic rays, electromagnetic radiation, magnetic and gravitational fields and dark matter particles. With all these constituents, the interstellar medium has complex physical interactions that are currently being unravelled step by step towards a complete picture of the universe.
The interstellar medium can be characterized in various ways according to physical/chemical composition (gas, dust, cosmic rays, radiation, magnetic fields, ...) or by temperature (hot ionized to molecular medium). Historically, a division in three phases (hot, warm, cold) was established (McKee & Ostriker, 1977) while today five main phases are distinguished (Draine, 2011).
About 50% of the galactic disk volume (volume filling factor $f_V \sim 0.5$) and most of the space above and below the disk (scale height $H \sim 1-3\,\mathrm{kpc}$) is filled with hot ($T \gtrsim 10^{5.5}\,\mathrm{K}$), ionized gas of low density ($n \sim 10^{-3}\,\mathrm{cm}^{-3}$). This hot, ionized medium or HIM is heated by shocks from supernovae and collisionally ionized.
Warm, ionized gas is found at colder temperatures of $T\sim 5000-10^4\,\mathrm{K}$ and appears in the galactic disk in two variations. Diffuse photo-ionized gas in the disk ($H\sim 1\,\mathrm{kpc}$) is called the warm, ionized medium or WIM with typical densities of $n \sim 0.1\,\mathrm{cm}^{-3}$ and volume filling factors of $f_V \sim 0.35$. Compact, dense HII gas (HII region) has sizes of up to a dozen of parsecs and can be as dense as $n\sim 10^4\mathrm{cm}^{-3}$. Another large portion of gas ($f_V \sim 0.15$) is warm and dense ($n\sim 1\,\mathrm{cm}^{-3}$) but electrically neutral (WNM) at $T\sim 5000\,\mathrm{K}$ and smaller scale height $H\sim 400\,\mathrm{pc}$ than for diffuse WIM ($H\sim 1000\,\mathrm{pc}$).
The warm medium is heated by photo-electrons from different origin. Low energy dust emission heats the WNM whereas the higher temperature of WIM gas is reached by photo-electrons from hydrogen and helium.
Even colder gas of $T\sim 100\,\mathrm{K}$ is called cold, neutral medium (CNM) and controlled by similar processes as the WNM. However, densities are higher ($n \sim 10\,\mathrm{cm}^{-3}$) and the volume filling factor is small ($f_V \sim 0.01$).
Compared to a whole galaxy, the molecular medium (MM) makes up only a tiny fraction of volume, $f_V \sim 0.001$, but can contain large amounts of mass due to the high densities[7] of $n > 100\,\mathrm{cm}^{-3}$. Temperatures are at the order of dozens of K with even smaller clumps of even denser gas at $T\sim 10-30\,\mathrm{K}$ in them, molecular clouds.
Although the filled volume is increasingly smaller for higher density gas, it is becoming more and more relevant for the process of star formation. Molecular medium and star formation are strongly correlated by the star formation law but

[7]Technically, densities for the molecular medium go up to $n \gg 10^{23}\,\mathrm{cm}^{-3}$ as “everything between stars” also contains planets such as earth.

it is still unclear if molecular gas forms in dense gas clouds that are collapsing to form stars or stars form from molecular gas (Glover & Clark, 2012).

1.3.1 A Note on Temperatures and Temperature Measurements in the ISM

The term temperature is used intensively in astronomy for various temperature and energy related quantities. Beside many terms in other fields like effective (black body) temperature (describing the spectrum) in stellar physics or brightness temperature (energy deposited in receiver) in radio astronomy, even in the individual field of ISM gas, different temperature measures are used to describe energies. In order to avoid confusion, this section shortly explains the different temperature measures used in this thesis.

The concept of temperature in the ISM is in contrast to the sense of temperature of humans because of the low gas densities compared to earth's atmosphere. Low collision rates even allow components to be out of thermal equilibrium like gas and dust in the Central Molecular Zone (e.g. Lis et al., 2001; Molinari et al., 2011; Nagayama et al., 2009)). Interstellar or intergalactic temperatures are difficult to infer but several molecules act as good thermometers because measurable properties are temperature depended like the excitation state distribution in ammonia. The variety of molecular thermometers like formaldehyde (H_2CO) or carbon monoxide (CO) allow independent measurements and therefore better constraints on the "real" temperature as a measure for internal kinetic energy.

For ammonia, whose temperature dependencies will be exploited in this thesis, three temperature definitions are particularly important: excitation, rotational and kinetic temperature, all of which are related via complex dependencies.

Excitation temperature T_{ex} is defined as a scaling factor in the Boltzmann distribution of any two states of a system (electronic, vibrational, rotational of a molecule) and describes at which temperature a given population ratio is present. By simply describing a distribution of energetic states, it has no physical meaning and can even be negative for population inversion in masers or lasers.

Rotational temperature T_{rot} is defined analogously to T_{ex} with the difference that only rotational states are considered.

Kinetic temperature T_{kin} is the physical temperature of gas defined by its internal motion properties and related to T_{rot} in a complex, non-linear way (see §1.3.2.3). This is the quantity that can be compared to other measurement or is used for further analyses.

A crucial component for estimating ISM temperatures is *opacity*, i.e. the the measure of impenetrability of a medium for electromagnetic waves by absorption or scattering:

> Initial steps for this ~~symposium~~ [thesis] began a few billion years ago. As soon as the stars were formed, opacities became one of the basic subjects determining the structure of the physical world in which we live. And more recently with the development of nuclear weapons

> operating at temperatures of stellar interiors, opacities become as well one of the basic subjects determining the processes by which we may all die.
>
> — *Harris L. Mayer*; *Opacity calculations, past and future* (1964)[8]

In astronomical spectroscopy, it is expressed as *optical depth* τ, the logarithmic ratio of incident power to transmitted power through a medium (molecular cloud). As it quantifies trapping of photons, and therefore energy in an ISM cloud, it directly influences temperature measurements. Often optically thin approximations are assumed to simplify calculation or because opacities are not known, although they may be relevant.
Opacity and optical depth will be used interchangeably in this thesis.

1.3.2 Interstellar Ammonia

One of the open questions in star formation is the causal relation of molecular gas and star formation: Does SF require dense molecular gas or does it form in collapsing clouds that later form stars? Although this relation and star formation in general is not yet understood fundamentally, dense molecular gas is certainly an important ingredient in the process. As the bulk of molecular gas in the form of H_2 is difficult or impossible to observe, other gaseous species provide easier and better measurements of ISM parameters such as temperature. Depending on (self-)shielding properties, it is necessary anyway to observe a molecular cloud in various species to get information from different parts of it. Ammonia is a very useful molecule for this purpose as it traces intermediate densities and its inversion lines are used to calculate several temperature measures. Furthermore, the well understood hyperfine structure allow calculations of physically important quantities like opacity.
As all spectral lines, ammonia lines are characterized by a certain line width which, in an attempt to avoid confusion, will always be expressed as full width at half maximum (FWHM) in this thesis if not explicitly noted otherwise.

1.3.2.1 Laboratory Properties

In ammonia, or NH_3 in chemical notation, three hydrogen and one nitrogen atoms are arranged in a tetrahedral structure that allows two configurations with the nitrogen atoms above or below the plane of hydrogen atoms. The planar configuration in between these states requires higher energies as is sketched in fig. 1.4 as a function of torsion angle, i.e. the dihedral angle on the intersection of H-N-H planes. The nitrogen atoms can tunnel through the energy barrier at 180° resulting in a so-called inversion transition.
The general options of molecular excitation of electrons as well as rotation and vibration with quantum numbers J and ν respectively are also present in ammonia.

[8] `http://www.sciencedirect.com/science/article/pii/0022407364900202`

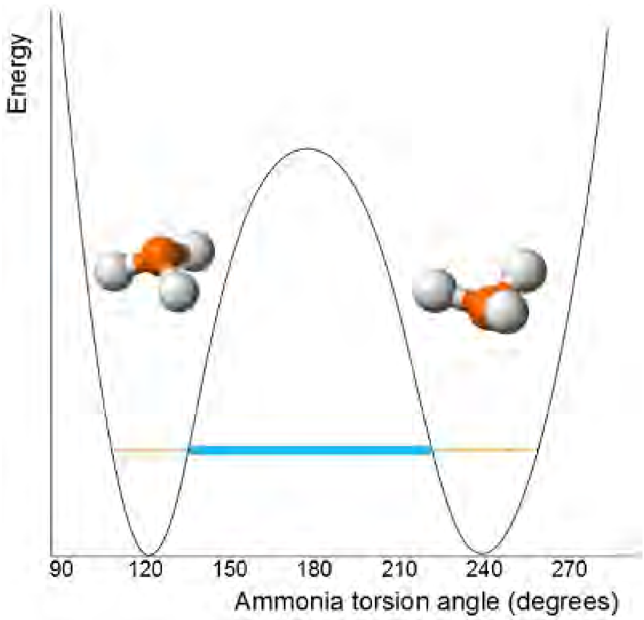

Figure 1.4: Inversion potential of ammonia as a function torsion angle. The two states (yellow dashed lines) are energetically identical but separated by a the more energetic planar configuration (blue) that can be tunnelled through. The switch between states is called inversion and its frequency depends on rotational state J. (source: `http://www.azoquantum.com/Article.aspx?ArticleID=12`)

At the low temperatures in the ISM, electronic states or vibration are unlikely to be excited and therefore inversion occurs mostly in the ground states S and $\nu = 0$. Rotation however, is much easier to excite at the order of $10\,\mathrm{meV} \sim 116\,\mathrm{K}$ and does affect the inversion frequency which is represented in the spectroscopically measured inversion doublet. In the oblate symmetric top molecule ammonia, two moments of inertia are identical resulting in only two distinguishable rotations, around the symmetry axis through the nitrogen atom (principal symmetry axis) and perpendicular to it. Any rotation is a combination of those two modes quantified by the quantum numbers J and K that define the magnitude of rotational angular momentum and its projection onto the principal symmetry axis, respectively. Notation of rotational states is given as (J,K), e.g. NH_3 (1,1).
Dipole selection rules $\Delta \mathrm{J} = 0, \pm 1$, $\Delta \mathrm{K} = 0$ apply which is why no transitions between K-ladders (K = *const*) are allowed. Higher J states decay rapidly in $10 - 10^2\,\mathrm{s}$ via far-infrared transitions of $\Delta \mathrm{J} = 1$ to the J=K state which is called meta-stable due to fast population but extremely slow decay. Collisions and other weak effects by vibration introduce $\Delta k = \pm 3$ ($\mathrm{K} = |k|$) transitions of $10^9\,\mathrm{s}$ timescale as the only decay channel of meta-stable states, hence the low decay rates and the name. Non-meta-stable states are therefore difficult to populate under normal astrophysical conditions and most gas is detected in meta-stable lines.
As for other molecules, two energetically distinct variations of ammonia exist in ortho and para state. The spins I_H of the three hydrogen atoms can all be aligned

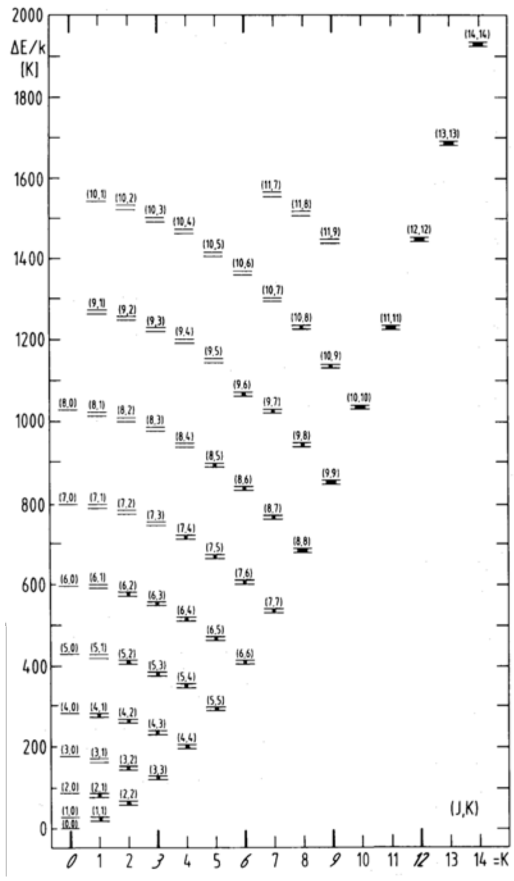

Figure 1.5: Energy level diagram of rotational inversion states in ammonia (fig. 1 of Wilson et al., 1993). K-ladders are drawn separated along the abscissa.

parallel $\mathbf{I}_{\sum H} = \frac{3}{2}$) which results in the lowest possible energy, the ortho state, or one of them can be anti-parallel ($\mathbf{I}_{\sum H} = \frac{1}{2}$) which is called para-$NH_3$ and has a higher energy As the total molecular spin includes atomic spins as well, ortho and para states can occur in specific rotational configurations only. For integers n, K$= 3n$ is ortho-NH_3 and K$\neq 3n$ has para alignment of spins.
Further line splitting is introduced as hyperfine structure mainly by the interaction of nitrogen nuclear spin $\mathbf{I}_N$ and electric field of the electrons. The total spin $\mathbf{F}_1 = \mathrm{J} + \mathbf{I}_N$ splits into a strong main line ($\mathbf{F} = 0$) and two pairs of satellites ($\mathbf{F} = \pm 1$) as listed in tables 1.1 and 1.2. Weaker magnetic interactions of $\mathbf{I}_N \cdot \mathrm{J}$ and $\mathbf{I}_{\sum H} \cdot \mathrm{J}$ cause a total of 18 hyperfine components for NH_3 (1,1). Spectral resolution of today's telescopes is high enough to resolve five hyperfine components while the weak splitting is blended into a single line (see table 1.1).

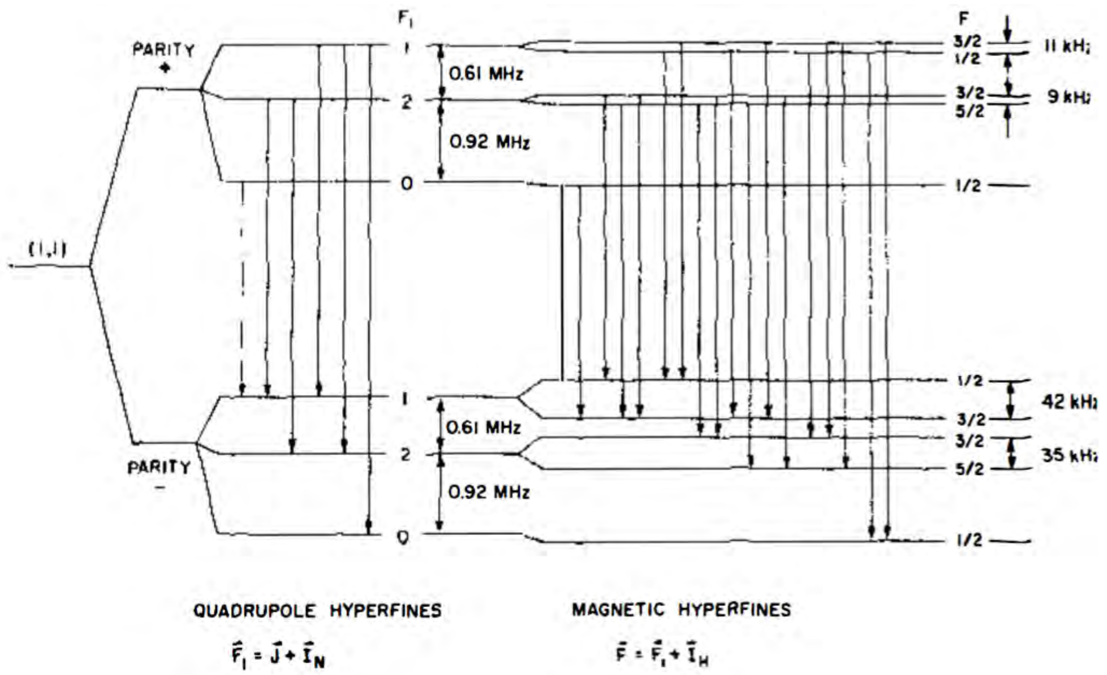

Figure 1.6: Hyperfine splitting of NH_3 (1,1) (fig. 2 of Ho & H., 1983). All 18 hyperfine lines are indicated to the right as arrows, the five observable spectral lines are the six arrows to the left of which two are identical in length, i.e. observed at the same frequency.

Table 1.1: Hyperfine transitions of ammonia of rotational state J,K= 1 to J,K= 1: Each block of transitions is summarized and averaged to compute the frequency difference as they are not resolved in astronomical observations. Velocities are given in the optical velocity definition $v = c\frac{\nu_0 - \nu}{\nu}$.

frequency [GHz]	state	Δf [MHz]	Δv [km/s]
23.69293	F_1: 1→0		
23.69297			
		0.94	11.89
23.69387	F_1: 1→2		
23.69390			
23.69391			
		0.59	7.46
23.69445	F_1: $\Delta F_1 = 0$		
23.69447			
23.69447			
23.69448			
23.69450			
23.69451			
23.69451			
23.69451			
		0.60	7.59
23.69507	F_1: 2→1		
23.69508			
23.69511			
		0.95	12.02
23.69603	F_1: 0→1		
23.69604			

Table 1.2: Ammonia hyperfine components as calculated from tabulated data in Townes & Schawlow (1975) and splatalogue.net. The top row lists spectral offset in km/s, the bottom row is relative line strength.

line	component					
	-2	-1	0	1	2	
NH_3 (1,1)	-19.48	-7.46	0	7.59	19.61	[km/s]
	0.111	0.139	0.500	0.139	0.111	
NH_3 (2,2)	-25.91	-16.30	0	16.43	26.03	[km/s]
	0.052	0.054	0.789	0.054	0.052	
NH_3 (3,3)	-29.14	-21.1	0	21.1	29.14	[km/s]
	0.027	0.029	0.888	0.029	0.027	
NH_3 (4,4)	-30.43	-24.22	0	24.22	30.43	[km/s]
	0.016	0.016	0.935	0.016	0.016	
NH_3 (5,5)	-31.41	-25.91	0	25.91	31.41	[km/s]
	0.011	0.011	0.956	0.011	0.011	
NH_3 (6,6)	-31.47	-26.92	0	26.92	31.47	[km/s]
	0.008	0.008	0.969	0.008	0.008	

1.3.2.2 Astrophysical Properties

The previously explained properties of ammonia make it an ideal tool for exploring the ISM. Rotation-dependent inversion frequencies are closely spaced ($\Delta f_{(1,1),(6,6)} \sim 1.3\,\mathrm{GHz}$) while covering a large energy range ($0 < \mathrm{T}_{kin}\,[\mathrm{K}] \lesssim 400$) meaning they can be observed with a single receiver of just one telescope.
Ammonia traces moderately dense gas at $10^4 - 10^6\,\mathrm{cm}^{-3}$ as it requires densities of at least the critical density $\rho_{crit} \sim 10^3\,\mathrm{cm}^{-3}$ to excite higher states. At very high densities of $> 3 \times 10^7\,\mathrm{cm}^{-3}$ (Walmsley & Ungerechts, 1983) or $10^8 - 10^9\,\mathrm{cm}^{-3}$ (Ho & H., 1983), non-metastable levels can be populated in relevant numbers to become observable as well.
Detections of ammonia span a large range of sources from circumstellar envelopes (Betz et al., 1979) over galactic dark clouds (Ho et al., 1978) and nearby galaxies such as NGC 253 (Ott et al., 2005) to heavily star-forming galaxies like ULIRGS (e.g. Arp 220 Ott et al., 2011).
The formation and destruction of interstellar ammonia is closely related to the nitrogen network shown in fig. 1.7. This figure also highlights the main formation channels via electron capture of NH_4^+ and at low temperatures also radiative association of H_2 on NH_2. Destruction proceeds mainly by ion-molecule interactions and the formation of NH_4^+ or photo-dissociation.

1.3.2.3 Ammonia as a Thermometer

Ammonia is a good thermometer because of its inversion lines that cover rotational temperatures from close to absolute zero to thousands of Kelvin when the rotational quantum number J increases. Another handy detail is the hyperfine structure that allows to directly calculate opacities which are needed in order to derive correct temperatures without the need for a background source. The simplest approach is to assume optically thin emission and derive temperatures from the column density, i.e. moment 0 maps. The more sophisticated approach of fitting spectra to solve for several parameters is more complicated but often needed when the thin approximation does not hold in dense gas.
As the occupation of the different rotational states depends on temperature, it is possible to derive this temperature by comparing the column densities of two states. This is done via a so called Boltzmann plot that shows the logarithm of correctly scaled column density of a given state versus the energy of that state above ground. The slope between two such points translates directly into a rotational temperature that in turn can be converted to a kinetic temperature using large velocity gradient (LVG) models. Some attention is needed to account for ortho- and para-ammonia.

Boltzmann Plot

The occupation of different rotational levels follows a Boltzmann distribution and as such the ratio of two column densities becomes a function of temperature. For

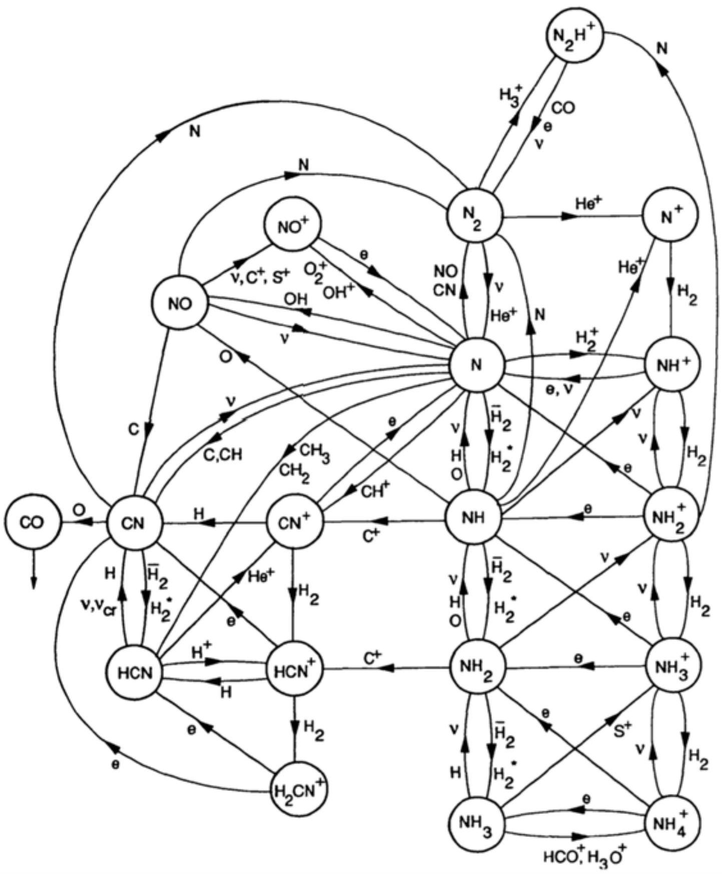

Figure 1.7: NH_3 is part of the complex nitrogen reaction network (fig. 5 of Sternberg & Dalgarno, 1995). Reaction arrows are labelled with reactants like electrons (e), photons (ν), ionized and neutral atoms (C, C^+, N, O, H) and molecules (e.g. H_2, HCO^+).

a state of energy E with excitation temperature T_{ex} of the system, the probability of the system to be in that state is given by

$$p \propto \exp \frac{\mathrm{E}}{k_B \mathrm{T}_{ex}} \tag{1.41}$$

where $k_B = 1.38 \times 10^{-23}$ J/K is the Boltzmann constant. For two metastable inversion lines with rotational numbers J = K, the relative probabilities are called Boltzmann factor and depends only the energy difference ΔE. For rotational states, the temperature T is accordingly called rotational temperature $\mathrm{T}_{JJ'}$ for states J, J' after considering the correct conversion. The probability of being in a certain state can be translated to the number of particles in that state which can be approximated by column densities because only the Boltzmann factor (relative ratio) is needed instead of absolute values. Therefore, the ratio of column density N_u in the upper rotational state u with J or J' can be expressed as

$$\frac{N'_u(J', J')}{N_u(J, J)} = \frac{g(J')}{g(J)} \frac{2J' + 1}{2J + 1} \exp\left(\frac{-\Delta E}{T_{JJ'}}\right) \tag{1.42}$$

with relative weight factors of 2J + 1 and statistical weights g that follow from quantum mechanical considerations as derived in Schilke (1989)
Statistical weights are $g = 1$ for para-ammonia and $g = 2$ for ortho-ammonia because two microscopic states of ortho-NH_3 or one of para-NH_3 make up one macroscopic state.
Eq. 1.42 can be rewritten as

$$\underbrace{\ln\left(\frac{N'_u(J', J')}{g'(2J' + 1)}\right)}_{y'} - \underbrace{\ln\left(\frac{N_u(J, J)}{g(2J + 1)}\right)}_{y} = -\frac{\Delta E}{\underbrace{k_B T_{JJ'}}_{\Delta x/T_{J'J}}} \tag{1.43}$$

which is an equation of simple linear form for the inverse temperature with slope m.

$$m = \frac{\Delta y}{\Delta x} = \frac{y' - y}{\Delta x} \tag{1.44}$$

The corresponding plot is called Boltzmann plot, with energy above ground state on the x-axis and y-axis values derived from measured column densities. For convenience, y is given in logarithms of base 10 instead of e as

$$y = \log_{10}\left(\frac{N(J, J)}{g(J)(2J + 1)}\right) \tag{1.45}$$

which leads to a correction factor of $\log_{10}(e)$ when calculating temperatures.

$$T_{rot} = T_{J,J'} = \frac{-\log_{10}(e)}{m} \tag{1.46}$$

Overall, this means the rotational temperature of ammonia gas can be derived from the slope between two measurements of column density for the known state energies.
This simple derivation is complicated for two reasons: Expressing excitation temperature T_{ex} by physically meaningful and measurable quantities and correctly deriving column densities.

Excitation temperature

For radio frequencies and the expected ISM temperatures ($10^1 \lesssim T\ [K] \lesssim 10^{2.5}$), the Rayleigh-Jeans approximation for black-body emission holds because

$\exp\left(-\frac{h\nu}{k_B\mathrm{T}}\right) \approx -\frac{h\nu}{k_B\mathrm{T}}$. With intensities expressed as line temperatures and considering the limited beam size of a telescope, radiative transfer can be expressed as

$$\mathrm{T}_L(\nu) = n_f \mathrm{T}_{ex}(1 - e^{-\tau}) + n_f \mathrm{T}_{BG}\, e^{-\tau} \tag{1.47}$$

according to Schilke (1989). T_L is the observed line temperature that results from source emission with excitation temperature T_{ex} and background T_{BG} that both passes through a medium with opacity τ. The beam filling factor n_f denotes the fractional area of the beam filled by the source on the sky. For completeness, it will be dragged along in further equations but set to unity in all calculations as it is generally unknown but close to 1 for the extended emission considered in this thesis.
Solving for T_{ex} results in

$$\mathrm{T}_{ex} = \frac{\mathrm{T}_L}{n_f(1 - e^{-\tau})} + \mathrm{T}_{BG} \tag{1.48}$$

Background temperature T_{BG} is set by the cosmic microwave background (CMB) at 2.7 K.

Column Density

The starting point for calculating column densities is identical for both optically thin emission and full opacity considerations. It is always given by

$$\mathrm{N(J,K)} = \frac{3h}{8\pi^3} \frac{\mathrm{J(J+1)}}{\mathrm{K}^2} \frac{1}{\mu^2} \frac{k_B}{h\nu_{\mathrm{JK}}} \int \mathrm{T}_{ex}\, \mathrm{d}v \tag{1.49}$$

$$\tag{1.50}$$

Differences are only in the calculation of the velocity integral over excitation temperature.

Column Density in the Optically Thin Limit

Assuming optically thin emission, column densities can simply be derived from observed intensities with the appropriate scaling factors because every detected photon directly corresponds to one molecule. Following Ott et al. (2005), Ott et al. (2014) and Mills & Morris (2013) based on Hüttemeister et al. (1993), Hüttemeister et al. (1995) and Mauersberger et al. (2003), the column density N in state (J,K) depends on electric dipole moment μ in Debye and line brightness temperature T_{mb} as

$$
\begin{aligned}
\mathrm{N(J,K)}\,[\mathrm{cm}^{-2}] = 1.6698 \cdot 10^{14} \cdot \frac{\mathrm{J(J+1)}}{\mathrm{K}^2} \frac{1}{\mu^2\,[\mathrm{D}^2] \cdot \nu\,[\mathrm{GHz}]} \\
\cdot \int_{line} \mathrm{T}_{mb}\; dv\,[\mathrm{K\,km/s}]
\end{aligned}
\tag{1.51}
$$

$$
= \frac{7.77 \times 10^{13}}{\nu\,[\mathrm{GHz}]} \frac{\mathrm{J(J+1)}}{\mathrm{K}^2} \int_{line} \mathrm{T}_{mb}\; dv\,[\mathrm{K\,km/s}] \tag{1.52}
$$

Eq. (1.51) lists the general formula for any symmetric top molecule with dipole moment μ whereas eq. 1.52 already includes $\mu = 1.472\,\mathrm{D}$ and shows the form given in the literature.
The data cube structure in discrete channels simplifies the integration in velocity over the spectral line to a summation of spectral channels, which in turn is just the definition (1.20) of moment zero flux F_{mom0}.

$$
\begin{aligned}
\mathrm{N(J,K)}\,[\mathrm{cm}^{-2}] = 1.6698 \cdot 10^{14} \frac{\mathrm{J(J+1)}}{\mathrm{K}^2} \cdot \frac{1}{\mu^2\,[\mathrm{D}^2] \cdot \nu\,[\mathrm{GHz}]} \\
\cdot \sum_{line} \mathrm{T}_i\; \Delta v_{chan}\,[\mathrm{K\,km/s}]
\end{aligned}
\tag{1.53}
$$

$$
= \frac{7.77 \times 10^{13}}{\nu\,[\mathrm{GHz}]} \frac{\mathrm{J(J+1)}}{\mathrm{K}^2} \mathrm{F}_{mom0}\,[\mathrm{K\,km/s}] \tag{1.54}
$$

The error is calculated by simple Gaussian error propagation that traces back to the RMS noise of the data cube used to calculate the moment map as explained in §1.2.5.3.

$$
\Delta\mathrm{N(J,K)} = \frac{7.77 \times 10^{13}}{\nu} \frac{\mathrm{J(J+1)}}{\mathrm{K}^2}\; \Delta \left(\int_{line} \mathrm{T}_{mb}\; \mathrm{d}v \right) \tag{1.55}
$$

$$
= \frac{7.77 \times 10^{13}}{\nu} \frac{\mathrm{J(J+1)}}{\mathrm{K}^2}\; \Delta\mathrm{F}_{mom0} \tag{1.56}
$$

Column Densities Considering Opacity

By solving the radiative transfer equation, it is possible to derive an expression for the column density without assuming high or low optical depth, because an exact solution for the relation of T_{ex} and observed brightness temperature is known (Schilke, 1989).
The derivation starts again from the general approach (1.49) but then solves the integral over a spectral line of Gaussian shape with excitation temperature as in (1.48). The area under a Gaussian is generally given by

$$
\mathrm{A} = \frac{\sqrt{\pi}}{2\sqrt{\ln 2}} \cdot \mathrm{peak} \cdot \mathrm{FWHM} \tag{1.57}
$$

where peak = T_L and FWHM = Δv_{int} for a hyperfine line. This means the integral becomes

$$\int \mathrm{T}_{ex}\, dv = \frac{\sqrt{\pi}}{2\sqrt{\ln 2}} \Delta v_{int} \frac{\mathrm{T}_{ex}\tau}{f_{\mathrm{J}}} \tag{1.58}$$

$$= \frac{\sqrt{\pi}}{2\sqrt{\ln 2}} \Delta v_{int} \frac{\mathrm{T}_L \tau}{n_f f_{\mathrm{J}} \left(1 - e^{-\tau}\right)} \tag{1.59}$$

T_L denotes line peak intensity and must not be confused with integrated line intensity T_{mb} used before. Δv_{int} stands for the fitted FWHM of a single hyperfine component.
Calculating all numerical factors and logically rearranging the parts to match eq. (1.51)-(1.56) results in

$$\begin{aligned} \mathrm{N(J,K)} = {} & 1.77745 \cdot 10^{14}\,\mathrm{cm}^{-2} \\ & \cdot \frac{\mathrm{J(J+1)}}{\mathrm{K}^2} \frac{\Delta v_{int}\,[\mathrm{km/s}]}{(\mu\,[\mathrm{D}])^2\ \nu\,[\mathrm{GHz}]} \frac{\tau\ \mathrm{T}_L\,[\mathrm{K}]}{f_{\mathrm{J}}\left(1 - e^{-\tau}\right)} \end{aligned} \tag{1.60}$$

$$\begin{aligned} \Delta \mathrm{N}_l(\mathrm{J,K}) = {} & 1.77745 \cdot 10^{14}\,\mathrm{cm}^{-2} \cdot \frac{\mathrm{J(J+1)}}{\mathrm{K}^2} \frac{1}{f_{\mathrm{J}}\ \mu^2\ \nu} \\ & \cdot \left[\left(\frac{\Delta \mathrm{T}_L\ \Delta v_{int}\ \tau}{(1 - e^{-\tau})} \right)^2 + \left(\frac{\mathrm{T}_L\ \Delta(\Delta v_{int})\ \tau}{(1 - e^{-\tau})} \right)^2 \right. \\ & \left. + \left(\mathrm{T}_L\ \Delta v_{int} \frac{e^{\tau}(e^{\tau} - \tau - 1)}{(e^{\tau} - 1)^2)} \right)^2 \right]^{1/2} \end{aligned} \tag{1.61}$$

The prefactor applies when the beam filling factor is set to unity, line width Δv_{int} is given in km/s, dipole moment μ in Debye, frequency of the inversion line in GHz and line peak intensity in Kelvin. f_{J} is a factor to correct the fitted opacity τ for its line profile and is basically the ratio of flux in the central hyperfine component (see Schilke (1989) for details). Table 1.3 lists all necessary parameters of the (J,K) = (1,1) to (6,6) that are needed in eq. (1.61).
As these formulae are derived in the most general way possible, it is not necessary to discriminate several opacity regimes (Chira et al., 2013).

Rotational to Kinetic Temperature Conversion

For low temperatures, rotational and kinetic temperature are almost identical but the deviation increases with temperature and quickly becomes too large to be negligible. Reasons for this behavior are the increasing number of energetically available non-metastable levels for depopulation of higher metastable states and radiative decay (Walmsley & Ungerechts, 1983). Towards high kinetic temperatures, the conversion flattens out which decreases the ability to correctly discern temperatures. Especially, the lower states are affected, effectively setting an upper

Table 1.3: Frequency, energy level and line form factor of the ammonia inversion transitions covered by SWAG.

(J,K)	ν [GHz]	E [K]	$f_{\rm JK}$
(1,1)	23.69447	24.4	0.500
(2,2)	23.72263	65.6	0.796
(3,3)	23.87013	124.7	0.894
(4,4)	24.13942	201.7	0.935
(5,5)	24.53292	296.5	0.956
(6,6)	25.05596	409.2	0.969

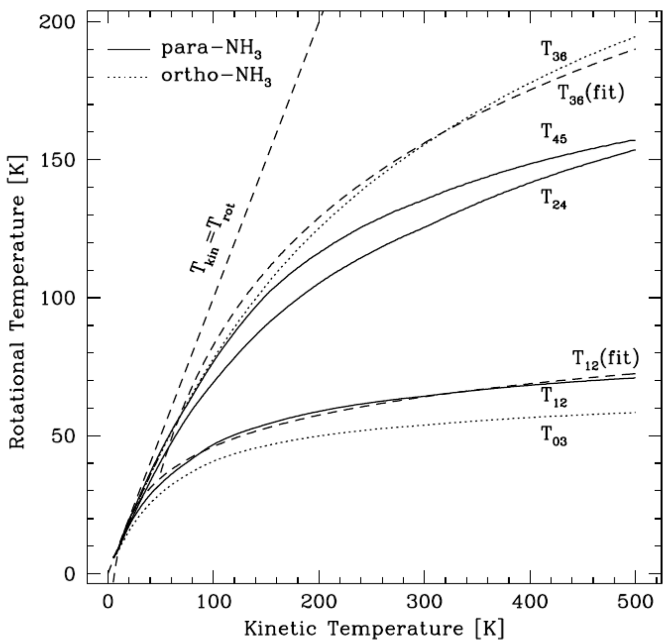

Figure 1.8: LVG simulations with exponential fits of the conversion factor between rotational temperature T_rot and kinetic temperature T_kin (fig. 5 of Ott et al., 2011).

limit above which the tracer becomes unreliable as even small changes in T_{rot} by fluctuations within the error margin translate to kinetic temperature changes of a factor $\gg 1$.

LVG radiative transfer models allow to derive approximations to the conversion of rotational to kinetic temperature. Ott et al. (2011) calculated LVG grids for temperatures up to 500 K for metastable ammonia species up to (6,6) and fitted the results with exponential functions. It can be seen in fig. 1.8 that the drawn fits for T_{12} and T_{36} and are not perfect but agree with the true curve within less than 5%.

The resulting formulae to convert T_{rot} to T_{kin} for four possible temperature measures that can be derived from ammonia lines up to (6,6) are listed below.

$$\mathrm{T}_{kin,12} = 6.05 \cdot \exp(0.06088\,\mathrm{T}_{rot,12}) \tag{1.62}$$

$$\mathrm{T}_{kin,24} = 1.467\,\mathrm{T}_{rot,24} - 6.984 \qquad 0\,\mathrm{K} \lesssim \mathrm{T}_{kin} \lesssim 100\,\mathrm{K} \tag{1.63}$$

$$= 27.085 \cdot \exp(0.019\,\mathrm{T}_{rot,24}) \qquad 100\,\mathrm{K} \lesssim \mathrm{T}_{kin} \lesssim 500\,\mathrm{K} \tag{1.64}$$

$$\mathrm{T}_{kin,36} = \mathrm{T}_{rot,36} \qquad 0\,\mathrm{K} \lesssim \mathrm{T}_{kin} \lesssim 50\,\mathrm{K} \tag{1.65}$$

$$= 28.87511 \cdot \exp(0.015\,\mathrm{T}_{rot,36}) \qquad \mathrm{T}_{kin} > 50\,\mathrm{K} \tag{1.66}$$

$$\mathrm{T}_{kin,45} = 1.143\,\mathrm{T}_{rot,45} - 1.611 \qquad 0\,\mathrm{K} \lesssim \mathrm{T}_{kin} \lesssim 50\,\mathrm{K} \tag{1.67}$$

$$= 21.024 \cdot \exp(0.0198\,\mathrm{T}_{rot,45}) \qquad 50\,\mathrm{K} \lesssim \mathrm{T}_{kin} \lesssim 500\,\mathrm{K} \tag{1.68}$$

1.3.3 Interstellar Dust

Despite the low amount of mass that is in the form of interstellar dust, it is a crucial agent in the ISM with complex physical interactions. Depending on environmental conditions and the specific element, 66 − 90% of metals are locked up in dust grains (Draine, 2011) and are not immediately available to astrochemistry but strongly influence the ISM's thermal balance.

Dust grains are dozens of Å up to cm sized accumulations of metals and ices of porous or compact structure providing large surface areas for interactions. Chemical compositions are diverse and include silicates, ices, metal oxides, hydrocarbons, polyaromatic hydrocarbons (PAHs), carbides and other carbon solids (e.g. graphite) but the detailed chemistry is still subject to fundamental research (Draine, 2003). Many chemical interactions cannot proceed efficiently in the gas phase but need a surface as catalyst that is provided by dust (grain surface chemistry). This is the case for many molecule formation paths such as H_2 or the important dense gas tracer CO which need a medium to absorb excess energy that would otherwise break up the molecule right after its formation.

Due to its composition, dust causes high optical extinction that provides shielding from energetic radiation to deeper layers of a cloud, but it is hard to study for the same reason, and observations are mostly done in infrared wavelengths. Important spectral features of dust are the 2175 Å extinction bump or diffuse interstellar bands (DIBs) in absorption that are not well understood, as dust is very complex in composition. Beside absorbing radiation, dust can also be heated by collisions (shocks) while it cools by emitting IR photons. Studies found 15% − 50%, typically 30%, of stellar radiation energy is absorbed and re-emitted by dust in the IR (e.g. Calzetti, 2001; Popescu & Tuffs, 2002). Because of the many available transitions in grain lattice vibrations, cooling is very efficient and dust can act as a coolant of the surrounding gas as in the Galactic Center (e.g. Lis et al., 2001; Molinari et al., 2011; Nagayama et al., 2009). Similar to molecules, the amount of emission at different wavelengths depends on temperature and by using radiative transfer models, it is possible to calculate dust temperatures from IR dust emission (e.g. Hi-GAL Molinari et al., 2011). In disk clouds, dust and dense gas temperature generally agree as they are coupled by collisions at high column densities; however,

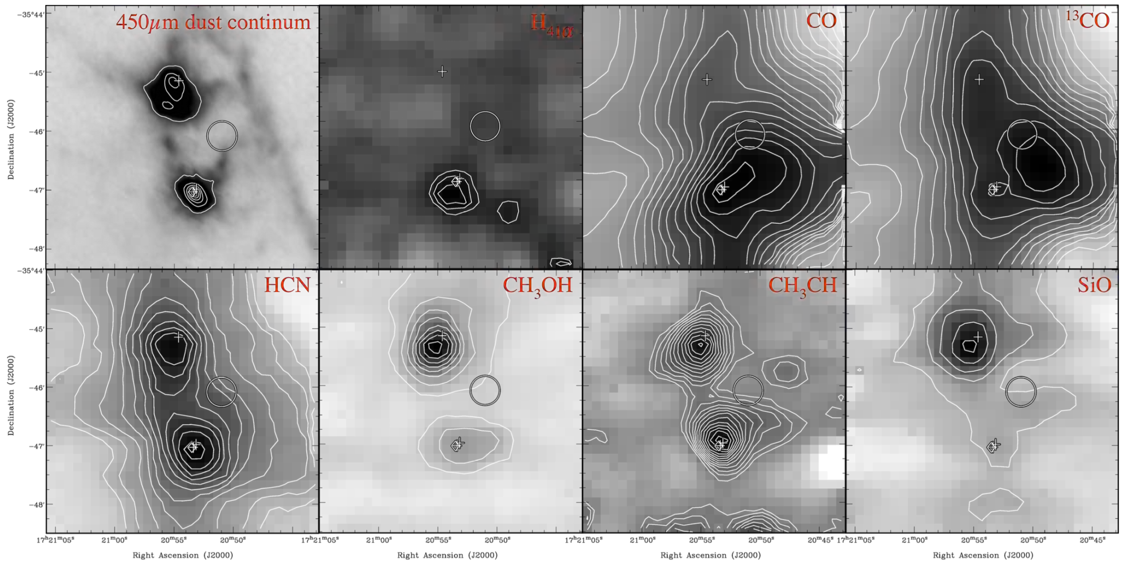

Figure 1.9: The giant molecular cloud NGC 6334 as seen in different tracers (figure adapted from Walsh et al., 2010). Contours and grey scales of the panels are independent and rather show the spatial distribution. Less dense gas traced by CO is widespread whereas higher density gas (HCN) is confined to a smaller region and the most complex molecules are detected in the two cores only.

this was found to be not the case in the Galactic Center (Lis et al., 2001; Molinari et al., 2011). Depending on the conditions, dust can act as an independent proxy for ISM gas temperature or reveal a more complex environment as in the GC which allows to understand the physical processes.

1.3.4 Molecular Clouds

Dense gas occurs in the form of filamentary structure and clouds of various sizes where most of the gas mass is found in giant molecular clouds (GMC) of $\sim 5-200\,\mathrm{pc}$. Their masses are typically $10^2 - 10^7\,\mathrm{M}_\odot$ with densities of several cm^{-3} up to $> 10^8\,\mathrm{cm}^{-3}$ in cloud cores. Despite their name, a significant amount of mass is still in atomic form and typical molecular abundance ratios $\mathrm{M}_{H_2}/\mathrm{M}_{HI} \sim 0.3$ with 0.4 dex scatter. Large amounts of dust can be formed and survive in molecular cloud conditions by (self-)shielding, which causes extinction not only in the visible spectrum, but also infrared light can be absorbed (infrared dark clouds). Surface densities range from tens to $> 200\,\mathrm{M}_\odot/\mathrm{pc}^2$ leading to visual extinction by gas and dust of $0.5 < \mathrm{A_V} < 5$. Cloud population masses follow a power law mass spectrum $\mathrm{dN/dM} \sim \mathrm{M}^{-\gamma}$ with $\gamma < 2$ (Krumholz, 2014, and references therein).
The molecular content of a cloud is mainly H_2 by mass that survives dissociation by the shielding effect of upper layers of gas and dust. Towards the central regions, densities and path lengths to the outside increase which is why more complex, less strongly bound and less abundant molecules are found there as shown in fig. 1.9 for a few tracers in the giant molecular cloud NGC 6334. The temperature

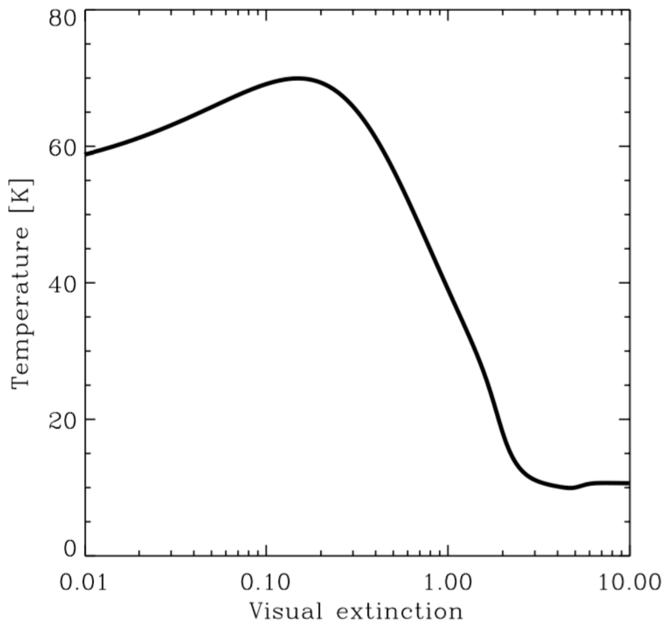

Figure 1.10: Molecular cloud temperature as a function of visual extinction. Extinction scales with column density and therefore is a proxy of optical path length or depth in the cloud. The central core can cool down to $< 30\,\mathrm{K}$, which is below the ambient temperature of the surrounding less dense gas.

accordingly decreases as we move inwards because radiative cooling is possible by escaping photons of infrared or sub-mm lines while external heating sources are shielded by upper cloud layers.
Some basic cloud properties were empirically found to be related by Larson (1981) in three so-called Larson laws. These scaling relations can be explained theoretically with the gravitational and hydrodynamic properties and were re-examined by Heyer et al. (2009) and others (e.g. Solomon et al. (1987), Blitz et al. (2007), Lombardi et al. (2010), or for extra-galactic GMCs in Bolatto et al. (2008)) found to be universal within scatter.

$$I \qquad \sigma = 1.10 L^{0.38} \qquad \text{dispersion - size relation} \tag{1.69}$$
$$II \qquad \sigma = 0.42 M^{0.20} \qquad \text{dispersion - mass relation} \tag{1.70}$$
$$III \qquad < n(\mathrm{H_2}) > = 3400 L^{-1.10} \qquad \text{column density - size relation} \tag{1.71}$$

where velocity dispersion σ [km/s], cloud size L [pc], mass M [$\mathrm{M_\odot}$] and mean H_2 column density $< n(\mathrm{H_2}) >$ [$\mathrm{cm^{-3}}$].
One of the major unknowns in molecular clouds is the question about their lifetimes and stability. The virial parameter $\alpha = 5\sigma^2 R/GM \simeq 2T/W$ parametrizes if a cloud of size R and mass M is a transient feature or gravitationally stable by quantifying the ratio between kinetic energy T and gravitational energy W (Bertoldi & McKee, 1992). According to the virial theorem, $\alpha \lesssim 1$ means the gravitational binding energy dominates and the cloud collapses on the free-fall

time scale $\tau_{ff} = \sqrt{\frac{3\pi}{32\mathrm{G}\rho}}$ if no other relevant forces are present whereas for $\alpha \gtrsim 1$, internal kinetic energy dominates and the cloud would disperse if not confined by external pressure. A cloud's development and ability to form stars by (partial) collapse is therefore crucially depended on the environment (e.g. Meidt et al., 2013).
Cloud collapse is described by Jeans instability (Jeans, 1902) that occurs when internal pressure cannot prevent a spherical cloud from becoming self-gravitating. At the edge of stability/instability, hydrostatic equilibrium must apply which can be translated to a comparison of time scales. If free-fall time τ_{ff} is shorter than sound crossing time $\tau_{sound} = R/c_s$, a compressive perturbation cannot be counteracted quickly enough by pressure to restore equilibrium and the cloud collapses. For $\tau_{ff} = \tau_{sound}$, an instability length scale $\lambda_J = c_s/\sqrt{G\rho}$ can be derived describing the typical sizes of molecular clouds at given density ρ. Although real clouds are not spherical but often form elongated filaments (for example due to shear), the argument roughly holds as can be seen in the Galactic Center for instance (§1.4). These time scales are of the order one to several of Myr for typical GMCs which is much faster than observed lifetimes in extra-galactic ($> 100\,\mathrm{Myr}$), and galactic ($\sim 25\,\mathrm{Myr}$) clouds. However, these numbers must be taken with caution as observed cloud sizes and masses differ in galactic and extra-galactic sources due to observational effects such as varying beam filling factors, sensitivity or resolution. The Jeans criterion of cloud stability does not include non-thermal motions (turbulence), rotation or magnetic fields whose influence on cloud evolution are currently researched and actively discussed. Turbulence adds additional energy to the system that helps counteracting gravitational pressure and can stabilize massive or dense clouds that would otherwise actively form stars. Magnetic fields are relevant for molecular clouds because even low ionization fractions of the gas allow magnetic coupling and flux freezing, which adds another cloud internal pressure term. Today, it is presumed that both turbulence and magnetic fields are important at varying fractions for cloud stability (e.g. Crutcher, 2012).
Beginning and end of the turbulent[9] life of a giant molecular cloud are more difficult to infer from the static observations over a human lifetime. Several mechanisms can locally enhance the gas density to form molecular clouds, such as formation by local converging flows, spiral-arm induced instability, gravitational instability or magneto-Jeans instability. A cloud's death by mass loss and disruption can be accompanied by star formation or proceed without any sign of star formation. Externally driven turbulence, for instance, can heat up and disperse the gas destroying molecules by energetic radiation and cosmic rays from the surrounding ISM without any cloud core forming a single star. If the cloud collapses and forms stars, it will not survive either because shocks, jets and radiation (in general called stellar feedback) will attack it inside out and blow away the remaining gas making them a transient feature of the ISM.

[9] pun intended

1.3.5 Star Formation

When a cloud collapses to smaller size and higher density, its core will eventually pass the limit for hydrogen fusion and a star is born. In massive clouds like GMCs that are relevant for this thesis, enough mass is present for the formation of dozens to thousands of stars bound in a cluster configuration. As a new star is still embedded in its birth cloud that is dispersed over a certain timescale, stages of early star formation (SF) are detected in infrared or as masers. The vastly deviating scales involved in star formation from $R_\odot \sim 10^{-8}$ pc sized stars in cloud cores of several pc in large GMCs that can be up to 200 pc across, make it difficult to understand and model these early phases.

When a cloud core collapses far enough to become a star, it is called young stellar object (YSO), which covers the two phases of protostar and pre-main sequence (MS) star. In the core, temperature and pressure start to rise because cooling becomes less efficient in the dense material while molecule dissociation absorbs the released gravitational energy. The now atomic core cannot maintain equilibrium but collapses further into a protostar with drastically higher temperatures and pressures. Accretion onto the protostar continues as onto the core before and is responsible for most of its luminosity $L_{acc} = GM_*/R_* dM/dt$ (Stahler & Palla, 2005). This emission itself and processing and re-radiation by surrounding dust is in mid- and far-infrared wavelengths and can escape the protostar and its birth cloud to be detectable as a compact source. The stellar radiation is mostly created at the accretion shock front where it hits the protostar's denser surface. In later evolution stages, pre-MS stars can also be detected by their outflows and jets.

The role of masers in high mass star formation is not fully understood today but they are known to occur in YSOs (Beuther et al., 2002). The population inversion is thought to be pumped by stellar winds and results in maser detections of various molecules. Theory suggest that H_2O masers originate near the protostar's surface while OH masers are situated higher up in the circumstellar material (Forster & Caswell, 1989; Genzel & Downes, 1977).

The general course of action of star formation is known today as outlined above. However, there are still fundamental problems which are mutually related and subject to current research. The initial mass function (IMF) which describes the mass distribution of stars is constructed empirically (e.g. Salpeter, 1955, Chabrier, 2003, Kroupa et al., 2013 and others) but is uncertain and can so far not be reconstructed satisfactorily from theoretical arguments. The other major problem in understanding star formation is the apparent inefficiency when comparing the amount of available gas to current SF and young stars.

Historically, the most simple picture was assumed that clouds collapse by becoming self-gravitating and subsequently convert most of the gas into stars. Simulations then found extremely high star formation rates that are not observed beside a few star bursting galaxies, most of them at high redshifts. Additional effects are obviously engaged in the process as well. Turbulence, magnetic fields and stellar feedback all prevent clouds from collapsing and slow down evolution.

As mentioned before, there is a correlation between (molecular) gas and star formation quantified by the star formation law (Kennicut-Schmidt law, Kennicutt, 1998; Schmidt, 1959). It relates star formation rate surface density Σ_{SFR} to total or molecular gas mass surface density Σ_{gas} in $\mathrm{M_\odot/yr/pc^2}$ as

$$\Sigma_{SFR} \propto \Sigma_{gas}^{n} \tag{1.72}$$

Kennicutt (1998) found $n = 1.4 \pm 0.15$ for HI observations as the average over 100 nearby galaxies while Schmidt (1959) originally suggested $n \sim 2$. Applying this scaling relation to the Central Molecular Zone in the Galactic Center would imply an enormous star formation rate of $\sim 0.7 - 0.9\,\mathrm{M_\odot/yr}$ (Longmore et al., 2013) whereas $\sim 0.1\mathrm{M_\odot/yr}$ is observed (e.g. $0.14\,\mathrm{M_\odot/yr}$, Yusef-Zadeh et al., 2009 and $0.08\,\mathrm{M_\odot/yr}$, Immer et al., 2012). Under the special conditions in this region, star formation must therefore be much more inefficient than in the galactic disk.
A third major problem is the lack of information about absolute time scales of SF, as for many astronomical processes that appear static to human perception. It is impossible to directly observe the star formation process from cloud formation over collapse to young unobscured stars and measure the duration of each phase. Chronological information must therefore be gained from logical organization of observed snapshots of different objects. Various approaches are followed to estimate durations and absolute time information beyond just ordering phases of star formation. By counting the abundance of sources of a given phase relative to the others, it is possible to derive relative durations that can be converted to absolute timescales if any duration is known (Kawamura et al., 2009). Another possibility is when cloud or star formation gets triggered at a known point in time, sources known to be located after that point can be assigned an absolute time. This was done by Meidt et al. (2015) for cloud formation by spiral arm density waves in M51 and yielded cloud lifetimes of $20 - 30\,\mathrm{Myr}$. Measures of star formation time-scales vary strongly due to strong differences in environment and employed technique. Cloud lifetimes as short as one free-fall time of $\tau_{ff} \sim 10^4 - 10^5\,\mathrm{yr}$ are observed in massive Galactic clumps (Tackenberg et al., 2012) while in nearby molecular clouds slow star formation occurs with molecular cloud depletion times $t_{dep} \sim 25\tau_{ff} = 40\,\mathrm{Myr}$ and $t_{dep} = 1.8\,\mathrm{Myr}$ in dense cores (Evans et al., 2009). Other groups found evolution time-scales of a few Myr (Hartmann et al., 2012, nearby molecular clouds) and further estimates can be derived from the Kennicutt-Schmidt law that yields depletion times of several hundred Myr up to Gyr when whole galaxies are taken into account. This means star formation time scales are strongly dependent on environment and the scale on which they are observed beside being extremely difficult to infer from observations.
As $\sim 50\%$ of today's star were formed at the peak of the cosmic star formation history at $z \sim 2 - 3$ (Madau & Dickinson, 2014), it is important to understand SF under those conditions, which were very different from the observed disks of today's star forming galaxies. High densities, pressures and radiation fields have a direct impact on star formation, its efficiency and the related time scales. Luckily, these conditions are matched by the relatively near ($\sim 8.5\,\mathrm{kpc}$) center of the Milky Way and a SF trigger may allow setting a starting point in time to construct an absolute time sequence (Kruijssen et al., 2015; Longmore et al., 2012). The aim

of this thesis is to test if such a star formation sequence in the Galactic Center actually is present or not by investigating potential evolution of molecular cloud properties as traced by ammonia.

1.4 Galactic Center and Central Molecular Zone

The central $\sim$ 500 pc of the Milky Way, the center being marked by the supermassive black hole Sgr A*, is called the Central Molecular Zone (CMZ) due to the large amounts of molecular gas found there. It is a peculiar environment that differs significantly from typical disk ISM and poses additional challenges but also a unique opportunity to understand star formation in high spatial resolution.
Fig. 1.11 shows the inner region on the CMZ, approximately 250 pc across, traced by ammonia (3,3) emission. Several landmarks emit this spectral line such as Sgr B2, one of the most massive GMCs in the Milky Way, that is thought to be the precursor of a massive stellar cluster (Walker et al., 2015). Some smaller molecular clouds at positive longitudes were named by Lis et al. (1999) along a coherent structure (Brick, cloud d, e, f, Sgr B2) that was dubbed "dust ridge" due the large amount of dust detected there. The asymmetry in gas distribution with Galactic longitude is immediately visible, only small and comparatively thin clouds are detected east of the 20 km/s cloud. Most of the projected emission is placed at Galactic Center distances and can be assumed to be part of the CMZ with a few exceptions, like a cloud at $l \sim -0.4°$ (Longmore et al., 2013). Two stellar clusters close to the Galactic Center (Arches and Quintuplett) are invisible in fig. 1.11 but located close to the gas streams in projection. Their 3D position is debated (e.g. Stolte et al., 2008) but might prove important for testing the kinematic star formation model by Longmore et al. (2013) and Kruijssen et al. (2015) explained in the following sections.
The large reservoir of molecular gas in the CMZ adds up to M $\sim 5 \times 10^7\,\mathrm{M}_\odot$ (Ferrière et al., 2007; Morris & Serabyn, 1996) at densities much higher than in the disk with a mean of $\sim 10^4\,\mathrm{cm}^{-3}$ compared to $10^2\,\mathrm{cm}^{-3}$ in the disk (Longmore et al., 2013). Such high densities imply a star formation rate of $\sim 0.7-0.9\,\mathrm{M}_\odot/\mathrm{yr}$ according to the star formation law (Kennicutt, 1998) while only $0.08-0.14\,\mathrm{M}_\odot/\mathrm{yr}$ is observed (Immer et al., 2012; Yusef-Zadeh et al., 2009). The reason is suspected to be the highly turbulent medium with Mach numbers up to $\mathcal{M} \sim 30$ and significantly higher temperatures than in disk of 50 to $> 100\,\mathrm{K}$ ($\mathrm{T}_{disk} \sim 10-30\,\mathrm{K}$ in the CNM). These conditions are similar to high-z star forming and star bursting galaxies at $z \sim 2-3$ which is why the CMZ was given the nickname of "nearest high redshift galaxy". Understanding the physics of the CMZ at moderate distance therefore enable us to understand how most of today's stars formed. The peak of the cosmic star formation history occurs around $z = 2-3$ and 50% of stars formed earlier than $z \sim 1.3$ (Madau & Dickinson, 2014).
Gas and dust in the CMZ is structured in a ring-like feature of $\sim$ 100 pc radius that follows the dust ridge (l^+, b^+ stream), turns to the far side near Sgr B2 (l^+, b^-) to pass behind Sgr A* and close the apparent "ring" through the negative longitude streams l^-, b^+, the GMC Sgr C, and l^-, b^-. Recent observational hints (Longmore et al., 2013) brought up the idea of a triggered star formation sequence in the dust ridge and two kinematic models to describe gas motions (Kruijssen et al., 2015; Krumholz & Kruijssen, 2015; Molinari et al., 2011). Understanding

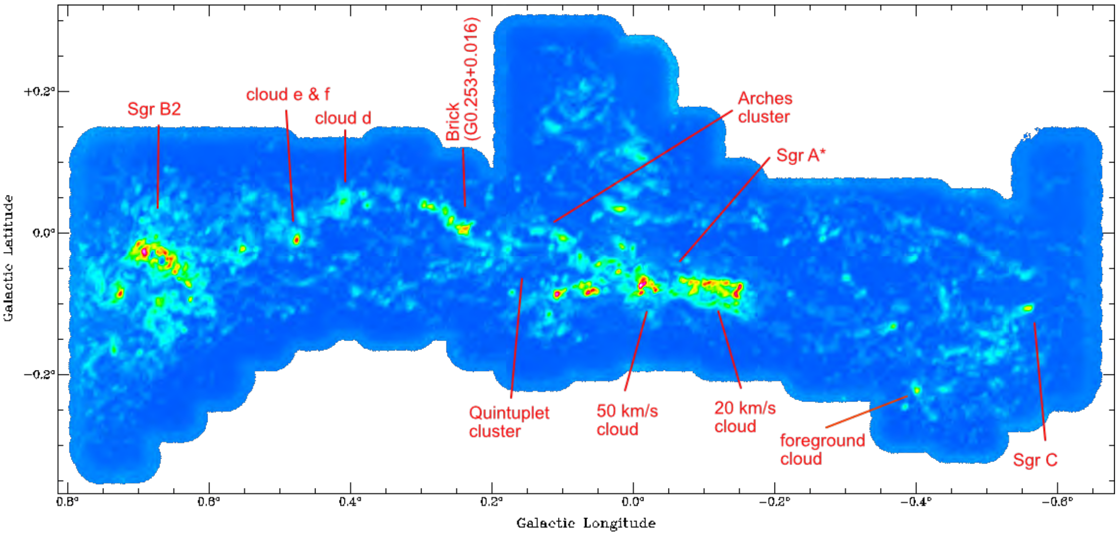

Figure 1.11: Molecular gas distribution in the CMZ (NH_3 (3,3) peak intensity; Krieger et al., 2016, in prep.). The warped ring-like structure of dense gas is immediately visible from Sgr C to the 20 and 50 km/s clouds, dust ridge (Brick, cloud d, e, f, Sgr B2) and less apparent on the far side at l^+, b^- to $l = b = 0$ and l^-, b^+.

the thermal properties of the dense gas is key to understanding star formation in this peculiar environment as temperature sets sound speed which in turn sets the Mach number $\mathcal{M}$ that is used to characterize turbulence which inhibits star formation.

1.4.1 Gas Kinematics in the CMZ

Currently, two models for the intermediate scale (30 pc $\lesssim$ r $\lesssim$ 250 pc, cloud size < r < whole CMZ) gas kinematics are known in the literature: the twisted ring model by Molinari et al. (2011) and a gas stream model by Kruijssen et al. (2015) as its successor. Gas at the smaller scales of clouds must be described for each cloud individually and take the differing phases of internal star formation or environment into account. Large scale dynamics are set by the Milky Way's bar potential that allows two families of orbits, namely $x1$ orbits along the bar and smaller[10] $x2$ orbits perpendicular to it (Binney et al., 1991). Qualitatively, gas and stars on $x1$ orbits make up the bar on scales of several hundreds of parsecs while $x2$ orbits were historically associated with the CMZ due to the matching sizes of $\sim$ 100 pc. However, the existence of gas or stars moving on $x2$ orbits is still unclear.
Star formation in the inner Milky Way in general and the CMZ specifically is fuelled by gas from the disk being funnelled to the center through the bar and $x1/x2$ orbits. The inward transport of matter requires losing angular momentum through shear. At Galactic radii of roughly 100 pc, however, a shear minimum occurs and infalling gas accumulates in a ring-like structure where densities are high enough to sustain

[10] meaning shorter major and minor axes

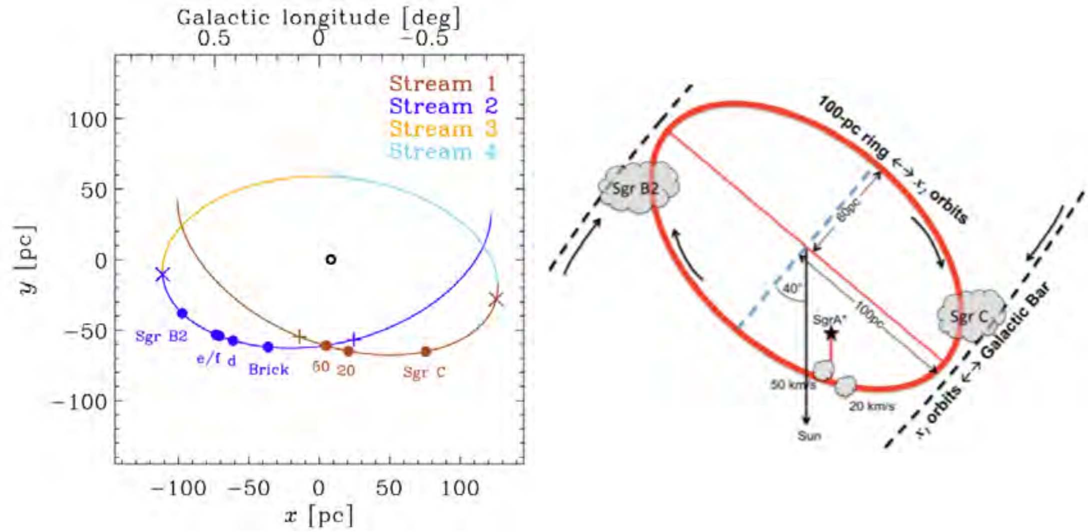

Figure 1.12: *left*: Fig. 6 of Kruijssen et al. (2015) showing a top-down view on the Galactic Center in the stream model. Note that Sgr A* (black circle) is at the center and streams do not connect to a closed ring. *right*: The corresponding view in the ring model (fig. 5 of Molinari et al., 2011) highlighting the close proximity of the gas/dust ring to Sgr A*.

substantial gas masses in molecular form, the CMZ. Individual clouds are formed in the streams at Jeans scale sizes ($10-30$ pc) by Jeans instability whereas a large scale asymmetry (l^+, l^-) is induced by a larger mode of instability (wavelength ~ 100 pc). This gas and dust is parametrized in two models: a ring and a stream model.

1.4.1.1 Molinari Ring Model

The accumulated gas in the Galactic Center was described as a closed elliptical ring of cold dust by Molinari et al. (2011) as it showed up in the Hi-GAL (Molinari et al., 2010b) survey temperature map that was derived from Herschel[11] observations at 70, 160, 250 and 350 μm. They applied a simple model of a twisted, elliptical ring to PPV (longitude, latitude, velocity) data with best-fit parameters of 100 pc and 60 pc semi-major axis at 40° inclination and 2:1:1 ratio of vertical to radial to polar frequency. The bottom of the Galactic potential marked by Sgr A* was found to be displaced from the center or the foci of the ring and located a mere 24 pc from the front side. This peculiar structure requires gas on the ring to pass deeply in the gravitational potential but be much farther from the center (> 100 pc) at the outer vertices.

[11] www.cosmos.esa.int/web/herschel/home

1.4.1.2 Kruijssen Stream Model

The kinematic model of Kruijssen et al. (2015) is more complex than the simple Molinari ring but provides a better fit to the data and is embedded in a more general model for the formation of gas rings in galactic centers where gas builds up and star bursts occur when certain thresholds are reached.

The model was originally derived from NH_3 data of the H_2O Southern Galactic Plane Survey (HOPS) (Walsh et al., 2011) in PPV space. Key properties of the ring model are preserved as is eccentricity of the orbit and vertical oscillation but a better fit as measured by reduced χ^2 was obtained. Observed gas distributions are explained as connected gas streams that do not close to a ring but instead are open ended which is much more likely as the extended mass distribution in the CMZ would need to be in a matching non-axisymmetric potential to form closed orbits. The discontinuity in phase space at $l \sim 0.2°$ (see fig. 1.13 bottom panel: connection of stream 1 to stream 2) is problematic for the ring model but can be explained naturally as ends in the stream model. Other major differences are better matching Sgr B2 proper motions, a larger orbital extend and the fact that Sgr A* is now placed in one focus of the orbit where it is expected. The key aspect of the the star formation theory explained in §1.4.2, however, is not affected: There is still significant variation in distance to the potential center along the orbit and therefore variation in strength of tidal forces.

The streams do not have a physical meaning but rather are just a way of specifying the kinematic group to which a particular cloud belongs. Fig. 1.13 shows two projections in g_{lon}, g_{lat} and g_{lon}, v_{los} that illustrate the problem of three distinct kinematic entities (streams 1, 2 and 3/4) lying atop each other in projection because the streams wrap around the Galactic Center 1.5 times. The better fit to the PPV data is achieved at the cost of more effort to correctly discern the streams and label a cloud correctly.

The model makes several predictions about proper motions, gas column densities and star formation. The latter will be tested in this thesis in chapter 3. Underlying assumptions are the axisymmetric gravitational potential and geometric properties that cannot be tested in this work. Remaining open questions of the model target the streams (gaps, asymmetry, relation to $x2$ orbits) and the relation to Arches and Quintuplett clusters in the context of a triggered star formation sequence.

1.4.2 Proposed Star Formation Sequence

The idea of a star formation sequence (SFS) in the CMZ was first published in Longmore et al. (2013) and is based on stochastic triggering of star formation in Galactic Center clouds by a close pericenter passage. If the model holds, an absolute time sequence of the progress of star formation can be established which is so far one of the main unknowns in star formation.

This model is embedded in a broader framework of gas accumulation and star bursts in galactic centers as described in Krumholz & Kruijssen (2015). The CMZ can be seen as one case that can be studied exceptionally well due to the close proximity among a more general frame of gas rings in galactic centers. As

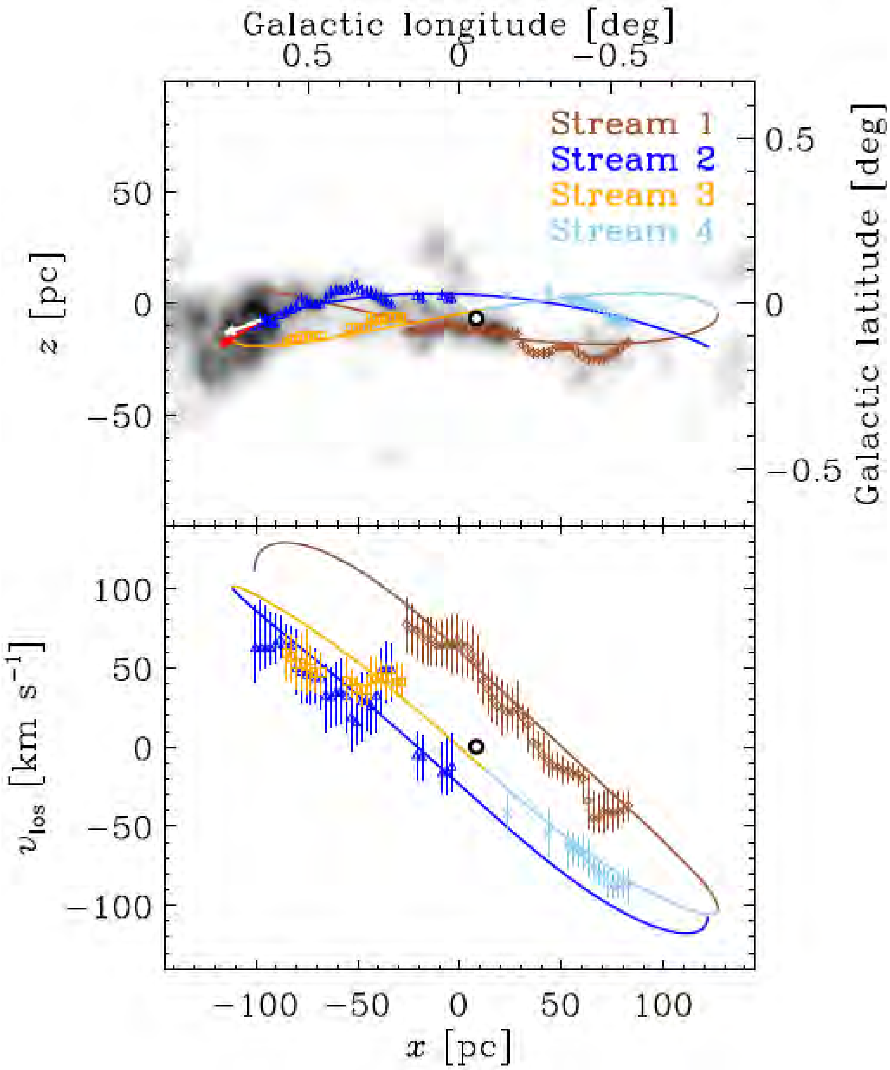

Figure 1.13: Fig. 4 of Kruijssen et al. (2015) shows the projected view (*top*) and position-velocity cut (*bottom*) of the streams. Gas in stream 1 and 2 is not seen as a coherent structure any more as it was the case in the Molinari ring model.

described before, gas is funnelled inwards from disk to CMZ and builds up at the shear minimum where turbulence remains high due to freshly infalling gas and therefore the reservoir cannot be depleted by continuous star formation. Ongoing infall increases gas densities above the limit sooner or later to reach a point where cloud collapse starts despite high turbulent pressures. Continuous star formation at rates that would be needed to convert all or most of the fresh gas into stars is not observed in the Galactic Center, which in turns means that the accumulated gas must be above or close to gravitational instability. Observations detect the clouds close to instability (Toomre Q $\gtrsim 1$) but at super-virial $\alpha > 1$ conditions (e.g. Longmore et al., 2012). In the toy model of Krumholz & Kruijssen (2015) for a Milky Way-like galaxy, after $\sim 5 - 10\,\mathrm{Myr}$ of cumulating gas, a starburst occurs that converts gas to stars over short periods of time ($\sim 4\,\mathrm{Myr}$) and at the same time expels much of the remaining gas by feedback with only $\sim 10\%$ of gas surface density remaining. However, this is just a qualitative picture of physically justified assumptions build on hydrodynamical simulations of gas evolution without stellar feedback implemented in the code. The whole cycle takes about 15-20 Myr to repeat with longer quiescent phases and shorter star bursting events.

It is important for understanding star formation in the CMZ that SF is not shut off completely in between star bursts and accumulating gas resides close to instability. This means even weak perturbations may push a cloud over the edge into self-gravitation, collapse and subsequently star formation. Observations suggest the CMZ might be exactly at this point, $\sim 4-5\,\mathrm{Myr}$ after a star burst and is currently forming stars at a decreased rate (Krumholz & Kruijssen, 2015).

In this context of increasing quantities of potentially available gas mass and recurring strong tidal forces along the gas' orbit, it can be expected that virtually every cloud that collapses does so at pericenter passage. However, the process of tidally triggering cloud collapse by tidal compression is still a stochastic process that is not identical for each cloud and the effect can be too small to seriously affect clouds farther from gravitational instability. Therefore, collapse and star formation in a cloud are likely to start at the same position along the orbit and thus trace a time sequence downstream pericenter passage possibly intermingled with gravitationally stable, non-collapsing clouds.

What later becomes a star formation sequence is initially triggered by a cloud being tidally compressed in z-direction (vertical direction) when passing deep in the potential while beginning to counter-rotate by shear. These effects act against each other as shear disrupts the cloud while vertical compression forces self-gravitation and it is not immediately evident why one would win over the other. The observation of dense clouds and star formation in the CMZ, however, indicate that clouds are indeed being pushed into self-gravitation as do numerical simulations (Kruijssen et al. 2016, in prep.).

While tidal triggering marks the start of the sequence, star formation can only be observed at later times. The free-fall time for a typical cloud of size $\sim 20\,\mathrm{pc}$ is $\tau_{ff} = 0.34\,\mathrm{Myr}$ which means it takes at least this long until first signs of embedded star formation may be observable. Outer shells around the cloud cores, however, continue to collapse and the cloud's evolution may become more complex as remaining tidal effects, collapse and star formation act at the same time. Once star formation sets in, a sequence of tracers should be observable from embedded star formation and masers to young stellar objects (YSO) that was already detected by Longmore et al. (2012) along the dust ridge. They, and other authors before, found hints of deeply embedded star formation in the Brick, tracers for embedded star formation in clouds d/e/f and high-mass cluster formation in Sgr B2. If star formation really is triggered by tidal compression, not only star formation can be observed along a sequence, but also molecular cloud properties should show evolutionary behavior. Gas temperatures were already marginally covered by Ginsburg et al. (2016) as they found a weak hint towards increasing dense gas temperatures traced by H_2CO. The first major analysis of a possible evolution or sequence in gas properties is given in this thesis in order to help answer the question if there really is a triggered star formation sequence and an absolute timeline starting at pericenter passage.

Survey of Water and Ammonia in the Galactic Center

The Survey of Water and Ammonia in the Galactic Center

A significant amount of time while working on this master thesis went into data reduction, i.e. calibration and imaging of the Survey of Water and Ammonia in the Galactic Center (SWAG). It is a large survey aiming to map all important regions of the Central Molecular Zone (CMZ) of the Milky Way from $\sim -1^\circ$ to $\sim +2^\circ$ in Galactic longitude at latitudes $|b| < 0.4^\circ$. The boundaries correspond to an integrated flux level of 0.1 K km/s of NH_3 (3,3) from Mopra single-dish observations (Ott et al., 2014). The achieved spatial resolution is $\sim$ 20” which at the Galactic Center distance corresponds to $\sim$ 0.8 pc and 0.4 km/s velocity resolution. The observations are performed in a mosaic of $\sim$ 6500 pointings at the Australia Telescope Compact Array (ATCA) interferometer taking 525 hours over three years (2014 - 2016). At a wavelength around 1.5 cm, 42 spectral lines are observed in the range of 21.2 - 25.4 GHz, amongst others six metastable and three non-metastable ammonia inversion lines, water and radio recombination lines and complex organic molecules. Various physical questions can be addressed with SWAG and will be by the SWAG team whereas this chapter only explains the data reduction and imaging procedure and presents selected maps. One key aspect of this survey will be used in chapter 3 to explore the existence of a star formation sequence in the Galactic Center.

SWAG logo designed by J. Ott

2.1 Australia Telescope Compact Array

The observations for SWAG were carried out at the Australia Telescope Compact Array (ATCA)[1] in Narrabi, New South Wales. The array consists of six antennas of 22 m diameter, thereof 5 moveable and one fixed, in an east-west or hybrid configuration. Five dishes can be moved to allow minimal baselines of 31-628 m whereas the sixth antenna is stationary at ~ 3 km distance from the array's center. The new backend system Compact Array Broadband Backend (CABB) installed in 2011 allows to take 2×2 GHz continuum observations in 32×64 MHz channels while simultaneously providing 2×16 so-called zoombands with 2048×32 kHz channels (CFB 64M-32k mode). The two continuum bands of 2 GHz can be placed freely in the range 16 GHz to 25 GHz and result in a continuum observation of 4 GHz total bandwidth, structured in $2 \times 32 = 64$ channels of 64 MHz width. Relative spectral positions of the zoombands are not fixed but can be chosen in the 4 GHz range covered by continuum observations. One zoomband provides 64 MHz total bandwidth in 2048 channels of 32 kHz width.

Figure 2.1: The five moveable antennas on the east-west track of the Australia Telescope Compact Array (ATCA) near Narrabri, New South Wales. (image by ATNF/CSIRO under CC BY 3.0)

[1]The Australia Telescope Compact Array is part of the Australia Telescope National Facility which is funded by the Australian Government for operation as a National Facility managed by CSIRO.

2.2 Survey Setup

Spatial Setup and Mosaicing Technique

The survey was setup to make use of the full capabilities of ATCA and CABB in order to keep the observation time at a manageable level. Achieving the intended resolution of $\sim 1\,\mathrm{pc}$ requires the most compact array configuration H75 with baselines of $31 - 89\,\mathrm{m}$. Additionally, antenna CA 06 outside the main array offers baselines of $4300 - 4400\,\mathrm{m}$. The resolution at 23 GHz for an 80 m baseline is therefore expected to be $c/\nu/b \approx 30$" or 1.3 pc at the Galactic Center distance of 8.3 pc (Reid et al., 2014) depending on weighting, while the primary beam FWHM is $\sim 2'.4$. Uniformly covering the CMZ at this resolution requires ~ 6500 pointings which are arranged in a hexagonal pattern of center to center distance $1/\sqrt{3} \approx 0.58$ relative to a non-overlapping quadratic grid. Hence, every position in the targeted area is covered by the primary beam of at least one pointing. Between 80 and 200 pointings are combined into stripes of $\sim 4'$ width as shown in fig. 2.3 that are observed in one track each. In order to maximize the u, v coverage, pointings are not observed one after the other, but in rows of even and odd numbers. The rows are aligned along Galactic longitude ("l-scan") while the first element of each row determines its parity. Pointings in the left-out rows are tracked along Galactic latitude ("b-scan") and observed at different local sidereal times (LST) and therefore other projected baselines, which increases the u, v coverage. The resulting typical u, v coverage of a single pointing is shown in fig. 2.4.
Single dish data is not taken for SWAG as it is not needed because diffuse emission that is filtered out by the interferometer obscures the target. In the K band regime, the H75 array configuration is not sensitive to emission extending over more than $\sim 1'.3$.

Times

The integration time of each pointing is set to $8 \times 30\,\mathrm{sec} = 4\,\mathrm{min}$ as a trade-off between low noise and total project time. Due to pointing overlap, the actual sensitivity is higher by a factor of $\sqrt{2}$ or $\sqrt{3}$ in some areas than can be expected from the integration time of a single pointing. The expected noise calculated from the radiometer equation

$$\sigma = \frac{T_{sys}}{\sqrt{\Delta\nu\tau}} \tag{2.1}$$

is $\sigma = 0.014\,\mathrm{K}$ for a typical $T_{sys} = 40\,\mathrm{K}$ in one channel of $\Delta\nu = 32\,\mathrm{kHz}$ and $\tau = 240\,\mathrm{s}$, which corresponds to $\sigma \sim 6\,\mathrm{mJy/beam}$ at $\nu = 23.695\,\mathrm{GHz}$ (NH_3 (1,1)) and a circular beam of 30". The eight individual integrations are scheduled by the mosaicing technique to be observed over the whole available range of local sidereal time (LST) from about 15:00 to 22:00 h.

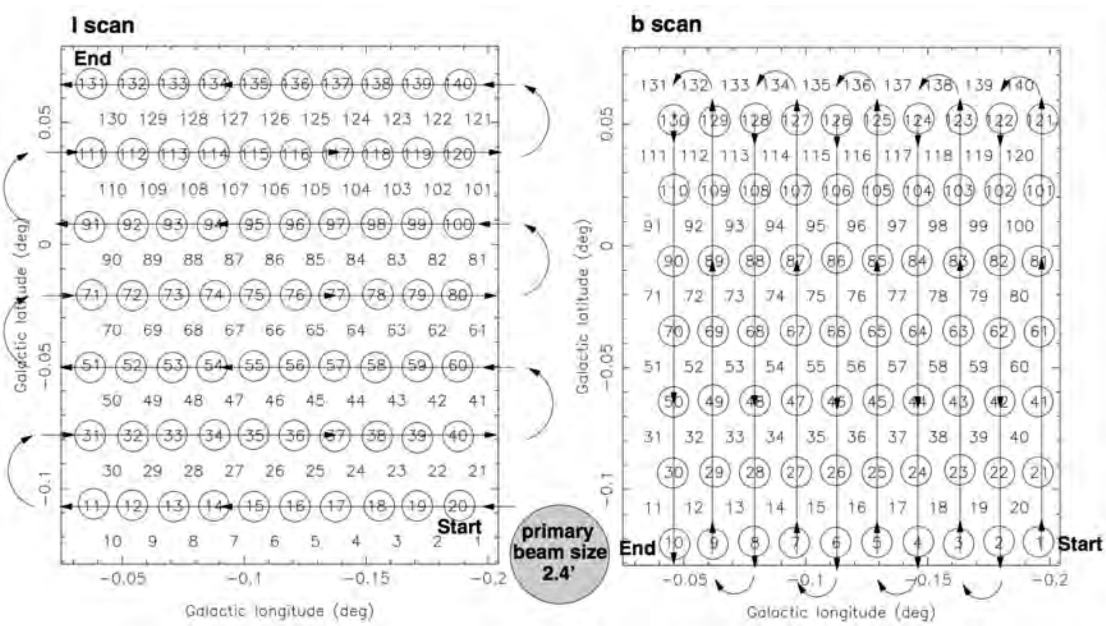

Figure 2.2: The scanning pattern used in SWAG is very similar to the approach in Ott et al. (2014). Instead of both, l- and b-scans, only scans of every second row ("odd" rows) along Galactic longitude were observed followed by l-scans of the "even" rows. The number of the first pointing in a row determines if it is called odd or even.

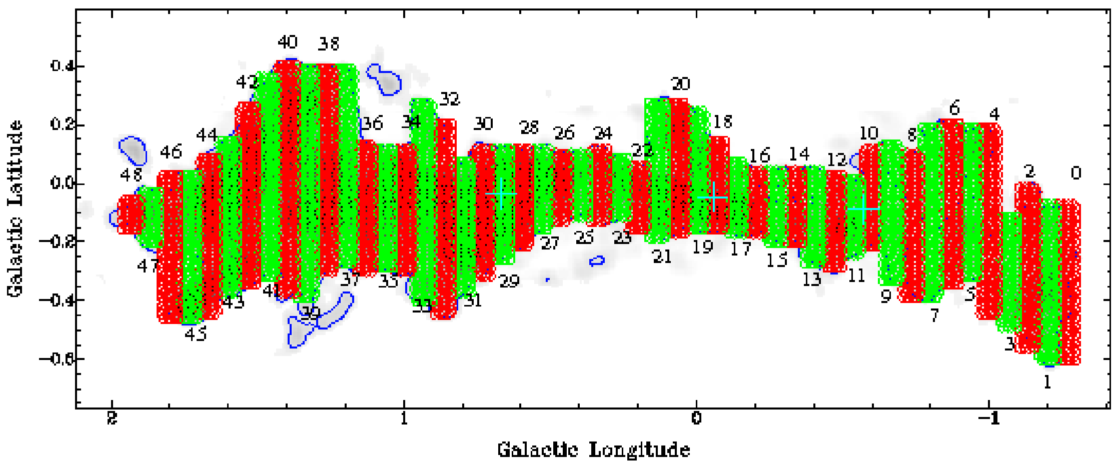

Figure 2.3: SWAG observing layout. The contours in the background are the CMZ survey by Ott et al. (2014) with the MOPRA telescope. This thesis is based on the first set of observations in 2014 that included stripes 10 to 30.

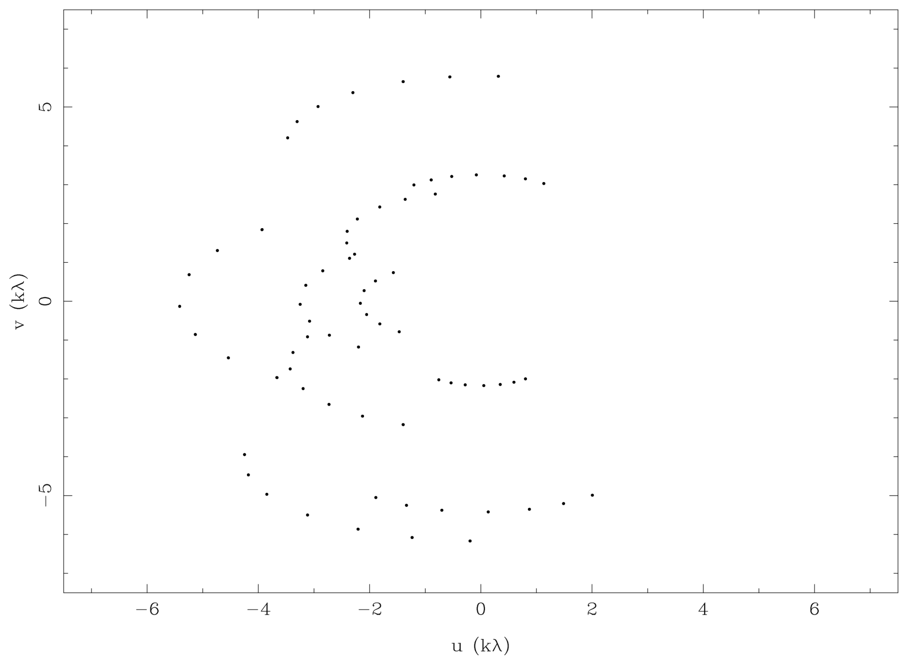

Figure 2.4: Typical u, v coverage of a single pointing of SWAG. Note that overlapping pointings increase u, v coverage by a factor of $1/\sqrt{3}$ that is not included in this plot. The u, v coverage was optimized by the scanning technique shown in fig. 2.3.

The total project time including calibration data is expected to be 525 hours including additional time needed to re-observe stripes 10/11, 20, 30/31 and possibly more stripes of later observation campaigns due to unexpected high noise levels (see §2.3.1.6 for details). In 2014 and 2015, 308 hours were already observed. Observations are scheduled for 3×3 weeks in July/August 2014 to 2016.

Spectral Setup

The full capabilities of CABB are used, including full polarization and a setup of 2×2 GHz in 32×64 MHz channels for continuum emission and 2×16 zoombands for high resolution line emission at 2048 channels of 32 kHz, which is ~ 0.4 km/s at 23 GHz. Two of the zoombands, one in each 2 GHz range, overlap the frequency range of an adjacent zoomband by half the bandwidth (32.8 MHz), creating two bands of increased bandwidth of 3072 channels. Fig. 2.5 illustrates this setup in a sketch. The spectral position of the zoombands was chosen to include the rest frequencies of as many known lines as possible. Table 2.1 gives an overview of all 42 lines covered by SWAG, listing their rest frequencies and potential tracer properties.

Table 2.1: All spectral lines covered by SWAG listed by increasing frequency. Tracer properties are listed in the last column. Zoomband "edge z3" means the line is not completely in the zoomband for velocities of ±200 km/s relative to the rest frequency (col. 1). Tracer properties in the last column are shortened: PDR - photon-dominated region, RRL - radio recombination line, vib. ex. - vibrationally excited. Question marks indicate suggested but so far uncertain properties.

frequency [GHz]	zoomband	transition	science/tracer
21.207334	z1	NH_2CHO (1_{01}-0_{00}, F=2-1)	shock, PDR
21.301261	z2	HC_5N (8-7)	
21.38315	z3	$HOCO^+$ (1_{01}-0_{00})	shock, PDR
21.38479	z3	$H_{67\alpha}$	RRL
21.39350	edge z3	$He_{67\alpha}$	RRL
21.39546	edge z3	$C_{67\alpha}$	RRL
21.58740	z4	c-C_3H_2 (2_{20}-2_{11})	shock, PDR
21.98147	z5	HNCO (1_{01}-0_{00})	shock
22.02974	z6	C_6H^- (8-7)	anion (rare)
22.23504	z8	H_2O (6_{16}-5_{23})	maser, vib. ex.
22.30767	z10	HDO	deuterated, very cold gas
22.34403	z11	CCS (1_2-0_1)	shock, PDR
22.36417	z11	$H_{66\alpha}$	RRL
22.36727	z11	trans-ethanol 2_{21}-3_{12}	
22.37328	z11	$He_{66\alpha}$	RRL
22.37533	z11	$C_{66\alpha}$	RRL
22.47118	z13	HCOOH	hot cores?
22.48987	z13	C_3H^+ (1-0)	
22.688312	z14	NH_3 (4,3) inversion	ammonia
22.82774	z15	CH_3OCHO (2_{12}-1_{11})	
22.834185	z15	NH_3 (3,2) inversion	ammonia
23.00525	z17	NaCN	
23.098819	z19	NH_3 (2,1) inversion	ammonia
23.69451	z21	NH_3 (1,1) inversion	ammonia
23.7017705	z21	CH_3CH_2CN (5_{05}-4_{14})	
23.72263	z21	NH_3 (2,2) inversion	ammonia
23.82662	z22	OH (23/2; J=9/2; F=5-5)	maser, vib. ex.
23.87013	z23	NH_3 (3,3) inversion	ammonia
23.96390	z24	HC_5N (9-8)	PDR?
24.13942	z26	NH_3 (4,4) inversion	ammonia
24.29649	z27	CH_3OCHO (2_{02}-1_{01})	
24.32593	z27	OCS (2-1)	shock, PDR
24.50628	z29	CCS (6_5-5_5)	
24.50990	z30	$H_{64\alpha}$	RRL
24.52213	z30	$C_{64\alpha}$	RRL
24.53299	z30	NH_3 (5,5) inversion	ammonia
24.65860	z32	CH_3CH_2CN (3_{12}-3_{03}, F=4-4)	
24.66030	z32	HCN (10-10; 1v2)	maser, vib. ex.
24.75575	z33	$H_{80\beta}$	RRL
24.78878	z34	CH_3C_3N (6_0-4_0)	
24.92872	z35	CH_3OH (3_{21}-2_{13})	maser, vib. ex.
25.056025	z36	NH_3 (6,6) inversion	ammonia
25.32441	z38	DC_3N	deuterated, very cold gas
25.39280	z39	SO_2	

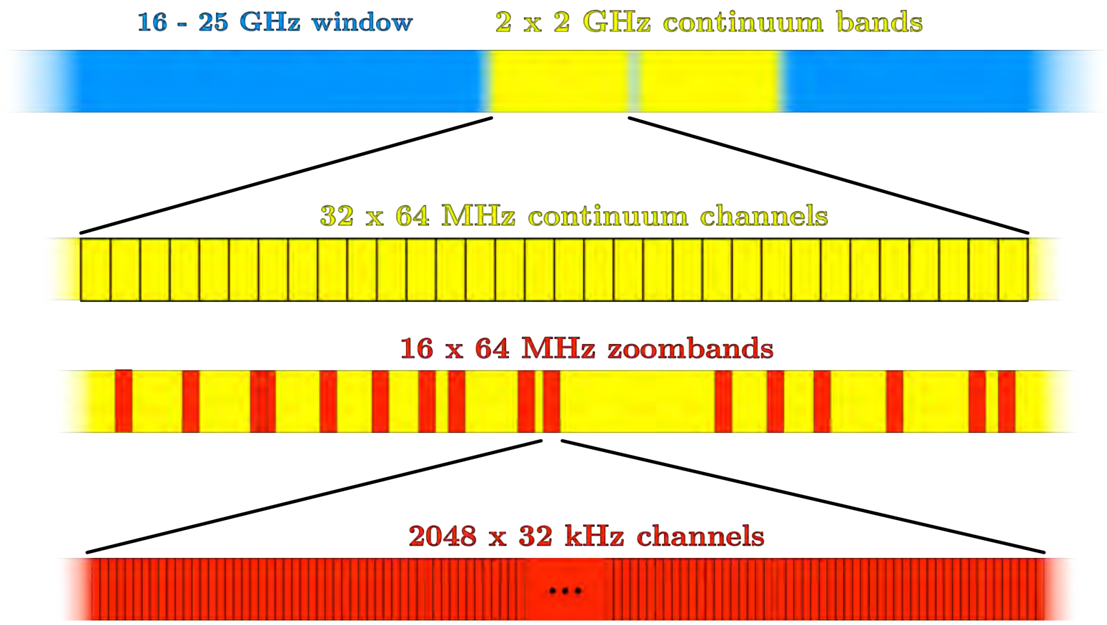

Figure 2.5: Sketch of the spectral setup used for SWAG. The 2 GHz continuum bands are placed between $\sim 21 - 25$ GHz to cover 4 GHz continuously. Each continuum band has 32 channels of 64 MHz bandwidth. 16 zoombands of 64 MHz per continuum band can be placed freely, but two zoombands overlap by half the bandwidth. Each zoomband has 2048 channels of 32 kHz, the overlapping zoombands create a larger set of 3072 channels.

Calibrators

Bandpasses and delay calibrations for each antenna are derived from daily 10 min integrations on PKS 1253-055, also known as 3C 279, a QSO at $z \approx 0.5$. Its flux of ~ 15 Jy at frequencies around 23 GHz is bright enough to derive accurate bandpass solutions.
The phase (complex gain) calibrator PKS 1710–269 is observed for 2 min every $20 - 30$ min, depending on the field, after each l-scan and in between l-scans if necessary. This quasar is close to the Galactic Center ($< 8°$) and unresolved in H75 configuration, why it can be used for pointing corrections every ~ 1.5 h as well.
Daily flux calibrations are performed on the radio galaxy PKS 1934–638, which is the standard primary flux calibrator at ATCA.

2.3 Data Reduction

Before exploring the possibility of a star formation sequence in the Galactic Center, the observed visibilities need to be flagged, calibrated and imaged. All steps from data import to imaging are performed with the ATCA specific version of the package MIRIAD[2]. The procedure described in the following sections is based on MIRIAD's user guide[3], as well as the ATCA users' guide[4]. The necessary steps were developed into a complete data reduction pipeline that provides a base for later reducing the whole survey, after each yearly part is observed. Here, however, only the first third of all pointings, together with some necessary re-observations which were available at the time being, are processed.

2.3.1 Calibration

This section on calibration summarizes all necessary steps performed on the visibility data prior to imaging.

2.3.1.1 Flagging

Raw data from ATCA is delivered in the rpfits format and needs to be imported as MIRIAD u, v data with the task `atlod`. Its options were set to `birdie`, `noif`, `opcorr`, `nocacal` and `noauto` to automatically flag resonant instrument modes (birdies), so-called cacal data which is needed for array calibration and auto correlations, furthermore set correct intermediate frequency mapping behavior as well as applying opacity corrections. Some of the array setup data (data type codes cacal, dcal) were not detected by the automatic routine and had to be flagged manually with `uvflag`.
Internal feedback in ATCA's backend system causes additional birdies in channels $n \times 1024 + 1$ $(n = 1, 2, ...)$ that are not identified during data import. Identifying and only flagging affected visibilities in those channels turned out to be impossible, which is why all these channels had to be flagged completely. The missing channels are interpolated later when averaging the visibilities to a common resolution of $2\,\mathrm{km/s}$.
The files were then split by `uvsplit` into one file per track per zoomband and observation, to which the calibration was applied individually. The options used in this task are `nosou` and `mosaic` for easier handling of sources in mosaics.
The intended use of the to date incomplete survey are development of a calibration and imaging pipeline, deriving inner CMZ maps for all observed lines and calculating temperature maps. Hence, polarizations and high spatial resolution are not needed and all crosshands/cross-polarizations (XY and YX for ATCA's linear feeds) and the whole antenna 6 were flagged. Initial tests showed the long baselines involving antenna 6 to be difficult to calibrate because of its position far outside the rest of the array and therefore high scatter in delay time and phase.

[2] `http://www.atnf.csiro.au/computing/software/miriad`
[3] `http://www.atnf.csiro.au/computing/software/miriad/userguide/userhtml.html`
[4] `https://www.narrabri.atnf.csiro.au/observing/users_guide`

At frequencies of ∼ 23 GHz very little radio frequency interference (RFI) is present, as the K band is marginally used for communication like satellite uplinks. RFI identification and flagging was done by eye in the interactive task `blflag`.
To identify any bad visibilities that might have slipped through the flagging procedure, calibrator data was clipped at 200 Jy and CMZ observations at 10 Jy. These values are motivated physically as it is not expected for the observed sources (quasars and CMZ gas) to measure larger fluxes. However, the values are low enough to not affect image quality in case a bad visibility (RFI, birdie) had not been flagged.

2.3.1.2 Bandpass and Gain Calibration

Without cross-polarizations being present, MIRIAD's task `mfcal` can be used to derive bandpass and complex gain solutions. First, bandpass amplitude and phase are calculated on the designated bandpass calibrator 1253-055 choosing antenna 2 as phase reference instead of the default antenna 3. This antenna never dropped out in all observations and solutions can be calculated without having to switch reference antenna. The found correction is then applied to the phase calibrator 1710-269 and flux calibrator 1934-638, and antenna complex gains are derived with `mfcal`.
Calibration solutions were inspected visually to identify remaining problems that were subsequently flagged. Re-calibrations were done until well-behaved solutions were found.

2.3.1.3 Flux Calibration

Setting the correct flux was done with `mfboot` using the source 1934-638 that has a built-in model in MIRIAD. The found calibration solutions were applied to the target data with `uvaver` without any averaging.
The calibration quality is assessed with fig. 2.6. Phase calibrator 1710-269 was imaged including all calibration corrections for all observation days and all zoombands and the peak flux listed. Measured fluxes per zoomband are constant within ∼ 15%, which is typical for radio observations. The origin of this variability cannot be identified without absolute measurements and can be due to changing atmospheric conditions or intrinsic luminosity variation in the QSO. Thus, fluxes cannot be determined more accurately than ∼ 15%.
Spectral lines observed in the same zoomband, however, share a common flux uncertainty and thus relative fluxes and derived quantities are more accurate. The most important of these cases are the ammonia (1,1) and (2,2) lines which provide the temperature T_{12}. For other common zoombands see table 2.1.

2.3.1.4 Continuum Subtraction

In order to obtain spectral line emission only, continuum emission must be subtracted. For channels with continuum and line emission, it is not possible to discern both, but in line-free channels, each pixel can be fitted for continuum flux

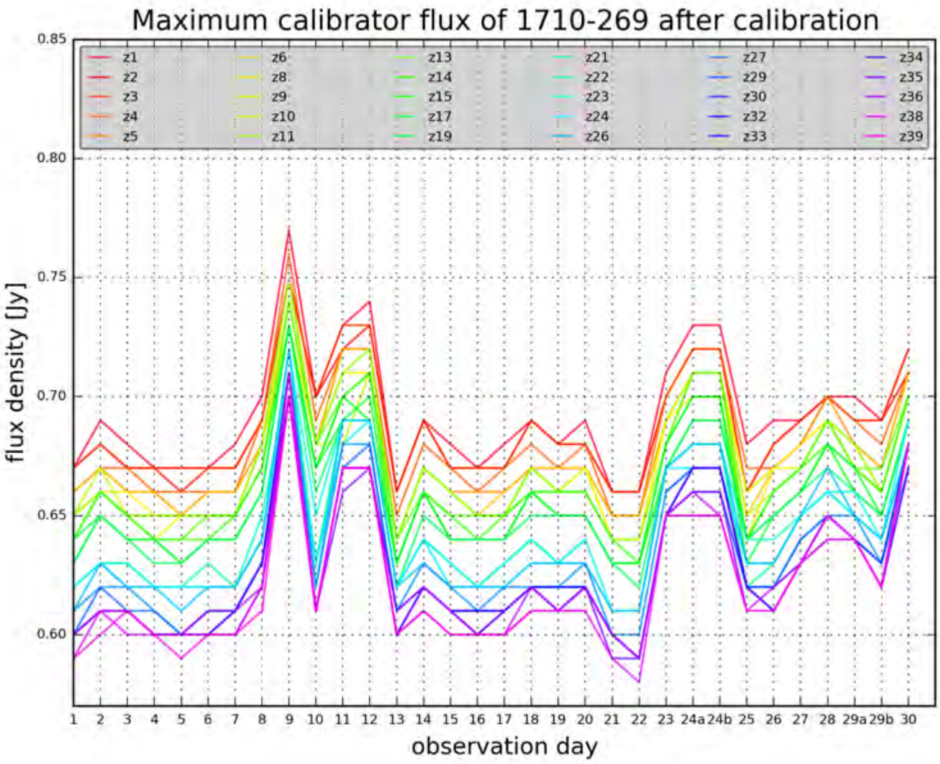

Figure 2.6: Flux of the phase calibrator 1710-269 per observation day after all calibration steps. Fluxes are constant within $\sim 15\%$. The increasing flux towards lower zoombands, i.e. lower frequency is an intrinsic property of the source: a quasar with spectral index ~ -0.5. Dropouts in some zoombands for day 21 and 22 are due to data being stored in the files of previous days for unknown reasons. Suffix a and b denotes individual files before and after a correlator crash on that day.

and interpolated towards line bearing channels. Over the small spectral range of a zoomband of $\sim 64\,$MHz, a linear approximation captures the spectral index but cannot produce an overfit to noise.
Line-free channels can be identified in two ways: in spectra from (dirty) images or visibilities, or by calculating the frequency range that includes the lines. In the case of SWAG, the former approach failed because most spectral lines are not bright enough to be discernible from noise without cleaning. In order to use the same approach for all zoombands, line-free channels are calculated from rest frequency values accounting for the typical velocity range in the Galactic Center, instead of using visibility spectra for the bright lines. Ammonia emission, especially in the low rotational states of J $\lesssim 3$, would be strong enough to measure the range of gas velocities. As described in §1.4.1, gas along the stream structure has line-of-sight velocities of $-150\,$km/s$\lesssim v \lesssim +150\,$km/s while other clouds may exceed this range. An interval of ± 400 channels (or $\pm 163\,$km/s) around each line's rest frequency is

broad enough to contain the strong emission originating from the Galactic Center, while all other channels are considered line-free. Possible emission outside these line-free windows is weak and will not affect the continuum fit. Fit and subtraction was done using the `uvlin` task forcing a first-order polynomial.

2.3.1.5 Further Visibility Preparation

Before imaging, several more steps of calibration need to be done. The calibrated files from each track or observation day were concatenated into a single file per zoomband and split again for each line. In order to include enough line-free channels for noise calculations, the file for each line covers the interval of $\pm 250\,\mathrm{km/s}$ around the rest frequency. Rest frequencies are set according to table 2.1 in `puthd` that lists values from Splatalogue[5]. Visibility files and therefore the image cubes can still contain emission from other nearby lines, e.g. some NH_3 (1,1) emission is included the NH_3 (2,2) file and vice versa.
Several spectral resolutions were calculated with `uvaver` at original ($0.4\,\mathrm{km/s}$), intermediate ($1\,\mathrm{km/s}$) and reduced ($2\,\mathrm{km/s}$) resolution. Merging five channels increases the signal-to-noise ratio by a factor of ~ 2.2, while the full spectral resolution is not needed for typical line widths of $5-25\,\mathrm{km/s}$ in ammonia emission.

2.3.1.6 Correlator Crashes, Positional Offsets and Re-Observations

Positional Offsets

Imaging tests revealed the problem of 36 out of 72 pointings in stripe 17 being shifted by 2.4° in declination and 18 of them additionally in both right ascension and declination by $\Delta\mathrm{RA}= 1.43^m$ and $\Delta\mathrm{DEC}= 30.7'$. Not all eight 30 sec integrations were affected but five were positioned correctly and one was offset in DEC for the pointings with shift in DEC only. Another integration was offset in RA and DEC, and one in DEC for the pointings affected by both offsets. The reasons for this could not be identified and no correlation with issues during observations could be found. The particular setup files list correctly formatted positions without any apparent difference to other files that could have lead the correlator to misinterpret the setup or introduce additional offsets. Back-shifting the pointing positions, however, was possible for the data that was offset in declination only. Tests showed that the calculated shift was exactly correct. Any mismatch would affect the phases (position of the visibility in the u,v plane) and introduce easily detectable patterns due to non-matching phases in the overlapping regions of different pointings. Transitions to other pointings that show no sign of positional mismatch are smooth and continue the intensity pattern as expected from the CMZ ammonia maps of Ott et al. (2014).
The pointings that could not be corrected were discarded and scheduled in 2015 to be re-observed so that uniform noise is achieved; otherwise, noise would increase according to the radiometer equation (1.4) when integration time is decreasing.

[5] `www.splatalogue.net`

Noisy stripes

Another unexplained image defect appeared in the form of stripes with increased noise levels. A moderate increase in noise is expected for stripe 17 due to missing integration time in individual pointings (data loss by the offset correction described above). However, this cannot explain why the whole stripe is affected rather than just some pointings. Additionally, stripe 10, one half of 20 and 28/29 are noisy for unknown reasons. There are weak correlations with atmospheric wet path, but the weather conditions cannot explain the amount of noise increase: other observations had similar or worse weather conditions without increased noise. Possibly, low intensity RFI or other interfering signals are to blame, but without a clear handle on how to find and flag them, the best approach was to re-observe the affected stripes with half of the original time in order to decrease the noise by increasing integration time (see eq. (2.2)). For stripe 20, this resolved the issue but had no effect for stripes 10/11 and 28/29. With the increased total integration time, it is now possible to replace some of the integrations taken in 2014 to down-weight their influence on the noise.

Correlator Crashes

ATCA's correlator sometimes is unstable and one or more correlator blocks drop out. SWAG, however, utilizes the instrument's full capabilities and every problem directly affects the survey. In the 2014 observation campaign, correlator crashes appeared on three out of 22 days but did not affect calibration. It was only necessary the flag bad visibilities. In 2015, out of 22 observation nights, 6 had correlator problems. In one case (July, 27^{th}), the whole array had to be re-calibrated with the standard routine, resulting in two independent calibrations in one night. For another observation (July, 22^{nd}) where the correlator had to be rebooted, the proper bandpass calibrator 1253-055 could not be used due to unstable amplitudes and bandpass calibration was done on PKS 1921-293 instead. The missing flux values were bootstrapped from the calibration after the correlator crash because the first flux calibrator observation was affected by the crash.

2.3.2 Imaging

2.3.2.1 Deconvolution

For imaging, MIRIAD is a used again. Future imaging of the whole survey may use CASA, as it offers more options for different cleaning strategies.
Fourier inversion is performed with the task `invert` that includes primary beam correction and combines the visibilities of single pointings into a mosaic. The robust weighting parameter is set to `+2`, i.e. natural weighting and additionally MIRIAD generally weights visibilities by integration time. The cell size (pixel size) is set to 5" in RA and DEC, which is six times the expected synthesized beam. Each pointing is imaged over 512 pixel ($42'.7$) and then integrated linearly into

the mosaic with another weighting function that smooths noise across regions of differing pointing coverage.
The extended emission of most spectral lines is generally better cleaned by an algorithm that does not use point sources for modelling. The only possibility that MIRIAD offers is the maximum entropy clean `mosmem`. A first run with up to 50 iterations cleans the dirty image deep enough to construct a mask that prevents cleaning regions without significant emission. Image restoration is done with `restor`. A clean mask is calculated with `maths` to contain all pixels with SNR above 5 which corresponds to 0.065 mJy/beam. The noise measurement is explained in detail in §2.3.2.4 and is typically $\sigma = 13.0$ mJy/beam in a 2 km/s channel.
Deconvolution is then repeated with 50 iterations in `mosmem` only inside the pixels that were set as relevant by the mask. The restored images still contain sidelobe structures, especially around strong sources and in strong lines. The apparent impossibility to obtain better images with `mosmem` is described in §2.3.2.2.
For easier handling of the final images, all restored data cubes were rotated from RA/DEC to Galactic coordinates using the built-in option in `regrid`.
To offer the possibility of getting rid of noise in subsequent analyses, a master cube is calculated for each line that can be used as a mask. The threshold below which all emission is considered noise is set to 3σ or 39.0 mJy and is stored as 0 while real emission is flagged 1. Due to the remaining extensive sidelobes in regions of strong emission, this criterion of real emission may fail and has to be taken with caution. For most of the 42 spectral lines this is not of concern, even in the Large Molecular Heimat. Ammonia inversion lines and H_2O lines, however, are affected strongly in the dust ridge and Sgr B2.

2.3.2.2 Cleaning Depth in MEM

As stated above, 50 iterations in `mosmem` leave considerable amounts of sidelobe structure that complicates analyses. Deeper cleaning by more iterations is therefore crucial to obtain more reliable data cubes, but faces problems that could not be solved so far.
Simply using a higher number of iterations (`niters`), results in one or more jumps in the spectra. Noise measurements are affected by the introduced offset as well as rendering affected data cubes unusable. The spectral position of each jump is coherent across spatial pixels but seems to be unpredictable in frequency for consecutive `mosmem` runs. Tests were carried out for iteration counts of 30, 50, 100, 150, 250 and 500 iterations.
While at 30 and 50 iterations no discernible signs of unstable fluxes in the line-free velocity range was found, all other deconvolutions induced sudden jumps or linear increases in flux.
At 100 iterations, appropriate scaling and RMS measurements are needed to detect the effect at a couple of mJy/beam. From a certain frequency onward, all consecutive channels towards lower frequency are offset by a few mJy/beam, while the noise properties seem not to be disturbed in any way. The effect must therefore

be introduced somewhere between 50 and 100 iterations. Considering the small magnitude at 100 iterations and the interpolated development with `niters`, it is safe to assume that at 50 iterations, the data quality is not impaired. Aside from this argument, spectra of all lines were examined visually to confirm that fluxes are indeed correctly restored in the final images presented in §2.5. Masking the data cube before running `mosmem` does not affect the result beside the small difference by the fact that some regions might not be cleaned directly when using a mask.
250 iterations introduces an offset of the order of 60-70 mJy/beam that again sets in abruptly. The channels at lower velocity than the jump seem to be unswayed in absolute value or noise fluctuation. When `niters` is set to 500, already the first channel is shifted by ~ 30 mJy/beam while later channels show up to 80 mJy/beam offset. The transition in between is close to linear over ~ 120 km/s.
The direction of increasing flux towards lower frequencies/higher velocities matches the order in which the visibilities are stored in the input vis file. The introduced shift is even present in completely flagged channels that by definition should have average fluxes of 0 mJy/beam. There might be a correlation with spectral resolution as these problems appeared already at 50 iterations when using the full spectral resolution of 0.4 km/s.
Another complication in finding a solution is the fact that `niters` denotes the maximum number of possible iterations but not necessarily the exact number of iterations that were applied. Log files confirm that the same number of iterations is used in a channel with little emission although more would be allowed by `niters`. Still, the restored image differs drastically in flux between the six test runs. Tests with a mosaic steer clean and noise scaling factor `rmsfac` for maximum entropy clean were not successful but not investigated further.
The final maps are therefore produced by a maximum entropy clean of up to 50 iterations per channel without a theoretical noise correction factor. Future maps will, if possible, be produced with multi-scale clean in CASA, which turned out to be an improvement over classic clean algorithms for extended emission of other sources (e.g. Krieger, 2013, for HI in nearby galaxies) and does not show unpredictable behavior as `mosmem` does.

2.3.2.3 Masking

Masks to include real emission and exclude noise depend on the purpose and will not be generated automatically for all lines. A general mask to get rid of the map's outer edges, a master cube, is needed nonetheless and can be applied to every SWAG map. Increased noise levels at the edges is due to non-overlapping pointings and therefore reduced coverage. These regions do not contain information relevant to the Central Molecular Zone and will be blanked by three masks that set the map edge inward by roughly 50", 80" or 100". 50" are enough to exclude all visible noisy edges in moment maps but spectral fitting can pick up increased noise up to 100" from the actual edge of the imaged region. Hence, moment maps are generated with the 50" mask while spectral analysis should use the more aggressive 80" or 100" masks.

2.3.2.4 Noise Measurements

The noise in the restored image cubes is measured as the root mean square (RMS) in line-free channels. As explained in §2.3.1.6, the SWAG data set used in this thesis suffers from higher noise in two regions of the eastern and westernmost observation stripes which should be accommodated for. The noise estimate is therefore calculated in three regions of stripes 30/31 (RMS_{west}), stripes 10/11 (RMS_{east}) and in the rest of the map (RMS_{main}). As RMS_{west} and RMS_{east} are very similar, they are combined. The result is a central area of low RMS (RMS_{low}) bordered by two high noise regions RMS_{high}.
The RMS estimates are an average of 10 (RMS_{low}) and 6 (RMS_{high}) positions at which the RMS is calculated over a 20×20 pixel box corresponding to ~ 20 beams in a 2 km/s channel. Furthermore, this is done in two line-free channels above and below the line in terms of frequency (channel 50 and 200, -150 km/s and $+150$ km/s, respectively). This range is far enough outside the expected emission of the CMZ of roughly -100 to +100 km/s but not too far from it that it can pick up other lines shifted in this range. This calculation is applied to each data cube to obtain individual noise estimates.
The resulting RMS measurements confirm the expectations: The noise level is low at mean values of $RMS_{low} = 12.9$ mJy/beam and $RMS_{high} = 17.6$ mJy/beam. The RMS is higher by 2-6 mJy/beam in channel 200 as compared to channel 50, but constant along frequency from NH_3 (1,1) to (6,6). Hence, this slope in RMS across channels is not the result of flux drop with increasing frequency, but may be introduced in the telescope already or during continuum subtraction. The 10 (and 6, respectively) estimates typically vary by less than ± 3 mJy/beam, so the averaged RMS is expected to describe the whole data cube reasonably well. Individual measurements for each line is given in table 2.2.
In the analyses performed in later chapters, only RMS_{low} will be used because the difference to RMS_{high} is less than 50% and only two major clouds, namely Sgr C and Sgr B2, lie in the area of elevated noise. Those, however, exhibit high signal-to-noise ratios anyway, without much impact on the analyses.

2.3.2.5 Moment Maps

Data cubes were collapsed along the spectral axis with the task `moment` in MIRIAD to obtain moment maps as explained in §1.2.5.3. Map edges are blanked with the 50" edge mask and individual 5σ masks, excluding noise and emission at low signal-to-noise.

2.3.2.6 Spectra

Spectra on three selected positions are shown in §2.5 and appendix A. Those were obtained with `imspect` at the tabulated positions of Sgr A*, B2 and C as given by SIMBAD[6]. The real world coordinates are listed in table 2.3.

[6] `http://simbad.u-strasbg.fr/simbad/`

Table 2.2: RMS noise of the 42 imaged spectral lines for a channel width of 2 km/s. Given values are an average over 20 (RMS_{low}) and 12 (RMS_{high}) measurements in two channels at ±150 km/s relative to the rest frequency for a beam size of 26".22 × 17".84. σ_{low} is relevant for most of the maps beside the two outermost stripes (see fig. 2.3) on each side that are described by σ_{high}.

line	σ_{low} [mJy/beam]	σ_{high} [mJy/beam]	line	σ_{low} [mJy/beam]	σ_{high} [mJy/beam]
NH_3 (1,1)	13.4	19.4	CH_3OCHO (2_{12}-1_{11})	13.2	18.2
NH_3 (2,2)	13.1	19.3	CH_3OCHO (2_{02}-1_{01})	12.6	16.3
NH_3 (3,3)	13.1	18.6	CH_3CH_2CN (3_{12}-3_{03})	12.1	15.6
NH_3 (4,4)	12.9	16.1	CH_3CH_2CN (5_{05}-4_{14})	36.6	33.8
NH_3 (5,5)	12.0	16.2	CH_3C_3N (6_0-4_0)	12.2	16.1
NH_3 (6,6)	13.2	16.2	CH_3OH	13.2	17.2
NH_3 (2,1)	13.2	17.2	C_3H^+	13.2	22.1
NH_3 (3,2)	13.0	19.9	HCOOH	13.7	21.0
NH_3 (4,3)	12.9	18.6	trans-C_2H_6O	13.5	19.5
$H_{64}\alpha$	12.3	16.2	$HOCO^+$	12.9	16.5
$H_{66}\alpha$	13.5	18.9	c-C_3H_2	12.1	16.7
$H_{67}\alpha$	12.0	15.3	HNCO	12.6	17.0
$H_{80}\beta$	11.9	17.2	C_6H^+	12.9	17.9
$He_{66}\alpha$	13.8	19.0	NH_2CHO	13.9	17.2
$C_{64}\alpha$	12.9	16.3	HC_5N (8,7)	13.4	15.5
$C_{66}\alpha$	13.5	17.2	HC_5N (9,8)	12.8	16.5
NaCN	12.7	18.1	HCN	11.9	16.4
SO_2	13.3	18.8	DC_3N	14.4	17.5
OCS	12.6	16.6	H_2O	13.5	19.2
CCS(1_2,0_1)	14.6	19.5	HDO	14.0	21.6
CCS(6_5,5_5)	13.0	17.6	OH	13.4	19.8

Table 2.3: Positions of Sgr A*, B2 and C in Galactic coordinates that were used to obtain the spectra shown in §2.5 and §A.1.

source	l [°]	b [°]
Sgr A*	-0.0558	-0.0462
Sgr B2	0.6667	-0.0362
Sgr C	-0.5712	-0.0898

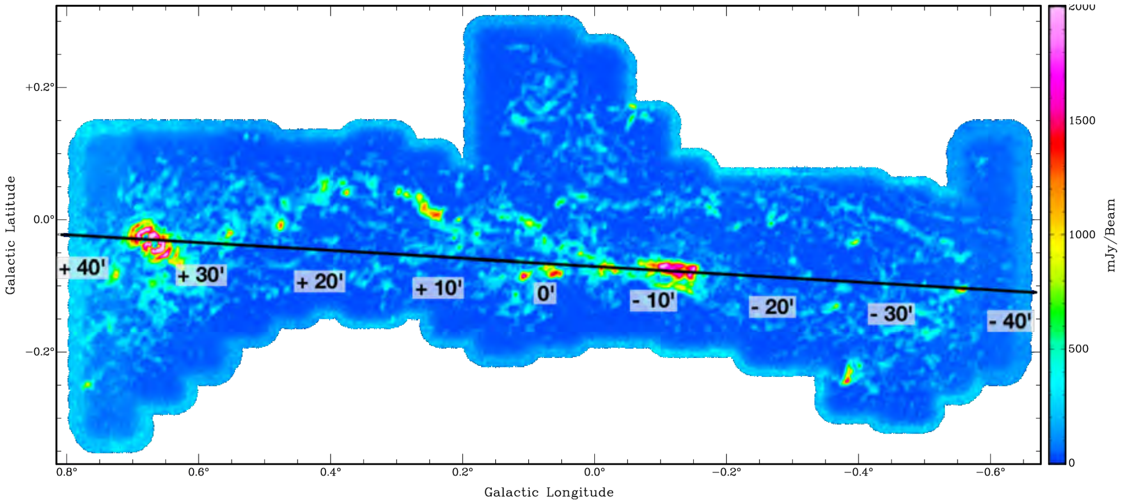

Figure 2.7: Illustration of the slice position used to obtain position-velocity diagrams in §2.5 and appendix A.

2.3.2.7 Position-Velocity Slicing

Position-velocity cuts through the restored data cube were calculated with CASA's task `impv` because it is possible to specify pixel positions as start and end point of the slice. This ensures that all pV-diagrams shown follow exactly the same line through Sgr B2 and Sgr C while passing close to Sgr A*. Each slice is averaged over $\pm 0.5'$ perpendicular to the line. An illustration of the orientation is given in fig. 2.7.

2.4 Ammonia Inversion Line Analysis

Further data products of SWAG are derived from the six ammonia inversion lines. Fitting the hyperfine structure offers maps of opacity and temperature throughout the CMZ.

2.4.1 Pixel by Pixel Hyperfine Structure Fitting

2.4.1.1 Masking

It is impossible to fit the ammonia hyperfine structure (§1.3.2.1) at each pixel of the SWAG maps because of low signal-to-noise and the need for large amounts of computation time. Selecting pixels that are likely to lead to a successful fit is therefore inevitable. A selection cut is applied in velocity, spatially and on intensity.

As a first step, channels outside the range of ± 190 km/s relative to the rest frequency are masked to exclude edge channel effects in some ammonia cubes. Edge channels show higher noise levels because real bandpasses do not follow step functions but transition from zero to unity transmissivity over a certain frequency range. The affected channels are not identical across pointings but differ by ± 1 channel of 2 km/s because the channel 0 frequency varies slightly with observation day or track.

The noisy edges of the maps where pointings do not overlap cannot be fitted and do not contain relevant information. They are excluded by applying the 100" edge mask.

Another mask is calculated from emission in the NH_3 (1,1) cube that selects individual pixels in a two-step process by intensity, first in the image cube and a second time on the collapsed map (moment 0). The first selection uses a threshold of 39 mJy $\simeq 3\sigma$ to include only emission that is likely to be real while excluding noise. The (1,1) cube is then collapsed into a moment 0 zero map and the second selection by flux density is applied. In manual tests, only pixels with flux densities above $\sim 3-5$ Jy/beam km/s were found to result in good fits for all six ammonia lines, thus the threshold is set to 5 Jy/beam km/s. It is still expected to reach lower ratios of successful fits for higher J lines as the SNR decreases with increasing J whereas the intensity selection does not change.

This procedure is applied to each ammonia image cube resulting in 24383 pixels that are considered "fittable".

2.4.1.2 Fitting in CLASS

The GILDAS[7] package CLASS[8] already offers a library to fit ammonia hyperfine structure up to NH_3 (3,3). Higher lines need to be specified manually and can be fitted with the same routine.

[7] `https://www.iram.fr/IRAMFR/GILDAS/`

[8] `http://iram.fr/IRAMFR/GILDAS/doc/html/class-html/`

Masked MIRIAD image cubes are exported to fits images by `fits` and imported into CLASS using `lmv`. The spectrum of each pixel satisfying the conditions listed above is fitted by selecting the appropriate line profile with `method` (built-in or user-specified) and minimising the deviation with `minimize`. Line profiles of NH_3 (1,1) to (3,3) are implemented as `method nh3(j,j)` while (4,4) to (6,6) lines are constructed from a text file listing hyperfine component positions and strengths and set as `method hfs`. Relative positions and strengths of the hyperfine structure components are taken from Townes & Schawlow (1975) as listed in table 1.2 in §1.3.2.1. The found best-fit parameters and the spectra with fitted profile are saved to allow for manual inspection if needed. CLASS fits the quantities line area $T_L \cdot \tau$, line-of-sight velocity v_{los} in the LSRK (Local Standard of Rest, Kinematic) frame, line width $FWHM$ and opacity τ with the respective errors. While the former are not restricted, τ is limited to $0.1 \leq \tau \leq 30$. The spectrum of a perfectly thin cloud with $\tau \equiv 0$ is still fitted as $\tau = 0.1$ and therefore introduces an factor in line temperature of

$$\lim_{\tau \to 0} \frac{0.1}{\tau} \frac{1 - e^{-\tau}}{1 - e^{-0.1}} = 1.051$$

according to the opacity term in eq. (1.61). This deviation by up to 5.1% is small compared to the flux uncertainties and can be neglected.
CLASS does not fit line brightness temperature T_L directly but outputs the parameter $p_1 = T_L \cdot \tau$. A calculation of T_L from p_1 and opacity[9] is given in the manual[10] $\tau = p_4$.

$$T_L = \frac{p_1}{p_4} \left(1 - e^{-\tau}\right) \tag{2.2}$$

$$\Delta T_L = \left[\left(\frac{\Delta p_1}{p_4} \left(1 - e^{-\tau}\right) \right)^2 + \left(\frac{p_1 \, p_4}{p_4^2} \, e^{-\tau} \left(\tau - e^{\tau} + 1\right) \right)^2 \right]^{1/2} \tag{2.3}$$

Another caveat when using CLASS for fitting is its inability to handle the number of emission sources along the line of sight as a free parameter. As it is not possible to specify the number of components manually for this many pixels and fixed values higher than one yield bad results for single components, only one component is assumed everywhere. The is that only the strongest emission peak is fitted when multiple components are present. Especially near the Galactic Center, multiple sources contribute to the emission measured in a single pixel with the spectrum clearly dominated by one of them. Other contributing sources are typically considerably fainter and the bias towards certain clouds is small. Still, all derived maps must be understood as something like intensity weighted[11] and biased towards the strongest sources along the line of sight.

[9] Note that the manual mixes up τ and p_4 in this formula. Eq. (2.2) is quoted literally.

[10] `https://www.iram.fr/IRAMFR/GILDAS/doc/html/class-html/node11.html`

[11] Or course, discarding emission of less intense sources is not intensity weighting but the maps can be understood in this way when resolution arguments are considered as well. One

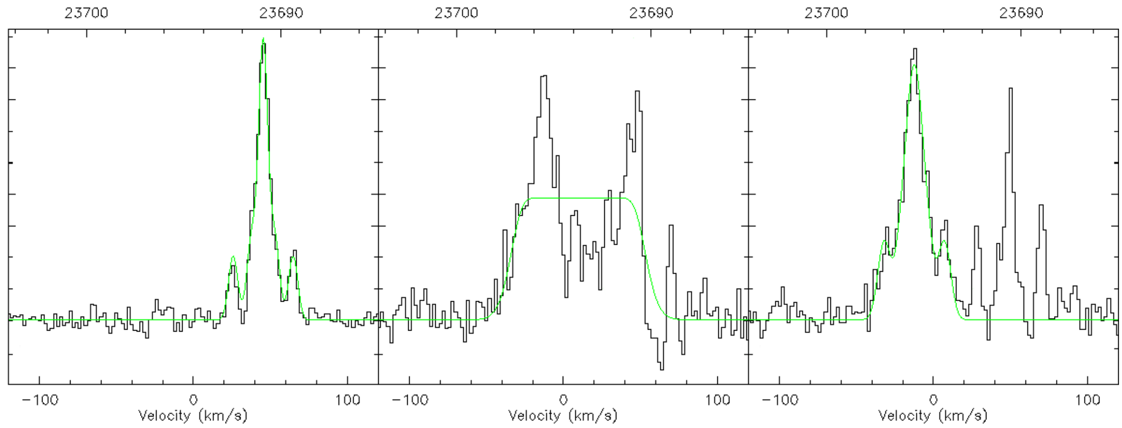

Figure 2.8: "The Good, the Bad and the Ugly" when fitting ammonia hyperfine structure. *left panel*: typical good fit *middle panel*: unsuccessful (bad) fit that is excluded due to the unphysically large line width *right panel*: multiple components along the line-of-sight of which only the strongest is fitted.

For simplicity, no initial guesses of the line position were used but CLASS's algorithm reliably finds the hyperfine structure. It is planned for future work to include an unconstrained Gaussian fit to find initial guesses for hyperfine fitting, thus increasing the rate of successful fits and decreasing the uncertainty of the fit parameters.

2.4.1.3 Fit selection

The masking procedure described above guarantees that virtually all fits are successful, i.e. a solution is found. However, this does not imply that every solution is good. Bad fits are characterized by low values in `lineRMS` and high uncertainties of the fit parameters. The thresholds at which a fit is rejected as 'bad' are `lineRMS`> 0.1, $\Delta v_{los} > 10.0\,\mathrm{km/s}$, $FWHM > 50.0\,\mathrm{km/s}$ and $\Delta FWHM > 10.0\,\mathrm{km/s}$ with Δx denoting the error of x. The distinction between good and bad fits is easily done based on `lineRMS` that describes the χ^2 of the fit and the errors, because for these quantities no intermediate values occur in this data set, it is either good or bad. The thresholds and characterization of what can be considered good or bad were derived by visual inspection of ~ 100 fitted spectra. Poor fits result mostly from unfortunate choice of initial guesses by the built-in routine and can be resolved by calling `iterate`. In cases that were already well

pixel is not totally independent from its neighbors due to beam smearing. Therefore, all derived quantities are correlated over approximately one beam ($\sim 26" \times 18"$ or 5×4 pixel). When fitting pixels independently, source 1 is stronger and defines the temperature whereas in another pixel close-by source 2 might win and define the temperature there. Reducing the artificially increased resolution (1 pixel, 5") to the observed resolution (1 beam, $26" \times 18"$) then averages temperatures from the two sources according to their abundance, which is similar to an intensity weighted average. This situation does not necessarily happen when two or more source are present, though, and the reality is certainly more complicated and might be somewhere in between the two extremes of one source winning always and random chances.

Table 2.4: Fit success rates for the six ammonia inversion lines observed with SWAG. For details about the definition of a successful (or good) fit see §2.4.1.3.

	(1,1)	(2,2)	(3,3)	(4,4)	(5,5)	(6,6)
selected pixels	24383	24383	24383	24383	24383	24383
fitted pixels	23790	23025	23646	19269	19261	19245
failed to fit	593	1358	917	5114	5122	5138
% fitted	97.6	94.4	96.2	79.0	79.0	78.9
bad fits	353	203	63	132	466	274
good fits	23437	22822	23403	19137	18795	18971
% good	98.5	99.1	99.7	99.3	97.6	98.6

fit by the first minimization, another iteration would decrease fit quality. Setting a selection on line width is justified physically as typical Galactic Center clouds show line profiles of $5 < FWHM\,[\mathrm{km/s}] < 25$. Fits broader than that are pixels of low signal-to-noise ratio where the algorithm tried to model noise by an offset over the whole image cube velocity range. Additional constraints, e.g. on opacity, are not needed and do not change the selection at all because bad fits show several unphysical or highly uncertain parameters.
The overall success rates defined as number of successful fits (after discarding bad fits) over number of pixel selected to be fitted is $> 98\%$ for all ammonia inversion lines (see table 2.4 for details). With a lower threshold of $\sim 3\,\mathrm{Jy/beam\,km/s}$ in initial masking, it might be possible to obtain more fits and eventually more temperatures without wasting large amounts of computation time.

2.4.1.4 Fit result maps

The results of pixel-by-pixel fitting are written back into an empty fits image with `setpix`, a tool of the WCSTools Collection[12]. This way, line-of-sight velocity, line width, opacity and column density maps are constructed along with the respective error maps. Note that this column density is calculated according to eq. (1.61) from fitted values which in turn only apply to the strongest line at that pixel position. The total column density derived from a moment 0 map thus differs depending on the number and strengths of multiple components along the line of sight.

2.4.2 Temperature Maps

Rotational temperatures are calculated from the slope (eq. 1.44) between two rotational states in a Boltzmann plot according to eq. (1.46). Column densities in the optically thin limit (eq. 1.54) and with full opacity correction (eq. 1.61) are considered to derive two maps. Maps in the thin limit are calculated, too, because they offer larger spatial coverage and are slightly more precise in optically thin

[12] `http://tdc-www.harvard.edu/wcstools`

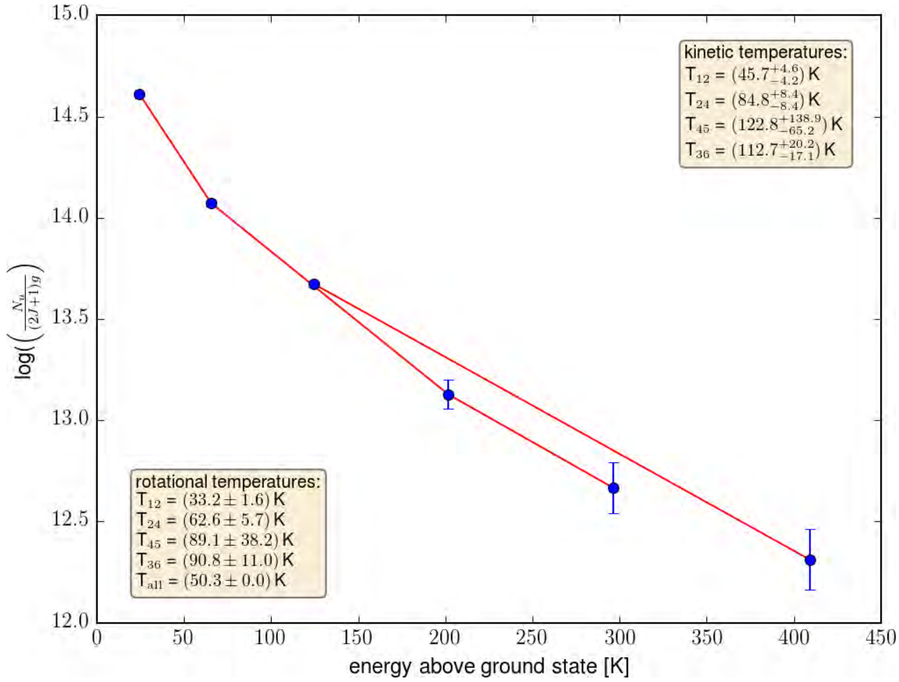

Figure 2.9: Boltzmann plot for J = 1, ..., 6 derived from opacity corrected column densities in a Galactic Center cloud at $l \sim -0.37°$, $b \sim -0.15°$. The slope flattens at J = 3 to J = 5.

regions due to the minimal optical depth of 0.1 in CLASS. Dense gas with strong emission lines is better represented by the maps that incorporate correct opacity treatment.

Without a prior on ortho-to-para ratio, it is impossible to derive temperatures from all combinations of rotational states. However, comparing ortho-ortho and para-para states is possible, but the respective states cannot be too different in energy before the non-constant slope must be taken into account. Out of 7 combinatorial possibilities, only four are reasonably relevant: T_{12}, T_{24}, T_{45} and T_{36}. Further para temperatures (T_{14}, T_{15}, T_{25}) do not deliver new information.

Rotational to kinetic temperature conversion is calculated according to eqs. (1.62) - (1.68) and the respective error by Gaussian error propagation.

These four temperature measures are calculated for each pixel where it is possible. In regions of low emission, temperatures of high J states cannot be calculated anymore because hyperfine structure fits fail more often. In these cases it is necessary to use moment map based temperature maps if a temperature estimate is needed.

2.5 Data Products

2.5.1 Image Cubes

Out of the 42 spectral lines observed by SWAG, two of them, NH_3 (1,1) and H_2O, are presented on the following pages to illustrate data quality. Further lines can be found in appendix A.1 in the printed version of this thesis. The full list of 42 lines is only contained in the online version of appendix A.1.
The data cube of each line is presented with a channel map, moments 0, 1 and 2, spectra at Sgr A*, B2 and C, and a position-velocity diagram.
The channel maps display every 7^{th} channel of 2.0 km/s width without averaging starting from a velocity of -132.0 km/s relative to the line's rest frequency. In each panel, the velocity is indicated in the top left corner. The color mapping changes between different lines and is shown in the bottom right panel.
Moment maps are shown for order 0, 1 and 2, which is integrated intensity, velocity field and velocity dispersion, respectively. See §2.3.2 for details on how these plots were produced.
Spectra of the three most important sources in the filed of view, Sgr A*, Sgr B2 and Sgr C, are included, too. The region around Sgr B2 is called Large Molecular Heimat because most molecules known to exist in space can be detected there. The spectrum can therefore help to decide if a line was detected at all.
Fig. 2.7 shows the position where a pV-slice was taken. In order to cut through Sgr B2 and Sgr C, it barely misses Sgr A* and contains much emission from the CMZ.

Table 2.5: SWAG Image properties. For noise estimates see table 2.2

imaged range (relative to ν_{rest})	$-250 - +250$ km/s
channel width	2.0 km/s
spatial resolution	5”
weighting (robust)	+2 (natural)
beam size	26”.22 × 17”.84
position angle	89.3°

NH_3 (1,1)

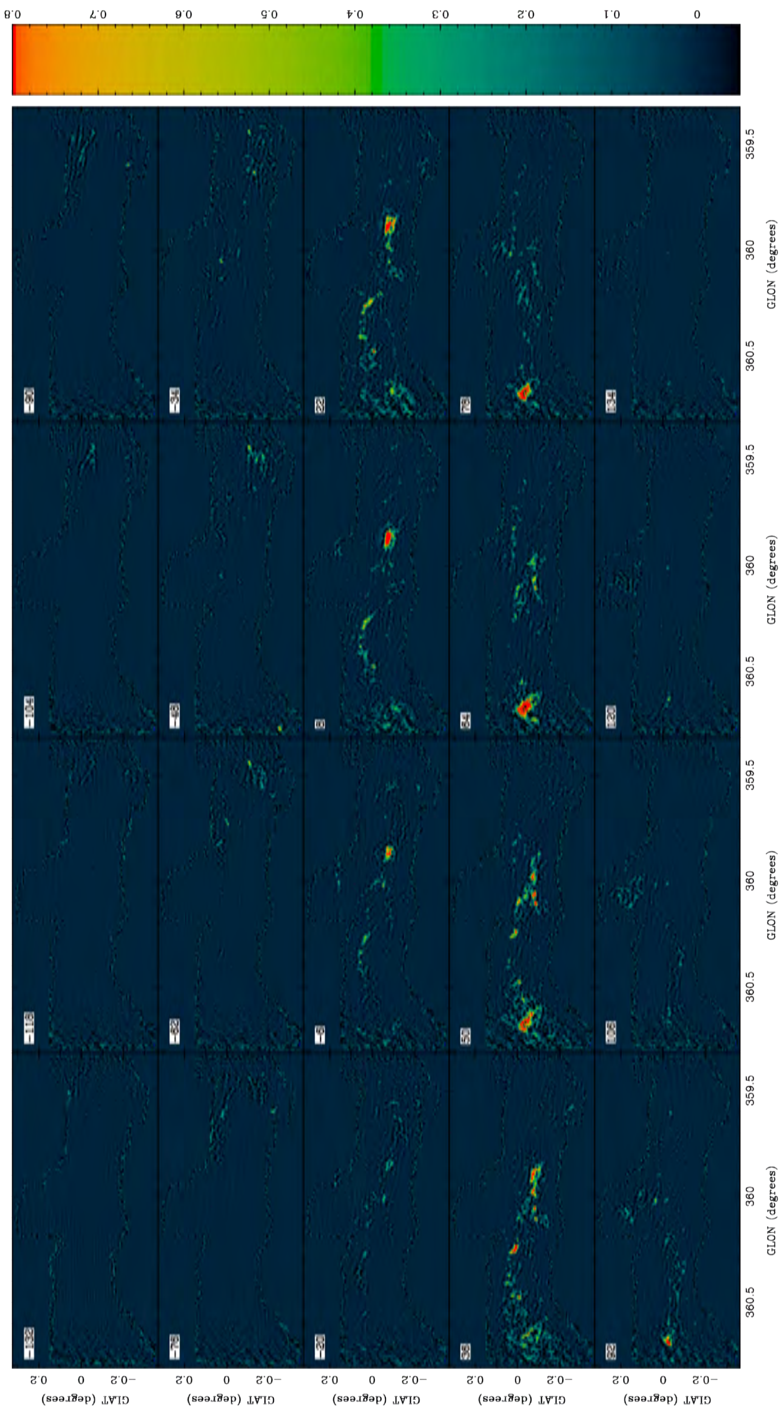

Figure 2.10: NH_3 (1,1) channel map showing every seventh 2 km/s channel. Velocity in km/s is indicated in the top left corner of each panel. Intensity scaling is $0 - 0.8$ Jy/beam.

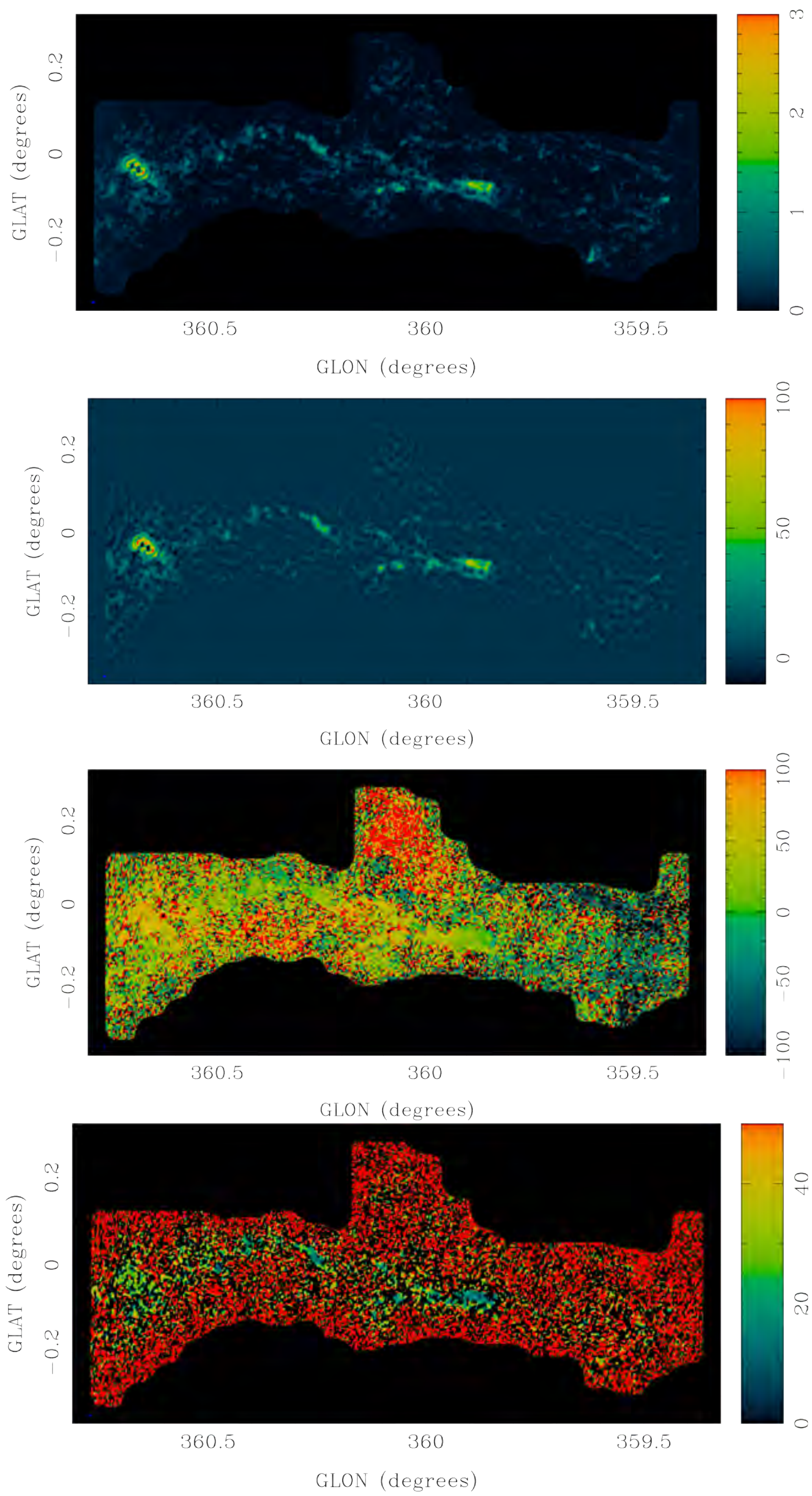

Figure 2.11: NH_3 (1,1) moment maps. From top to bottom: peak intensity (moment -2, in Jy/beam), integrated intensity (moment 0 in Jy/beam km/s), velocity (moment 1, in km/s), velocity dispersion (moment 2, in km/s).

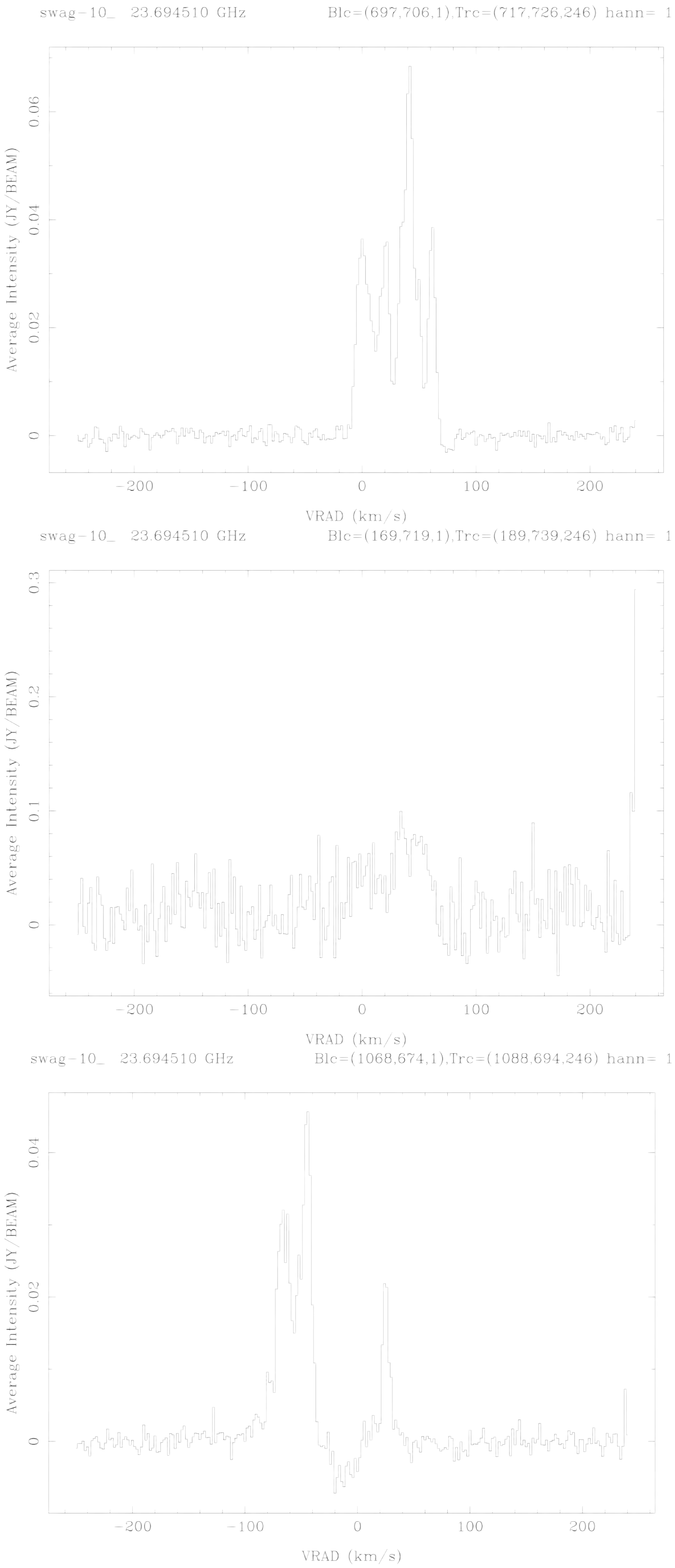

Figure 2.12: NH_3 (1,1) spectra at the positions of Sgr A* (top), Sgr B2 (center) and Sgr C (bottom).

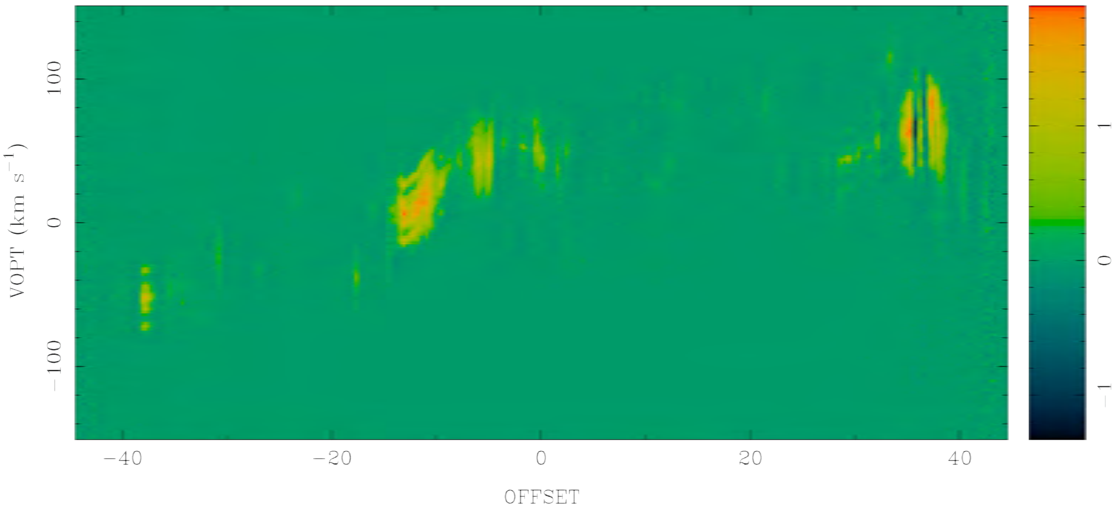

Figure 2.13: NH_3 (1,1) position-velocity diagram through Sgr B2 (~ -30" to -40") and Sgr C ($\sim +35$").

H_2O

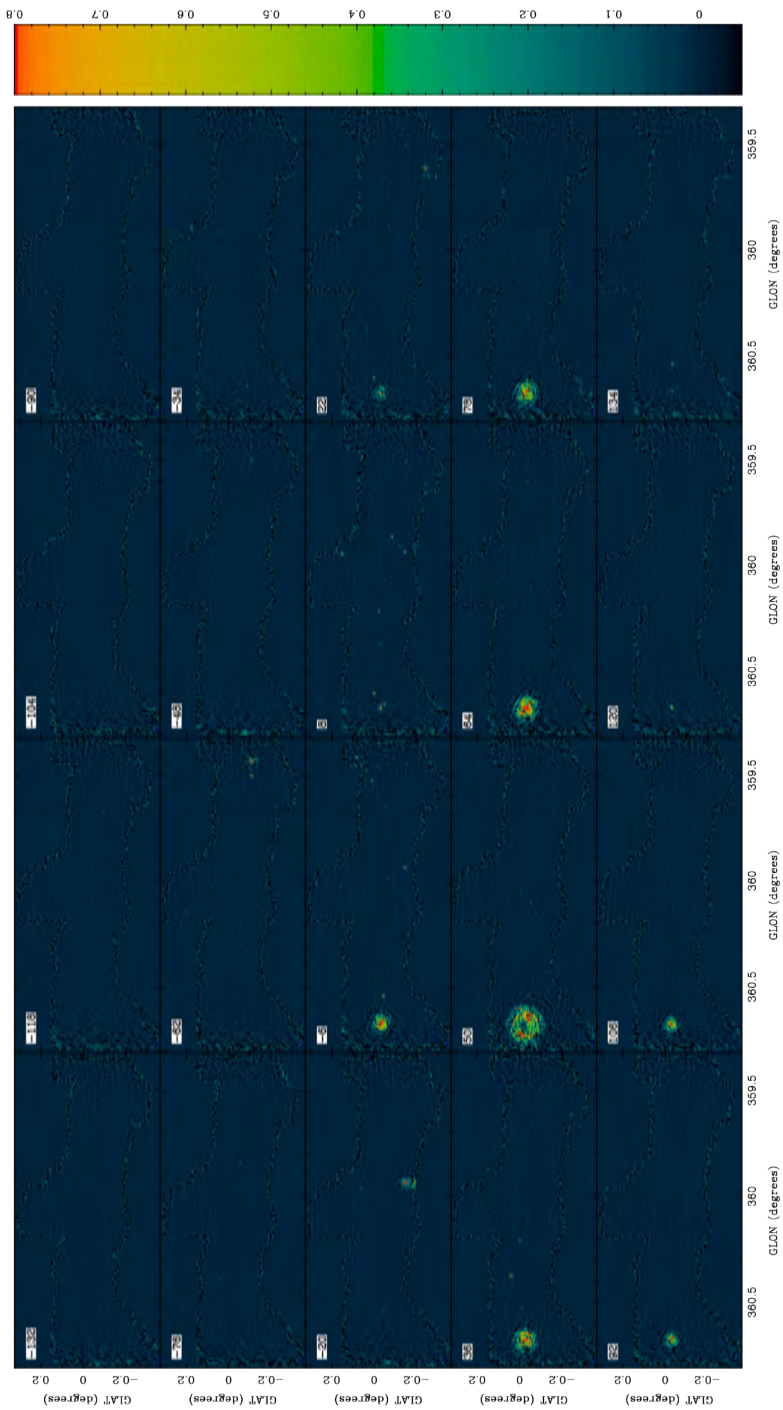

Figure 2.14: H_2O channel map showing every seventh 2 km/s channel. Velocity in km/s is indicated in the top left corner of each panel. Intensity scaling is $0 - 0.8$ Jy/beam.

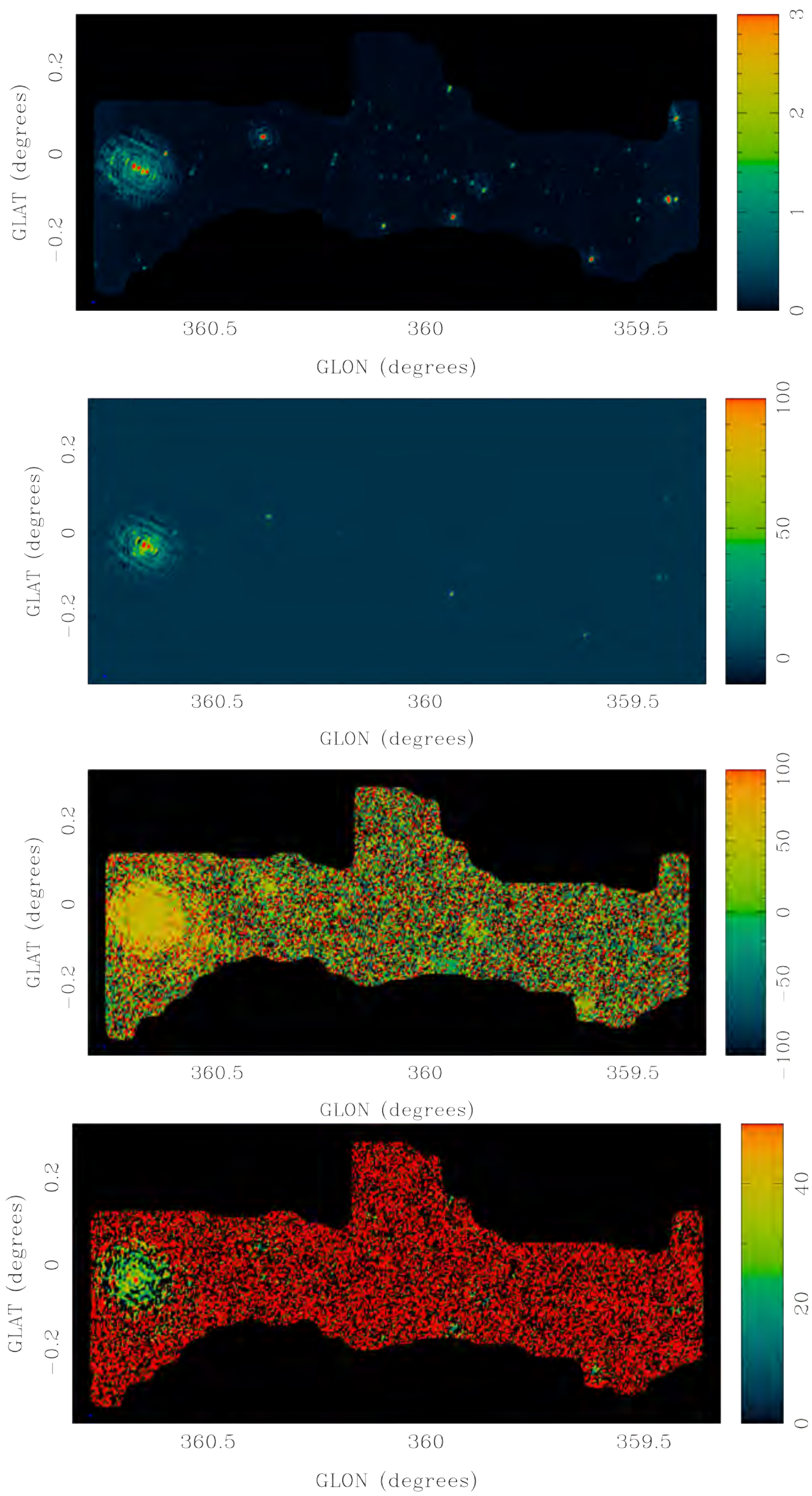

Figure 2.15: H_2O moment maps. From top to bottom: peak intensity (moment -2, in Jy/beam), integrated intensity (moment 0, in Jy/beam km/s), velocity (moment 1, in km/s), velocity dispersion (moment 2, in km/s).

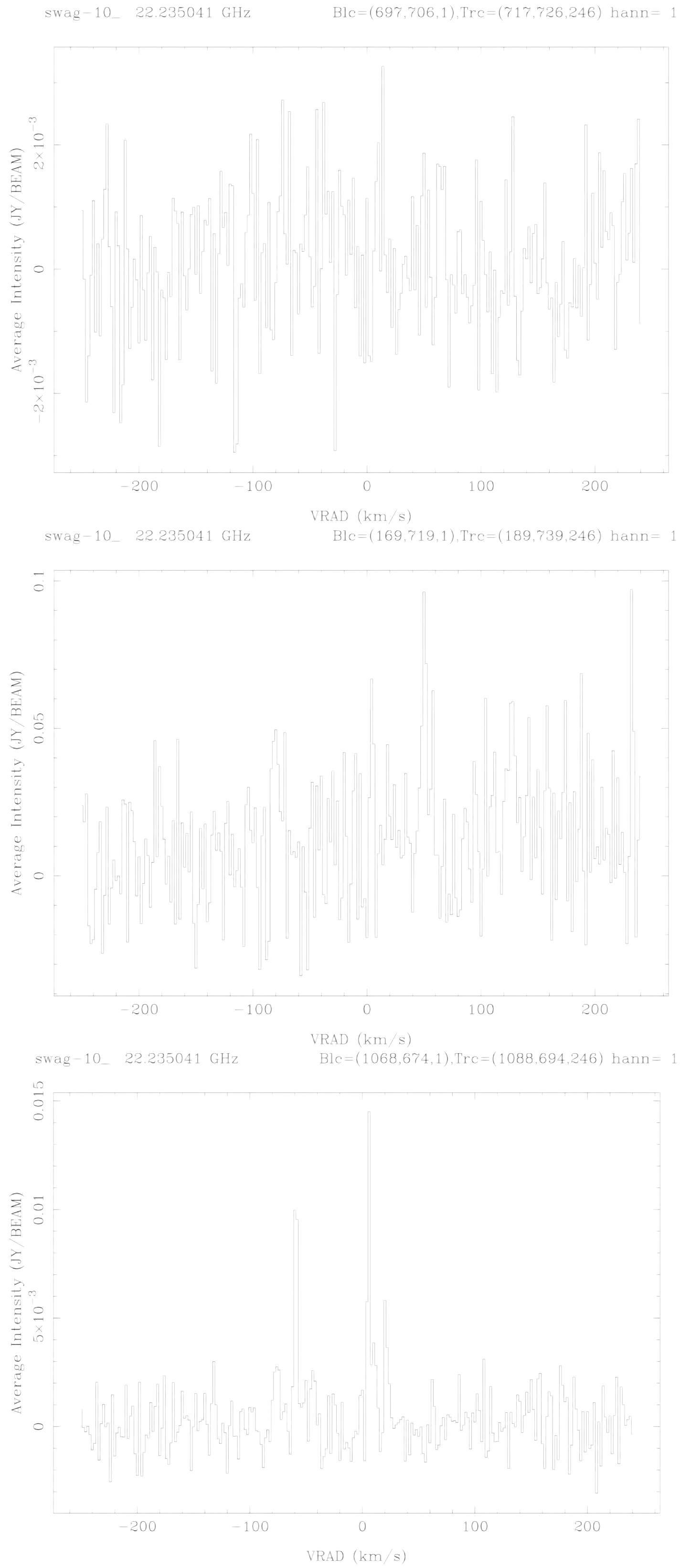

Figure 2.16: H_2O spectra at the positions of Sgr A* (top), Sgr B2 (center) and Sgr C (bottom).

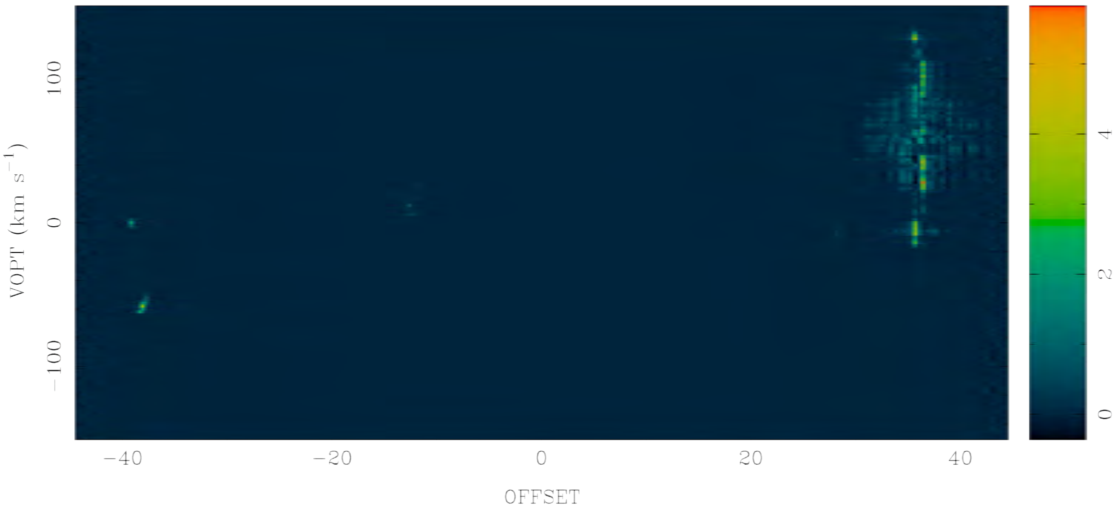

Figure 2.17: H_2O position-velocity diagram through Sgr B2 (~ -30"to -40") and Sgr C ($\sim +35$").

2.5.2 Ammonia Hyperfine Structure Fit Results

For all of the following maps derived from hyperfine structure fits, error maps were derived by Gaussian error propagation. Results for NH_3 (1,1) are shown here, while higher J transitions can be found in appendix A.2.

Successful Fits

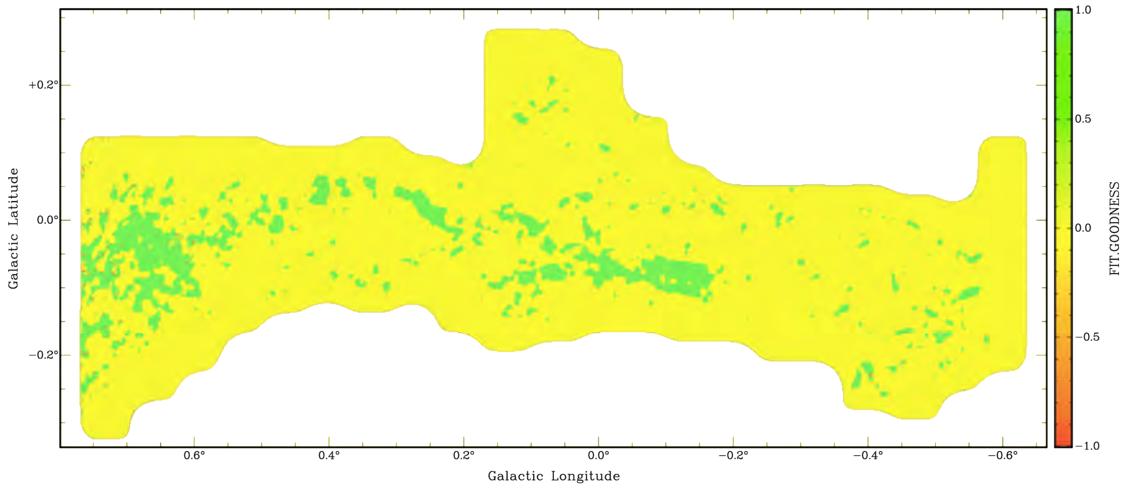

Figure 2.18: NH_3 (1,1) map of successful fits. The yellow region inside the grey contours is searched for possible emission to be fitted according to §2.4.1.3. Green pixels could be fitted with by CLASS and are subsequently classified as good or bad. For very few red pixels, the algorithm failed and no fit to the spectrum is found.

Line-of-sight velocity v_{los}

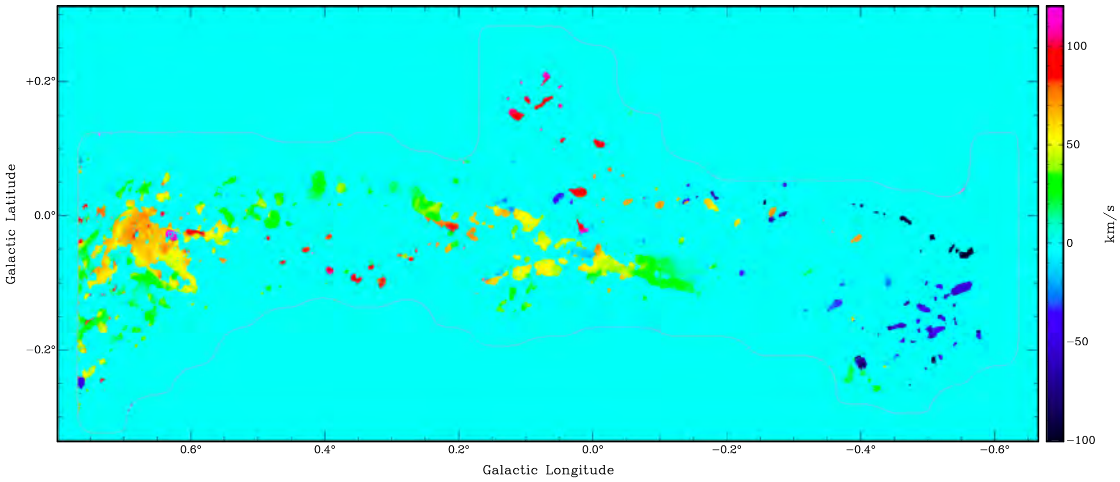

Figure 2.19: NH_3 (1,1) line-of-sight velocity map. The smooth velocity field strengthens the confidence that there are no significant errors.

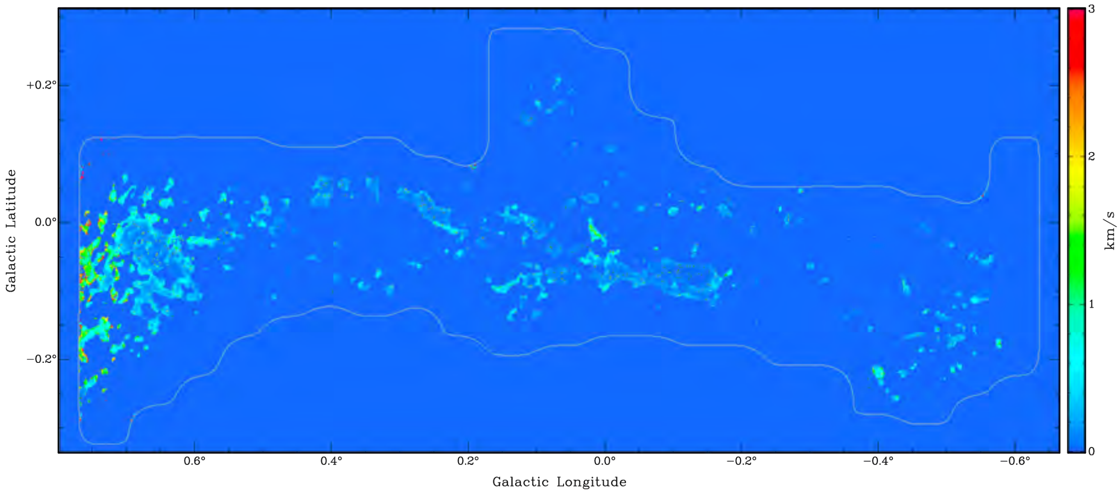

Figure 2.20: NH_3 (1,1) line-of-sight velocity error map. Errors are typically in below 0.5 km/s with only some pixels above that value. The left-most 0.1° suffers from high noise, which leads to an enhanced number of pixels satisfying the threshold criteria for fitting although a good fit might not be achieved. For further investigation of the star formation sequence, this region is not of importance as the dust ridge contains enough emission from molecular clouds to constrain the evolution.

Line width FWHM

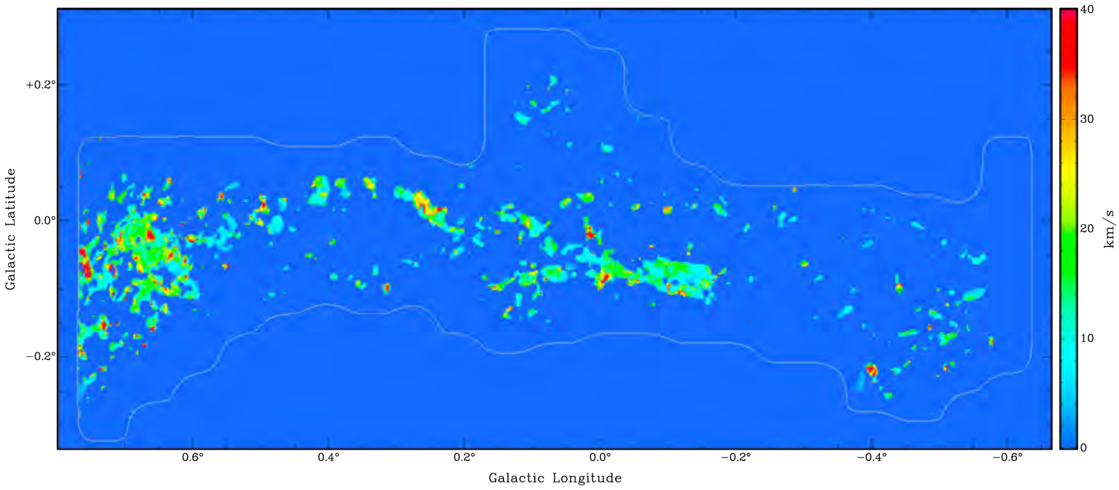

Figure 2.21: NH_3 (1,1) line width (FWHM) map.

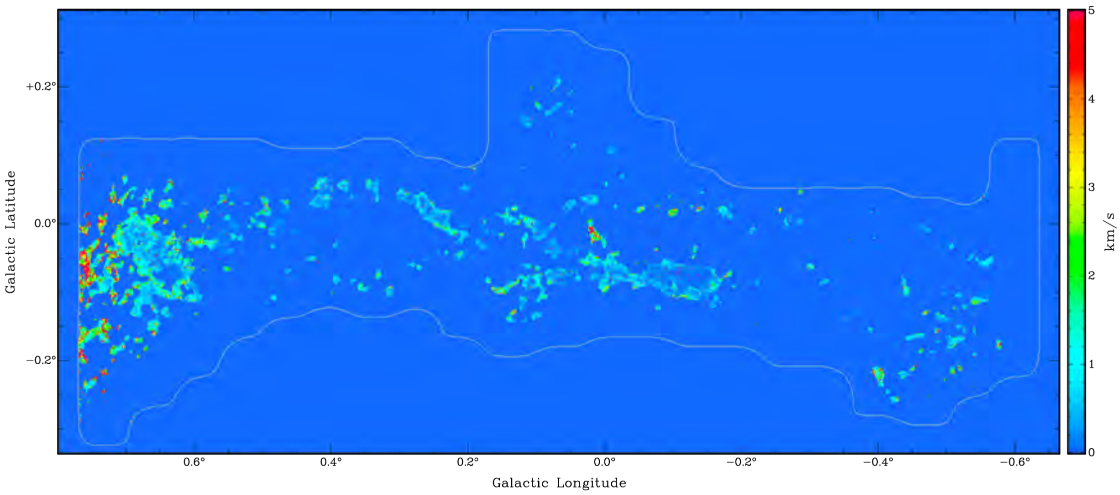

Figure 2.22: NH_3 (1,1) line width (FWHM) error map. The same properties as in above's line-of-sight velocity error map apply with the error of line width being typically below 1 km/s.

Opacity τ

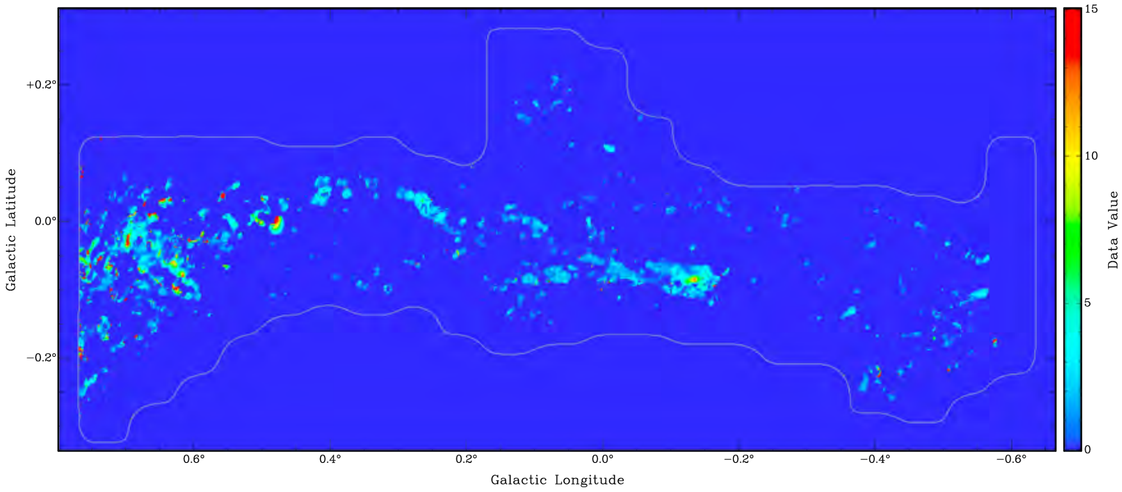

Figure 2.23: NH_3 (1,1) opacity map. This map shows some interesting features. While most emission is moderately thick, several cores show high opacities up to more than 15. On the other hand, thin NH_3 (1,1) emission below 1 is rare.

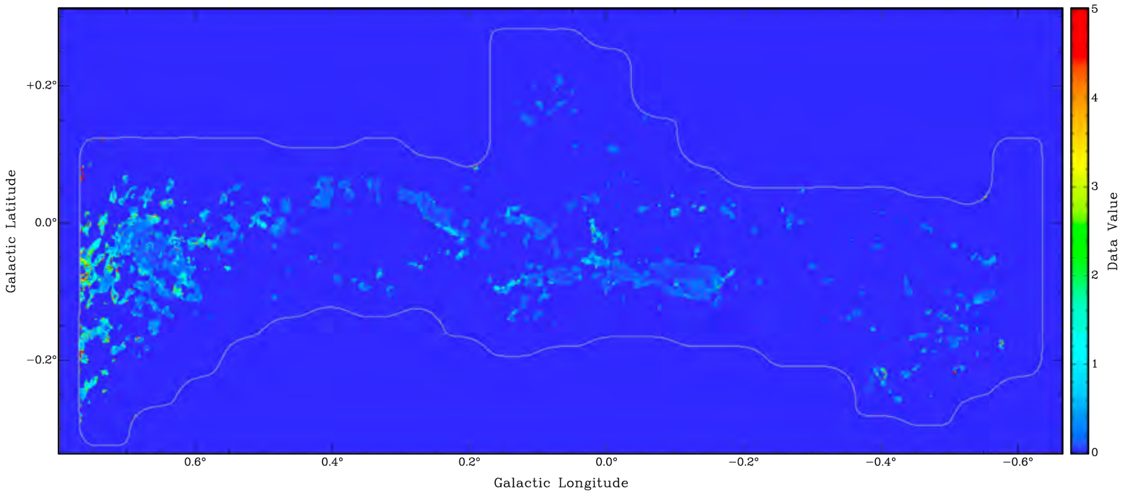

Figure 2.24: NH_3 (1,1) opacity error map. Besides the high noise region at $l > 0.7$, opacity errors are mostly below 0.3 which allows precise differentiation between regions where different approximations (optically thin or thick) can be justified.

Column density N

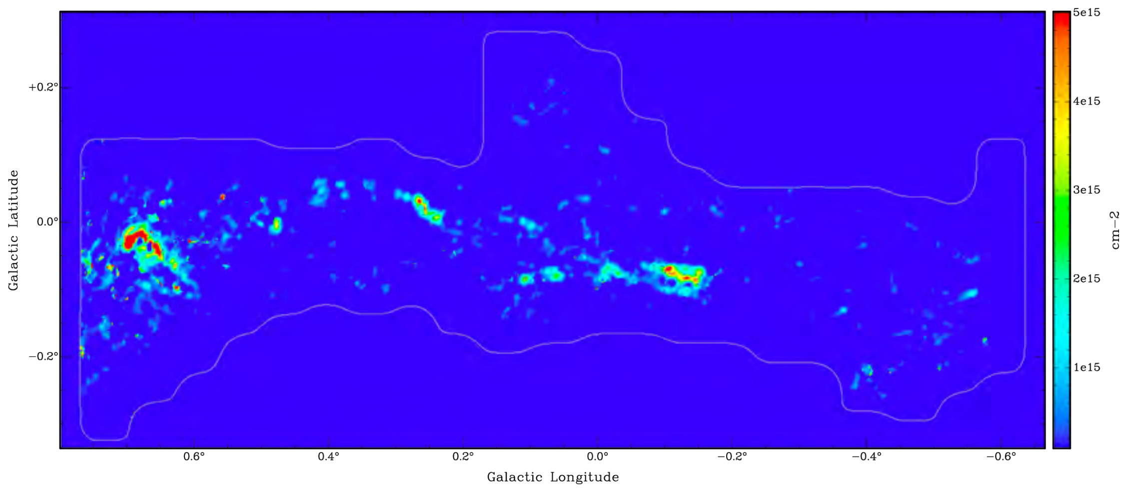

Figure 2.25: NH_3 (1,1) column density map. Areas of high column densities do not generally coincide with regions of high opacity as could be expected. Several cores can be identified in the larger clouds.

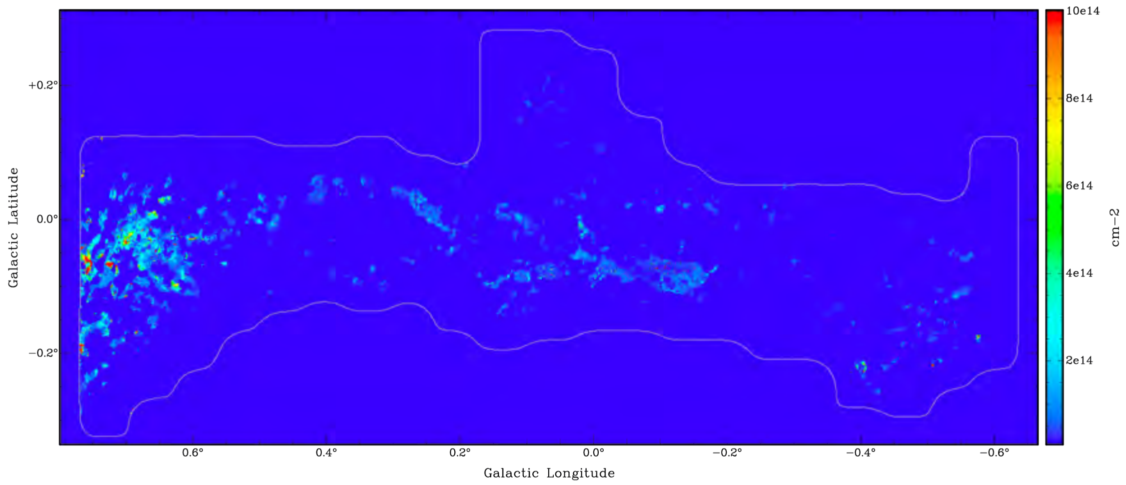

Figure 2.26: NH_3 (1,1) column density error map.

2.5.2.1 Temperature Maps

Temperature Maps including full Opacity Corrections

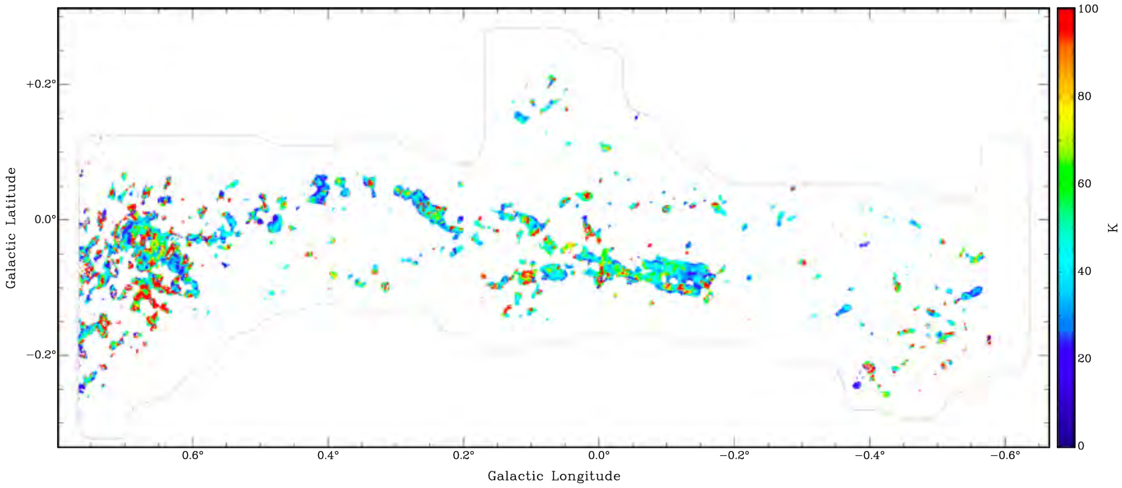

Figure 2.27: $T_{12,kin}$ map. As is shown in fig. 1.8, kinetic temperatures derived from ammonia (1,1) and (2,2) lines are only justified up to $\sim 60\,\mathrm{K}$, i.e. blue and green colors. However, this map shows higher values in order to prove that there are higher gas temperatures that need to be measured by higher excitation lines. Due to the temperature calculation involving divisions and exponential, the map is not as smooth as the column density maps from which it was derived.

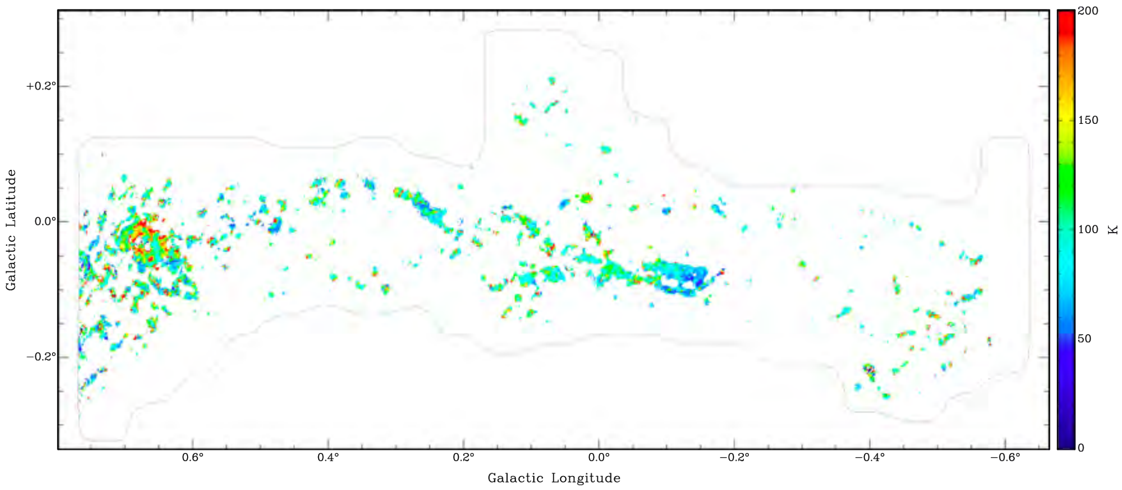

Figure 2.28: $T_{24,kin}$ map. T_{24} is susceptible to temperatures of $\sim 50\,\mathrm{K}$ (blue) to $\sim 150\,\mathrm{K}$ (green-yellow). In some regions, an anti-correlation with $T_{12,kin}$ can be observed.

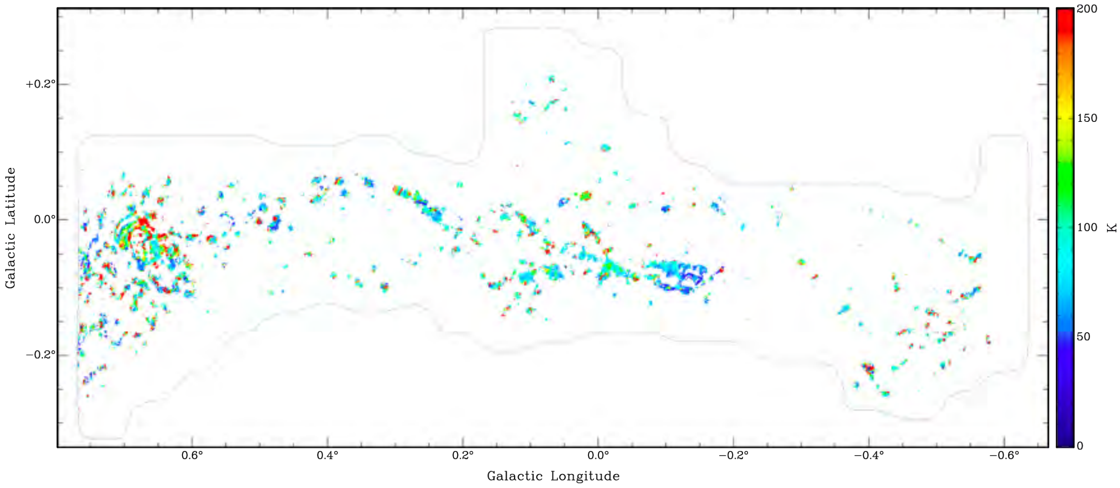

Figure 2.29: $T_{45,kin}$ map. Highly excited ammonia gas in the inversion states (4,4) and (5,5) is sensitive to gas temperatures of up to ~ 200 K but cannot be trusted below ~ 100 K.

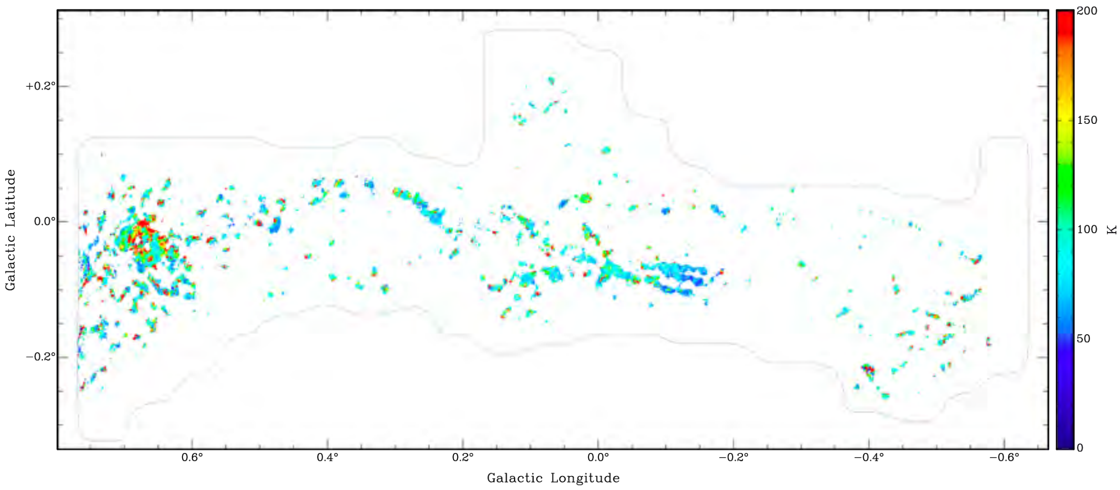

Figure 2.30: $T_{36,kin}$ map. $T_{36,kin}$ is the only ortho temperature that can be derived using SWAG measurements only without having to extrapolate the NH_3 (0,0) population. The map is very similar to $T_{45,kin}$ with the major difference being fewer successful calculations in $T_{45,kin}$.

Temperature Maps assuming optically thin Emission

The following temperature maps are calculated at every pixel of SNR > 3σ of the NH_3 (1,1) to (6,6) cubes under the assumption of optically thin emission. In the outermost stripes with increased noise level, pixels are selected from the same noise as in the center and therefore noise gets translated into a temperature for a significant amount of pixels. Compared to the hyperfine fitted temperature maps, the number of pixels with temperature estimate is much larger by a factor of about two (T_{45}) to four (T_{12}).

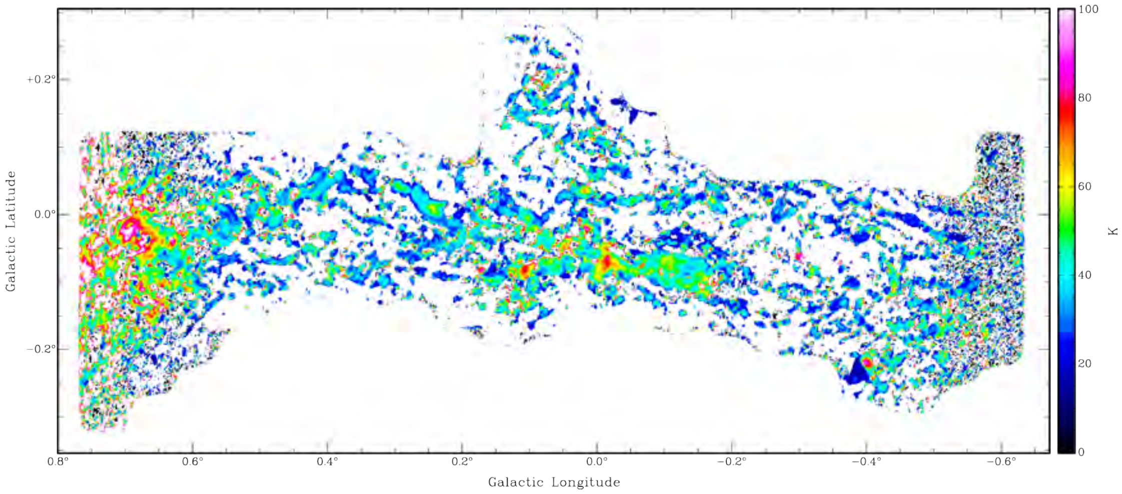

Figure 2.31: Kinetic temperature map derived from the line ratio of ammonia's (1,1) and (2,2) metastable lines.

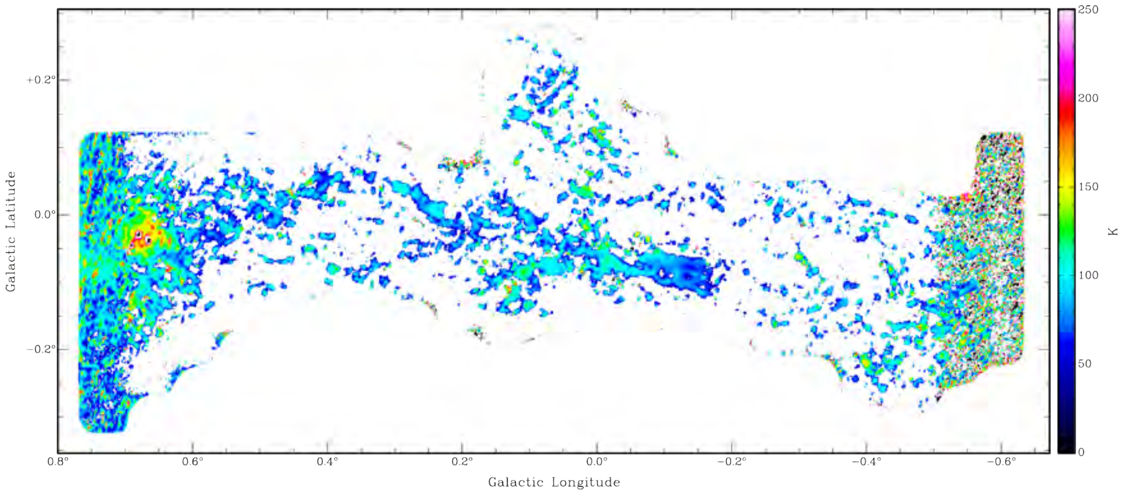

Figure 2.32: Kinetic temperature map derived from the line ratio of ammonia's (2,2) and (4,4) metastable lines.

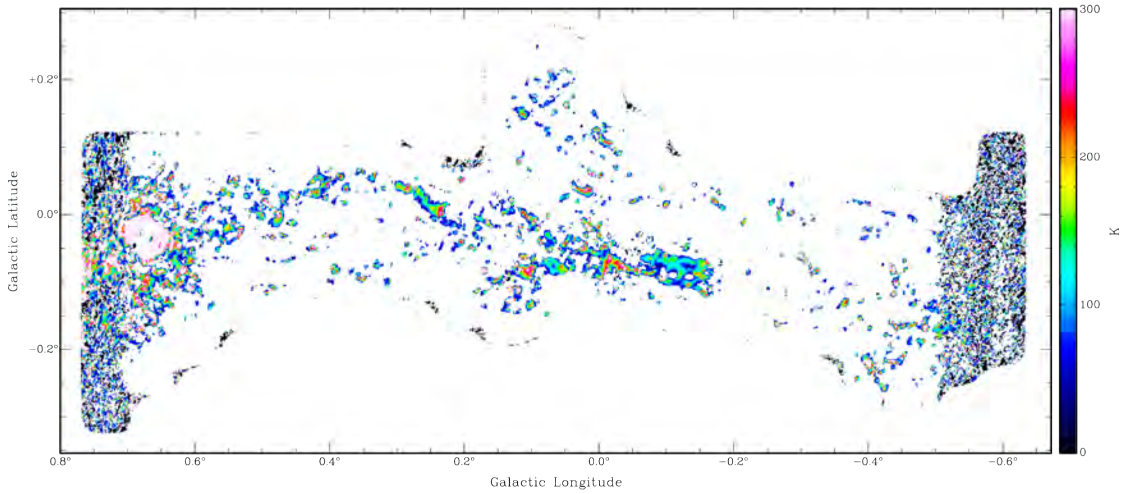

Figure 2.33: Kinetic temperature map derived from the line ratio of ammonia's (4,4) and (5,5) metastable lines.

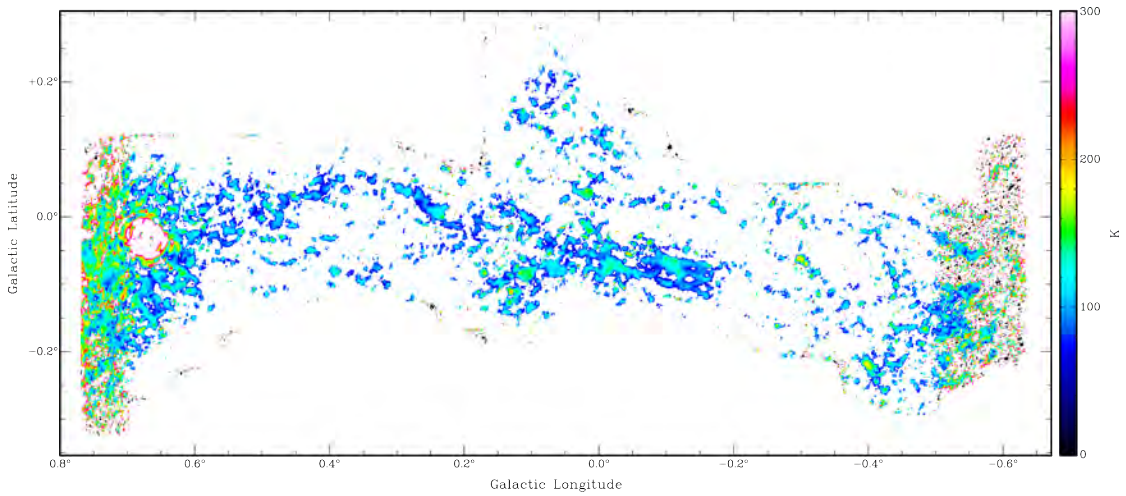

Figure 2.34: Kinetic temperature map derived from the line ratio of ammonia's (3,3) and (6,6) metastable lines.

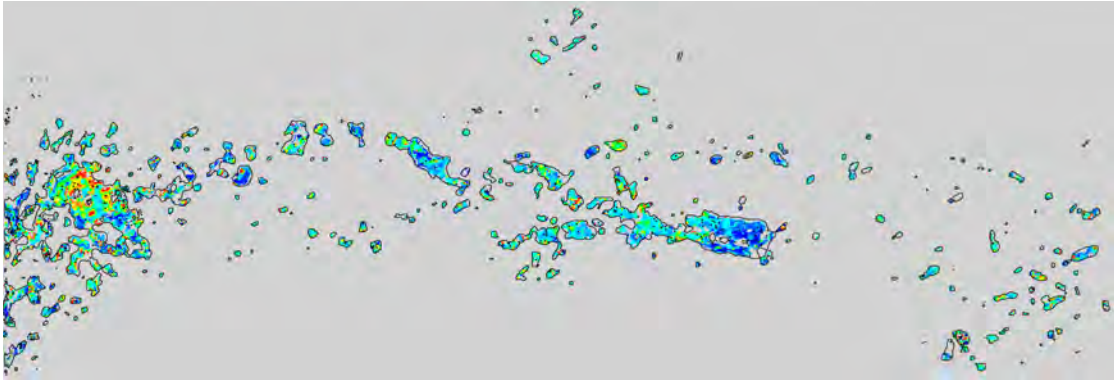

SWAG: A new Resource to Study Star Formation

The Survey of Water and Ammonia in the Galactic Center (SWAG) provides a wealth of data in unprecedented detail with even more possible applications. The direct results, maps and spectral information for 42 lines, are already shown in §2.5, together with plenty of new information about the dense gas in the Central Molecular Zone (CMZ) derived from ammonia hyperfine structure fits. Other applications include further ISM related data like ammonia gas formation temperatures derived from ortho-para ratios, but also an unbiased water maser survey and a molecular cloud catalogue via clump decompositions. Not shown in this work is continuum related data that offers maps of radio continuum emission, spectral index and curvature, which are especially sensitive to thermal sources and free-free emission.
One particularly interesting opportunity of SWAG is to exploit the new ammonia data and study star formation. Data reduction and imaging of a large survey already takes a significant chuck of the limited time for a master thesis; so, a concise scientific question must be addressed. A convenient possibility is the Galactic center star formation sequence (SFS) proposed by Longmore et al. (2013) as described in §1.4.2. Reliably testing this model was not possible with existing observations, but can now be done with SWAG. This analysis, however, utilizes only a small portion of the whole survey, the six metastable ammonia lines, because no further information regarding the scientific question can be drawn immediately from other spectral lines (§3.2.2). In order to derive the needed tools and gain understanding, a sequential approach was chosen. First tests were run on 20 selected clouds and the 113 positions used by Kruijssen et al. (2015) to derive their orbital model. The methods found to work were then applied to all pixels where it is possible and the results interpreted in the general framework of star formation and star bursts in galactic center gas rings as well as its application to the CMZ (Kruijssen et al., 2015; Krumholz & Kruijssen, 2015; Longmore et al., 2013).

NH_3 T_{24} temperature map obtained from SWAG

3.1 Data

The data used in this chapter originate from three sources, namely the surveys SWAG and Hi-GAL (Molinari et al., 2011) as well as a list of orbital parameters by Kruijssen et al. (2015).

3.1.1 SWAG: Ammonia Gas

The analysis makes use of image cubes and pixel-by-pixel fit maps of meta-stable ammonia lines from the Survey of Water and Ammonia in the Galactic Center without any additional editing. The creation of these data products was already described in §2.

3.1.2 Hi-GAL: Dust Temperature Map

Dust temperatures are provided by The Herschel Infrared Galactic Plane Survey (Hi-GAL Molinari et al., 2011). This survey mapped a strip of the Galactic plane at $|l| \leq 60°$, $|b| \leq 1°$ with the Herschel Space Observatory[1] in five infrared bands at 70, 170, 250, 350 and 500μm with Herschel's PACS and SPIRE cameras (Molinari et al., 2010b). Dust temperatures are derived from a pixel-by-pixel fit to the $70 - 350\,\mu$m data based on the DustEM model by Compiègne et al. (2011) and shown in fig. 3.1. The better resolution of the $70 - 250\,\mu$m maps is matched to the ~ 25" beam of the $350\,\mu$m observations which is comparable to the beam size of SWAG (17."84 × 26."22 $\sim 0.75\,\Theta_{Hi-GAL}$). The papers on Hi-GAL published so far do not include further information about dust temperatures, like error maps or a note on sensitivity, which has to be considered during analysis and interpretation.

3.1.3 Kinematic Model

A detailed list of parameters and observables of the orbital model (§1.4.1.2) is included in the online supplementary material of Kruijssen et al. (2015). The list of positions in Galactic coordinates and line-of-sight velocity is given at time steps of 0.01 Myr and sets the resolution for all analyses involving time. A test of the analytic approach of constructing sequences was performed on exactly the 113 positions used by Kruijssen et al. (2015) to constrain the model. These positions are not published but were obtained from Diederik Kruijssen personally.

[1]Herschel is an ESA space observatory with science instruments provided by European-led Principal Investigator consortia and with important participation from NASA.

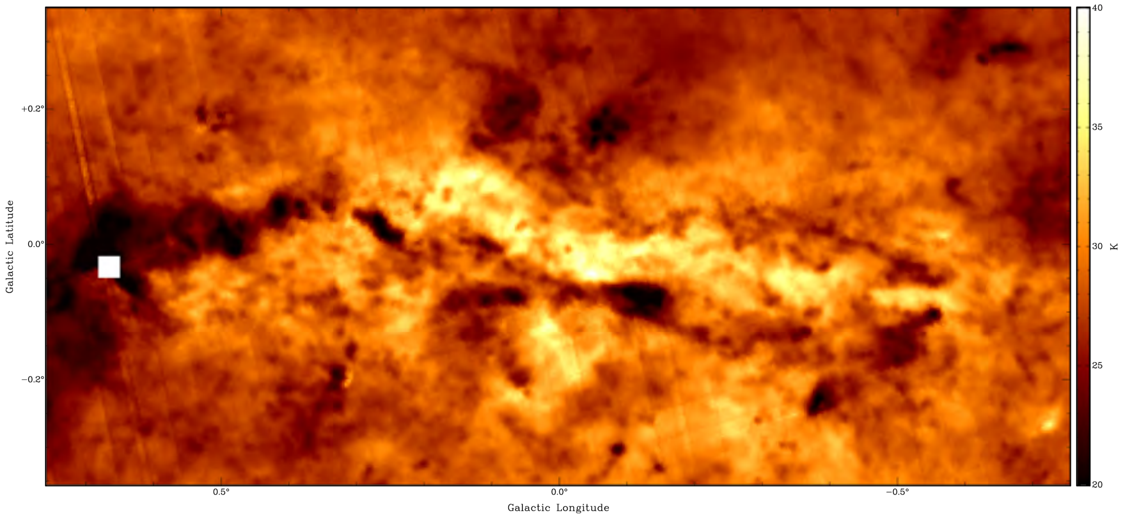

Figure 3.1: Hi-GAL dust temperature map (Molinari et al., 2011). The twisted ring or streams of dust can be identified due to their lower temperature ($< 25\,\mathrm{K}$, black) compared to the surrounding warm dust ($> 30\,\mathrm{K}$, orange/yellow).

3.2 Analysis

Similar analysis procedures were carried out on three different sample sizes: A first test on a selected sample of 20 molecular clouds showed the feasibility and set some constraints on subsequent runs. Further advancement of the analysis pipeline was gained using the exact same sky positions that allowed Kruijssen et al. (2015) to develop their orbital model. The final results are obtained from pixel-by-pixel fitting at every pixel where this approach is possible as described in §2.4.1.
The general course of action for all three cases is to fit spectral lines at the selected positions first, then determine the corresponding time since pericenter passage according to the orbital model using the measured kinematics, and finally apply statistics to reliably characterize the evolution. For the checks with limited number of sources (20 and 113 positions), spectral fitting was done separately for each pixel while the full analysis employs the various pixel-by-pixel fitted maps. Assigning a time value is independent from the sample size and done identically for each cloud or pixel (§3.2.4). As is explained in §3.2.6, a statistical approach is needed to quantify possible evolution over time.

3.2.1 Cloud Selection

3.2.1.1 20 Clouds

Fig. 3.2 shows the 20 clouds that were chosen to cover strong sources across the whole CMZ. One cloud at $(l, b) \sim (-0.4, -0.25)$, known to be in the foreground (Longmore et al., 2013), is included as well to act as a test. The analysis must be able to exclude this cloud by its parameters (e.g. v_{los} or line width) in order to be reliable. Although 20 samples is not enough to conclude the (non-)existence

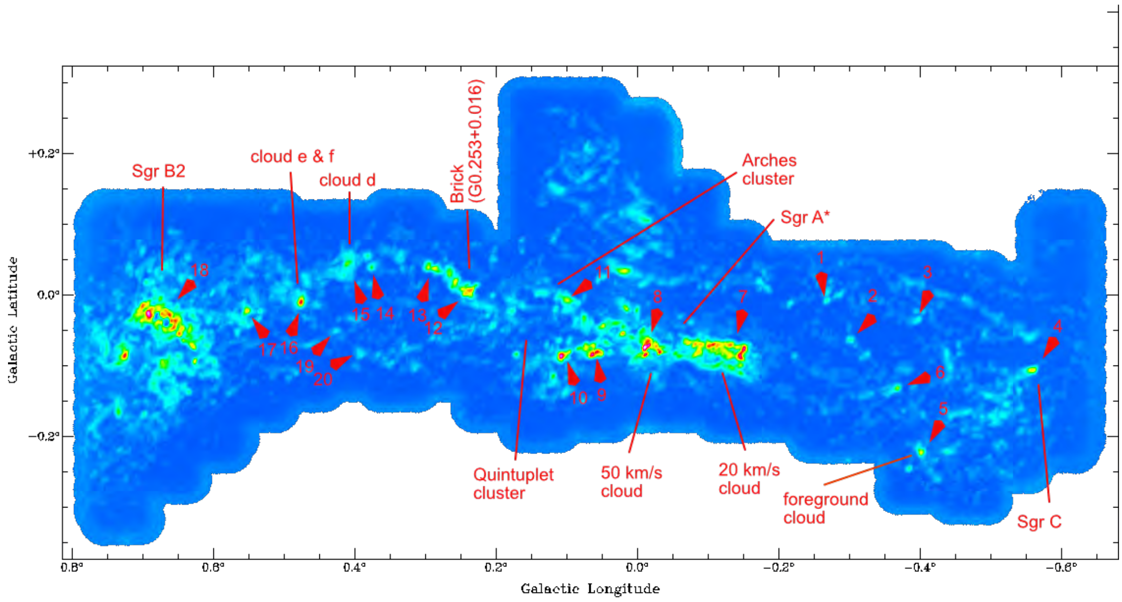

Figure 3.2: The 20 clouds selected for the first tests and some landmarks superimposed on the NH_3 (3,3) peak flux map (moment -2).

of a sequence, especially as only six of them lie in the dust ridge, it can still be expected to find some evidence favoring certain scenarios.

3.2.1.2 113 Positions

The orbital model of Kruijssen et al. (2015) was derived from 113 positions throughout the CMZ. As an obvious test of the star formation hypothesis in the kinematic model, identical positions are chosen to derive gas parameters. The gas distribution is mapped along continuous features in position-position-velocity space of NH_3 (1,1) as explained in detail in Kruijssen et al. (2015). Starting at Sgr C, they follow stream 1 on the lower latitude branch, jump to stream 2 and continue along stream 3 and 4 (figs. 1.12, 3.3). At 1' spacings in longitude, the corresponding latitude of the strongest emission feature at the coherent velocity structure is selected. Note that positions obtained this way do not necessarily trace intensity peaks in NH_3 (1,1) or higher J, but are constructed to follow coherent phase space structures. Hence, they are not chosen to allow for the construction of a sequence in temperature, but using these positions, the orbital model is followed as closely as possible.

3.2.1.3 Pixel Map

Final results are derived from all available information, i.e. as many pixels of the SWAG maps as possible. A two-fold selection is applied to restrict computa-

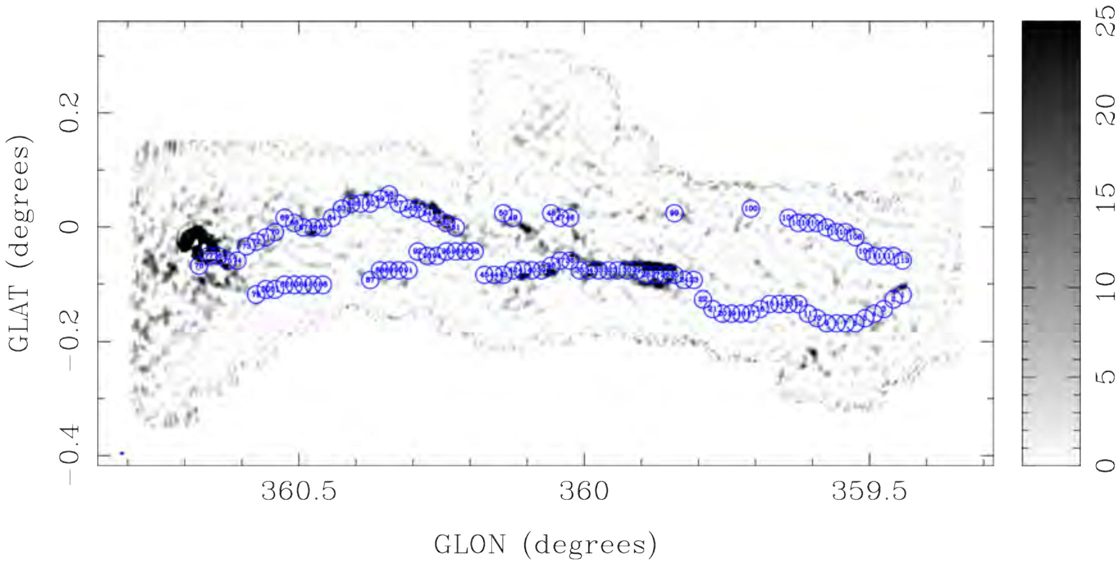

Figure 3.3: Positions according to Kruijssen et al. (2015) that were used to construct the kinematic model (background map as in fig. 3.2, NH_3 (3,3) moment -2, in Jy/beam).

tional efforts to pixels that are likely to be reliably hyperfine fitted and afterwards discarding bad fits. As described in more detail in §2.4.1.1 and 2.4.1.3, between $\sim$ 23400 (NH_3 (1,1)) and $\sim$ 19000 (NH_3 (6,6)) pixels could be hyperfine-fitted successfully.

3.2.2 Spectral Line Selection

Beside ammonia inversion lines, several other spectral lines observed in SWAG are strong enough to deliver kinematic information on the molecular clouds. Most of the smaller and less dense clouds are not detected in more complex molecules or hydrogen recombination lines, as can be seen in fig. 3.4 for cloud e/f. Fig. 3.5 shows typical kinematics for the example cloud e/f, derived from line fits for spectral lines that were sufficiently well detected. Metastable ammonia lines are fitted without any opacity corrections, while all other lines are fitted by Gaussians. Line-of-sight velocities are virtually identical (ignoring two obvious outliers), while line widths do not show strong discrepancies. Varying FWHM are due to optical depth effects and differing tracer properties because different lines do not originate from the same region in a cloud.
Regarding temperature evolution of the proposed star formation sequence, no additional information can be gained from simple spectral line fits other than what is already known from ammonia inversion lines. Of course, other tracers do contain more information on the ISM, which are related to gas evolution, but including more measurements and their complex relation to ammonia gas exceeds the time limit for a master thesis. The analysis will therefore concentrate on the six metastable ammonia inversion lines NH_3 (1,1) to (6,6).

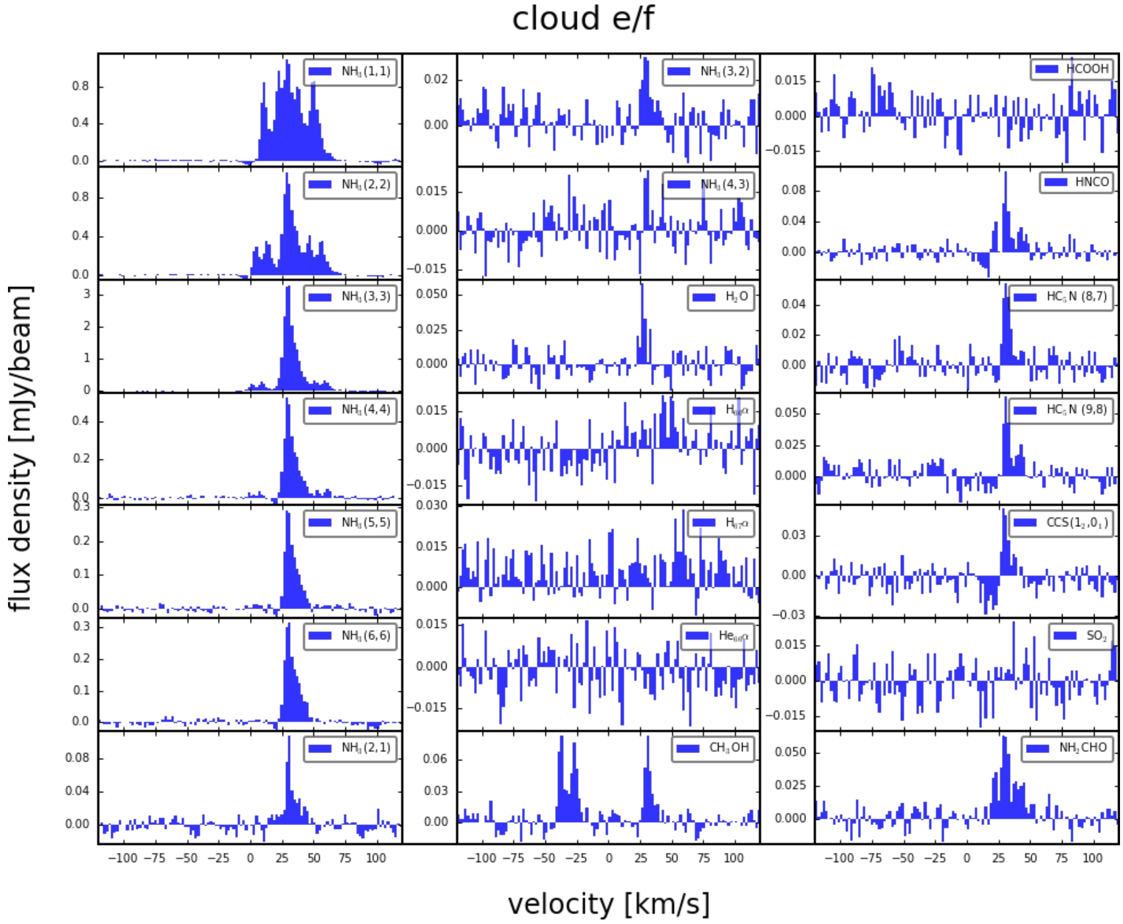

Figure 3.4: Spectra of cloud e/f for all six ammonia inversion lines, three non-metastable ammonia lines and other potentially relevant lines covered by SWAG. The cloud is detected in all of the selected 18 lines beside HCOOH, SO_2 and radio recombination emission.

3.2.3 Opacity Consideration

It is expected that opacity is only relevant for the three lowest meta-stable ammonia lines of SWAG. At infinitely high temperature all para (ortho) states would be populated equally. For real temperatures, higher states are less populated and therefore less gas in this state is visible along the line-of-sight that may absorb emission, i.e. higher lines are less optically thick. For typical CMZ gas temperatures of $< 150\,\mathrm{K}$, opacities are expected to become negligible for NH_3 (4,4) and higher J transitions. Ortho-NH_3 (3,3) and (6,6) is twice more abundant because of the statistical weight $g = 2$. Hence, NH_3 (3,3) may still be optically thick in a non-negligible amount of pixels.

Fig. 3.6 confirms these assumptions as even for NH_3 (1,1) most lines-of-sight are optically thin (CLASS limit: 0.1) but some clouds show $\tau > 10$ and the optically thin approximation is not justified even for high values of J. Therefore, the temperature maps of §2.4.1 are used to obtain temperatures, which consider fitted

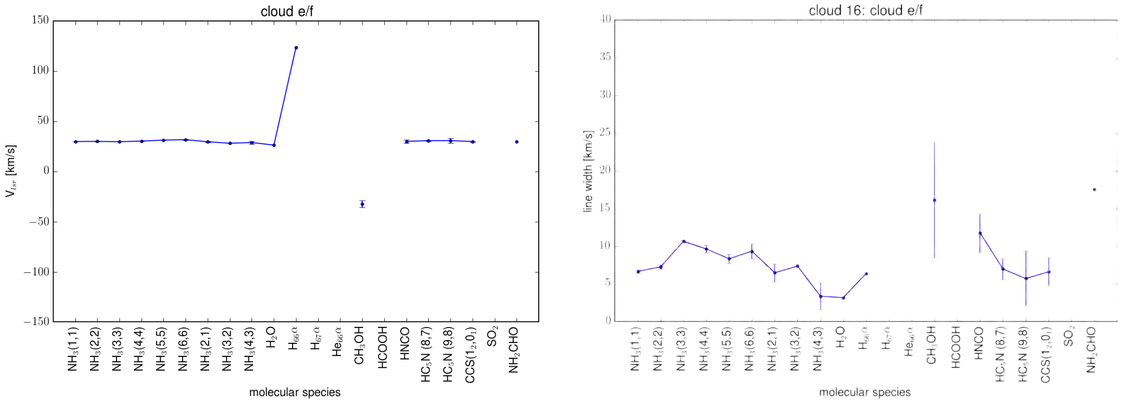

Figure 3.5: Velocity characteristics. *left*: Line-of-sight velocity of cloud e/f. Due to low SNR, some spectral lines could not be fitted at all ($H_{67\alpha}$, $He_{66\alpha}$, HCOOH, SO_2) or a noise peak was fitted at wrong velocities ($H_{66\alpha}$, CH_3OH). *right*: Line width (FWHM) of cloud e/f. The line widths generally agree, considering that this simple fit does not include opacity corrections and the fact that the different species do not trace the same region in a cloud. The large error for CH_3OH confirms that this fit is unreliable and should be excluded.

opacities for all six ammonia lines at the disadvantage of having lower temperature map coverage than assuming thin emission.

3.2.4 Orbital Fitting (Time Fitting)

The online material of Kruijssen et al. (2015) lists several parameters of the orbital model that allow fitting a time value to coordinates in position-position-velocity space for selected clouds. From this table of orbital states, only the four parameters "time in Myr since far side pericenter passage", line-of-sight velocity v_{lsr} and position in Galactic longitude and latitude are utilized because other quantities (e.g. proper motions) are not available in SWAG. For a simple model like the Molinari ring, fitting is easy and for most clouds there would be no confusion. The more complicated stream model with open orbits, however, uses three streams to explain the gas in the very center around Sgr A* whereof the streams 1/2 are on the front side and stream 3/4 is on the far side. Disentangling stream 2 and 3/4 is close to impossible, because the clouds are not perfectly centered on the orbit and the difference in v_{los} is only $\sim$ 20 km/s. It is therefore not possible with the data obtained from SWAG to decide unambiguously if a cloud belongs to stream 2 or stream 3/4 in the region where both are close together in the Galactic longitude-latitude plane.
The process of fitting a time value to a given cloud should find the position along a stream that is closest to the given cloud in the 3D phase space of two spatial coordinates and velocity. The corresponding tabulated orbital time is then assigned to that cloud.

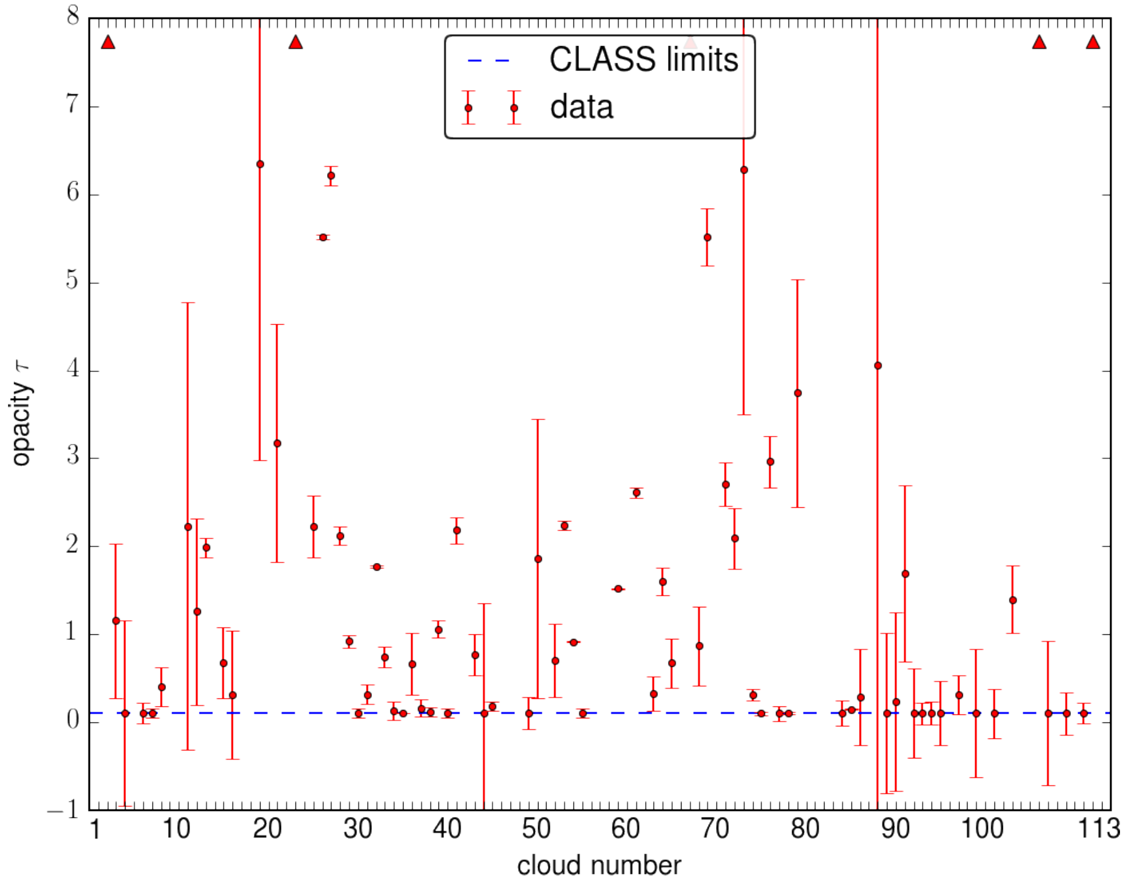

Figure 3.6: NH_3 (1,1) opacity for the 113 positions of Kruijssen et al. (2015). Many sources are optically thin even in the lowest NH_3 inversion line while a significant number of sources with $\tau \gg 1$ requires correct optical calculations.

$$t_{cloud} = t_{stream}(\Delta x_{min}) \qquad \Delta x_{min} \text{ as minimum of } \Delta x(g_{lon}, g_{lat}, V_{los}) \tag{3.1}$$

$$\Delta x = \sqrt{\left(\frac{\Delta g_{lon}}{\mathrm{ref}_{lon}}\right)^2 + \left(\frac{\Delta g_{lat}}{\mathrm{ref}_{lat}}\right)^2 + \left(\frac{\Delta V_{los}}{\mathrm{ref}_{los}}\right)^2} \tag{3.2}$$

The 3D phase space distance Δx between cloud and stream relies on some sort of scaling or parametrization that is not obvious. One possibility is to choose the reference values ref_i as the maxima encountered along the orbit. Typically, the uncertainties in velocity are much larger than positional errors because of the line widths of up to $\sigma \sim 80\,\mathrm{km/s}$ found in previous surveys[2] and high spatial resolution of ~ 20". This means, streams that are close in velocity cannot be disentangled and an easier 2D approach is reasonable.
The streams are chosen to match the velocity with deviations less than a predefined threshold of $20\,\mathrm{km/s}$. This value is justified by the maximum velocity offset in fig. 1.13 (lower panel) between real cloud and theoretical orbital v_{los} as it was found

[2]The line widths in SWAG are much smaller at $\mathrm{FWHM} = 10 - 35\,\mathrm{km/s}$ or $\sigma = 18 - 41\,\mathrm{km/s}$.

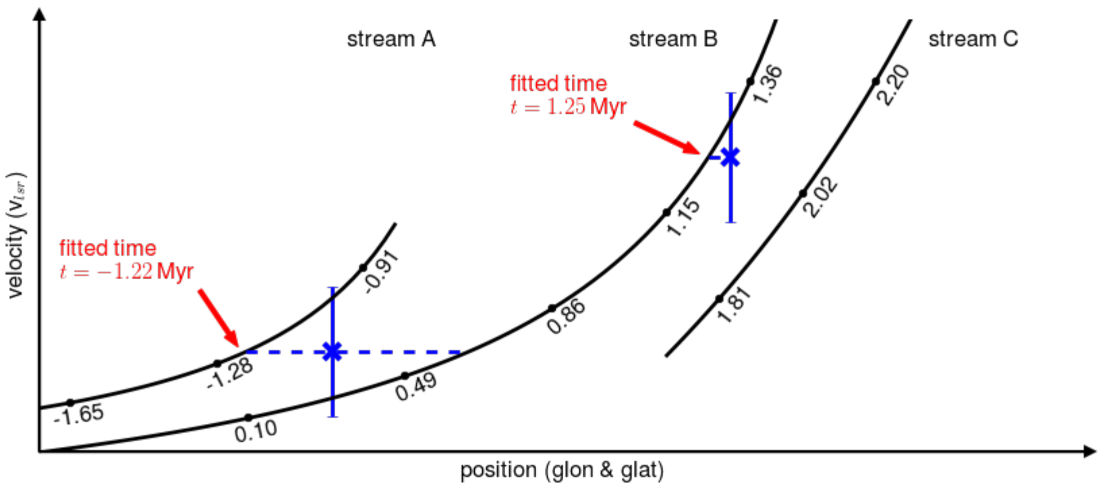

Figure 3.7: Schematic of time fitting. Two measurements are plotted in blue at a certain position in Galactic longitude and latitude with line-of-sight velocity v_{lsr} obtained as the mean of the six hyperfine structure fits. Model orbits (stream A to C) shown in black are labeled with time since pericenter passage at some positions. To assign times to a measurement, only streams with compatible velocities (± 20 km/s) are considered. Therefore, stream C is excluded for the right data point and it is given the time of the nearest point of stream B in the 2D space of g_{lon}, g_{lat}. The other measurement is compatible with belonging to both stream A and B. However, the 2D distance (blue dashed line) to stream A is shorter and the respective time is listed for this measurement. In the case of no stream matching a given point in pV-space, it is discarded.

by Kruijssen et al. (2015). The line-of-sight velocity for each pixel is determined as the mean velocity of all successful fits ($J = 1, ..., 6$) at that position. Typically all six meta-stable inversion lines could be fitted but some pixels have their velocity assigned from the mean of only two or three line fits. Then, a simple 2D distance minimization is performed in the plane of the sky to find the best fitting point along the orbit. In the case of a cloud near the Galactic Center, e.g. the 50 km/s cloud ($g_{lon} \sim -0.03°$, $g_{lat} \sim -0.07°$, $V_{lsr} \sim 50$ km/s), stream 2, 3 and 4 are excluded by velocity and the positional fit is applied to stream 1 only. The resulting time after far side pericenter passage of the nearest orbital point is 1.94 Myr, which matches the expectation, as pericenter passages are spaced $\sim$2 Myr and the 50 km/s cloud is close to the front side pericenter, which in turn is close to Sgr A* in projection. Fig. 3.7 shows a schematic illustration of the time fitting process in velocity and simplified spatial coordinate for two examples, one of them in the problematic situation of being compatible with two streams.

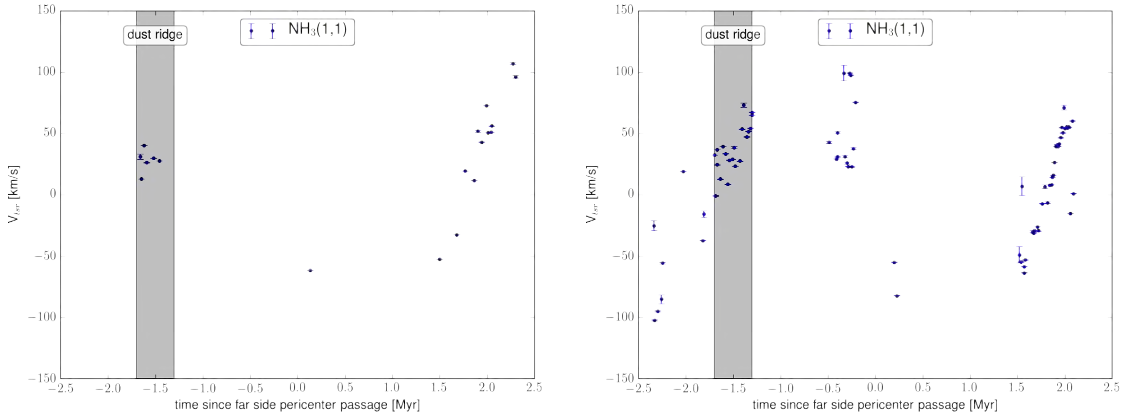

Figure 3.8: Line-of-sight velocity as a function of time since far side pericenter passage for 20 clouds (*left*) and 113 positions (*right*). Sampling of the expected periodic oscillation is too weak for 20 clouds but can be resolved with more and better placed measurements.

3.2.5 The Need for a Large Sample Size

Absorption can render a spectrum impossible to fit due to self-absorption[3] or because a line is observed in absorption against a background continuum source like in Sgr B2. When using a very limited number of clouds, this can be a major concern, as an important part of the sequence may not be covered. Even if clouds are properly selected to trace gas in emission, sampling a time range of ~ 5 Myr needs > 50 evenly spread measurements to draw conclusions about the proposed periodicity of triggered sequences. The peculiar asymmetry of gas in the CMZ complicates uniform coverage of the time domain and may restrict the analysis to certain ranges.
Fig. 3.8 shows these effects of missing time coverage for line-of-sight velocity. The radial periodicity of the streams of 2.03 Myr cannot be recovered with 20 clouds (19 successful fits) whereof six are in the dust ridge. Comparing both panels in fig. 3.8, it becomes clear that a much better sampling, i.e. many more clouds, are needed to reliably recover gas structure in the CMZ.
The other reason why as many clouds as possible should be included in constructing a sequence is to minimize errors during data reduction and intrinsic variability of cloud properties. Calculating kinetic ammonia temperatures without assuming optically thin emission is a complex process that introduces non-negligible errors and a significant amount of outliers. The large sample size of more than 20,000 pixels in the SWAG temperature maps allows to treat results statistically, which avoids these effects.
Fig. 3.9 shows the effect of increasing the sample size for the relation of gas and dust temperature versus time. While 20 clouds are clearly not enough to draw any conclusions about temperature changes, 113 measurements already hint towards

[3] At least impossible with the simple approach of using only one line-of-sight component in CLASS.

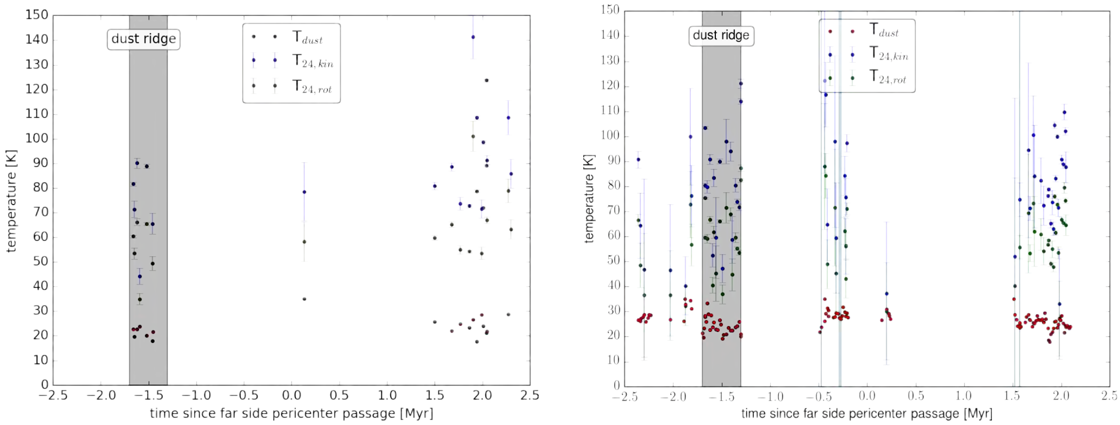

Figure 3.9: Dust, kinetic and rotational ammonia gas temperature as a function of time for 20 selected clouds (*left*) and 113 positions (*right*). Errors are calculated conservatively as the maximum deviation of slope in the respective Boltzmann plot. Large errors occur due to lower signal-to-noise ratio when using the 113 positions of Kruijssen et al. (2015) because they are not selected to match intensity peaks. A much larger sample size of $\gg 1000$ is needed to be able to switch from error propagation to statistical calculations that are unaffected by the large errors of individual measurements.

the suspected rise of gas temperature in the dust ridge. The problem of outliers and large errors distorting the gradients is still present, but can be resolved by statistical methods explained in §3.2.6.

3.2.6 Binning and Linear Fitting

Temperature sequences cannot be fitted reasonably without applying statistical methods because of outliers at high temperatures. As the temperature scale ends at 0 K, outliers cannot scatter symmetrically around a certain value and the mean is shifted towards higher temperatures. In the case of $T_{12,kin}$ with its low dynamical range of 0 to $50-60$ K, the mean is shifted above physically meaningful values, and simply cutting at 60 K strongly distorts the distribution. It is therefore necessary to calculate median temperatures that are not as strongly affected by outliers.
Physically implausible values are discarded, that is, rotational temperatures above 500 K and kinetic temperatures above T_{ij}-dependent thresholds as listed in table 3.1, and all temperatures below zero Kelvin. These limits are justified by the flattening in T_{rot}-T_{kin} conversion. Slightly negative temperatures result from positive slopes in a Boltzmann plot (higher levels are more populated) that can occur as a result of noise.
Median temperatures are calculated in bins of 0.01 Myr, but only if the bin contains more than 10 members and therefore the sample size is large enough to be considered unaffected by outliers. All linear fits in the time domain are applied to these medians only.
Errors in a median cannot be calculated directly but, instead, a statistical uncer-

Table 3.1: Ammonia temperature limits used to exclude unphysical values as justified by flattening in the T_{rot}-T_{kin} relation (fig. 1.8).

	T_{12} [K]	T_{24} [K]	T_{45} [K]	T_{36} [K]
rotational	500	500	500	500
kinetic	60	200	200	300

tainty range can be given that display the range wherein 50% of all measurements are included. Due to the asymmetric distribution of measurements, errors do not have to be symmetric around the median, but they are typically larger on the bottom, e.g. 30% below and 20% of the error interval above the median, while 50% of measurements lie outside the interval. This error estimate is hereafter referred to as “error interval”.

3.3 Results of Pixel-by-Pixel Analysis

Plots in these sections are calculated for several quantities like kinetic ammonia temperatures T_{12}, T_{24}, T_{45} and T_{36}, and the metastable ammonia lines. As mentioned before, they are not equally meaningful, as the rotational to kinetic temperature conversion becomes problematic towards high values of T and low transition temperatures are not sensitive to high kinetic gas temperatures. Therefore T_{24} and NH_3 (1,1) is shown here to represent results that appear in all temperature measures or ammonia inversion lines if not explicitly noted otherwise. Plots of the other temperature measures and ammonia lines can be found in appendix B.
As only part of the maps are close enough to the theoretical orbit in projected distance and velocity, only 96% - 77% of hyperfine structure fitted pixels make part of these plots. Table 3.2 lists the amount of pixels with good fits that match the orbital model for each ammonia line.
The origin of the time scale in plots versus time is chosen to match Kruijssen et al. (2015) and as such identifies 0.0 Myr (+2.03 Myr) with far (near) side pericenter passage, respectively. In the context of temporal evolutions, the term "dust ridge" refers to the whole sequence (~ -1.0 to ~ -2.0 Myr) that includes the actual dust ridge structure (highlighted in the plots at -1.7 to -1.3 Myr).
Data density contours, in rainbow colors, are plotted on top of individual measurements (grey data points) for most plots, in order to reflect the influence of a single measurement on the mean and median of a bin and highlight the typical (most common) values. colored contours from blue to red are spaced in steps of 10% maximum data density.

Table 3.2: Number of selected pixels and fits that match the Kruijssen et al. (2015) orbit within ±20 km/s (§3.2.4 for details).

	(1,1)	(2,2)	(3,3)	(4,4)	(5,5)	(6,6)
selected pixels	24383	24383	24383	24383	24383	24383
match orbit	23722	22911	23392	18745	16783	17276
% match	96.1	93.6	96.0	78.5	77.1	77.8

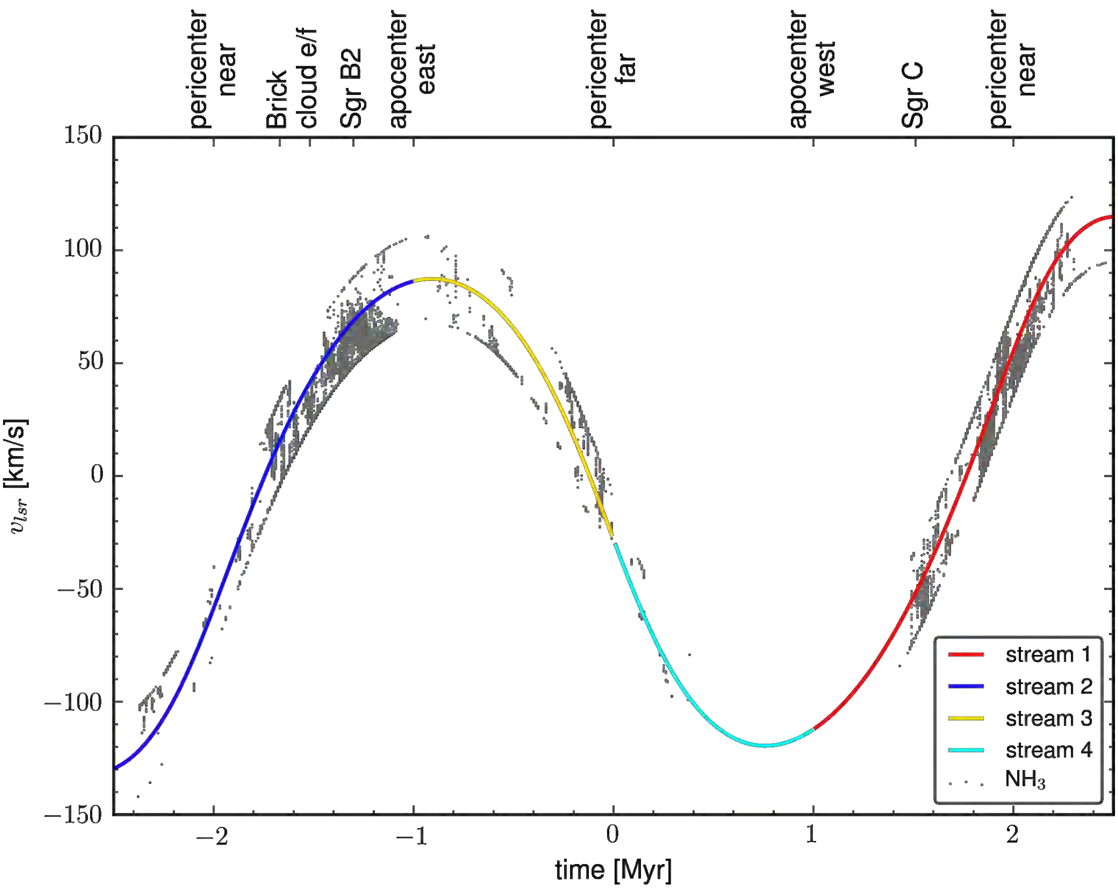

Figure 3.10: Mean fitted line-of-sight velocity v_{lsr} as a function of time. The mean was calculated over all six ammonia lines from NH_3 (1,1) to (6,6). Measurements scatter ±20 km/s around the model by design of the time fitting procedure.

3.3.1 Kinematics

Simple kinematics can act as a proxy for fit quality. Line-of-sight velocity v_{lsr} and line width FWHM are direct results of spectral fitting which in turn were used to fit times with the only assumption being the kinematic model.

Fig. 3.10 shows the mean line-of-sight velocity as a function of time since far side pericenter passage. The measurements follow the model by design of the fitting routine with up to 20 km/s offset. Pile-up of data points near the edge of the velocity window is caused by the nearest position fit in the plane of the sky. The used approach does not include a spatial cut-off distance beyond which a cloud is considered not compatible with a stream any more although the velocities match. As a result, the spatially nearest matching stream will typically have the maximum allowed v_{los} deviation of 20 km/s. Further research will have to use spatial constraints or find a reasonable way to parametrize and minimize true phase space distance. The amount of affected pixels is smaller than fig. 3.10 implies as the data density is significantly higher around the model curve than at the edge of the 20 km/s window. Additionally, the statistical approach compensates these

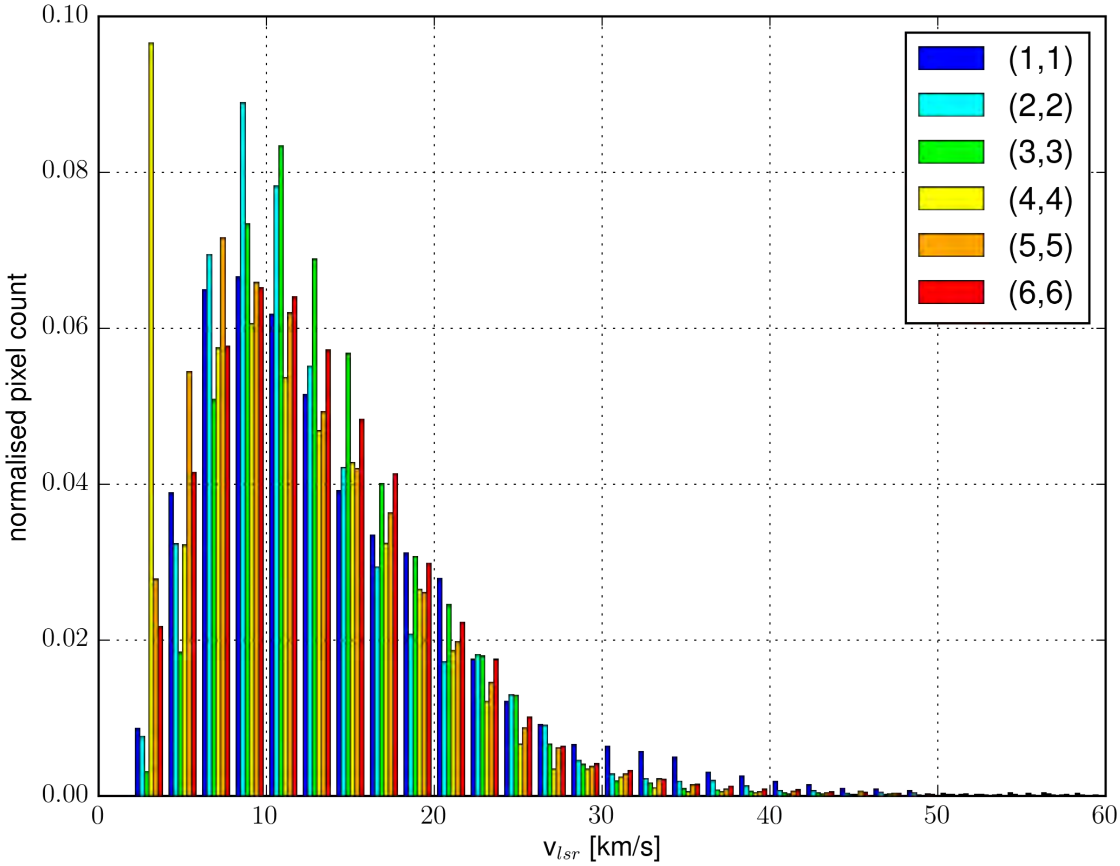

Figure 3.11: Normalized histogram of ammonia inversion line widths (FWHM).

edge effects and the following analysis is only weakly influenced.
Although fits were derived at the projections of all streams, several time ranges are not well sampled. Especially, $0.3 \lesssim t\,[\mathrm{Myr}] \lesssim 1.5$ is not covered at all. These times correspond to stream 4 or the [l^-, b^+] section where very little gas is be found due to the large scale $\mathrm{l}^+/\mathrm{l}^-$ asymmetry of the CMZ. The most interesting time ranges, however, are well sampled. In the dust ridge stream between ~ -2.0 and ~ -1.0 Myr, the star formation sequence is expected, while around 0.0 Myr and +2.0 Myr pericenter passages occur.

One of the selection criteria to identify bad fits is line width. Fig. 3.11 confirms that, beside NH_3 (3,3), no significant amount of artificially broad or narrow fits made it into the analysis. Mean line widths are similar across ammonia states and peak in the bins of $8 - 10$ km/s or $10 - 12$ km/s. The large amount of 3.3 km/s broad lines of NH_3 (3,3) is due to spectral channels at the edge of the bandpass window which can exhibit strong or distorted noise, strong enough to be fitted as a line by the line fitting routine. Their line widths results from a Gaussian fit to an noise peak in a single 2.0 km/s channel at $v_{lsr} \sim 190$ km/s, which makes these artificial detections easily identifiable. They are excluded in all subsequent analyses, but shown here to illustrate a typical problems of spectral line fitting.

The line width is independent of time as can be seen fig. 3.12 for NH_3 (1,1). Results are very similar for the other ammonia lines at slightly varying absolute level between ~ 5 and 25 km/s as could already be seen in the line width histogram (fig. 3.11). Slopes in the dust ridge and pericenter near (+2 Myr) are close to zero in the range of $\sim +2$ to ~ -3 km/s/Myr with steeper slopes in NH_3 (1,1) and (6,6) of ~ -4 and $\sim +6$ km/s/Myr respectively (see appendix B.4 for NH_3 (2,2) to (6,6)). Around the far side pericenter passage, slopes are consistently higher at $\sim 10 - 20$ km/s/Myr for all rotational states, but they are strongly influenced by the outlier median value at 0.0 Myr that forces a high positive slope which would otherwise be compatible with ~ 0 km/s/Myr. This region has to be taken with care anyway because there are much fewer bins, and therefore slopes are less constrained.
Line widths increase significantly in dense regions of the plot, i.e. gas clouds that are more extended, such as the brick, Sgr B2 and the 20 and 50 km/s clouds. This behavior is most pronounced in NH_3 (J,J), J=2,4,5,6 in Sgr B2 where the line widths approximately double to ~ 20 km/s compared to neighboring[4] clouds in the dust ridge that are ~ 10 km/s broad.

[4]in time, not necessarily in space

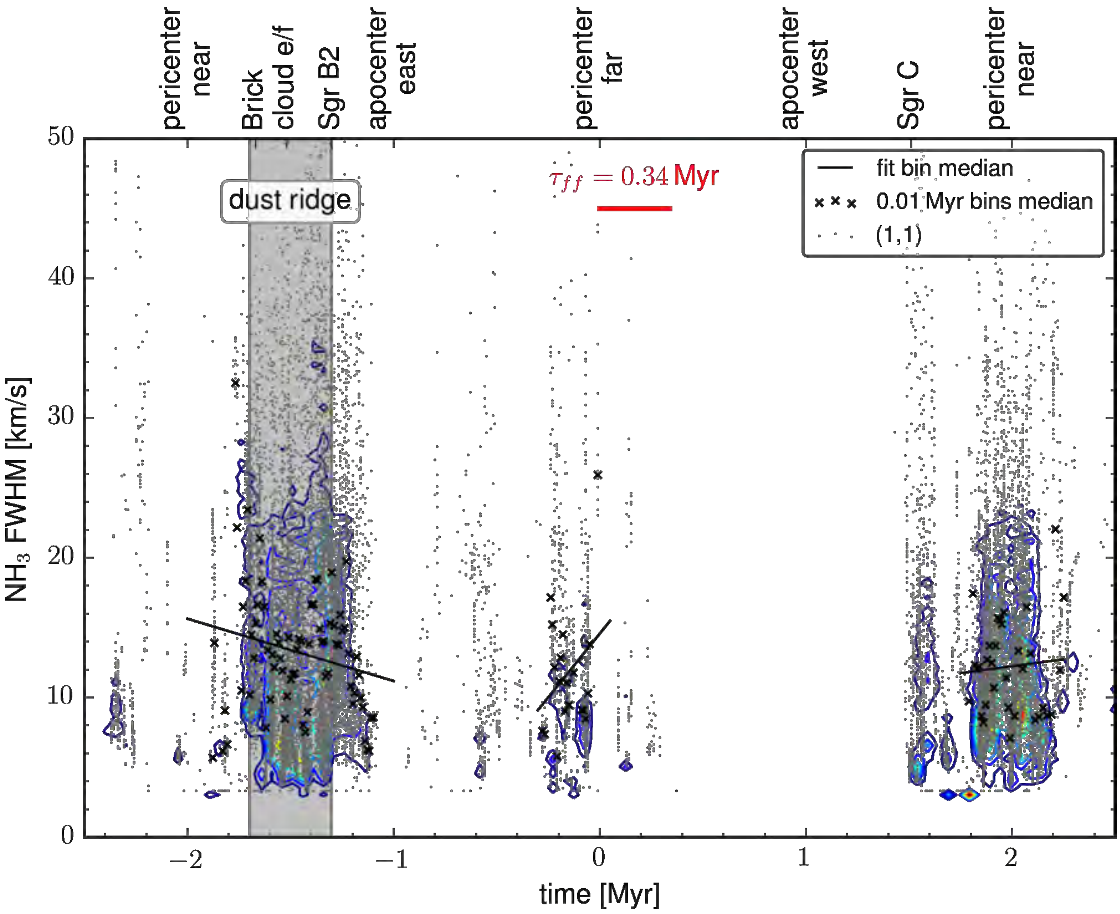

Figure 3.12: NH_3 (1,1) FWHM as a function of time since far side pericenter passage. Massive clumps like Sgr B2 exhibit broader lines as indicated by median widths, but no consistent trend over time is found.

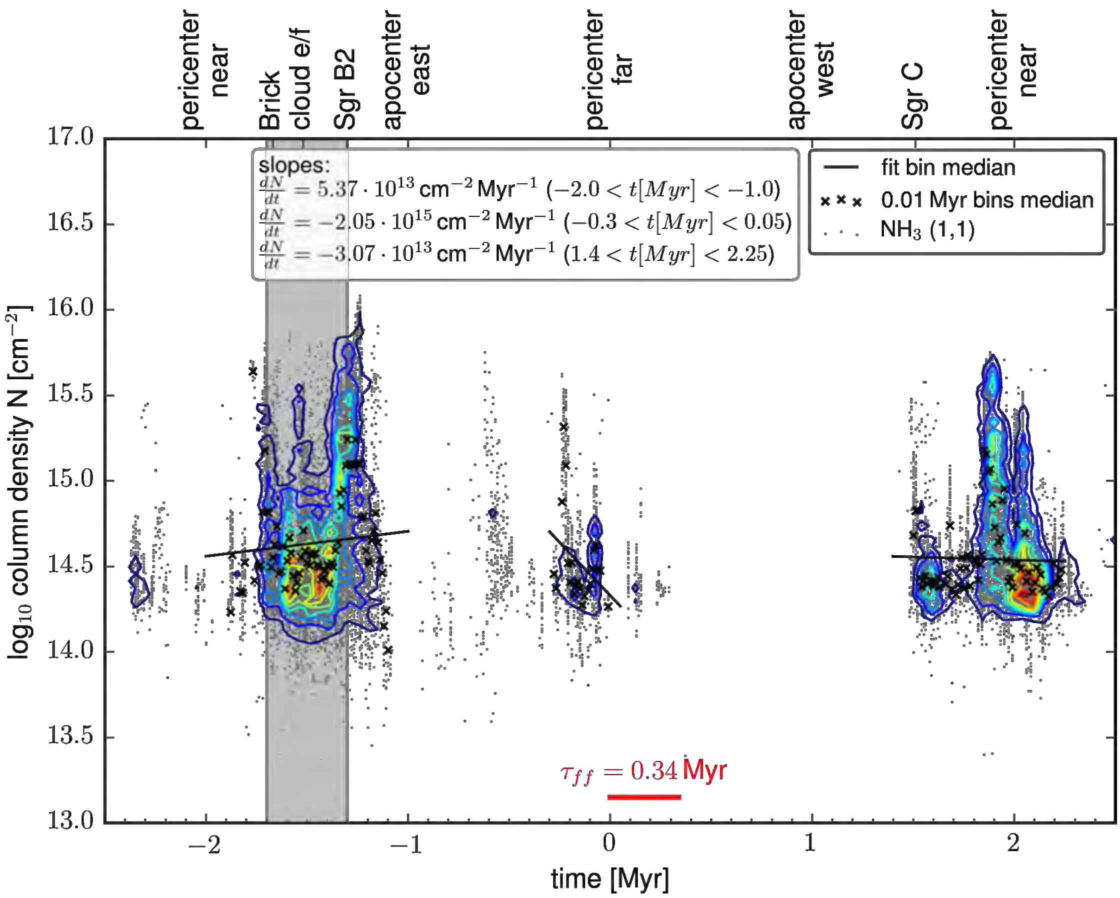

Figure 3.13: NH_3 (1,1) column density as a funtion of time since far side pericenter passage. Column density does not evolve with time but traces dense clouds in the dust ridge and the 20 and 50 km/s clouds.

3.3.2 Column density

Column density does not show clear evidence of a sequence in all three well-ssampled regions (fig. 3.13). In the dust ridge, rising column densities of $5.4 \cdot 10^{13}\,\mathrm{cm}^{-2}\,\mathrm{Myr}^{-1}$ to $4.4 \cdot 10^{14}\,\mathrm{cm}^{-2}\,\mathrm{Myr}^{-1}$ can be fitted but these are strongly influenced by low bin medians at beginning and end of the fitted range and high values in the Brick and Sgr B2. Especially, Sgr B2 is much denser ($N_{J=1} \sim 10^{15.5}\,\mathrm{cm}^{-2}$) than other clouds in the dust ridge and thus forces positive slopes. At the far side pericenter, even median column densities scatter at ~ 1 dex and a decision about falling or rising column density is not possible. Slopes at the near side pericenter passage are almost flat and vary within $-3.1 \cdot 10^{13}\,\mathrm{cm}^{-2}\,\mathrm{Myr}^{-1}$ and $5.8 \cdot 10^{13}\,\mathrm{cm}^{-2}\,\mathrm{Myr}^{-1}$. As for the dust ridge, individual clouds have more influence on the fit than a possible evolution with time. The bimodal distribution of gas at 1.9 Myr and 2.2 Myr encourages negative slopes for $J = 1, 2, 3$ for which the earlier region is denser than the later, while for $J = 4, 5, 6$ both are comparable in density. The plots corresponding to fig. 3.13 for $J = 2, ..., 6$ can be found in appendix B.6.

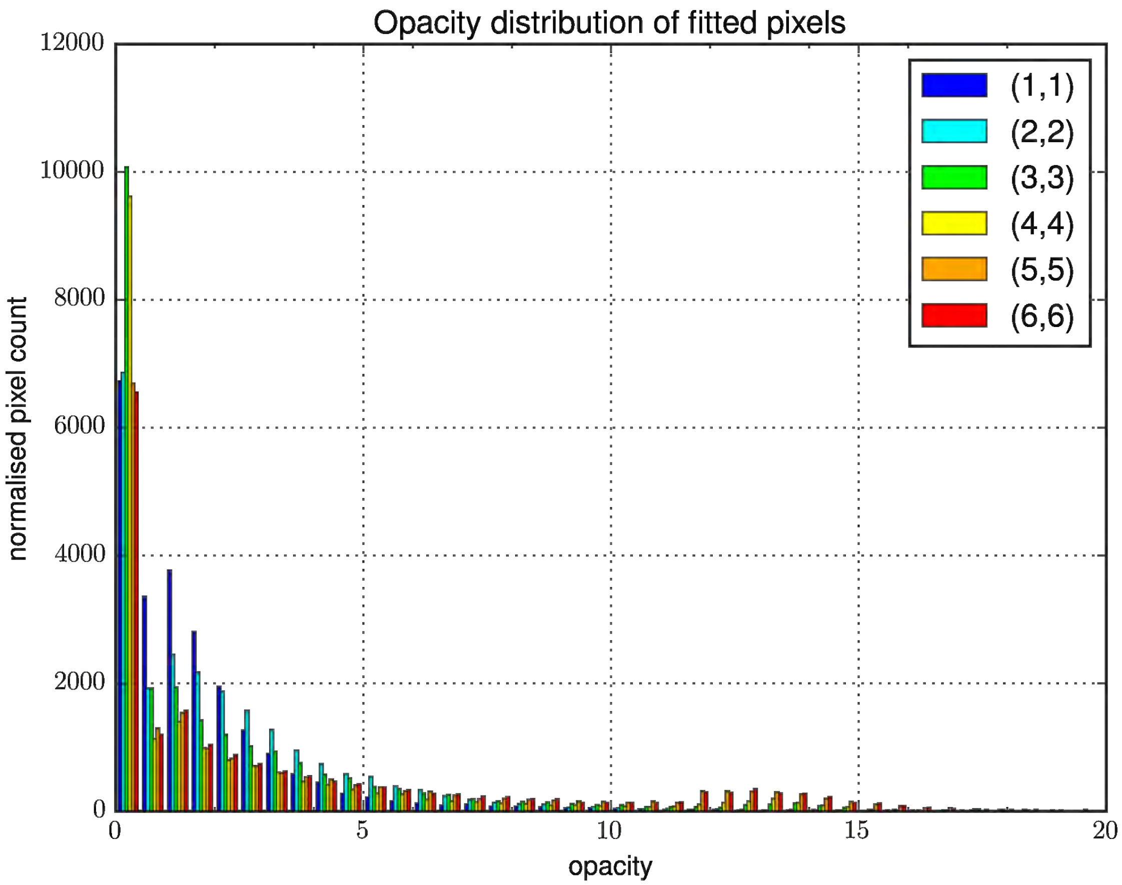

Figure 3.14: Histogram of NH_3 opacities in the fitted region as described in §2.4.1.

3.3.3 Opacity

Most of the ammonia emission is optically thin as can be seen in fig. 3.14 for the meta-stable inversion lines. As CLASS fits opacities in the range of $0.1 - 30$, thin emission is grouped in the lowest bin of $[0, 0.5]$. For $J = 1$ and $J = 2$, a considerable amount of gas is found in intermediate ($0.5 \leq \tau \leq 1$) and thick ($\tau > 1$) conditions where the thin approximation cannot be used any more. The bump of high opacity gas for $J = 5$ and $J = 6$ around $\tau \sim 13$ is due to bad/unreliable fits that could not be excluded by the limits described in §2.4.1.3.
Fig. 3.15 shows the evolution of opacity as a function of time for NH_3 (1,1). There is no trend in opacities but τ_{median} scatters strongly. When comparing the different rotational states J=1, ..., 6, weakly positive slopes are favored in the dust ridge, whereas negative slopes occur in the other two regions. This qualitative picture, however, is not consistent but subject to large scatter and influenced by bins with only optically thin emission ($\tau_{median} = 0.1$). Hence, no strong sign of increase in opacity is found, which could be expected by collapsing gas becoming denser over time.

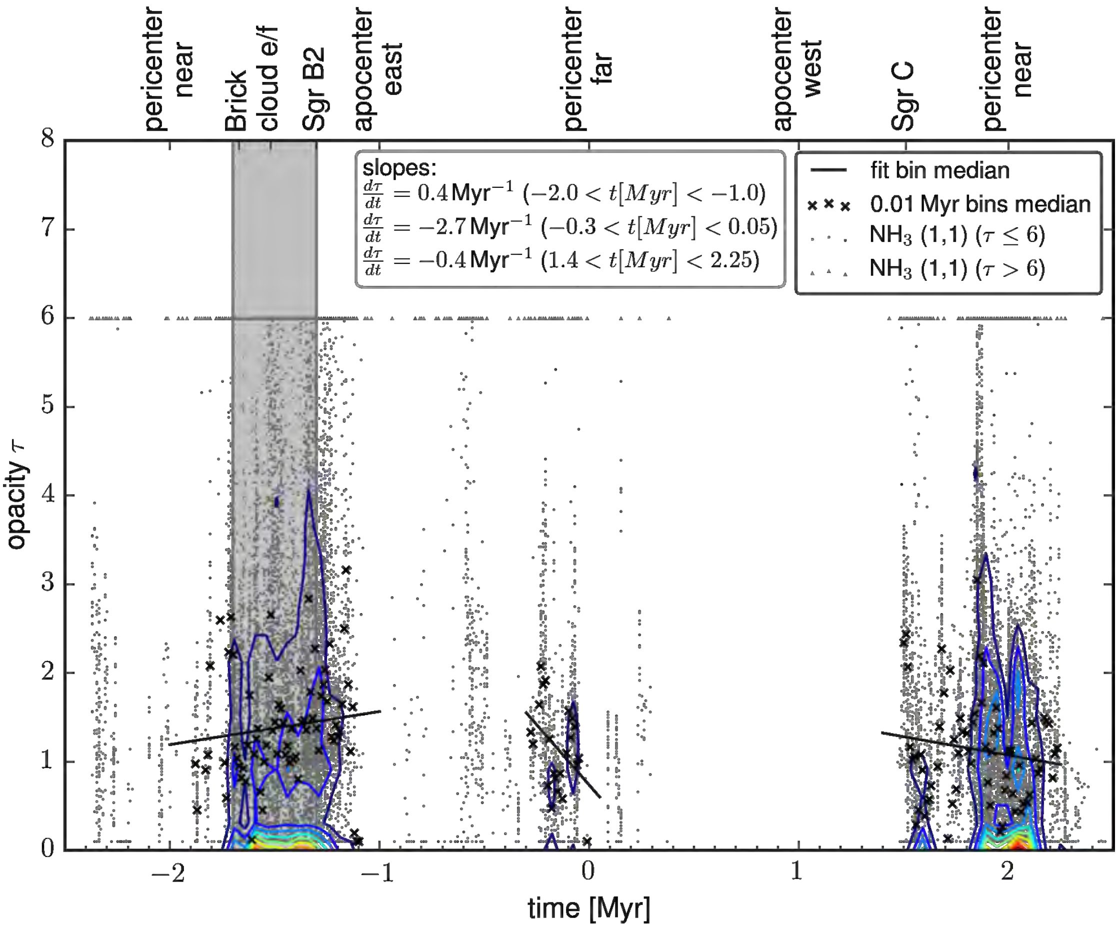

Figure 3.15: NH_3 (1,1) opacity as a function of time since far side pericenter passage. Slight increases of τ are favored in the dust ridge while at 0 Myr and t$>$ 1.5 Myr decreasing opacity is observed. Large scatter in median opacity and bin medians of $\tau = 0.1$ affect the linear fit such that no trend ($d\tau/dt = 0$) is compatible with the data as well.

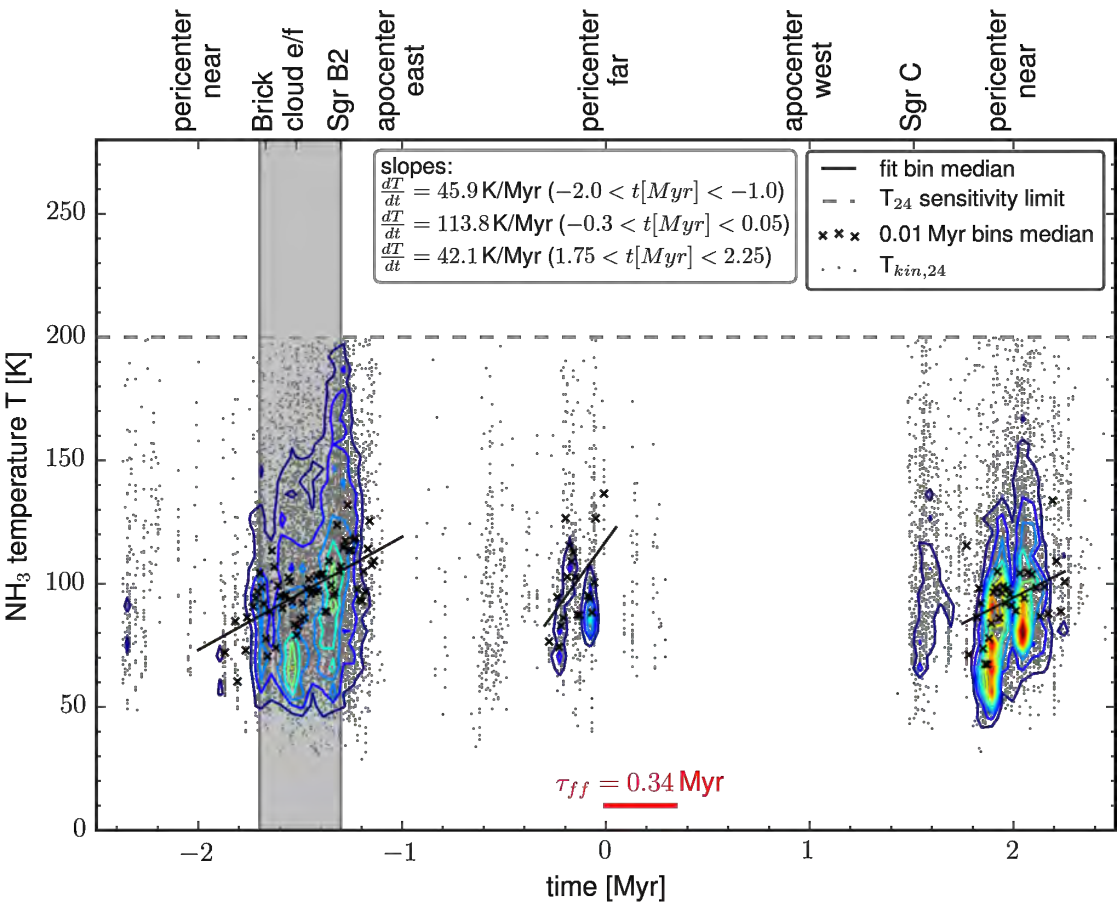

Figure 3.16: $T_{24,kin}$ as a function of time since far side pericenter passage. Consistently increasing temperature is found in all three region where the binning approach is feasible. The offset between the region of highest measurement density and best-fit temperature line is due to the sparse high temperature points. A fit without any binning at all, as well as a fit through maximum density at each time bin, yields nearly identical slopes with higher and lower intercept, respectively.

3.3.4 Temperature

Fig. 3.16 shows kinetic ammonia temperature T_{24} as a function of time, with clearly rising temperatures in the three time ranges where bins are sufficiently dense populated to derive median values (see §3.2.6). Corresponding intervals that include 50% of the values in a bin are plotted in fig. 3.17 together with data density and median temperature.
Positive temperature gradients are derived by linear fitting but they are not due to outliers or regions of elevated temperatures. Instead, the trend in median temperature is consistent over the full range of considered times in all three cases. Three zoom-ins show more detail in figs. 3.18 to 3.20. The error intervals are in principle consistent with constant temperature independent of time.
The size of a cloud sets the measurement density and therefore contours do not have immediate physical meaning. However, they highlight the most likely temperature

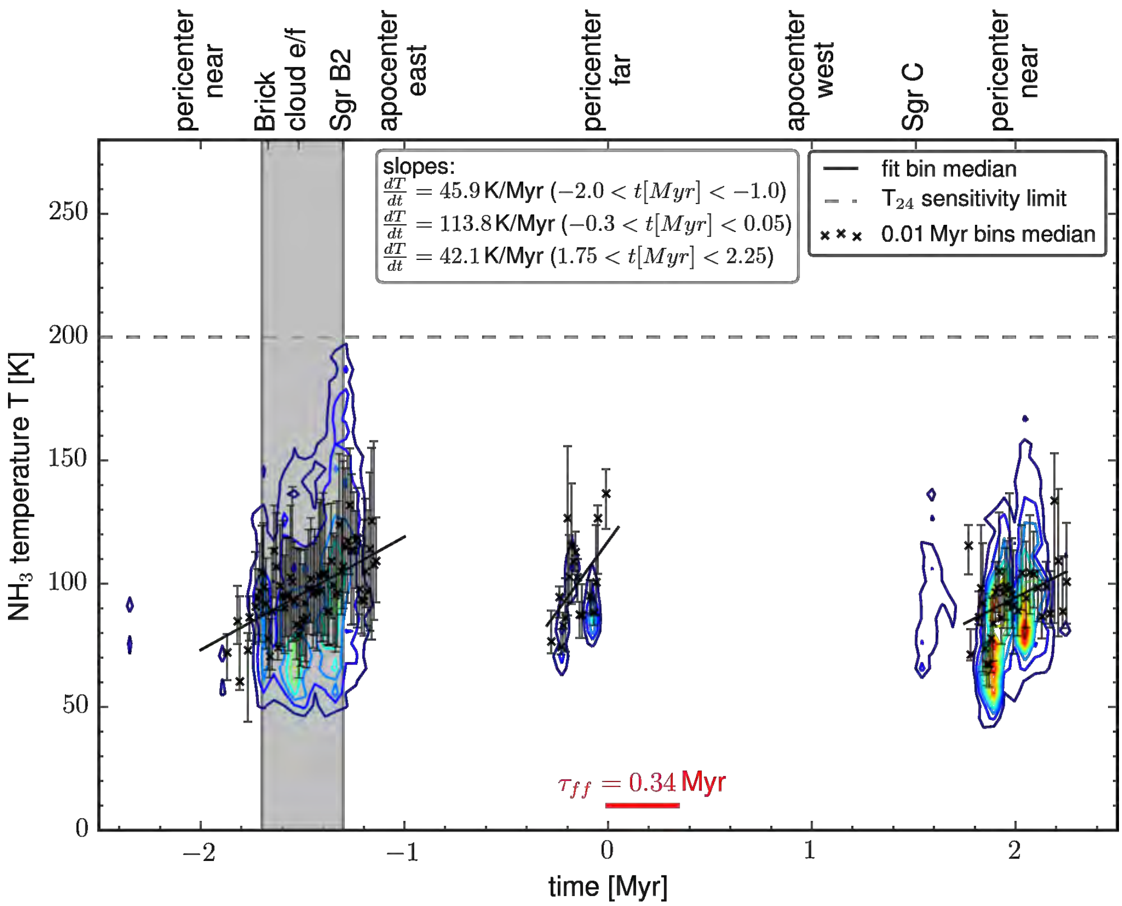

Figure 3.17: $T_{24,kin}$ as a function of time overlaid with the error interval (§3.2.6). The large values of these ranges is caused by the analysis setup that applies equal weight to each pixel (measurement), irrespective of the location inside (higher T) or at the edge of a cloud (lower T, closer to ambient temperature). The CMZ is a peculiar environment where the clouds are generally hotter than the surrounding, rather than typical molecular clouds in spiral arms which cool down below ambient temperature.

at a certain time step which is increasing in all three regions.

Zoom-in: Dust Ridge

Fig. 3.18 provides a zoom-in on the dust ridge (highlighted in grey) that spans roughly one free-fall time of 0.34 Myr of a typical molecular cloud in the CMZ (Kruijssen et al., 2015). The label "Sgr B2" matches the position of Sgr B2 (M) with most data in the range of -1.4 Myr to -1.2 Myr being part the Sgr B2 complex around the radio sources (M), (N) and (S). Kinetic temperatures in the dust ridge range from $\sim$ 50 K up to 200 K where a cut-off is applied due to the T_{rot}-T_{kin} conversion. Median temperatures are restricted to $60 - 125$ K and appear to be monotonically increasing at $\sim$ 45 K/Myr with 15 K scatter. A linear fit matches

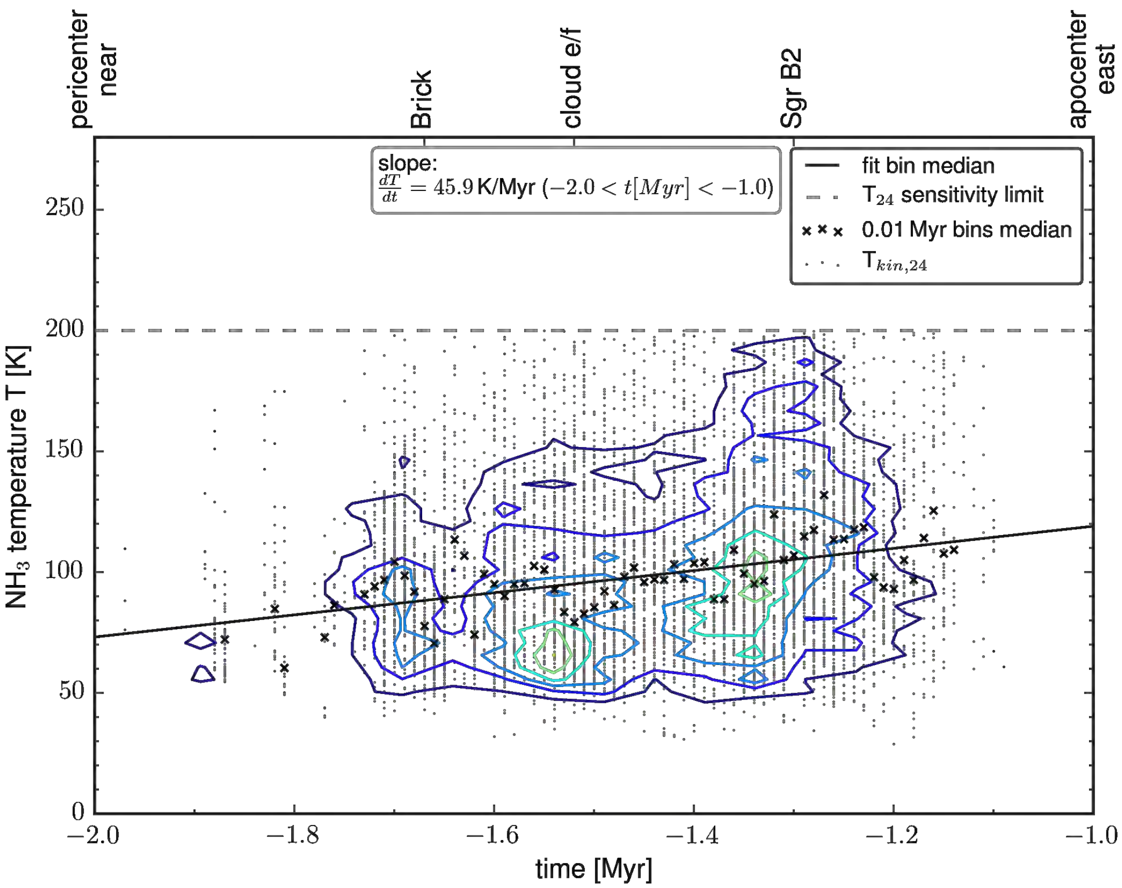

Figure 3.18: Zoom in of fig. 3.16 on the dust ridge. The turnover point where streams reach their greatest Galactic longitude before turning to the back side occurs at ~ -1 Myr. Sgr B2 in the foreground shields those clouds if there are any and the sequence can only be tracked to ~ -1.25 Myr.

the median temperature very well, without any sign that a higher order fit might improve fit quality. Peaks in density contour are consistently lower than the median temperature due to asymmetric scatter in temperature. Still, there is a contour trend of rising temperature from ~ -1.5 Myr onwards, after being constant or slightly dropping from -1.8 to -1.5 Myr. The overall temperature distribution shows the same rising trend in the upper contour edges that increase with time. Drops at ~ -1.65 Myr and ~ -1.45 Myr are due decreasing number and density of measurements because of smaller clouds. The lower cut-off in temperature distribution is constant at ~ 50 K.

Zoom-in: Far Side Pericenter Passage

The large scale asymmetry of gas in the GC reduces the amount of clouds that could potentially trace a sequence after being triggered at the far side pericenter passage around 0.0 Myr. As fig. 3.19 shows, there are still enough measurements of consistently increasing temperature over a range of ~ 0.3 Myr ($\sim 1 \times \tau_{ff}$).

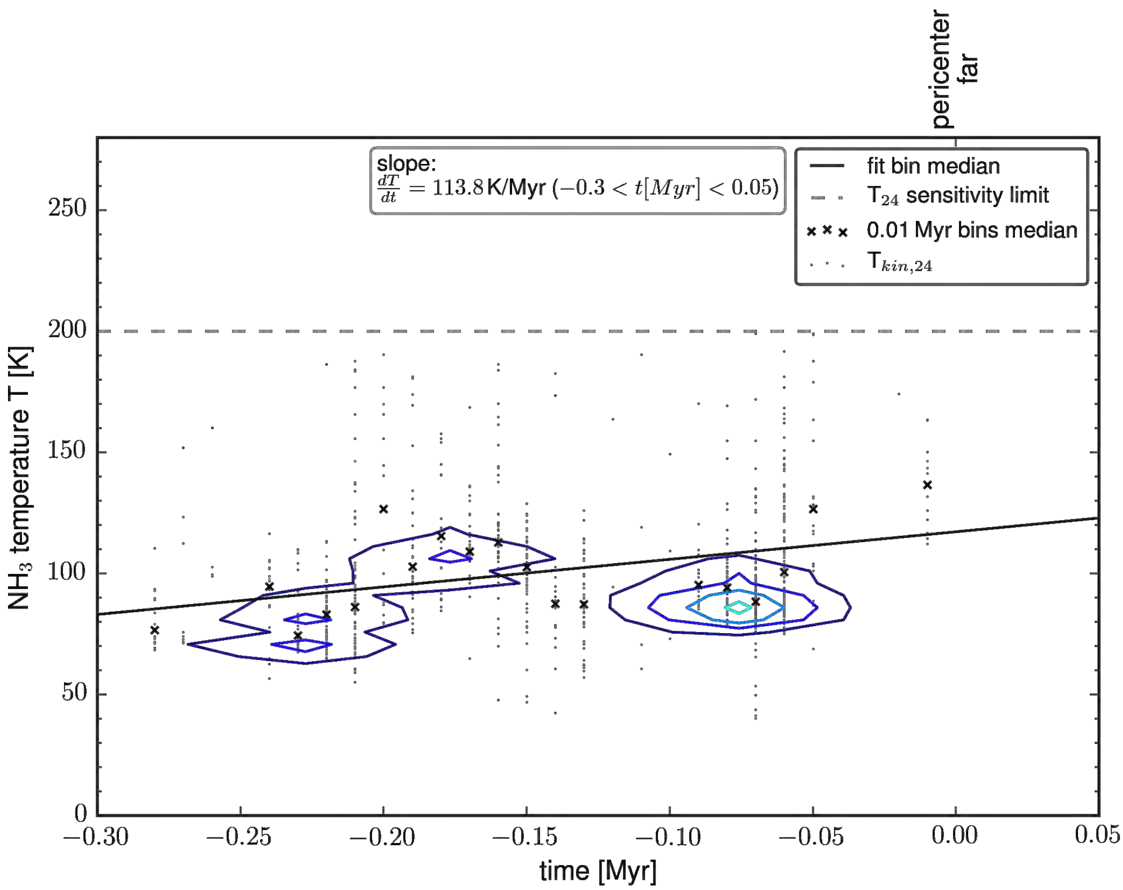

Figure 3.19: Zoom in of fig. 3.16 on the far side pericenter passage around $t = 0\,\mathrm{Myr}$.

Scatter of $20 - 30\,\mathrm{K}$ around the fitted slope of $\sim 114\,\mathrm{K/Myr}$ is significantly higher than in the dust ridge, which is partly due to the lower number of temperature measurements. Despite the short time range and few measurements it is likely safe to confirm the existence of a temperature sequence, but the quantification is subject to large errors and must take the diminished gas mass into account when compared to the front side sequences.

Zoom-in: Near Side Pericenter Passage

At the near side pericenter passage in front of Sgr A*, similar results are derived as in the dust ridge. The temperature gradient of $\sim 42\,\mathrm{K/Myr}$ with typically $< 20\,\mathrm{K}$ scatter in all four temperature measures is surprisingly close, although this sequence occurs at a phase of tidal compression, whereas in the dust ridge star formation additionally comes into play. As before, the general temperature distribution is increasing with time. Density peaks are slightly shifting up and more noticeably, top and bottom edges of the distribution (purple and blue contours) follow similar slopes as the median. This means the whole distribution is heating up instead of just a shifting median.

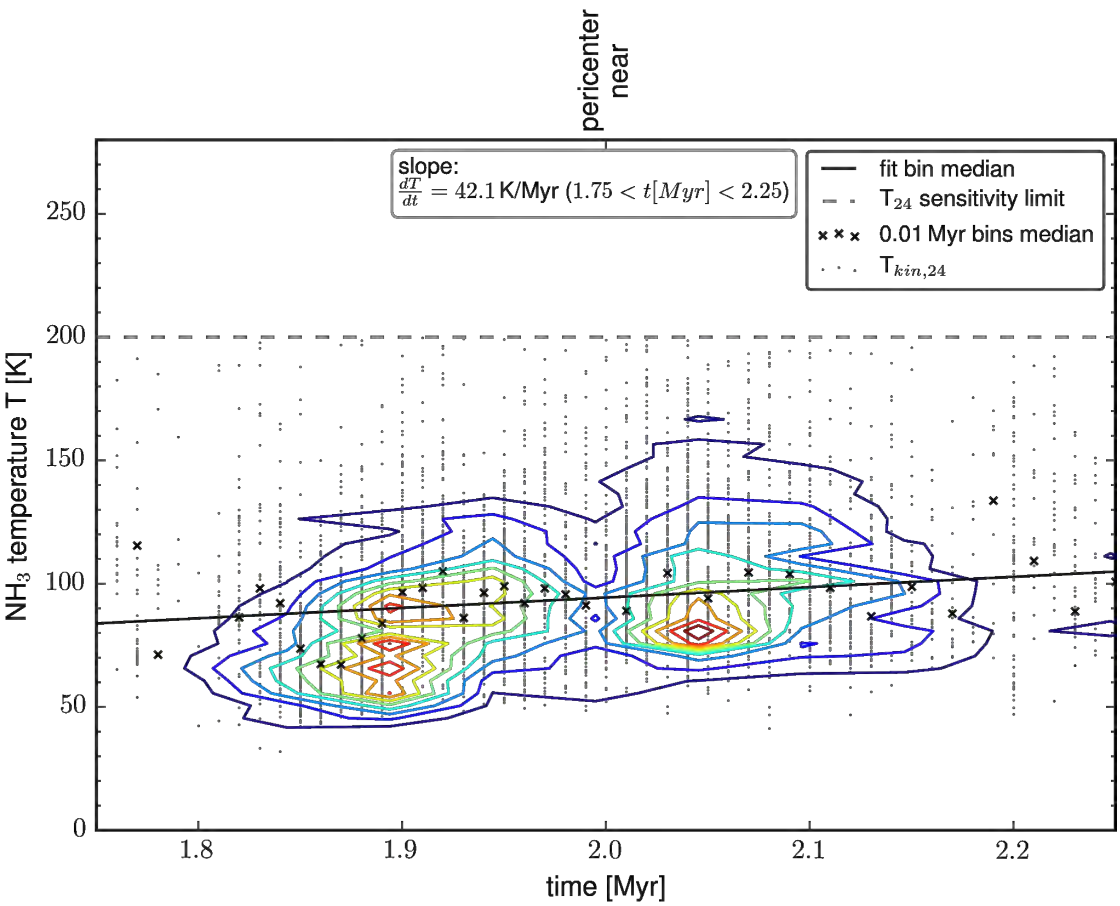

Figure 3.20: Zoom in of fig. 3.16 on the near side pericenter passage around $t = 2\,$Myr.

Positive slopes as presented here for T_{24} are found for all temperature measures (T_{12}, T_{24}, T_{45}, T_{36}) in all time ranges beside T_{12} at far side pericenter passage. Plots of T_{12}, T_{45} and T_{36} as a function of time are printed in appendix B.1 and table 3.3 summarizes the fitted temperature gradients.

Table 3.3: Ammonia kinetic temperature slopes of the three regions that have sufficient measurements to derive temperature evolutions.

	$\frac{T_{12}}{dt}$ [K/Myr]	$\frac{T_{24}}{dt}$ [K/Myr]	$\frac{T_{45}}{dt}$ [K/Myr]	$\frac{T_{36}}{dt}$ [K/Myr]
$-2.00 < t\,[\mathrm{Myr}] < -1.00$ dust ridge	4.2	45.9	52.1	42.0
$-0.30 < t\,[\mathrm{Myr}] < 0.05$ pericenter far	-22.6	113.8	67.7	77.3
$1.75 < t\,[\mathrm{Myr}] < 2.25$ pericenter near	7.7	42.1	19.0	26.7
combined (phase plot)	-3.6	15.8	21.9	16.0

Orbital Phase

Instead of plotting against linear time, the kinematic model suggest the three sequences can be overplotted as temperature versus orbital phase. A new temperature sequence can be expected to start near each pericenter passage at 0 and ± 2.03 Myr, likely some tenths of a Myr earlier as tidal compression becomes relevant already before reaching the orbital point deepest in the potential. A crude division in tidal compression dominated and star formation dominated regime is done based on the orbital model and the observed onset of early embedded star formation in the brick (Longmore et al., 2012). Data for the tidal compression phase is mainly derived from gas at the near side pericenter passage (20 km/s cloud, 50 km/s cloud) and the few measurements at far side passage whereas the main contributor to the star formation phase is the dust ridge.
Fig. 3.21 shows ammonia temperature as a function of orbital phase in terms of time since *last* pericenter passage. The same analysis of binning and linear fitting as before is used to derive a common temperature slope of ~ 16 K/Myr in the the range of 0.25 Myr before to 1.0 Myr after pericenter passage. This fit window covers approximately the same time ranges as the individual sequences before that were $-0.3 - 0.05$ Myr, $-0.25 - 0.25$ Myr and $0.0 - 1.0$ Myr since the respective last pericenter passage.
As the three sequences found individually are similar in absolute temperature, it is not surprising to find an overall evolution as well. Scatter of the median temperature is higher at ~ 20 K in the combined plot than in the well-constrained sequences of the dust ridge and near side pericenter passage. As before, a constant gradient fits the median temperature well without significant mismatches. Using two individual slopes for compression and star formation phase does not improve the fit more than it will necessarily do when introducing another degree of freedom. Similar results are obtained for T_{36} and T_{45} as listed in table 3.3. T_{12}, however, deviates strongly with a negative slope of -3.6 K/Myr. If fitted individually, both

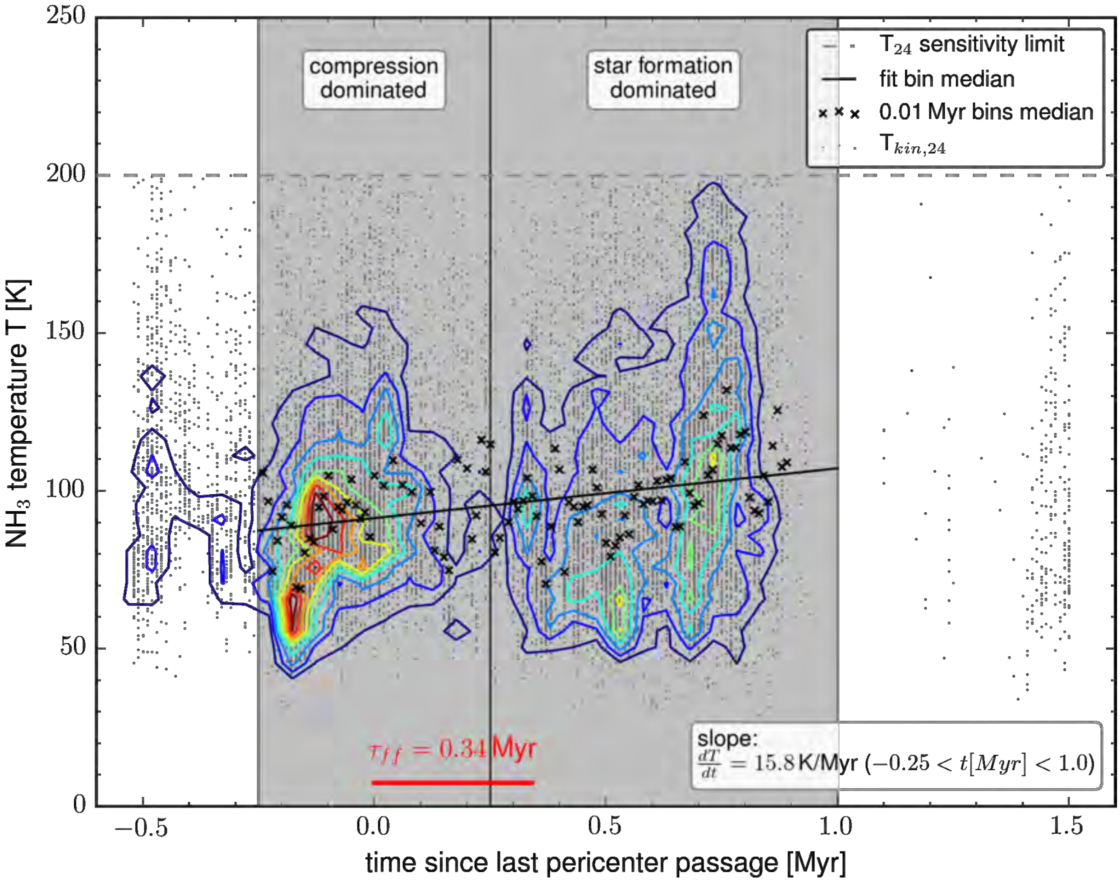

Figure 3.21: $T_{24,kin}$ as a function of time since the last occurrence of pericenter passage. A single linear slope fits the median temperatures reasonably well when keeping in mind that this relation is derived from gas throughout the whole CMZ at relative distances up to 200 pc.

regimes would still show decreasing median temperatures despite increasing temperatures at peak data density. This mismatch is introduced by restricting T_{12} to the reliable range of $0-60$ K that distorts the distribution. As for the other plots of T_{12}, this result must be taken with care and physical interpretation should be based on the more reliable T_{24}, T_{45} and T_{36}.

A Note on Temperature Errors

Temperature errors are not mentioned above because they need more careful treatment. Simple linear fitting by χ^2 minimization with error estimates derived from the error intervals, as calculated according to §3.2.6, result in large temperature slope errors on the order of, or a few times, the slope.
The short sequence at far side pericenter passage is especially affected due to the low number of < 20 bins[5] and has computed slope errors of $dT_{ij}/dt > 500$ K/Myr.

[5]The exact number varies within 16 and 19 for the four different T_{ij}

Visual inspection of the data does reveal that a slope is justified within the bin's error margins despite the enormous mathematical error. Hence, any conclusion for this time range should be treated as a hint but not as proof of existence or quantitative result.
In the dust ridge and near side pericenter passage, more bins over a longer time span ($60-68$ and $30-35$, respectively) can be used to derive more precise slopes with typical errors $\Delta(\mathrm{T}_{ij}/\mathrm{dt})\sim \mathrm{dT}_{ij}/\mathrm{dt}$. This means all derived fits are mathematically compatible with zero or marginally negative slope and twice the given value at the other extreme. A more detailed interpretation can include the information of measurement distribution that was discarded during binning and reveals consistent temperature evolutions as discussed for the zoom-in plots.
The large mathematically derived errors can therefore be interpreted as a too large estimate of the real errors introduced by the chosen statistical analysis. A better (but more complicated and time-consuming) approach should take the data distribution into account, but at the same apply statistical methods to exclude or down-weight outliers and unidentified bad measurements. If an approach satisfying these requirements does exist for this data set, it likely needs heavy testing and calibration in order not to introduce any bias that might not immediately stand out from the large amount of measurements. The simple bin and fit approach, on the other hand, is obviously too simple but can easily be checked visually and interpreted accordingly.

Dust Temperature

The relation between dust and gas temperature is shown in fig. 3.22. T_{24} is offset well above the one-to-one relation by a factor of ~ 3 to > 5. Not even a single gas temperature measurement is at or below $\mathrm{T}_{gas} = \mathrm{T}_{dust}$. A linear best-fit calculated in bins of 1 K for $18\,\mathrm{K} \leq \mathrm{T}_{dust} \leq 30\,\mathrm{K}$ yields a slope of 1.8 and fitting without binning results in no correlation (slope ~ 0.0) due to cut-off effects of the limited temperature reliability range. The fact that dust is thermally decoupled from gas and acts as a coolant is already known in the literature for quite a long time (e.g. Ginsburg et al., 2016; Güsten et al., 1981; Molinari et al., 2011) and can be confirmed once again with improved accuracy. Similar results are obtained for T_{12}, T_{45} and T_{36} ($\mathrm{dT}_{12}/\mathrm{dT}_{dust} = 0.5$, $\mathrm{dT}_{45}/\mathrm{dT}_{dust} = 2.4$, $\mathrm{dT}_{36}/\mathrm{dT}_{dust} = 1.4$). Plots can be found in appendix B.3.
The same evolution plots as for ammonia gas temperature can be calculated for dust temperature. An identical script is run on the dust map but as the Hi-GAL beam is $1.3^2 \sim 2$ times larger than SWAG's beam, each pixel in the dust map is retrieved about twice. The number of (partially)[6] independent measurements is therefore decreased by a factor of two. Fig. 3.23 shows the resulting evolution of dust temperature over time. The two pericenter passages qualitatively match the behavior found in gas temperature with moderately increasing temperature on the near side and much steeper increase at the far pericenter. The evolution

[6] Pixels are still somewhat correlated due to the beam size.

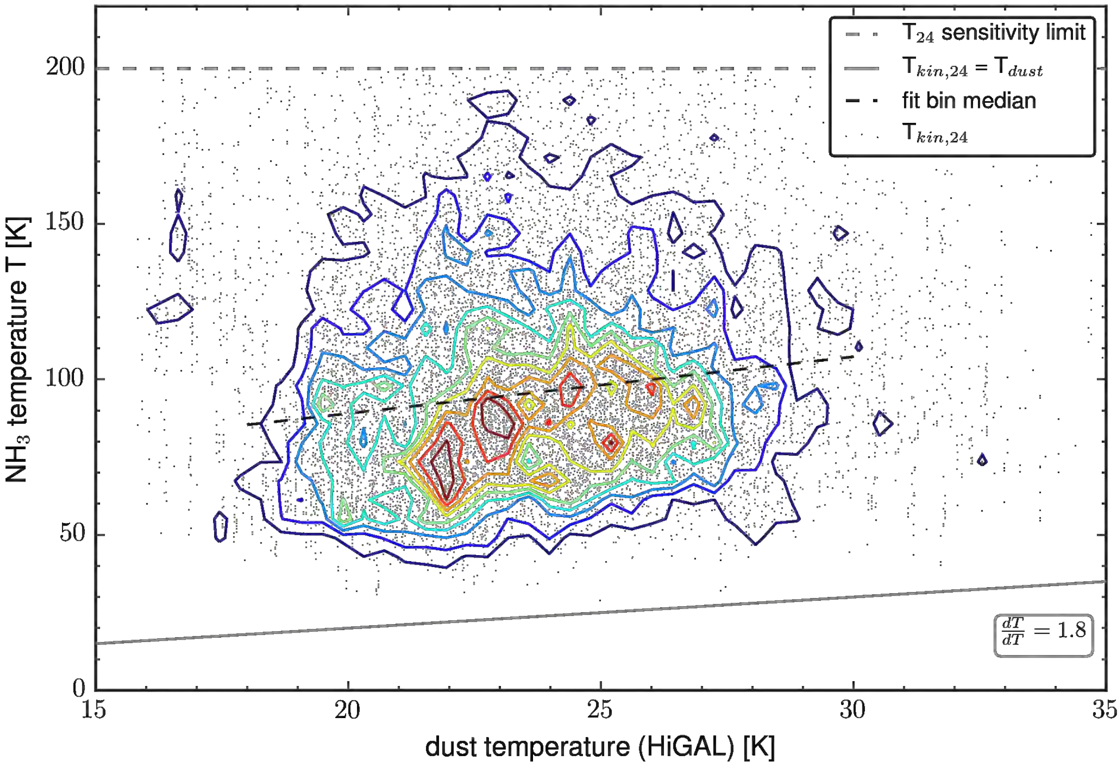

Figure 3.22: Gas temperature traced by NH_3 T_{24} vs. Hi-GAL dust temperature. The relation between dust and gas temperature is complex as gas is significantly hotter than dust ($\sim$ factor $3-4$) but scales linearly with slope steeper than unity, $dT_{gas}/dT_{dust} = 1.8$.

throughout the dust ridge contradicts gas temperatures and is likely to be an artefact as discussed in §3.4.3.

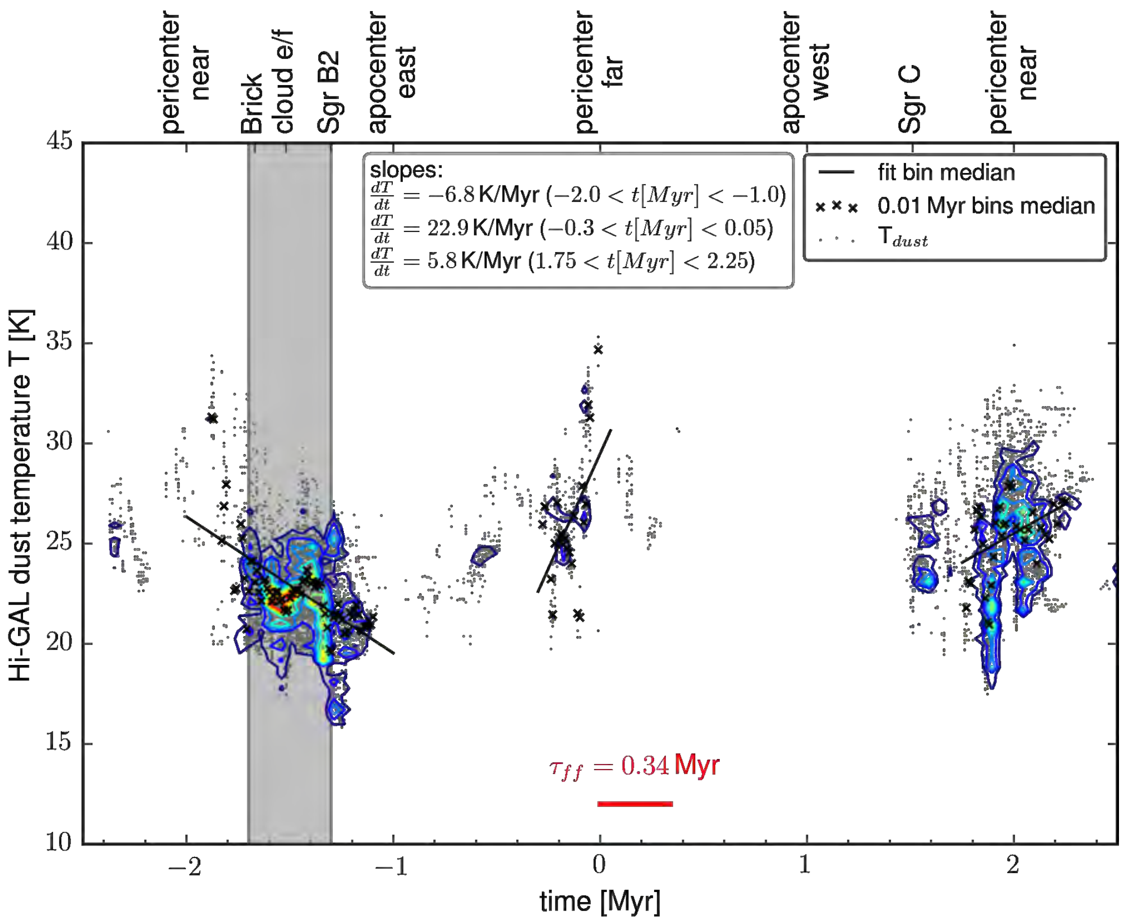

Figure 3.23: Hi-GAL dust temperature as a function of time since far side pericenter passage. Temperatures do not change much in absolute value (~ 5 K) in the two regions of interest around -1.5 Myr and +2.0 Myr, however, relative cooling (dust ridge) and heating (20 and 50 km/s clouds) is significant in the cold dust in the CMZ. For a discussion of dropping dust temperatures in the dust ridge see §3.4.3.

3.4 Discussion

As shown in §3.3, three sequences at or after each pericenter passage are recovered, but the coverage is not sufficient to span the full duration of some tenths of Myr before until $1.5 - 2.0$ Myr after pericenter passage. In the context of the Kruijssen et al. (2015) orbital model, each sequence can be split into a *tidal compression dominated phase* at pericenter passage and a second phase when star formation starts and becomes non-negligible (*star formation phase*[7]). From theoretical considerations, energy input into the clouds during the first phase results from gravitational sources, such as tidal compression and subsequent collapse when clouds become self-gravitating. Star formation starts later in cloud cores, while the surrounding clouds still collapse, and additionally, are subject to tidal forces. This second phase can therefore be more complicated and may differ from the first phase. Section 3.4.1 and 3.4.2 focus on the phases individually, while §3.4.4 covers their relation.

3.4.1 Evolution during Tidal Compression

In principle, conclusions about the tidal compression phase can be drawn from both sequences at ~ 0 Myr and $\sim +2$ Myr, while in the dust ridge sequence, measurements cover mostly the star formation phase. Therefore, this section focuses on the former while §3.4.2 discusses primarily the dust ridge.

Kinematics

There is no consistent evolution in line width with time in both sequences but they are roughly constant with scatter of ~ 10 km/s as presented in §3.3.1. From simple gas dynamics, compression should result in rising pressure and increasing line width as does the dissipation of shear through turbulence. Two explanations for the mismatch of observation and theoretical expectation are possible that cannot be discerned with this analysis. From the observational point of view, any evolution in line width may be covered by the much larger scatter. The measurements are taken over a large area with varying properties and include denser regions (cores or regions that may become a core) that are typically cooler and more narrow, and surrounding thinner gas. Binning and averaging cannot prevent such scatter as the streams are not a continuous gas filament but individual clouds separated by lower density gas. Comparing similar regions (core to core, boundary layer to boundary layer) should reduce the scatter and may bring out a trend in line width. This approach, however, needs a clump find algorithm or any other method to find similar regions in different clouds. A clump catalogue of SWAG sources will be constructed but is currently not available.

[7] Keep in mind that the term star formation phase should denote star formation in addition to tidal effects. Tidal and gravitational effects may still be important.

A more theoretical explanation for the lack of a sequence is that tidal compression acts perpendicular (z-direction) to the plane of the gas[8] and introduces shear in the plane. Pressure building up by compression in the z-direction may be small as the cloud can expand in x and y, and the effect on line width might be too small to be observable. Beside such simple arguments, simulations are needed to make predictions, because orbital kinematics and varying cloud properties must be taken into account.
According to the ideal gas law $p = nk_BT$ and the fact that a certain molecular tracer always traces gas of roughly the same density, any temperature evolution should be reflected on pressure as well. Assuming that line widths are dominated by pressure broadening, the temperature sequence translates into a sequence in line width. Indeed, a linear relation of line width FWHM_i and temperature T_{ij} is observed for $i = 2, 4$ with slopes of 1.2 and 1.1 (fig. 3.24)[9]. The relative temperature increases of $\sim 100\%$ per Myr in T_{24} would imply a line width increase of $\sim 8 - 12\,\mathrm{km/s/Myr}$, which matches the observed scatter. Although this argument only considers a pressure dominated line width, neglecting any other effect of temperature increase or line broadening, the scatter in the data is already of the same order as the expected variation and high enough to hide such a sequence. It is therefore likely that a sequence is hidden within the data, but a more sophisticated approach is needed to reduce scatter and confirm this.

Column Density and Opacity

The time line plots of column density and opacity (figs. 3.13, 3.15) are consistent with no evolution at all during tidal compression. Observed temporal variations trace a sequence of individual clouds that cannot be attributed to a continuous sequence, as the variation from one cloud to the next is larger than any evolutionary changes. The correlation between column density and opacity is high as both show similar (bin median) distributions and slopes; this is expected, as opacity is related to density and its observable, column density. Therefore, both depend on cloud mass because, under otherwise identical circumstances, more massive clouds are denser. Using the projected cloud size as a proxy for mass, typical CMZ clouds are 10-30 pc in length, which is within by a factor of two from the theoretically expected value $\lambda_J \sim 20\,\mathrm{pc}$ derived from Jeans analysis. This scatter is reflected on column density and opacity, and hides potential sequences if they actually exist.

[8] The amplitude of the vertical oscillation is much smaller than the major or minor axis of the elliptic motion in the plane of the disk.

[9] For $i = 1$, the temperature reliability cut-off prevents a linear relation above $\sim 15\,\mathrm{km/s}$ because the kinetic temperature cannot rise above 60 K. Ortho ammonia ($i = 3$, T_{36}) shows an unexpected negative slope of -0.3 due to unknown reasons. This behavior needs to be investigated further.

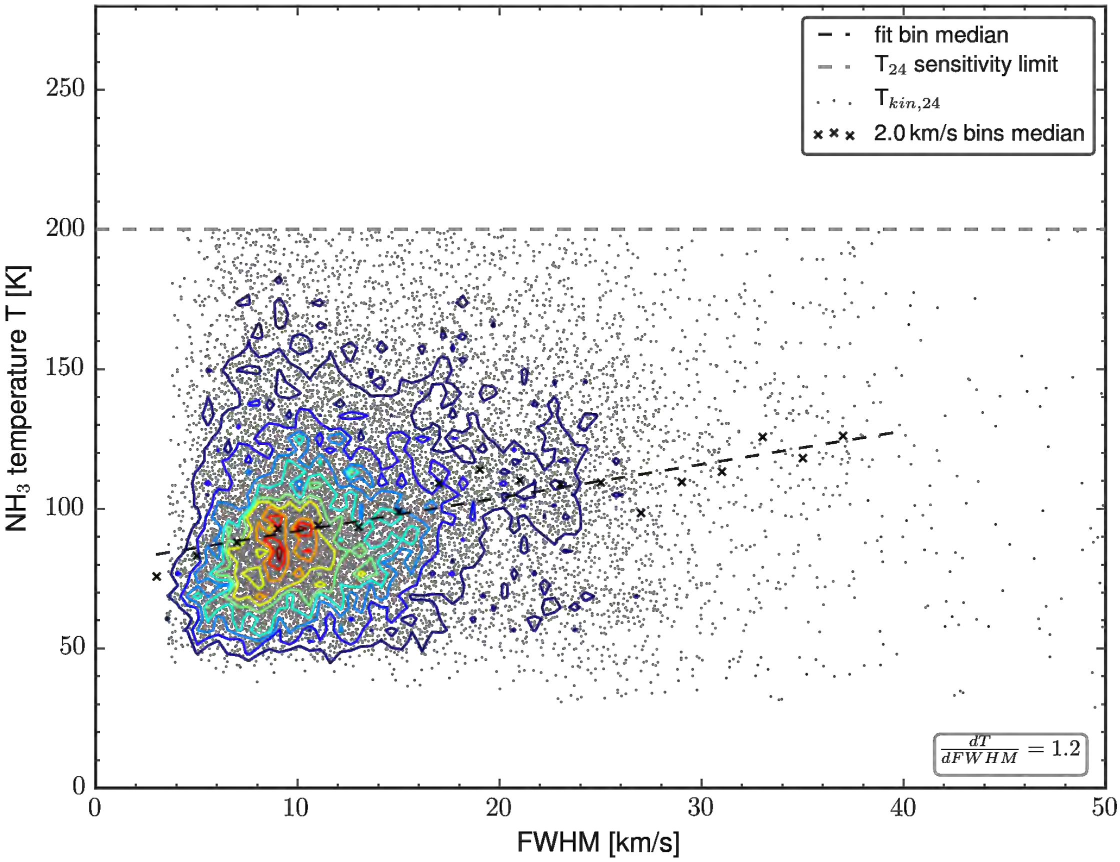

Figure 3.24: Ammonia temperature T_{24} as a function of line width (FWHM) of NH_3 (2,2). The scaling is roughly linear as can be expected from the ideal gas law when the line width is dominated by pressure broadening.

Temperature

The temperature slope during tidal compression is inconsistent in the two occurrences of fig. 3.16 (T_{24}) and corresponding figures for T_{45} and T_{36} in appendix B.1.
At 0 Myr, much steeper slopes are found than at the second event at +2 Myr (table 3.3), which should be roughly equal in the frame of the kinematic model. There are no fundamental differences in orbital parameters at far and near side pericenter passages that can be used to explain this difference. The more likely explanation for the difference in temperature gradient is the very short time range sampled at 0 Myr. The scatter in median temperature in these few clouds is higher than at +2 Myr and the dust ridge, and for T_{12} even a negative slope is fitted where visual inspection cannot find a slope at all. In the other three temperature measures, positive slopes are found that are reasonable by eye, although much less steep increase or even constant temperatures could be justified by the data. The temperature evolution at the far side pericenter passage should therefore be understood as a qualitative result, a hint towards increasing temperatures without

reasonable quantification.
At +2 Myr, the picture is more consistent and easier to interpret. The slopes are of similar order for T_{24}, T_{45} and T_{36} while T_{12} shows the same qualitative result at lower strength. This is due to the sensitivity limit at 60 K that prevents an absolute temperature rise of more than $10-15$ K from a base level of $35-40$ K. The other temperature measures are similar in magnitude ($19.0-42.1$ K/Myr), absolute rise ($12-20$ K) and base level ($75-85$ K). These ranges are not unrealistically large, but they cannot be interpreted without a detailed simulation that incorporates all kinematic and hydrodynamic properties of a molecular cloud. A key feature that prevents any simple order-of-magnitude estimations is the efficiency of cooling by photon escape that depends on optical depth. Such a simulation is currently run by Kruijssen et al. (2016, in prep.) and will allow quantitative comparison of observational and theoretical temperature gradients introduced by tidal compression. Without these simulations, it is also not known at which time before pericenter passage tidal effects start to become non-negligible and affect temperatures. The same applies to the time after pericenter passage when compression and shear decrease in intensity. Fig. 3.16 suggests that at least 0.25 Myr before reaching pericenter a temperature change is detectable. At 0 Myr, the deepest point in the potential is reached at $R_{peri} \sim 59$ pc while 0.25 Myr corresponds to $R \sim 1.22\ R_{peri} = 72$ pc. Apocenter is reached at $R\sim 120$ pc, so tidal effects becoming relevant at $\sim 75-80$ pc from the center of the potential is plausible. The Galactic center potential is symmetric and, therefore, tidal effects are expected to play a role until at least 0.25 Myr after pericenter passage. However, triggering of gravitational instability and early star formation cover the weakening tidal effects, making it difficult to define an end point of strong tidal influence from the observational data.
Although dust and ammonia temperatures are strongly offset, a linear correlation is present (fig. 3.22) and T_{dust} follows nearly identical relative evolutions in both regions of tidal compression. The increase is $\sim 100\%\,\mathrm{Myr}^{-1}$ at 0 Myr and $\sim 25\%\,\mathrm{Myr}^{-1}$ at +2 Myr in dust and ammonia temperature over the respective sampled time range. As before, the far side passage sequence should be understood as merely a hint, while the much better sampled near side pericenter passage yields reliable quantities. This is an independent confirmation for increasing ISM temperatures during tidal compression and verifies that gas and dust react proportional to the interaction at different absolute levels.

3.4.2 A Sequence in the Dust Ridge

Kinematics

Similar kinematic arguments as mentioned in the previous section apply to the dust ridge. There is no sign for a systematic evolution of line width with time, but rather individual clouds show consistent deviations. High mass clouds as the Brick and Sgr B2 show increased line widths with respect to other clouds of lower mass. The cloud-to-cloud variations and amount of scatter is larger than a possible change over time. As stated in the corresponding section for the tidal compression phase, a meaningful analysis must ensure that similar regions of clouds are compared (core to core, envelope to envelope) instead of giving every pixel the same weight irrespective of its position in the cloud.

Column Density and Opacity

Although the increase in column density and opacity along the dust ridge is consistent in NH_3 J $= 1, ..., 6$ (column density) and J $= 1, 2, 3, 5, 6$ (opacity), it is mainly caused by Sgr B2 and does not necessarily show an evolution. Instead, it can be explained with the same argument as for the tidal compression phase of cloud-to-cloud variation of physical properties. However, it might still be the case that gas later in the sequence is becoming more dense due to triggered collapse. For detecting such an underlying sequence, a more sophisticated analysis is needed than for the kinematic analysis in order to be sure to compare only regions similar in physical properties (e.g. cores vs. cloud envelopes or mass and size).

Temperature

In the dust ridge, gas temperatures traced by different ammonia lines are very similar in base temperature at the beginning of the fitted evolution ($60 - 70\,\mathrm{K}$) and rise over 1 Myr ($42 - 52\,\mathrm{K}$). This is surprising, as in the tidal compression phase differences were much larger and might hint towards less variation in the underlying physics. However, during this phase, star formation, ongoing cloud collapse and decreasing tidal effects can affect gas temperatures. As an estimate, star formation can set in as early as one free-fall time after pericenter passage, which is 0.34 Myr for a typical CMZ cloud, and coincides with the time since the Brick passed pericenter (Kruijssen et al., 2015). Accordingly, signs of embedded star formation have been found there (Longmore et al., 2012). While the central region of the cloud has collapsed into a core after τ_{ff}, the envelope layers continue to collapse and release gravitational energy that continues to heat the gas afterwards. Additionally, tidal effects may still be non-negligible as estimated from the observations in the previous section. All of these effects increase the temperature if the gas cannot cool efficiently enough which apparently is the case here as shown by the decoupled dust at significantly lower temperatures. Therefore, the increase in temperature cannot simply be attributed to a single of these physical processes without detailed knowledge of their relative strengths, which is not known at the moment for Galactic Center conditions. In order to disentangle the contribution of star formation from the kinematic and gravitational effects, a complex hydrodynamic gas simulation including star formation feedback is needed.
A hint towards increasing temperature in the dust ridge has already been found by Ginsburg et al. (2016) traced by formaldehyde (H_2CO). They applied a similar time fitting routine as described in §3.2.4 to dendrogram-extracted clumps with a linear fit of temperature evolution. Until $\sim 0.8\,\mathrm{Myr}$ after pericenter passage, they find kinetic temperatures increasing from $< 50\,\mathrm{K}$ to $> 100\,\mathrm{K}$ over a time range

of ~ 0.6 Myr which is a slope of ~ 75 K/Myr. The linear fit, however, is heavily influenced by warm gas in the Brick ($\sim 70 - 100$ K) and Sgr B2 ($\sim 130 - 190$ K) that can be seen in fig. 3.16 as well. The many more measurements in this work mediate outlier effects and are thus more reliable to conclude the existence of a temperature sequence in the dust ridge. The difference in absolute temperature scale between formaldehyde and ammonia is likely due to the lower energy of the states $E_l = 10.5$ K (3_{03} - 2_{02}) and $E_l = 57.6$ K (3_{21} - 2_{20}) of H_2CO compared to $63.3 - 406.9$ K in NH_3 (2,2) to (6,6), which results in the observations being more sensitive to colder H_2CO and warmer NH_3 gas. A small amount of the difference might also be related to differing tracer properties of H_2CO ($n_{crit} \sim 10^4 - 10^5$ cm^{-3}) and NH_3 ($n_{crit} \sim 10^3 - 10^4$ cm^{-3}). As the critical density for H_2CO is higher than that of NH_3, regions slightly deeper in the dense center of clouds are observed in H_2CO where temperature changes can be somewhat different from the more peripheral shells in higher cloud layers observed in NH_3. The stronger increase in temperature deeper inside clouds (or in cloud cores) can be explained reasonably with the closer proximity to stars forming in the cores and their energy release in the surrounding medium. Temperatures can then increase more because cooling is less efficient due to longer optical path length and thus higher opacity.

3.4.3 Decreasing Dust Temperature in the Dust Ridge

Decreasing temperatures along the dust ridge are unlikely to be real because the dust is already cold and cannot cool down further under CMZ conditions, especially while gas is heating up at the same time. Dust temperature is highly offset from gas temperature in the Galactic Center as was shown in fig. 3.22 but still linearly correlated, which is in contrast to the apparent inverse coupling implied by time evolution.
The reason for decreasing dust temperatures is a systematic error in deriving dust temperatures. The optically thin approximation used by Molinari et al. (2011) to fit the dust emission does not hold in dense clouds in the dust ridge. Other clouds in the CMZ, like the ones making up the sequences at near and far pericenter passages, are little to not at all affected as they are far less dense in dust. Preliminary corrections assuming optically thick emission would be 2-3 K for conditions similar to cloud d/e/f and 4-5 K in the central regions of Sgr B2 (Molinari, private communication). A corrected version of fig. 3.23 is therefore expected to show no or very limited changes in temperature along the dust ridge at constant $T_{dust} = 24 - 25$ K. As there is no updated dust temperature map available, quantitative comparisons are not possible. The qualitative behavior of $T_{dust} = const$ can likely be explained by the excellent cooling properties of dust. Dust is able to radiate away the energy input by gravitation and star formation even under optically thick conditions due to the multitude of possible lines available for cooling. However, this explanation conflicts with the increasing dust temperatures in the compression dominated phase. A definite answer about any dust temperature evolution in the star formation dominated phase must therefore be postponed until new maps become available that are reliable throughout the whole CMZ.

3.4.4 Linking Tidal Compression Phase and Star Formation Phase

According to the Kruijssen et al. (2015) model, the empirically found sequences are directly associated in the sense that the star formation dominated phase (dust ridge) follows the tidal compression dominated phase (near and far pericenter passage).

Observational data recover this behavior reasonably well (fig. 3.21). It should be kept in mind that this plot relates gas in regions as far as 200 pc from each other (Sgr C to Sgr B2) and cloud properties (e.g. size, mass) vary significantly.

Temperatures at the end of the tidal compression dominated phase at t = +2 Myr since far side pericenter passage are of the same order ($80 - 100$ K) as at the beginning of the star formation dominated phase in agreement with the model. Due to a mismatch of most probable temperature (peak of measurement density contours) and median temperate (used for fitting), a conclusive decision on the quality of connecting both phases is difficult. Median temperatures seem to transition more smoothly but with increased scatter at $t_{last} = 0.25$ Myr, whereas the density contours also show a large amount of gas colder than at the end of the compression phase, without an immediately obvious discontinuity. This qualitative behavior is consistent in T_{24}, T_{45} and T_{36} (figs. 3.21, B.5 and B.6) with matching temperature slopes and can therefore be seen as reliable. From these plots, it seems likely that the clouds at (near and far side) and after pericenter passage (dust ridge) are similar but not identical in properties, and the general model describes the process correctly within the range of scatter. It should be kept in mind that individual cloud properties as well as collapse triggering are statistically distributed and are not identical for subsequent occurrences.

Despite the fact that both phases can be fitted well with a common slope (figs. 3.21, B.5, B.6), table 3.3 suggests steeper slopes during star formation. For the reliable measures T_{24}, T_{45} and T_{36}, slopes are marginally up to $> 100\%$ steeper in the dust ridge than at near side pericenter passage. As discussed before, values derived for the far side pericenter passage should only be taken qualitatively rather than quantitatively, and T_{12} is affected by its low temperature range. This behavior might hint towards different underlying physical processes (gravitational effects vs. gravitational effects plus star formation) but should not be over-interpreted and must be examined in more detail.

3.4.5 Conclusion: A Tidally Triggered Star Formation Sequence in the Galactic Center

As discussed in the previous sections, consistently increasing temperatures of dense gas in Galactic Center streams are found in two domains where gravitational effects or star formation are expected to dominate the evolution, and linking both is possible in the theoretical framework of the triggering model suggested by Longmore et al. (2013). Although the analysis is based on the kinematic stream model of Kruijssen et al. (2015), similar results would be obtained assuming a different

orbital model as long as the basic requirement of varying tidal field strength is met. In the context of a dense gas torus (Molinari et al., 2011) instead of streams, the basic requirement for tidal triggering of cloud collapse is still present (as argued by Longmore et al., 2013): gas passes close to the bottom of the Galactic Center gravitational potential. It is irrelevant if this is due to a displaced orbit (ring model) or elliptical streams. The only difference in the context of this thesis is the question if another trigger point on the far side of the orbit is present or not, which only marginally affects this analysis as there is very little gas detected and the results are therefore discussed qualitatively only. Thus, a definite distinction between both models is not possible but the hints of a third trigger point at far side pericenter passage favors the Kruijssen et al. (2015) model. With the change in orbital velocity between models, times since triggering would change, i.e. scaling of the x-axis in previous plots and 20 and 50 km/s clouds (tidal compression phase) are naturally followed by the dust ridge (star formation phase) without having to rely on an orbital phase plot (fig. 3.21). Hence, interpretation is slightly different but there are no fundamental changes in the observed relations.
Finding a gas temperature sequence in the CMZ streams confirms predictions that followed from the star formation triggering model by Longmore et al. (2013), but does not directly confirm that the clouds themselves evolve as expected. Heating or cooling of molecular clouds does not necessarily have to be associated with star formation or collapse in the theoretically expected way, but can be related to other mechanisms such as cosmic ray heating as well. It is therefore essential to gain more insight in cloud evolution in the streams and link it to observations of star formation tracers (in the dust ridge) and stars (star clusters; Arches, Quintuplett). If Arches and Quintuplett could be included in the Galactic Center star formation model, the time scale would greatly increase from pre-collapse to evolved stars and span the whole time range of star formation. Immediate insights for cloud evolution could be gained from a study of internal cloud kinematic, size, form and density. After triggering gravitational instability, clouds are expected to collapse, which is reflected in infalling motions, decreasing sizes and increasing density. Unfortunately, such parameters are very difficult to obtain because only projected spatial quantities plus line-of-sight velocity information are known and the cloud-to-cloud variations are likely too high to identify sequential behavior. Masses and radii of dust ridge clouds are known to vary by factors > 2 (Immer et al., 2012; Lis et al., 1999) and figs. 3.12 and 3.13 show that NH_3 line width and column density do not allow the identification of a sequence.
Beside the ISM ingredients gas and dust, the key to a better understanding of star formation in extreme environments as the CMZ are the stars themselves. Evolution in gas and possibly also in dust is accompanied by increasing signs of star formation along the dust ridge that partially powers the rise in temperature. Starting from an increased base level after initial heating by tidal effects, the Brick is still cold and shows little star formation (Kauffmann et al., 2013; Longmore et al., 2012; Rodríguez & Zapata, 2013) while cloud d contains a methanol maser suggesting massive star formation (Immer et al., 2012) and Sgr B2 is heavily forming stars heating the surrounding medium. From the qualitative picture, gas and stars seem

to go in hand providing a rough picture that needs to be tested in more detail in order to reach the goal of a well-calibrated absolute timeline of star formation.

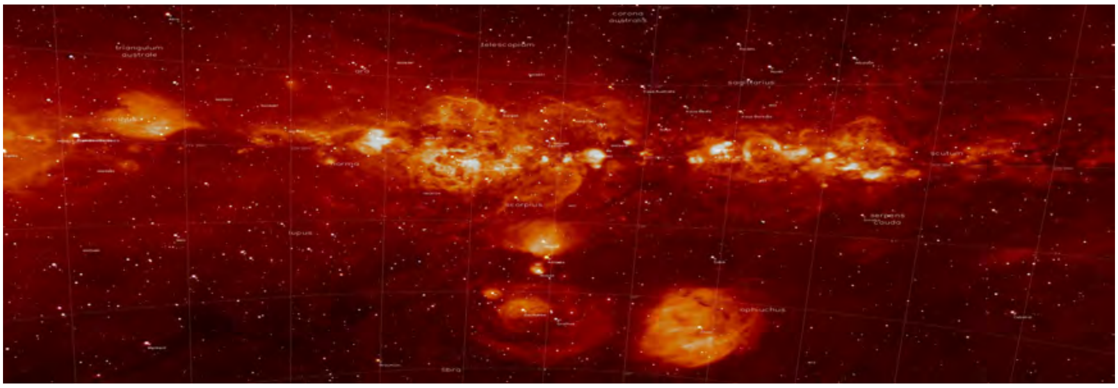

Summary and Outlook

This thesis presents data reduction and analysis of the Survey of Water and Ammonia in the Galactic Center (§2). The inner $\sim 200\,\mathrm{pc}$ of the Galactic Center were observed with the Australia Telescope Compact Array at $21 - 25\,\mathrm{GHz}$ covering 42 spectral lines of molecular and atomic species, particularly six metastable ammonia inversion lines. A data reduction and imaging pipeline was developed based on observations taken in 2014 and 2015 (~ 1800 pointings, > 200 hours) that yielded a catalog of maps and spectra in unprecedented detail with $2\,\mathrm{km/s}$ spectral resolution and $\sim 20"$ ($0.8\,\mathrm{pc}$) spatial resolution. The ammonia hyperfine structure lines of NH_3 (1,1) to (6,6) were fitted to obtain maps of line-of-sight velocity, line width, column density, opacity and four measures of kinematic gas temperature, as well as error maps for all quantities. This data set builds the legacy of SWAG and will be used to investigate various scientific questions related to star formation, stellar evolution and the physics of the interstellar medium.

The second part (§3) tackles one scientific question that could not be addressed with previous observations: Does the proposed tidally triggered star formation sequence in the Central Molecular Zone exist? Using the SWAG maps of ISM gas properties, absolute time dependencies of line width, column density, opacity and temperature could be derived by assigning each pixel a time according to the kinematic model of Kruijssen et al. (2015). It was found that gas temperatures increase as a function of time in both regimes, before and after the corresponding cloud passes pericenter, where its collapse is triggered. Fig. 3.16 exemplifies this evolution for the kinetic temperature measure T_{24}. Zoom-ins (figs. 3.18, 3.19, 3.20) provide a more detailed view on the three time regimes that are sufficiently well sampled to provide qualitative and quantitative evidence for consistently rising gas temperatures. Over the range of up to 1 Myr, temperatures increase by $\sim 20 - \sim 50\,\mathrm{K/Myr}$. Dust temperatures given by the Hi-GAL survey (Molinari et al., 2011) support the finding of rising ISM temperatures in the phases near

The Galactic Center in Hα. (image from `http://www.nuiverse.com/extras/category/eb1d9b07-8e5a-479c-a0e1-57af4fd6cf0f`) pericenter passage, but cannot be used in the later phase when star formation is expected to dominate the energy input because of the wrong assumption of optically thin emission. Other quantities (line width, column density, opacity) do not show strong signs of time dependence, which is likely covered by dominant cloud-to-cloud variations.

These results have been discussed regarding the concept of tidal triggering of cloud collapse and orbital kinematics, and found to generally match the predictions. Increasing temperatures of molecular clouds around pericenter passage are likely caused by tidal compression and maybe induced turbulence by shear, which is why this phase is termed compression dominated phase in this work. After pericenter passage, the influence of tidal forces diminish and star formation can be expected to dominate a cloud's energy budget causing slightly faster temperature increase than before. Together with observations of evolving star formation activity along the dust ridge in the star formation dominated phase (Immer et al., 2012; Kauffmann et al., 2013; Longmore et al., 2012; Rodríguez & Zapata, 2013), a coherent, but still sketchy, picture of triggered star formation in the Galactic Center can be drawn. Theoretical modelling and simulation of CMZ clouds is currently being advanced, and must now be tested further and possibly adapted to match these new observations setting empirical constraints.

In the context of star formation in general, the confirmation of a (temperature) sequence in the Galactic Center is exciting as it demonstrates again[1] the applicability of the triggering hypothesis that allows measuring timescales of star formation processes directly. Other studies aiming at identifying timescales by counting abundances of star formation phases or collapse triggering in spiral arms were done in less extreme environments, such as disk spiral arms or the Large Magellanic Cloud. Galactic Center conditions correspond to star forming galaxies at $z \sim 2-3$, the important time when most of today's stars were formed. This will enable us to develop better models and theories of star formation in high-z targets in which we will not be able to resolve individual GMCs any time soon, but rather have to rely on measuring global, averaged properties. An intermediate step between Galactic Center and high-z galaxies is offered by the partner survey SWAN (Survey of Water and Ammonia in Nearby Galaxies, Gorski et al. (2015)) at $\sim 63\,\mathrm{pc}$ resolution. New instruments, such as ALMA, that already delivers incredible results, or potentially SKA in the more distant future, will allow resolutions and sensitivities in nearby galaxies similar to what we can achieve in the Galactic Center today and thus offering comparison of the found properties.

[1]Basic advances in this direction were already done in Ginsburg et al. (2016)

A SWAG Data Products

A.1 Immediate Data Products

The print version of this thesis contains a shortened appendix A of the most important data products of SWAG. A full list of all 42 spectral lines is given in the online version (pdf file).
The data cube of each line is presented with a channel map, moments -2, 0, 1 and 2, spectra at Sgr A*, B2 and C, and a position-velocity diagram.
The channel maps display every 7^{th} channel of 2.0 km/s width without averaging starting from a velocity of -132.0 km/s relative to the line's rest frequency. In each panel, the velocity is indicated in the top left corner. The color mapping changes between different lines and is shown in the bottom right panel.
Moment maps are shown for order -2, 0, 1 and 2 which is peak intensity, integrated intensity, velocity field and velocity dispersion, respectively. See §2.3.2 for detail on how these plots were produced.
Spectra of the three most important sources in the filed of view, Sgr A*, Sgr B2 and Sgr C, are included, too. The region around Sgr B2 is called Large Molecular Heimat because most molecules known to exist in space can be detected there. The spectrum can therefore help to decide if a line was detected at all.
Fig. 2.7 shows the position where a pV-slice was taken. In order to cut through Sgr B2 and Sgr C, it barely misses Sgr A* and contains much emission from the CMZ.
The plotting program KVIS, which was used in this work, does not display units for the color wedge. Position-velocity diagrams, channel and peak intensity (moment -2) maps are given in Jy/beam, integrated intensity maps (moment 0) in Jy/beam km/s, whereas velocity fields (moment 1) and velocity dispersion maps (moment 2) are given in km/s.

A.1.0.1 $NH_3(1,1)$

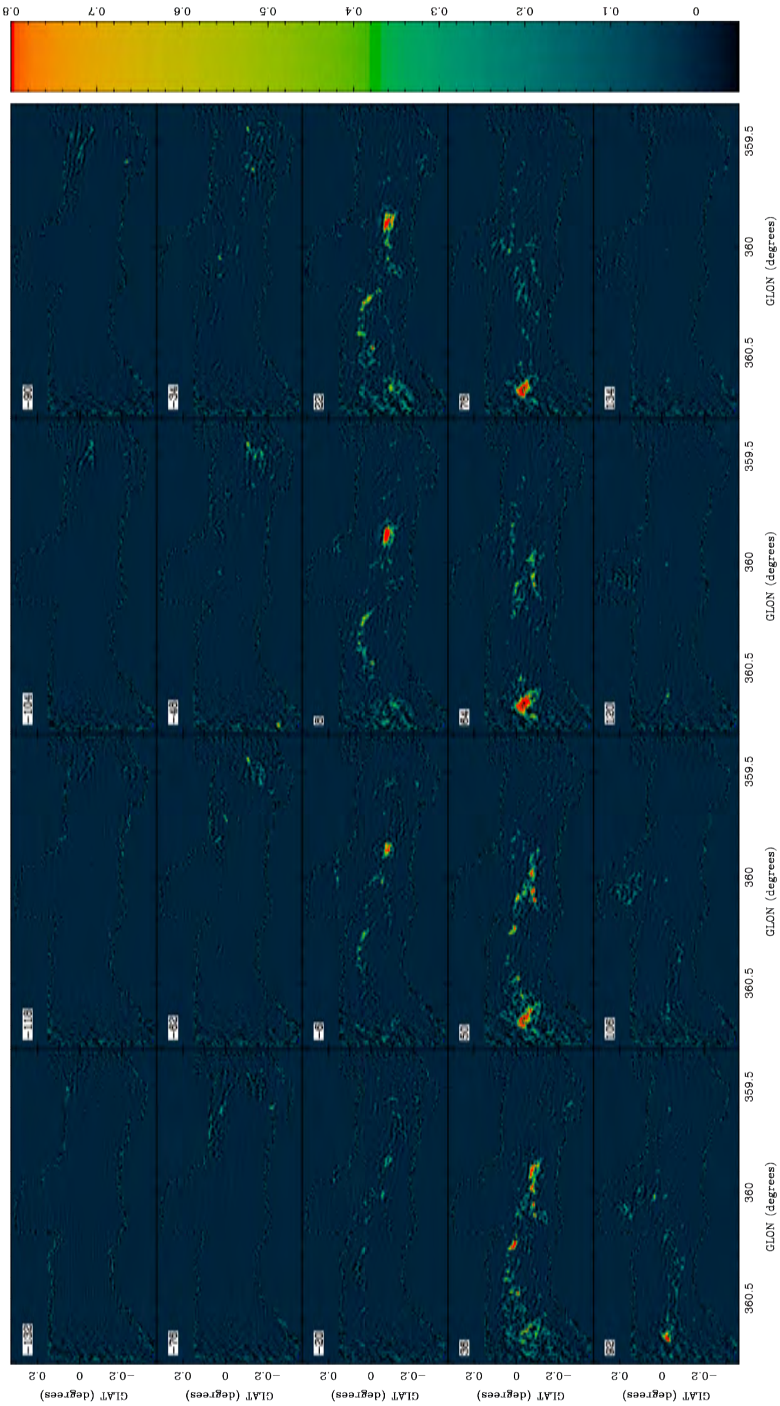

Figure A.1: Channel map of $NH_3(1,1)$

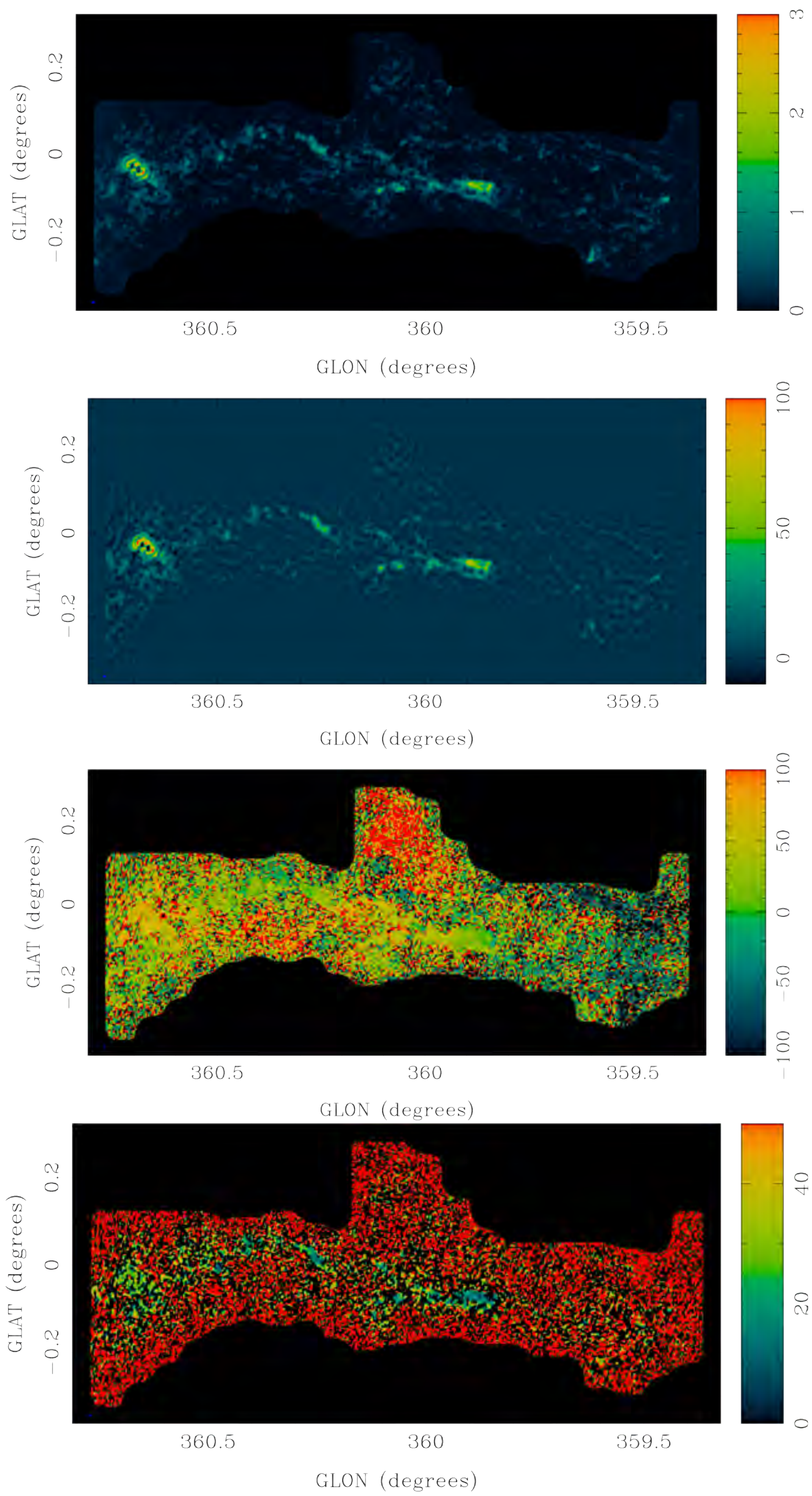

Figure A.2: NH_3(1,1) moment maps. *top to bottom*: peak intensity (moment -2), integrated intensity (moment 0), velocity (moment 1), velocity dispersion (moment 2)

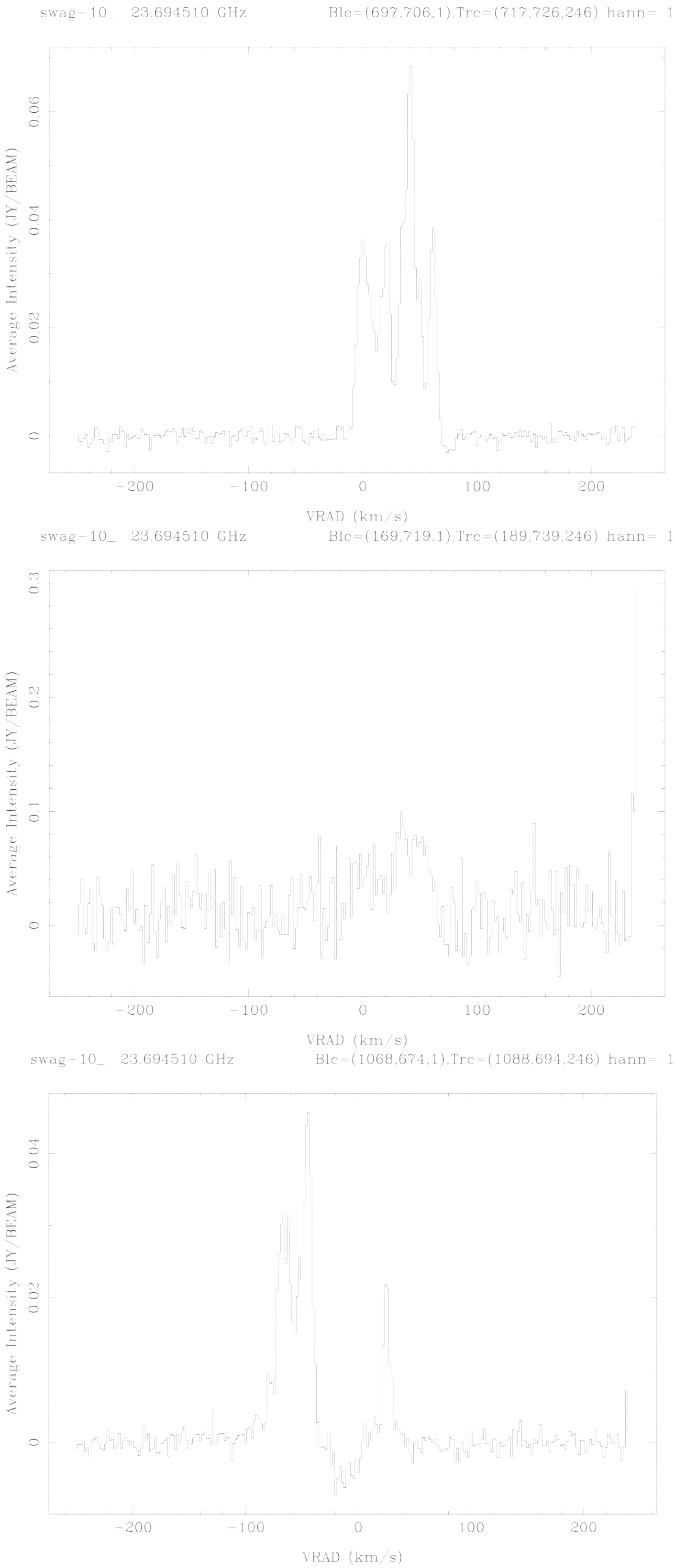

Figure A.3: $NH_3(1,1)$ spectra. *top to bottom*: Sgr A*, B2, C

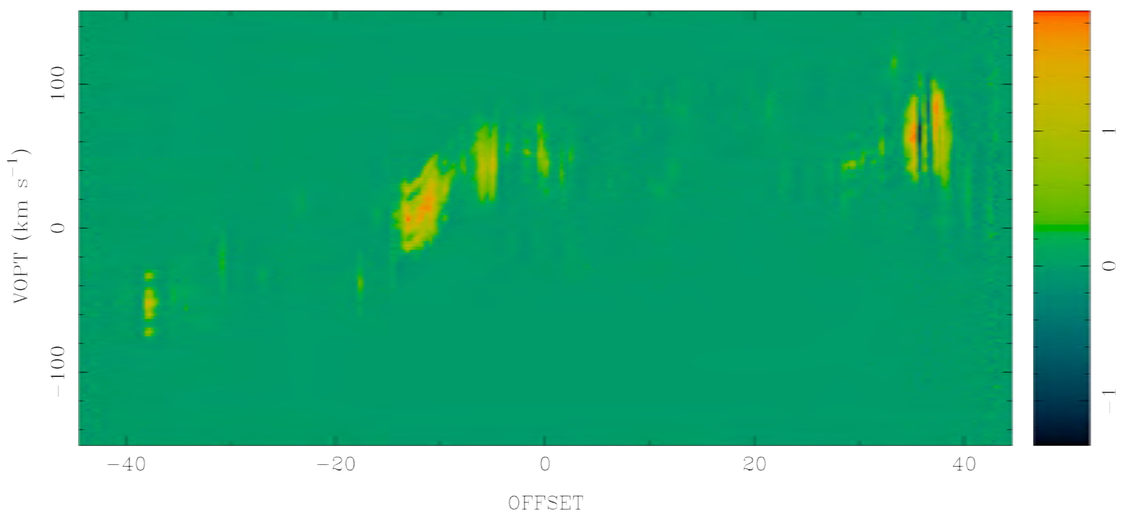

Figure A.4: $NH_3(1,1)$ position velocity diagram through Sgr B2 ($\sim -30 - -40$") and Sgr C ($\sim +35$")

A.1.0.2 NH_3(2,2)

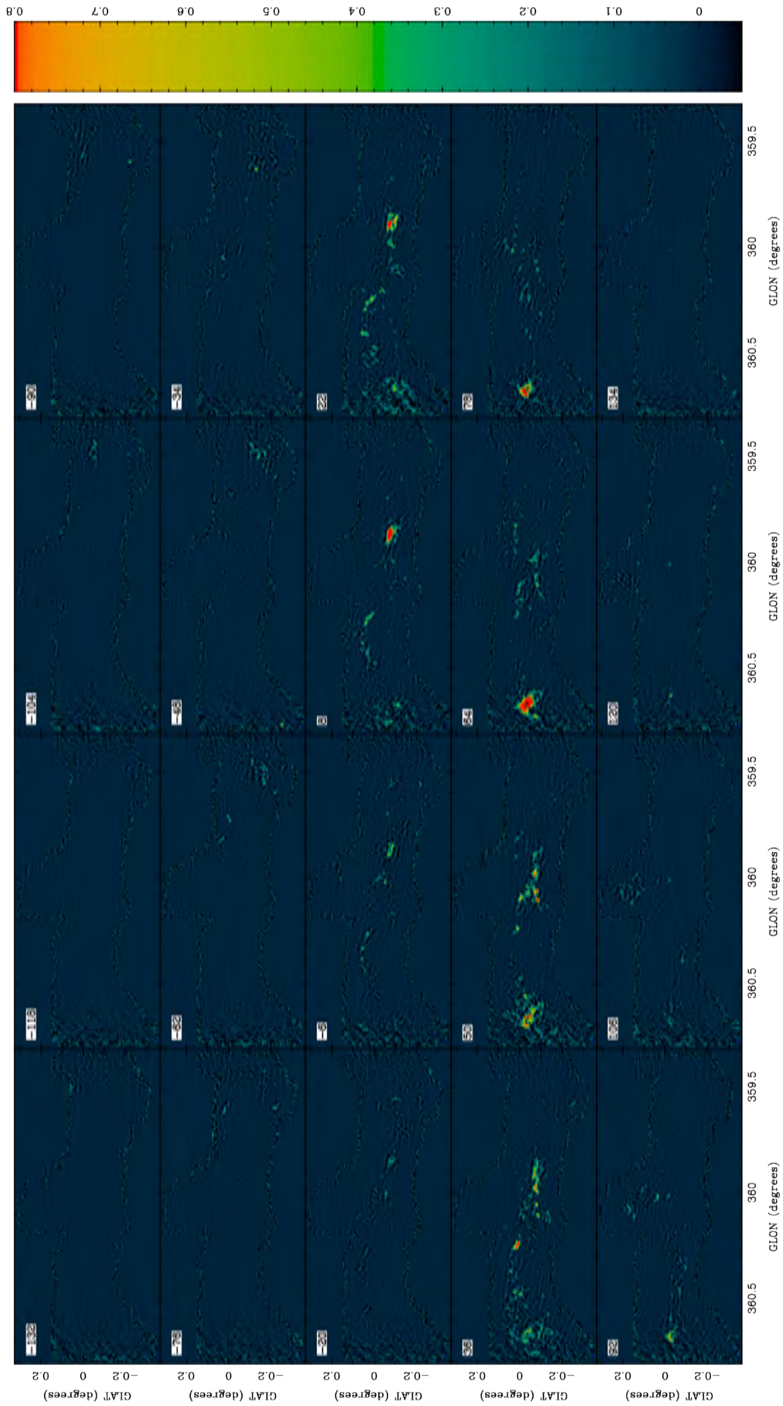

Figure A.5: Channel map of NH_3(2,2)

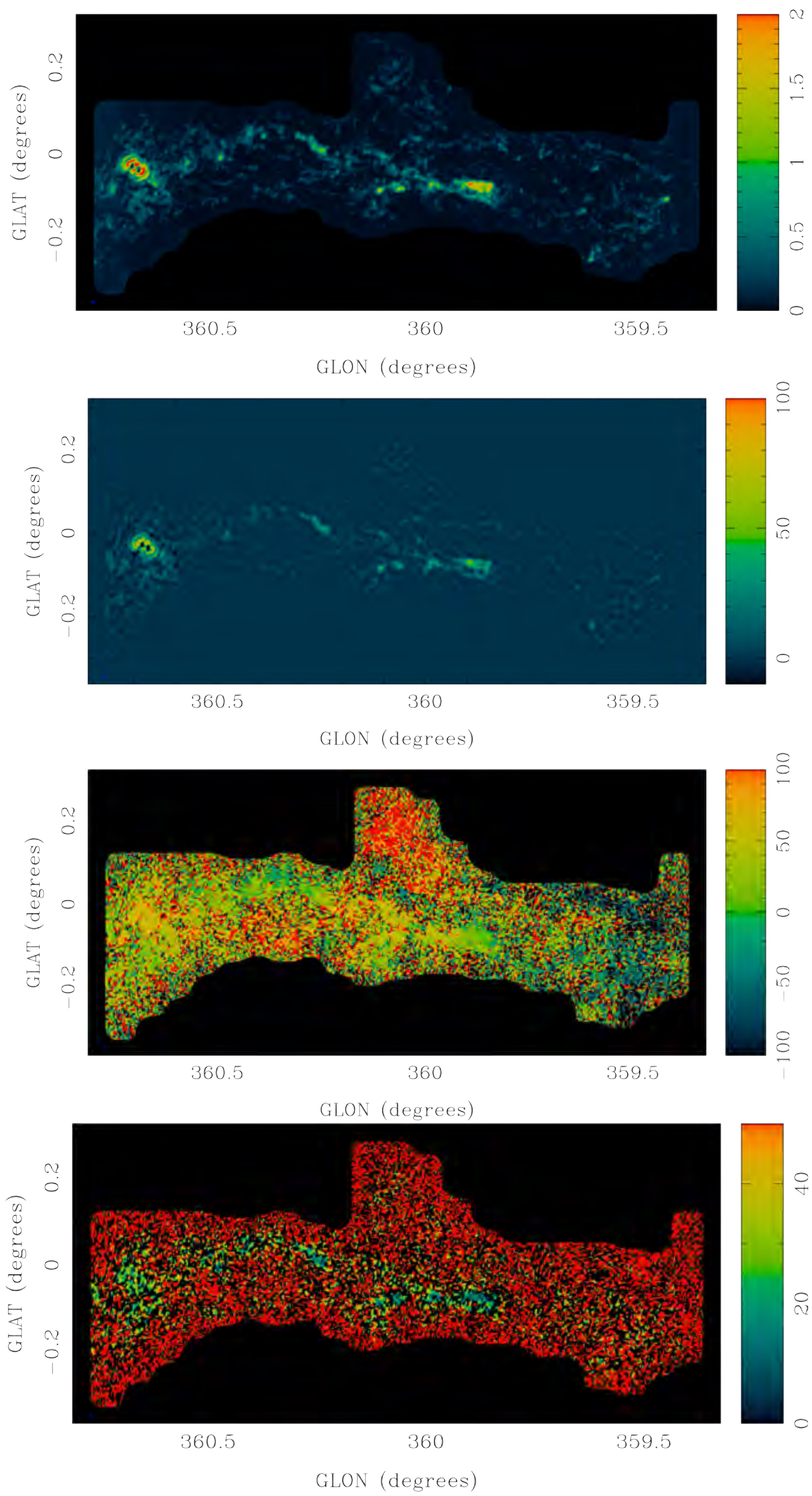

Figure A.6: NH_3(2,2) moment maps. *top to bottom*: peak intensity (moment -2), integrated intensity (moment 0), velocity (moment 1), velocity dispersion (moment 2)

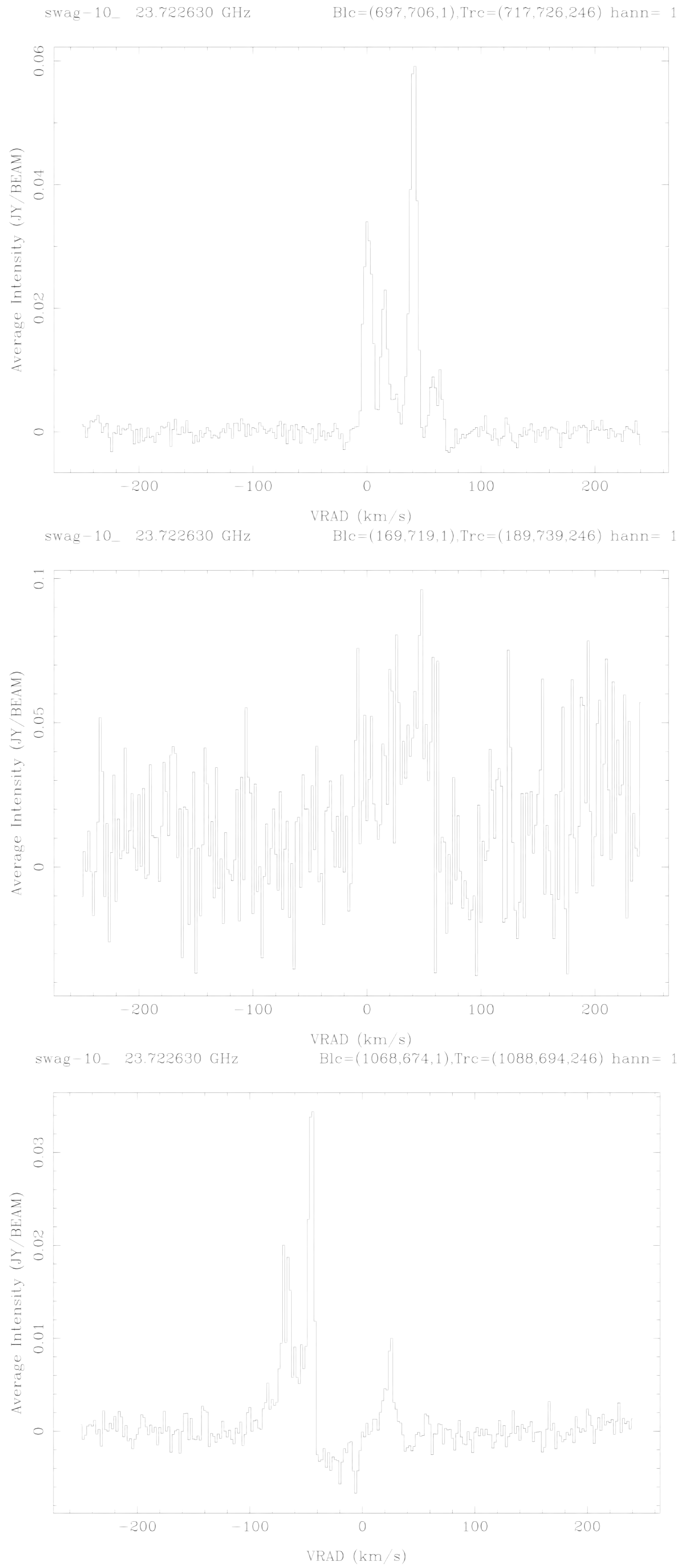

Figure A.7: NH_3(2,2) spectra. *top to bottom*: Sgr A*, B2, C

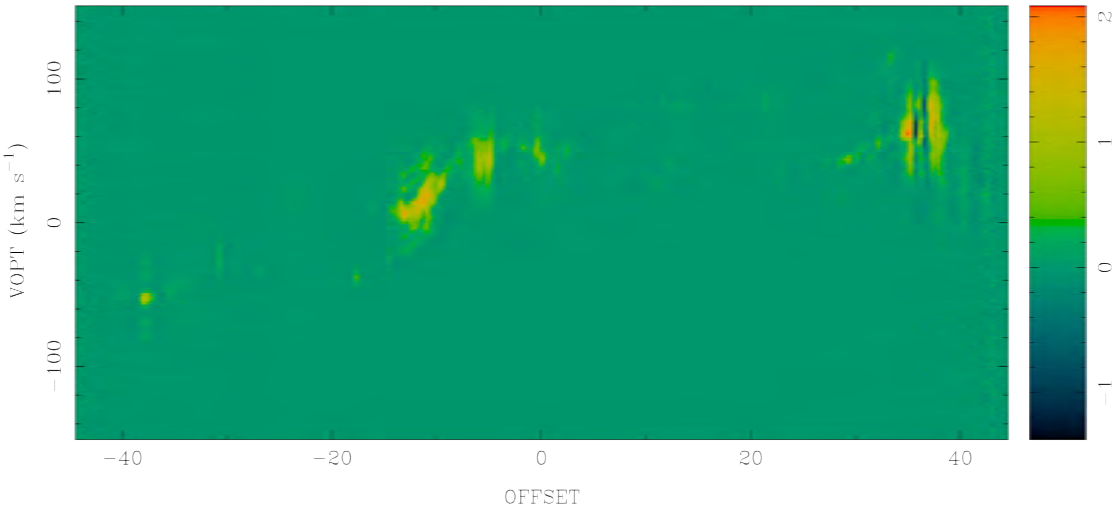

Figure A.8: $NH_3(2,2)$ position velocity diagram through Sgr B2 ($\sim -30 - -40$") and Sgr C ($\sim +35$")

A.1.0.3 $NH_3(3,3)$

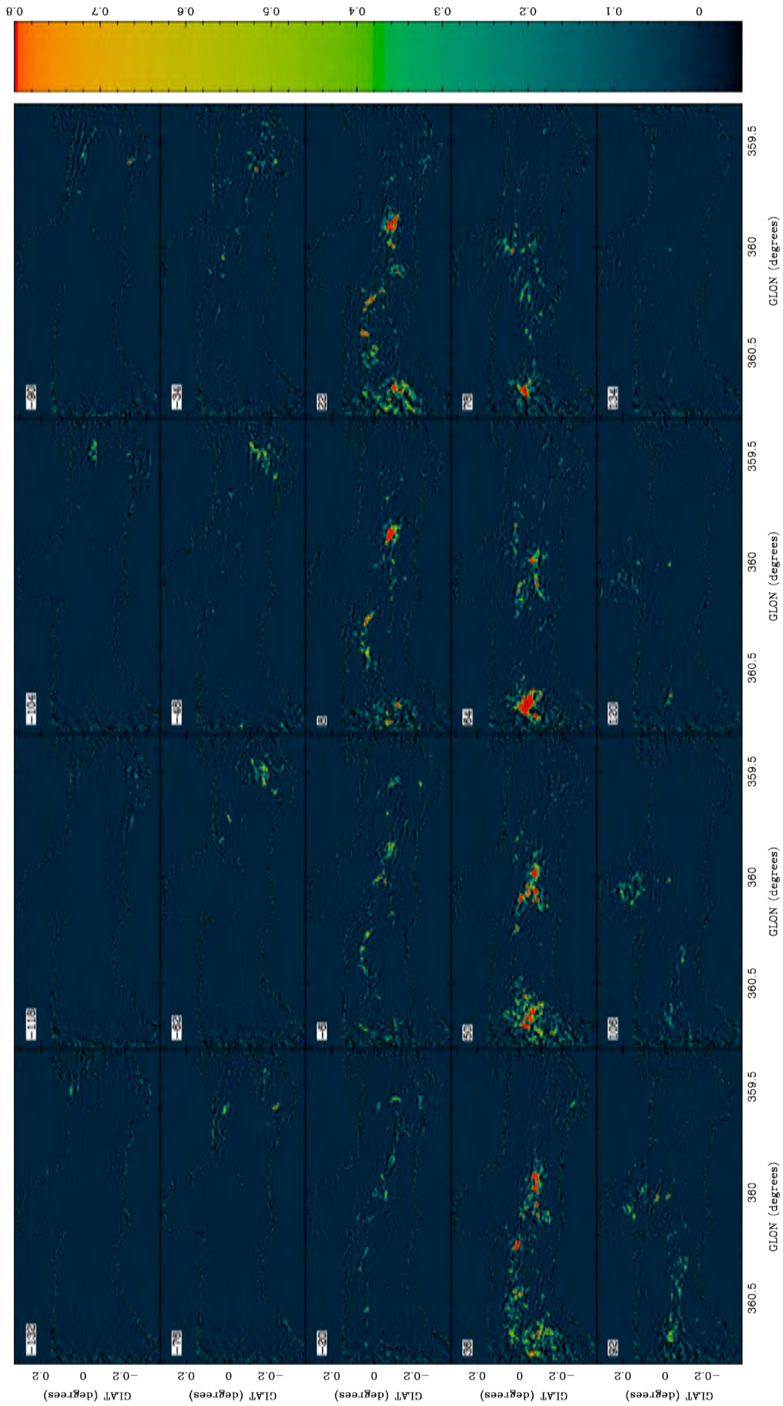

Figure A.9: Channel map of $NH_3(3,3)$

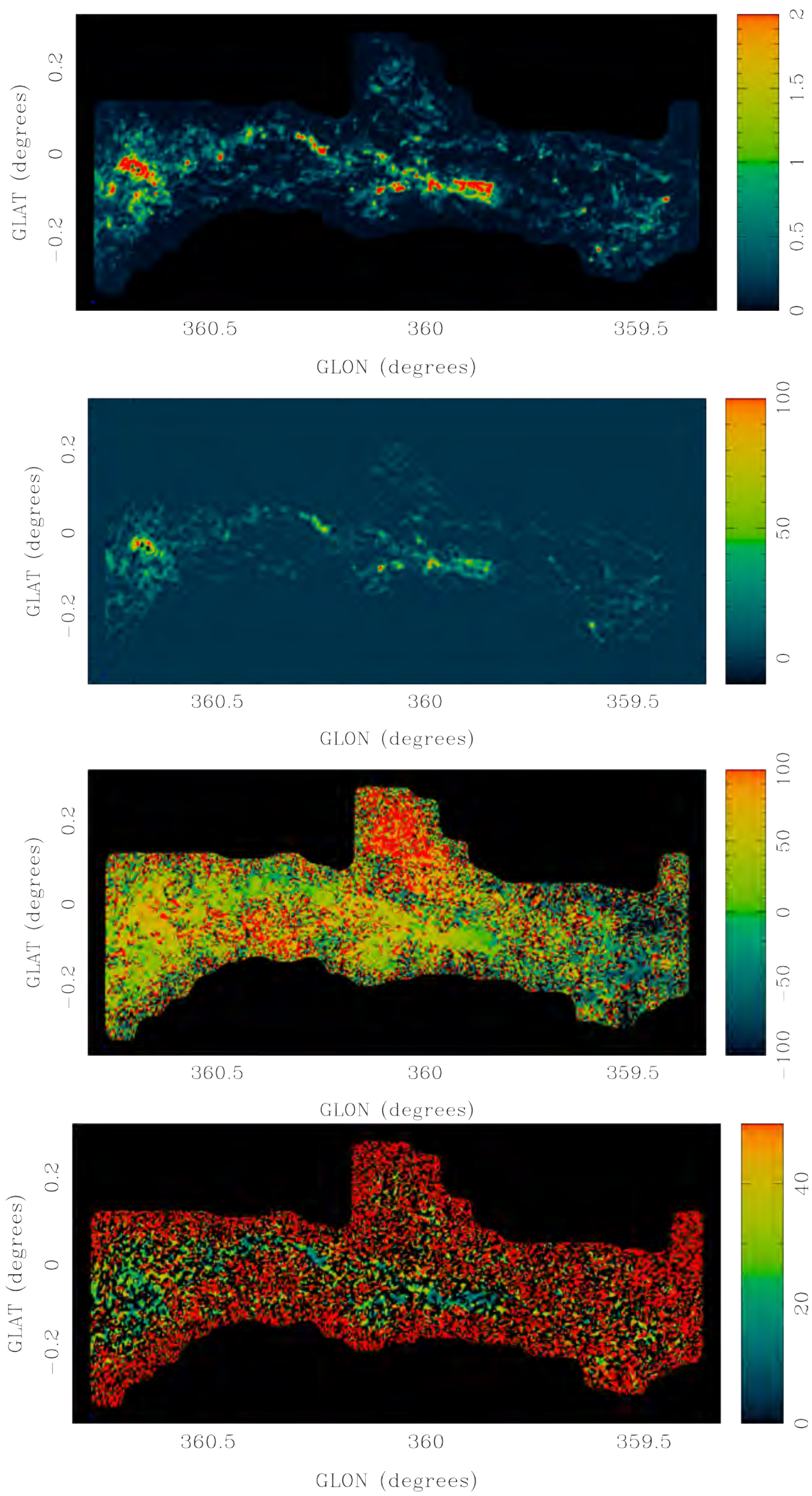

Figure A.10: NH_3(3,3) moment maps. *top to bottom*: peak intensity (moment -2), integrated intensity (moment 0), velocity (moment 1), velocity dispersion (moment 2)

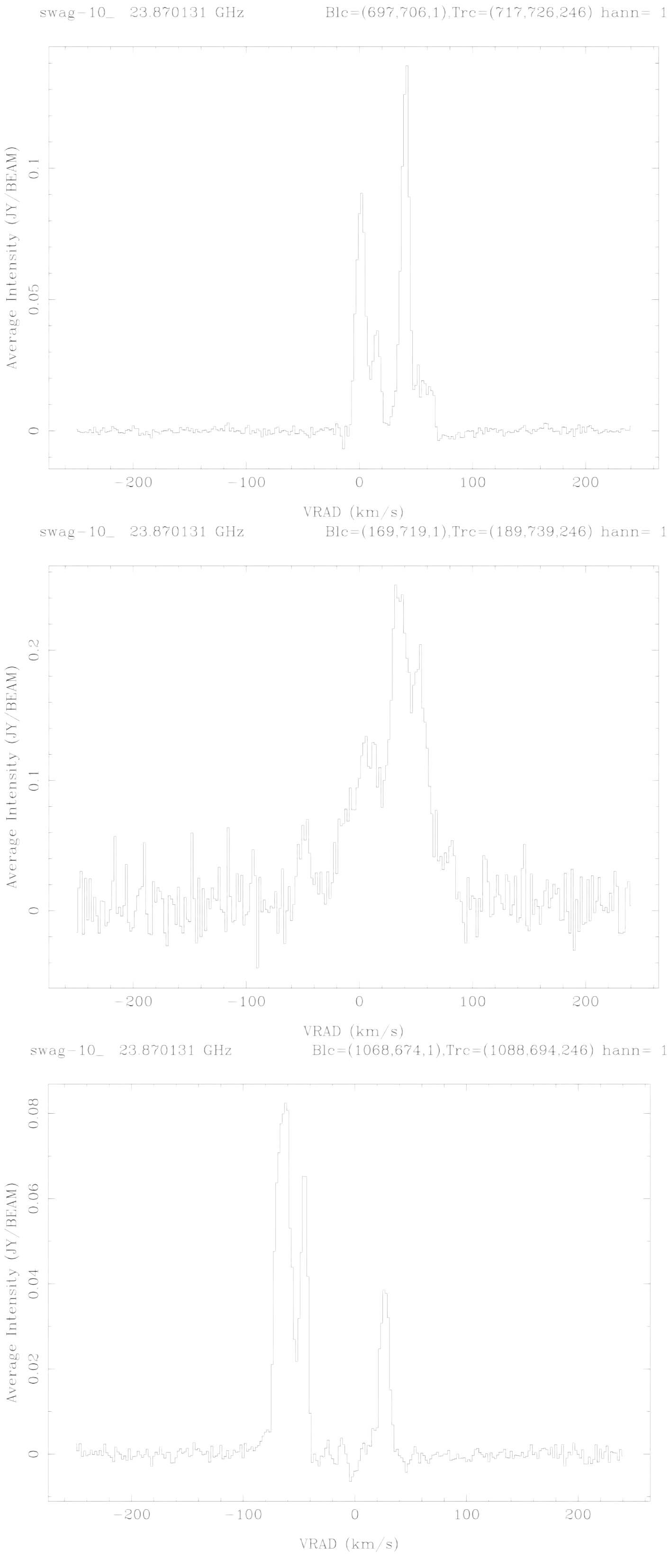

Figure A.11: NH_3(3,3) spectra. *top to bottom*: Sgr A*, B2, C

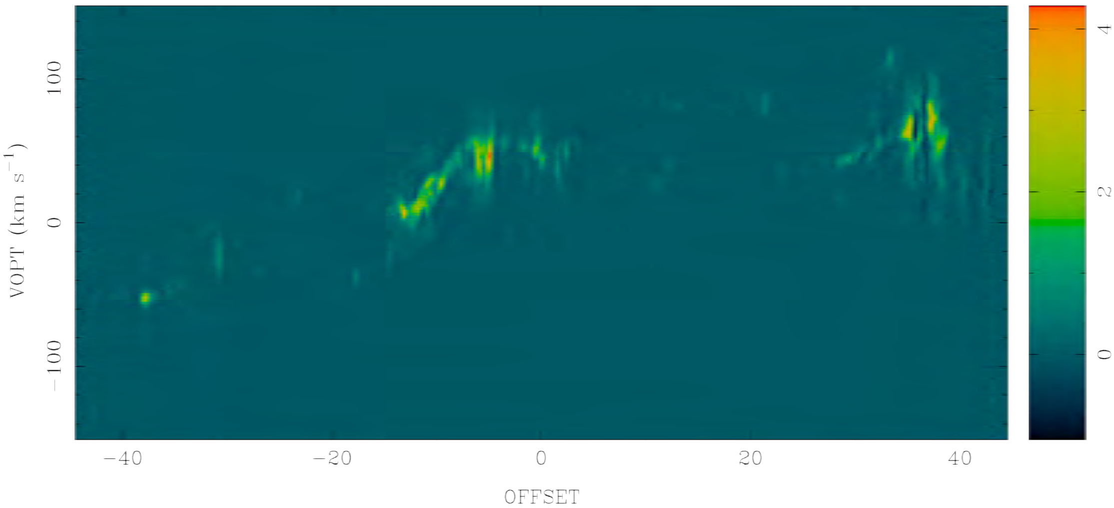

Figure A.12: $NH_3(3,3)$ position velocity diagram through Sgr B2 ($\sim -30 - -40$") and Sgr C ($\sim +35$")

A.1.0.4 $NH_3(4,4)$

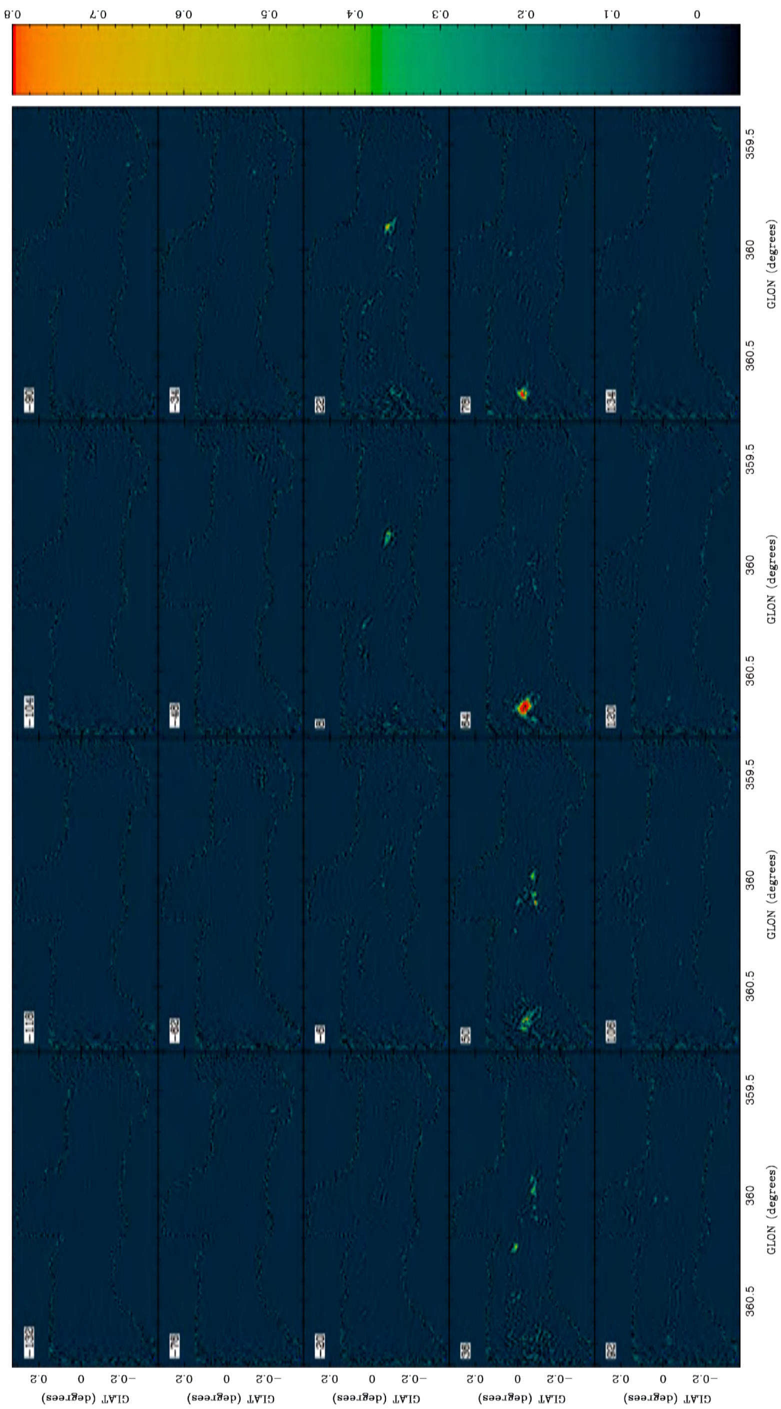

Figure A.13: Channel map of $NH_3(4,4)$

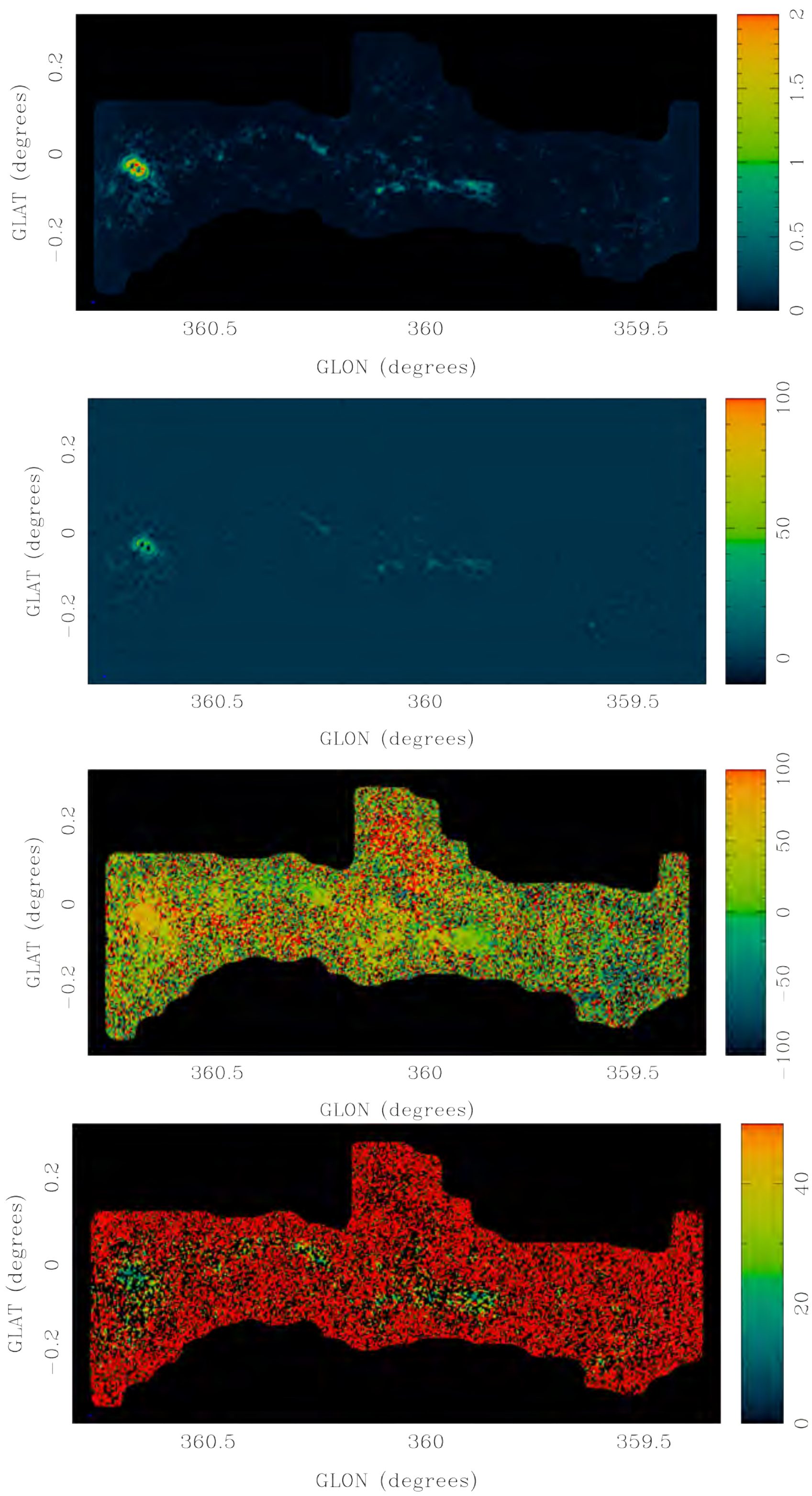

Figure A.14: NH_3(4,4) moment maps. *top to bottom*: peak intensity (moment -2), integrated intensity (moment 0), velocity (moment 1), velocity dispersion (moment 2)

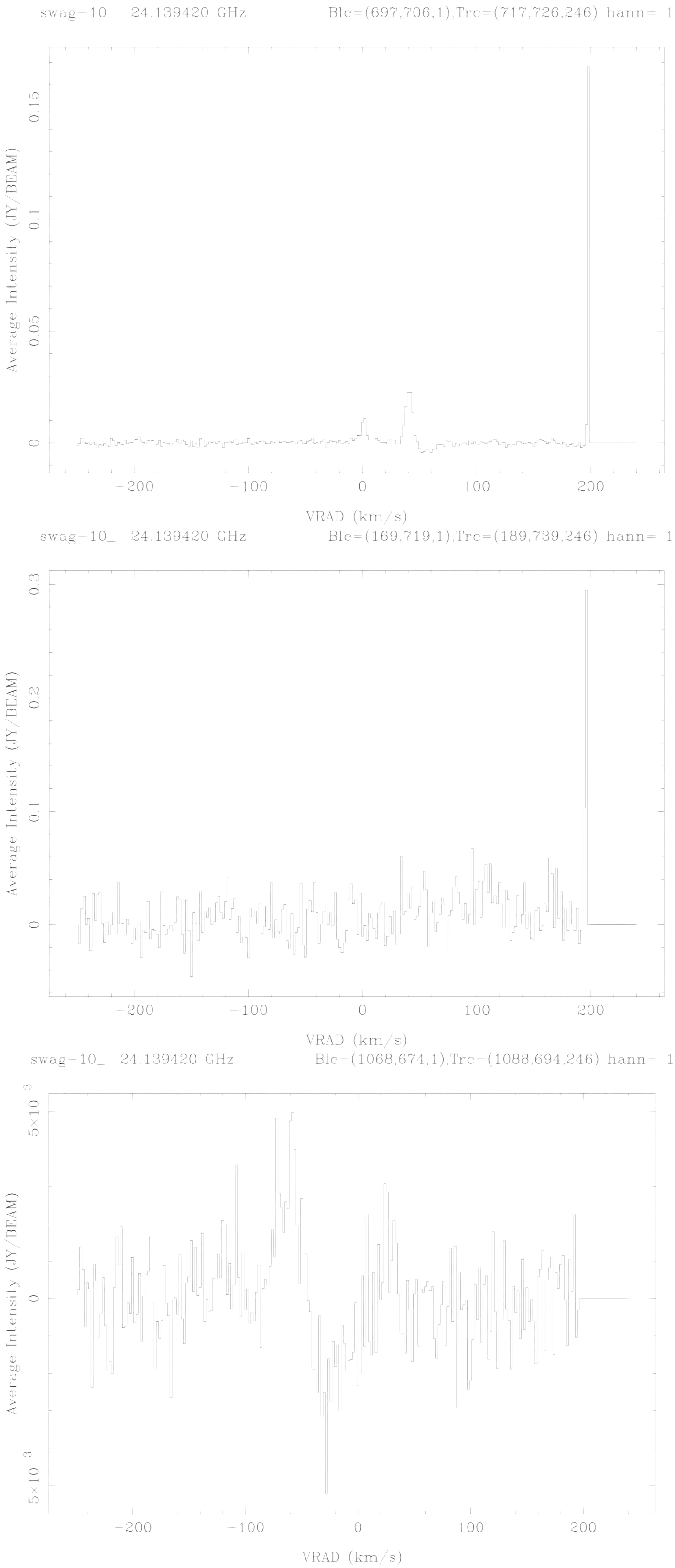

Figure A.15: NH_3(4,4) spectra. *top to bottom*: Sgr A*, B2, C

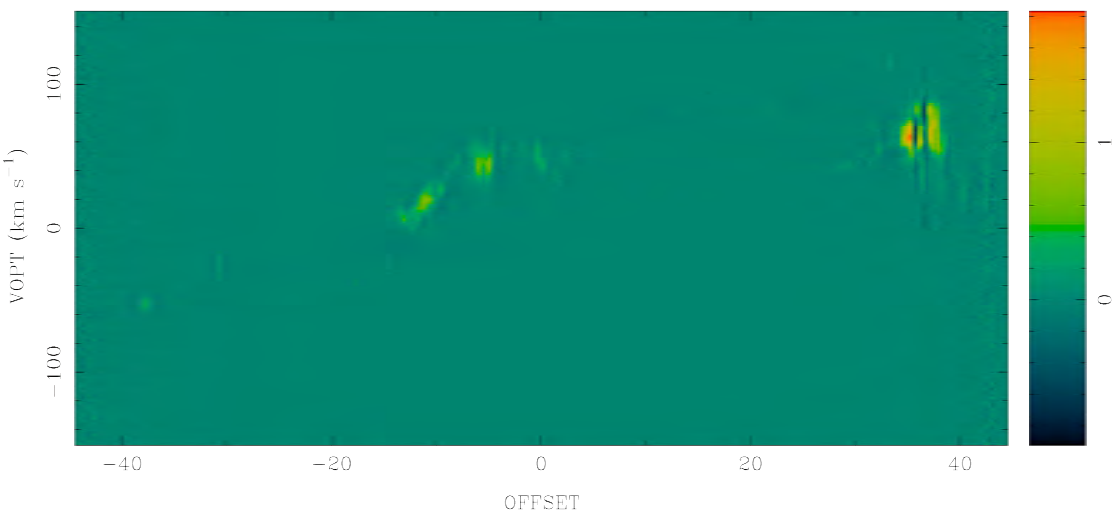

Figure A.16: NH_3(4,4) position velocity diagram through Sgr B2 ($\sim -30 - -40$") and Sgr C ($\sim +35$")

A.1.0.5 $NH_3(5,5)$

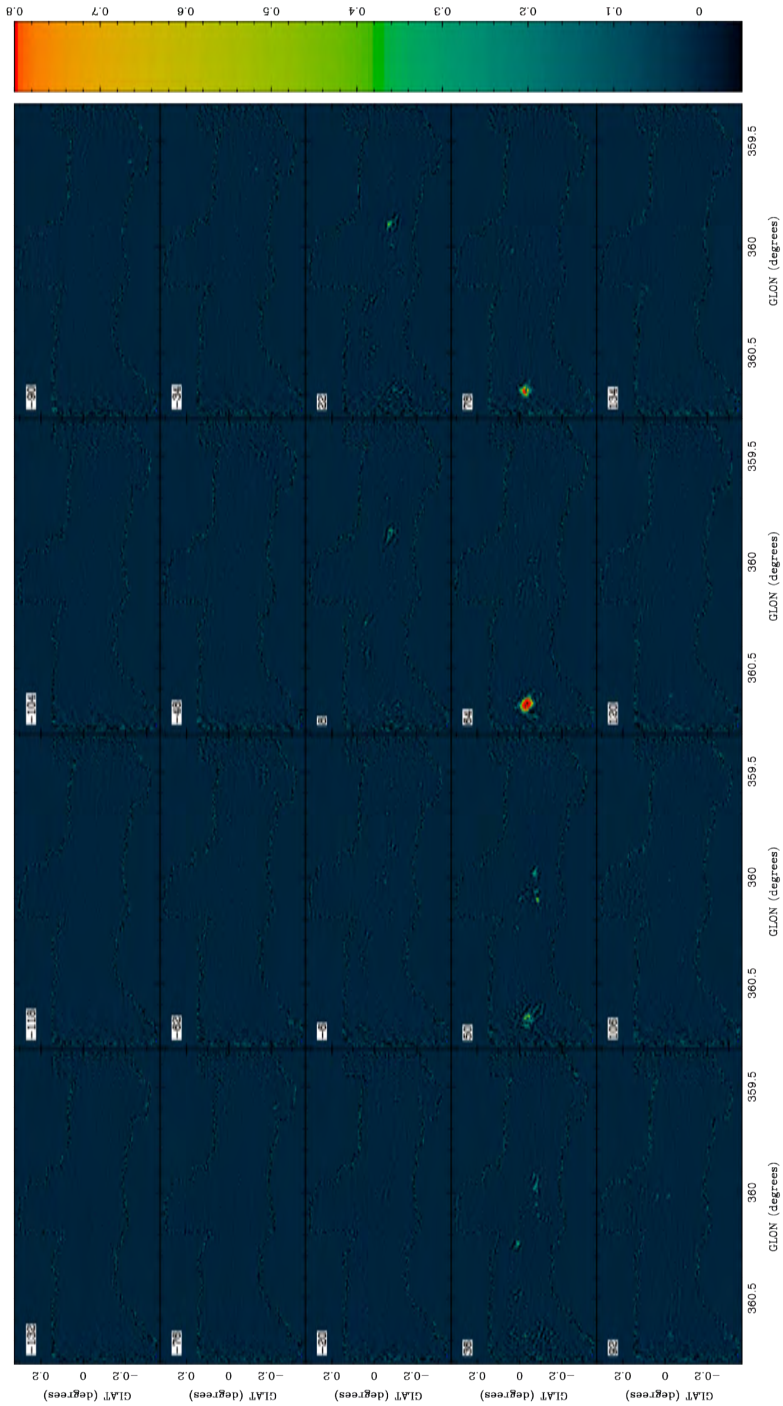

Figure A.17: Channel map of $NH_3(5,5)$

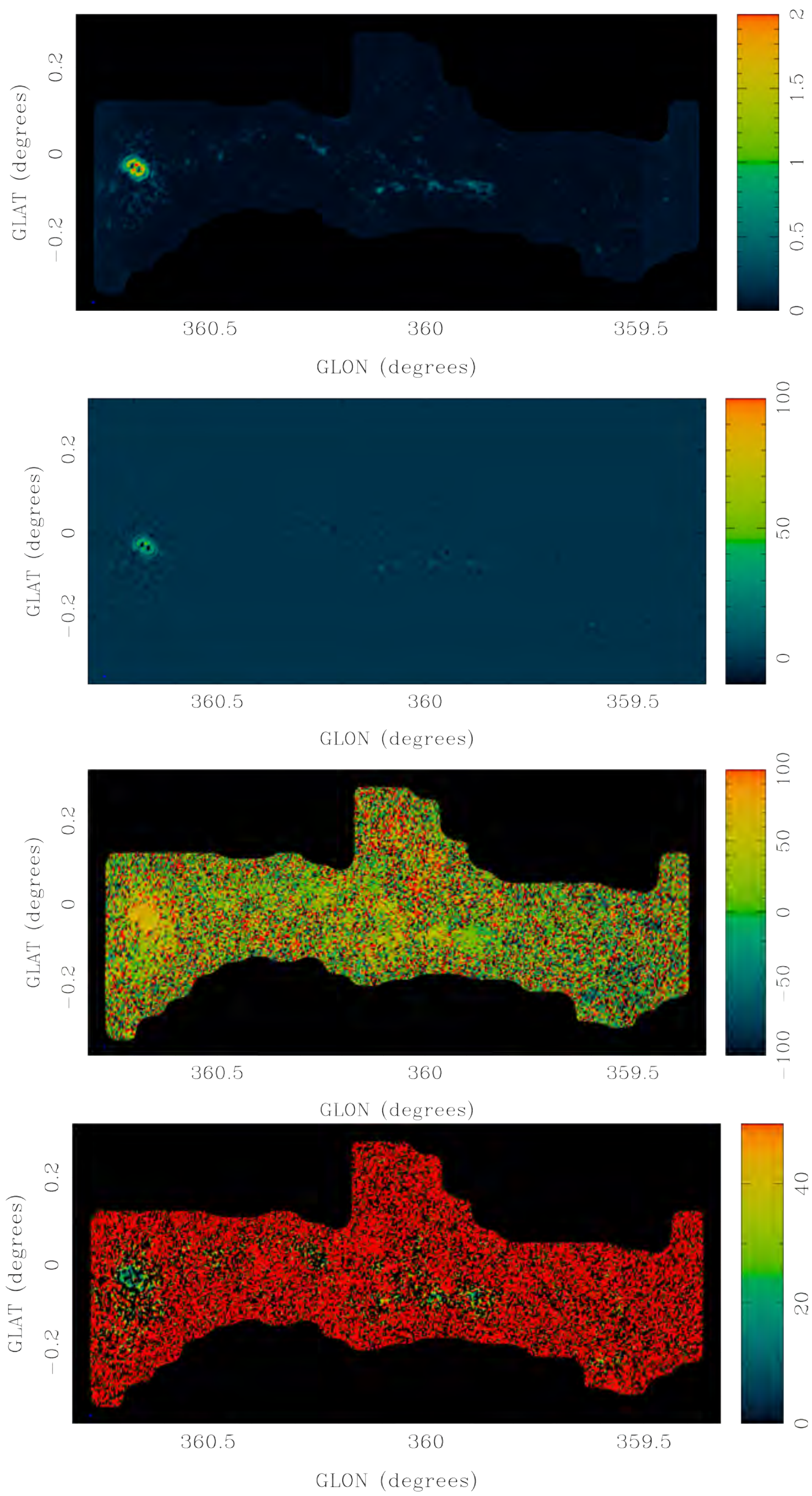

Figure A.18: NH_3(5,5) moment maps. *top to bottom*: peak intensity (moment -2), integrated intensity (moment 0), velocity (moment 1), velocity dispersion (moment 2)

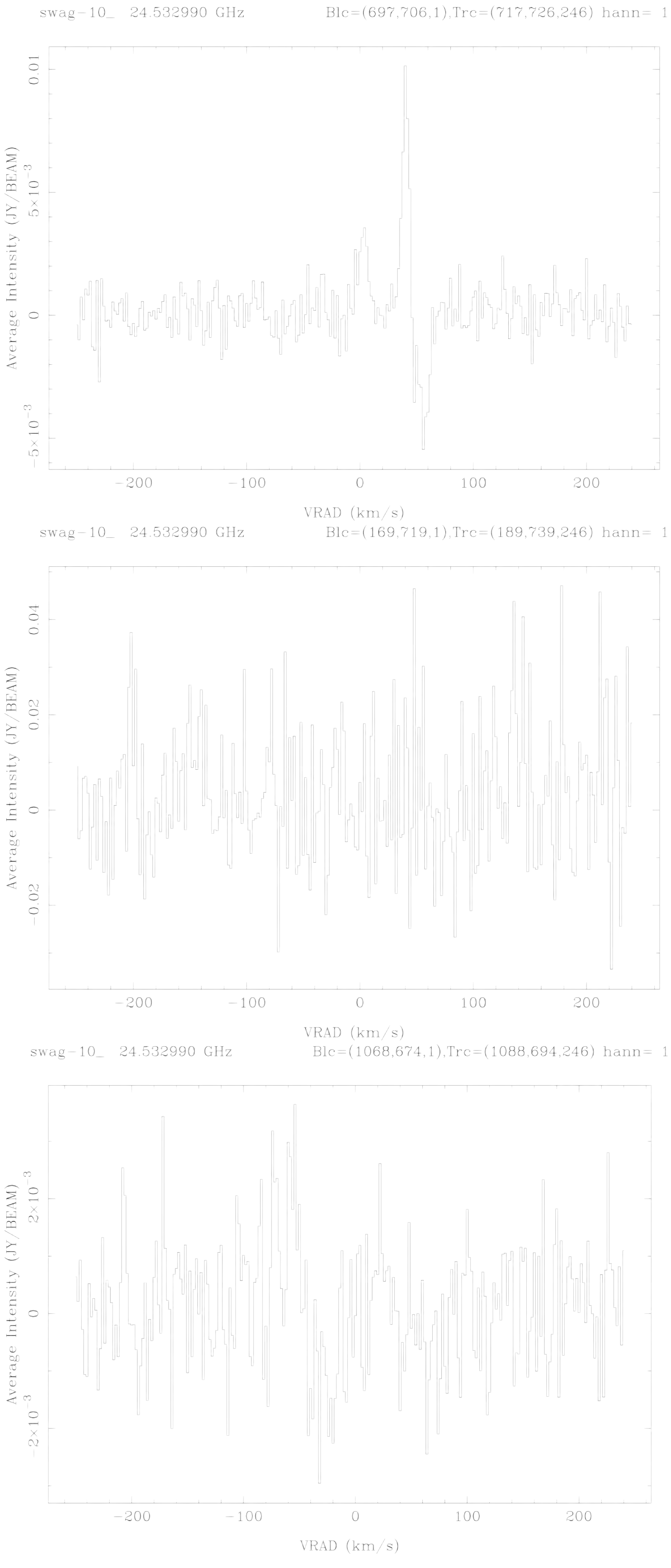

Figure A.19: $NH_3(5,5)$ spectra. *top to bottom*: Sgr A*, B2, C

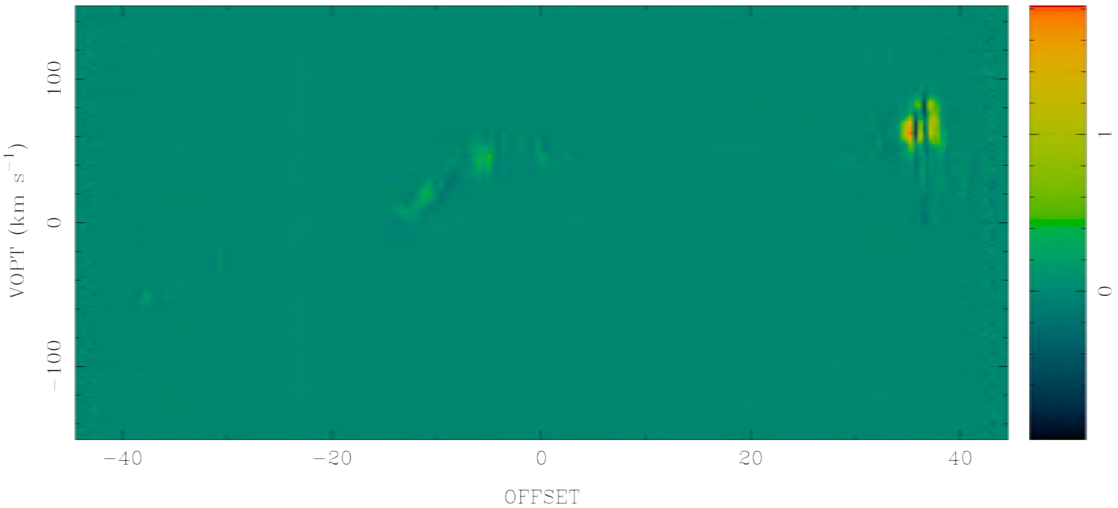

Figure A.20: $NH_3(5,5)$ position velocity diagram through Sgr B2 ($\sim -30 - -40$") and Sgr C ($\sim +35$")

A.1.0.6 $NH_3(6,6)$

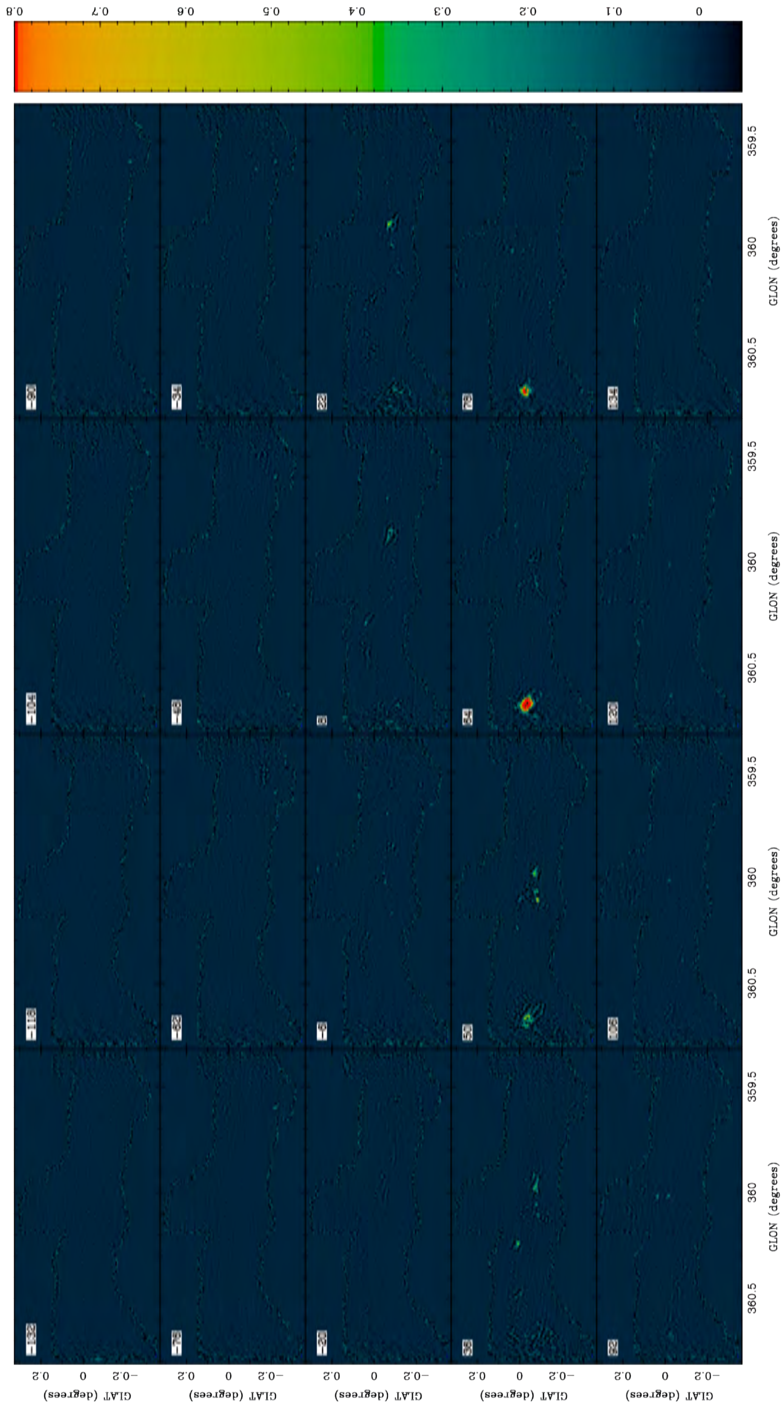

Figure A.21: Channel map of $NH_3(6,6)$

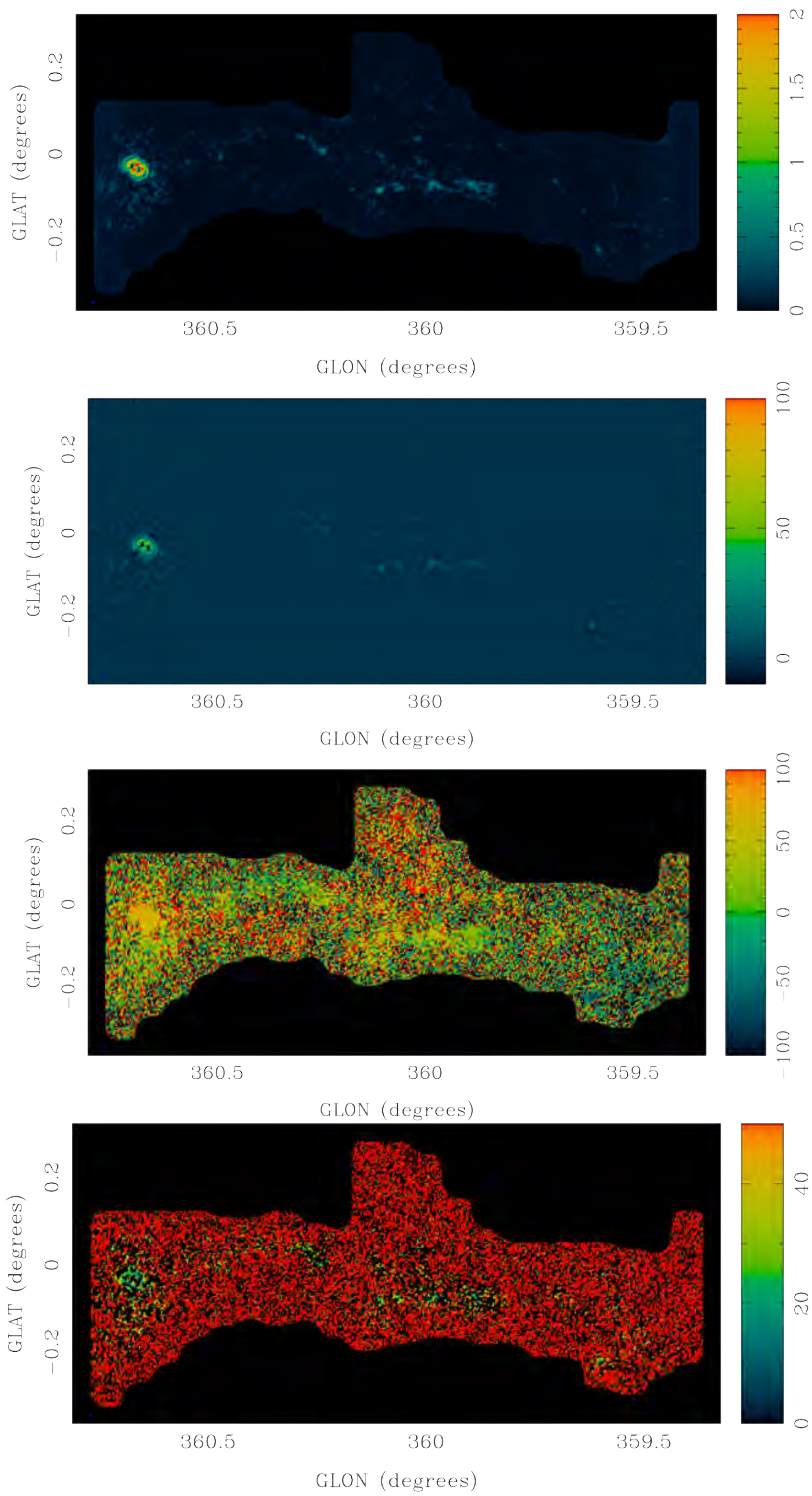

Figure A.22: NH_3(6,6) moment maps. *top to bottom*: peak intensity (moment -2), integrated intensity (moment 0), velocity (moment 1), velocity dispersion (moment 2)

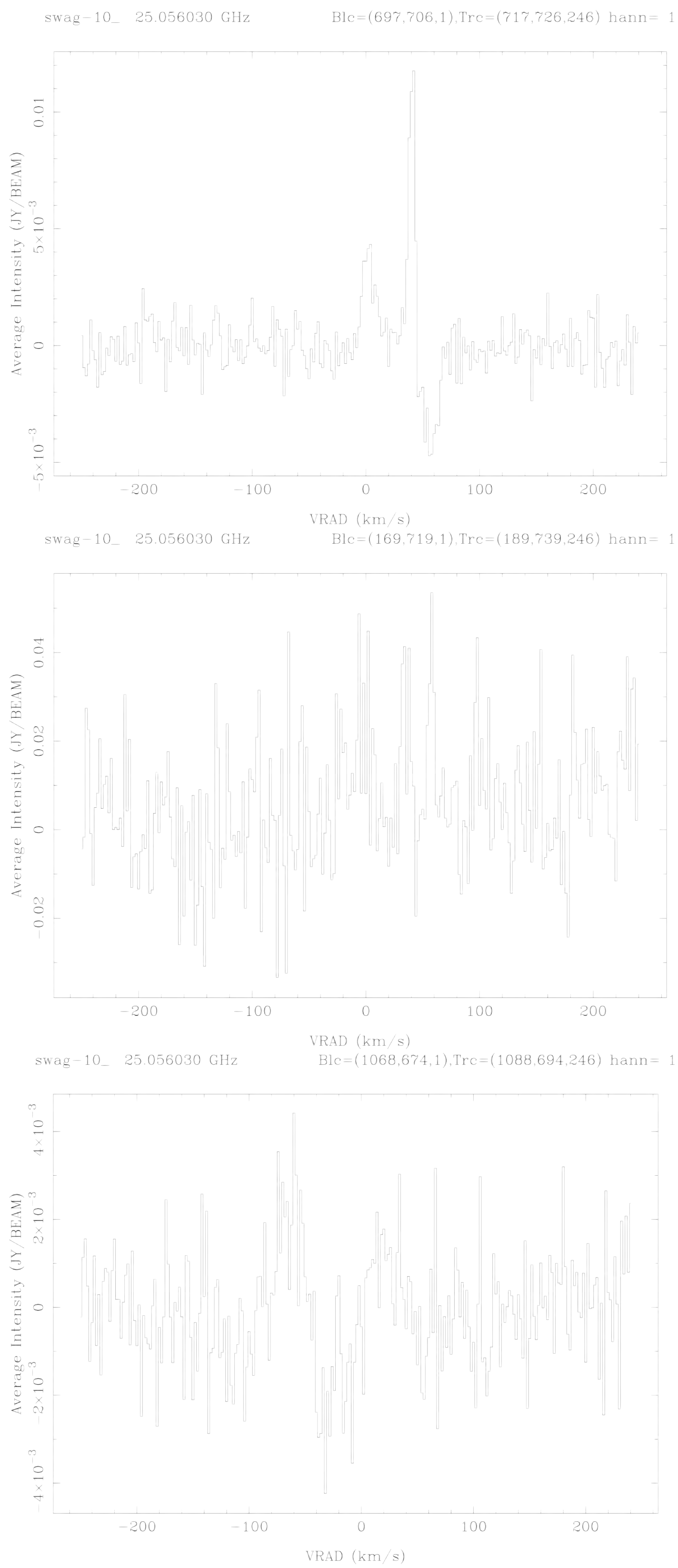

Figure A.23: NH_3(6,6) spectra. *top to bottom*: Sgr A*, B2, C

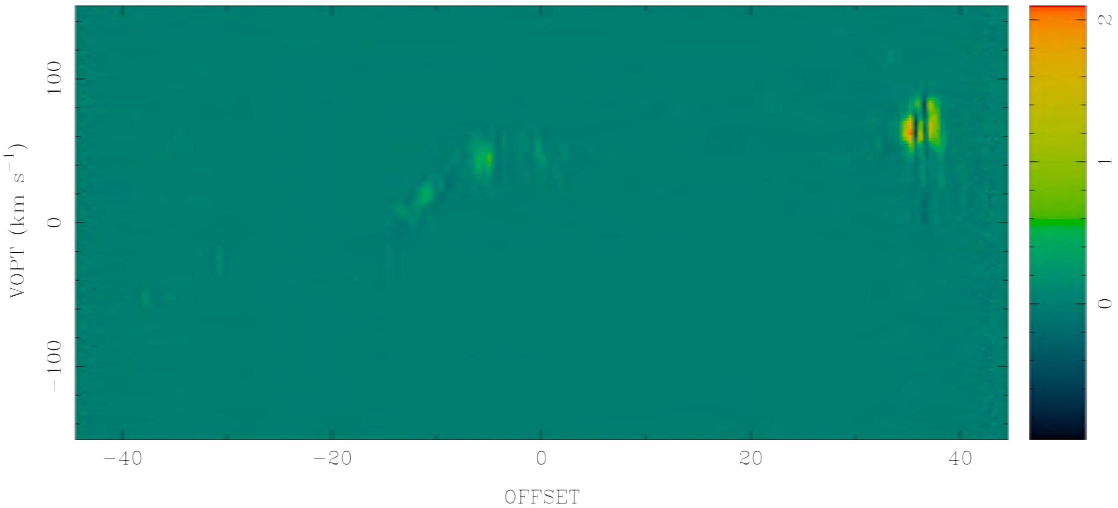

Figure A.24: NH_3(6,6) position velocity diagram through Sgr B2 ($\sim -30 - -40$") and Sgr C ($\sim +35$")

A.1.0.7 $H_{66}\alpha$

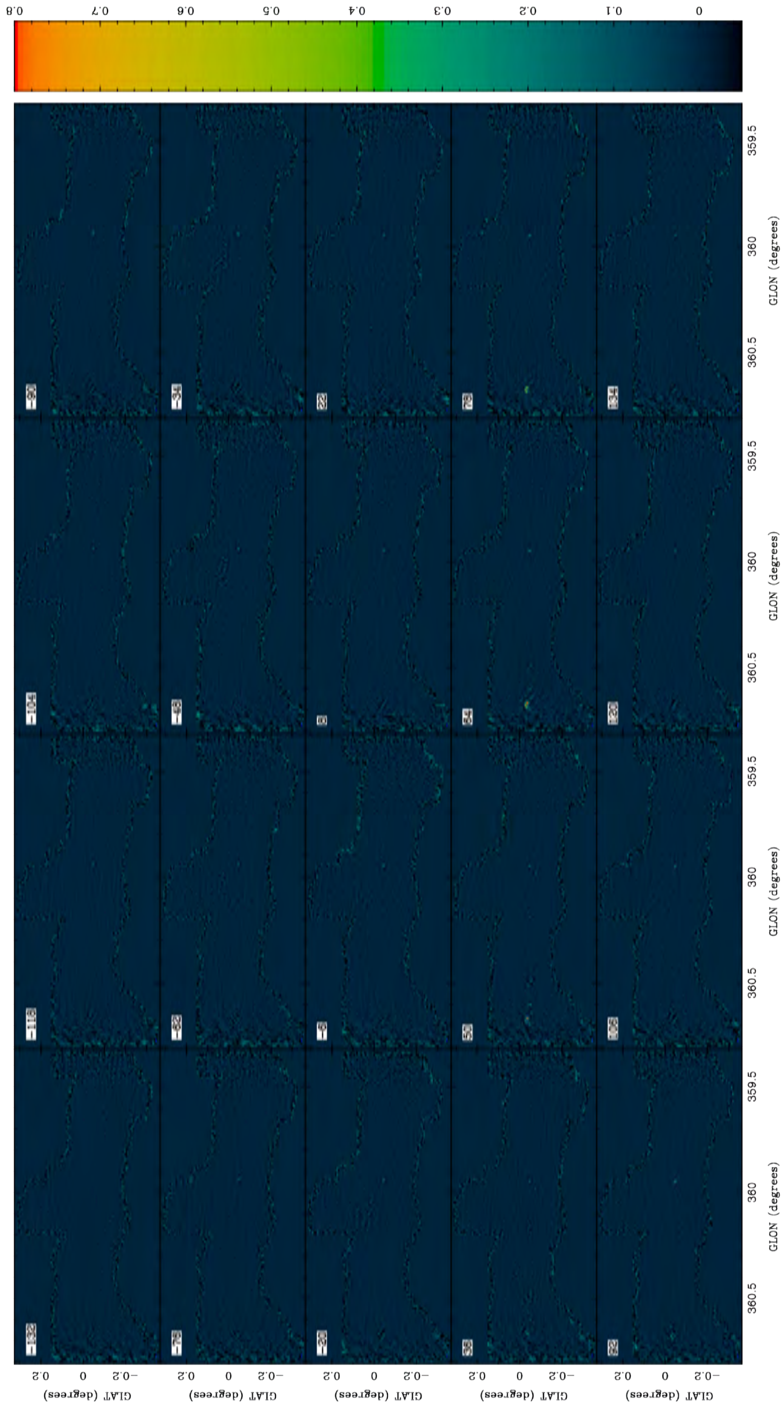

Figure A.25: Channel map of $H_{66}\alpha$

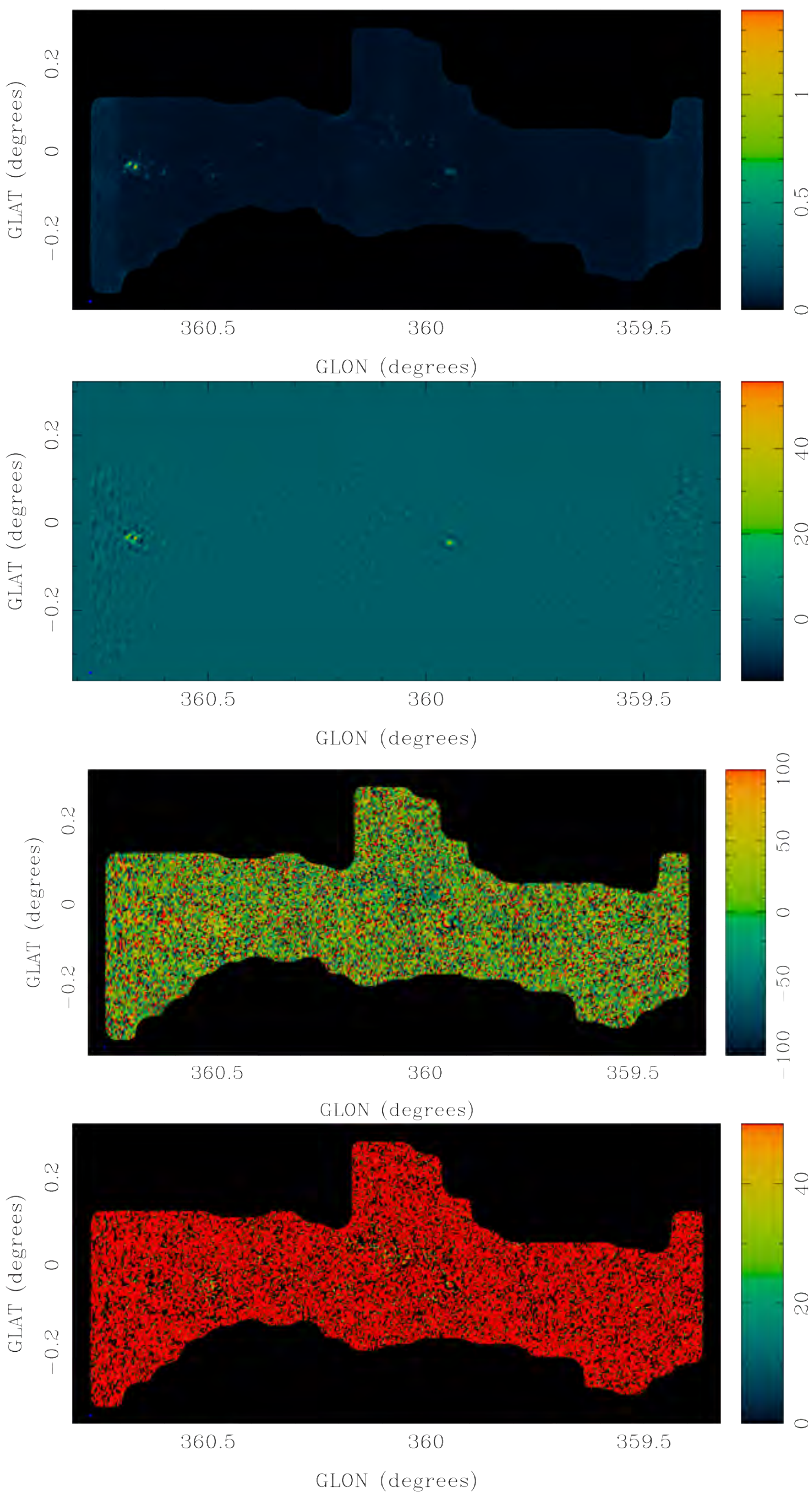

Figure A.26: $H_{66}\alpha$ moment maps. *top to bottom*: peak intensity (moment -2), integrated intensity (moment 0), velocity (moment 1), velocity dispersion (moment 2)

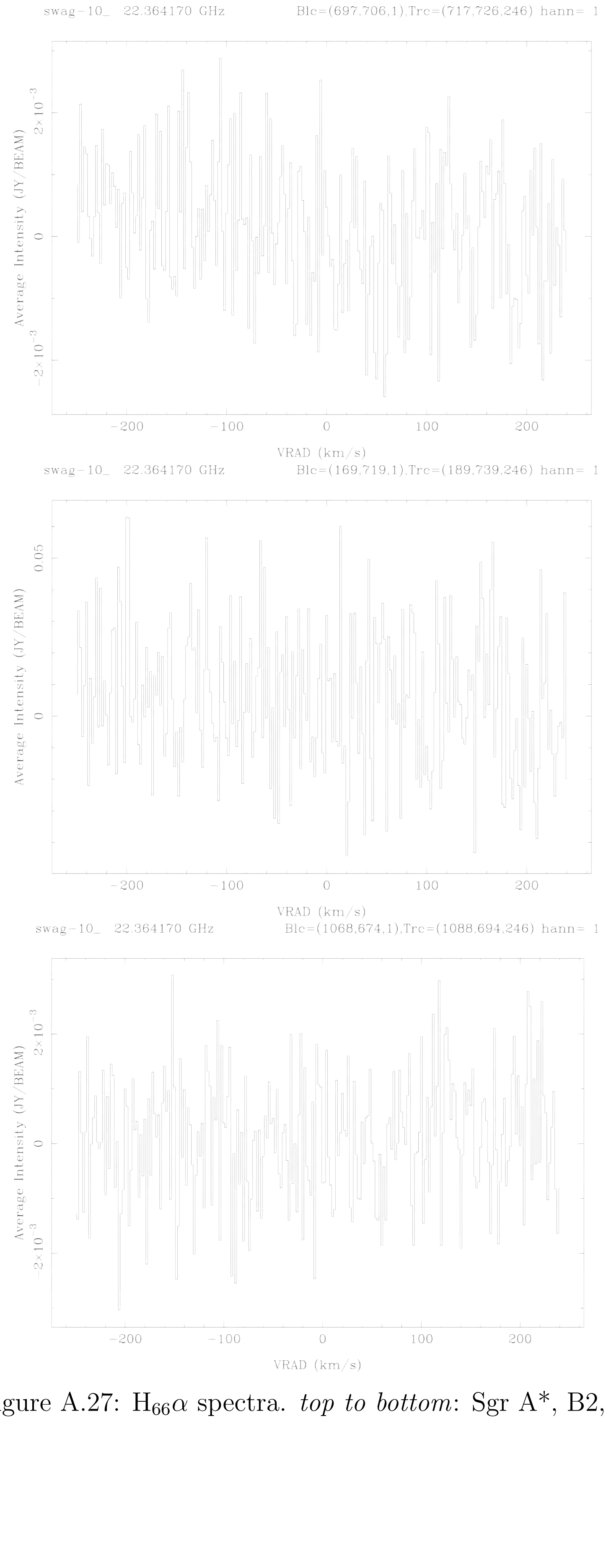

Figure A.27: $H_{66}\alpha$ spectra. *top to bottom*: Sgr A*, B2, C

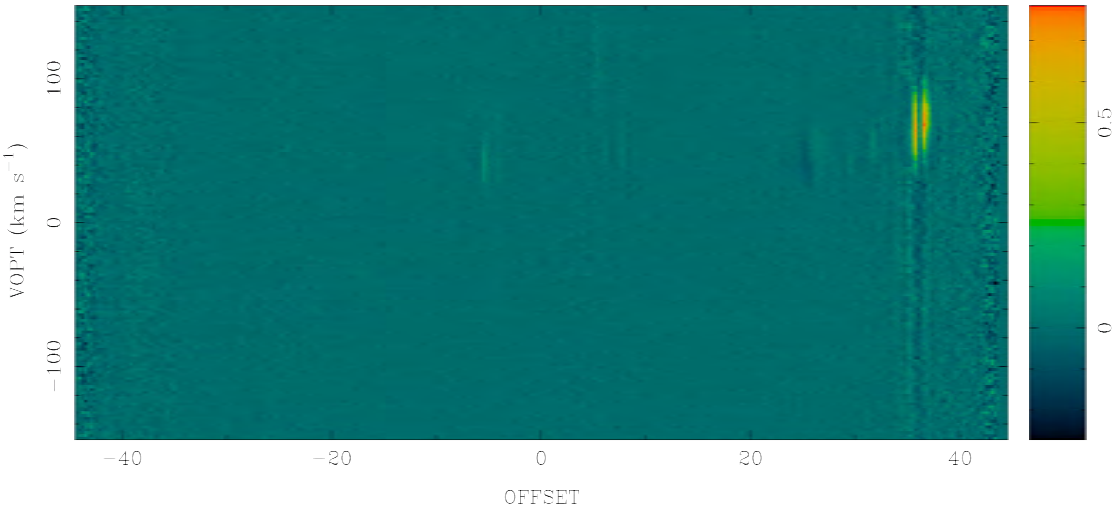

Figure A.28: $H_{66}\alpha$ position velocity diagram through Sgr B2 ($\sim -30 - -40$") and Sgr C ($\sim +35$")

A.1.0.8 $C_{64}\alpha$

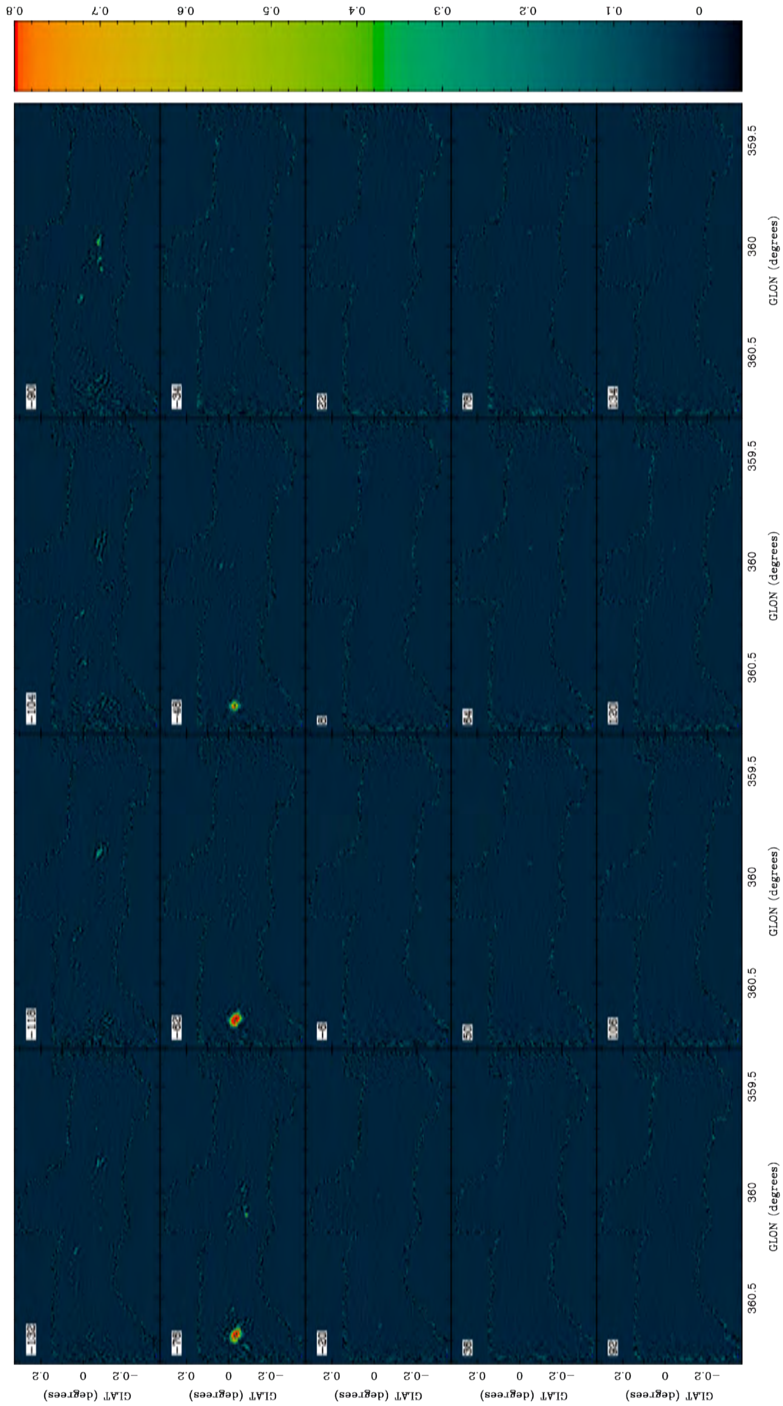

Figure A.29: Channel map of $C_{64}\alpha$

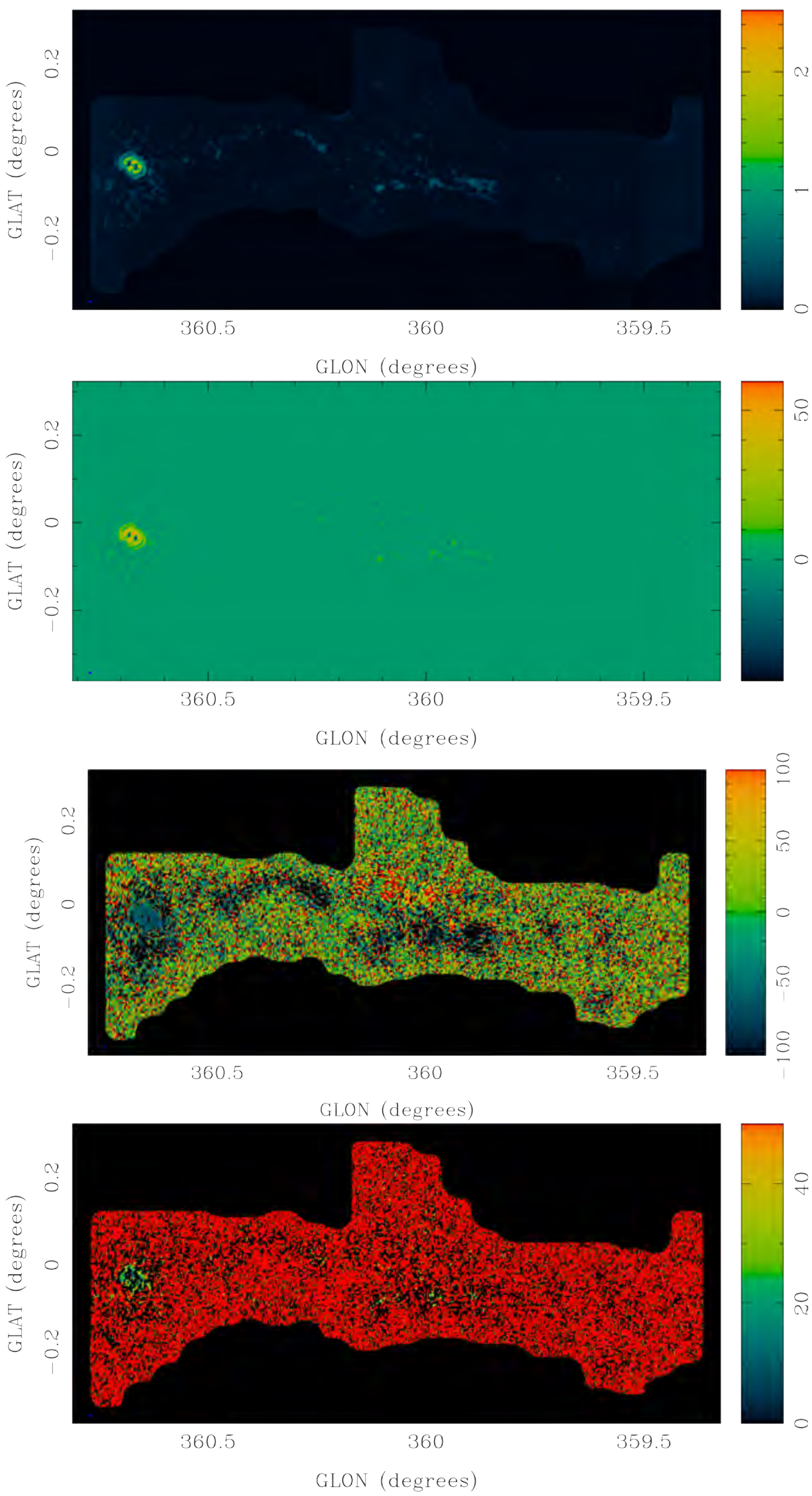

Figure A.30: $C_{64}\alpha$ moment maps. *top to bottom*: peak intensity (moment -2), integrated intensity (moment 0), velocity (moment 1), velocity dispersion (moment 2)

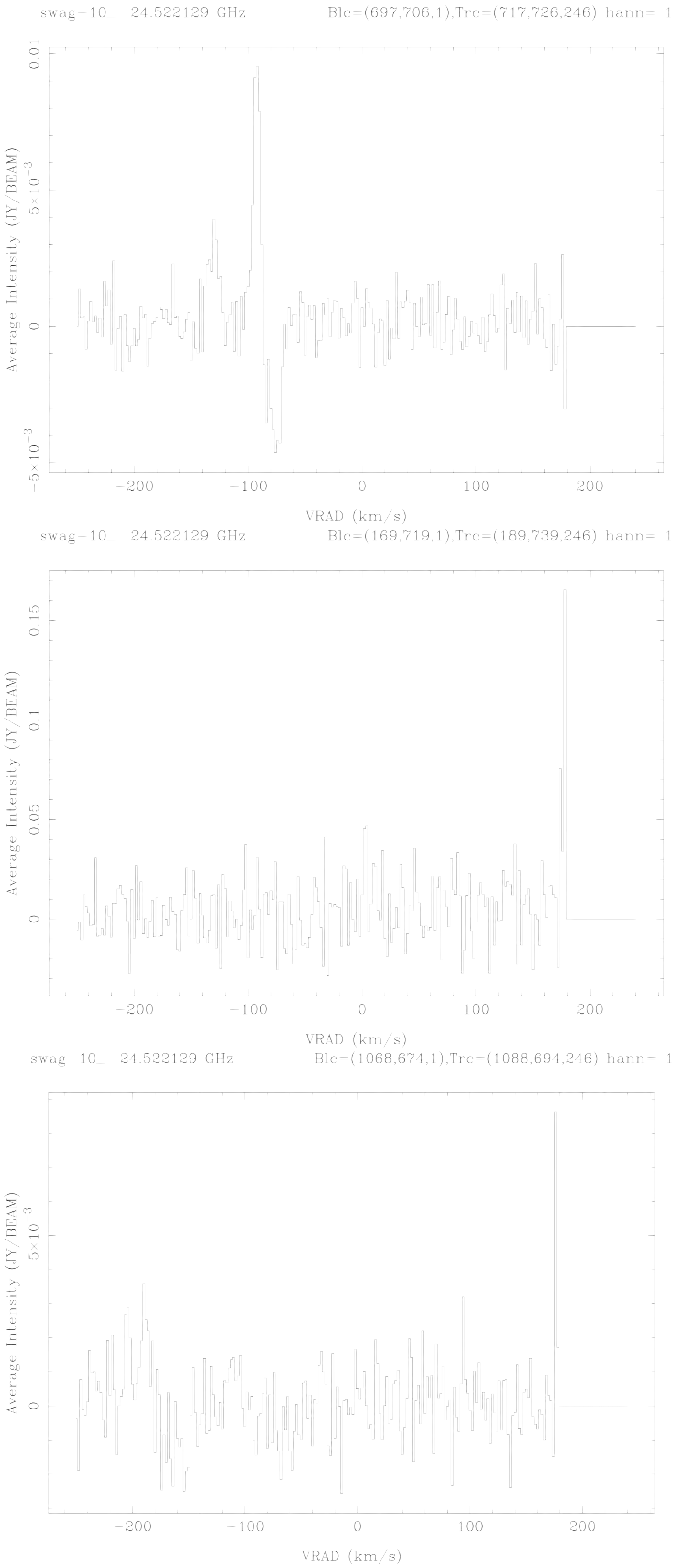

Figure A.31: $C_{64}\alpha$ spectra. *top to bottom*: Sgr A*, B2, C

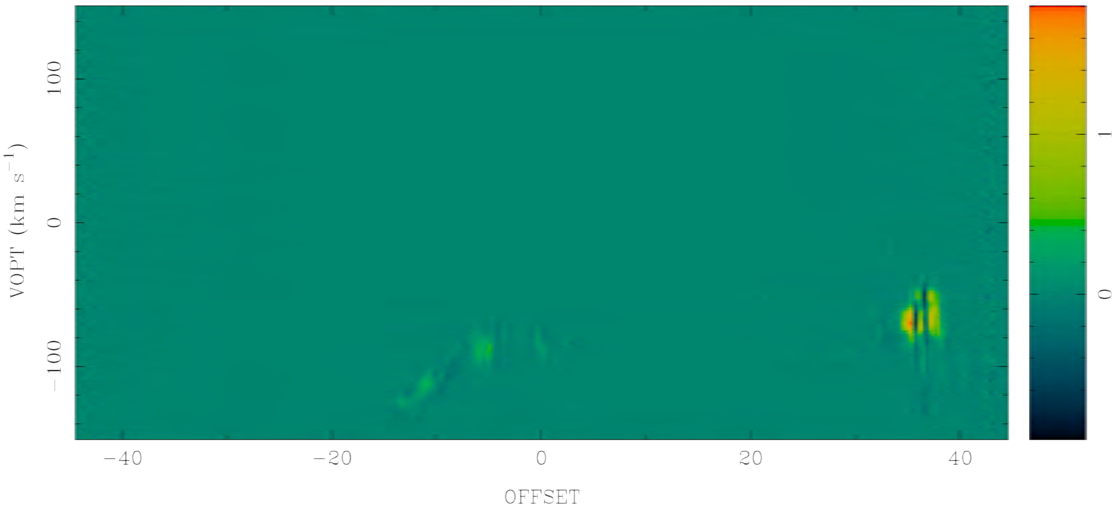

Figure A.32: $C_{64}\alpha$ position velocity diagram through Sgr B2 ($\sim -30--40$") and Sgr C ($\sim +35$")

A.1.0.9 H_2O

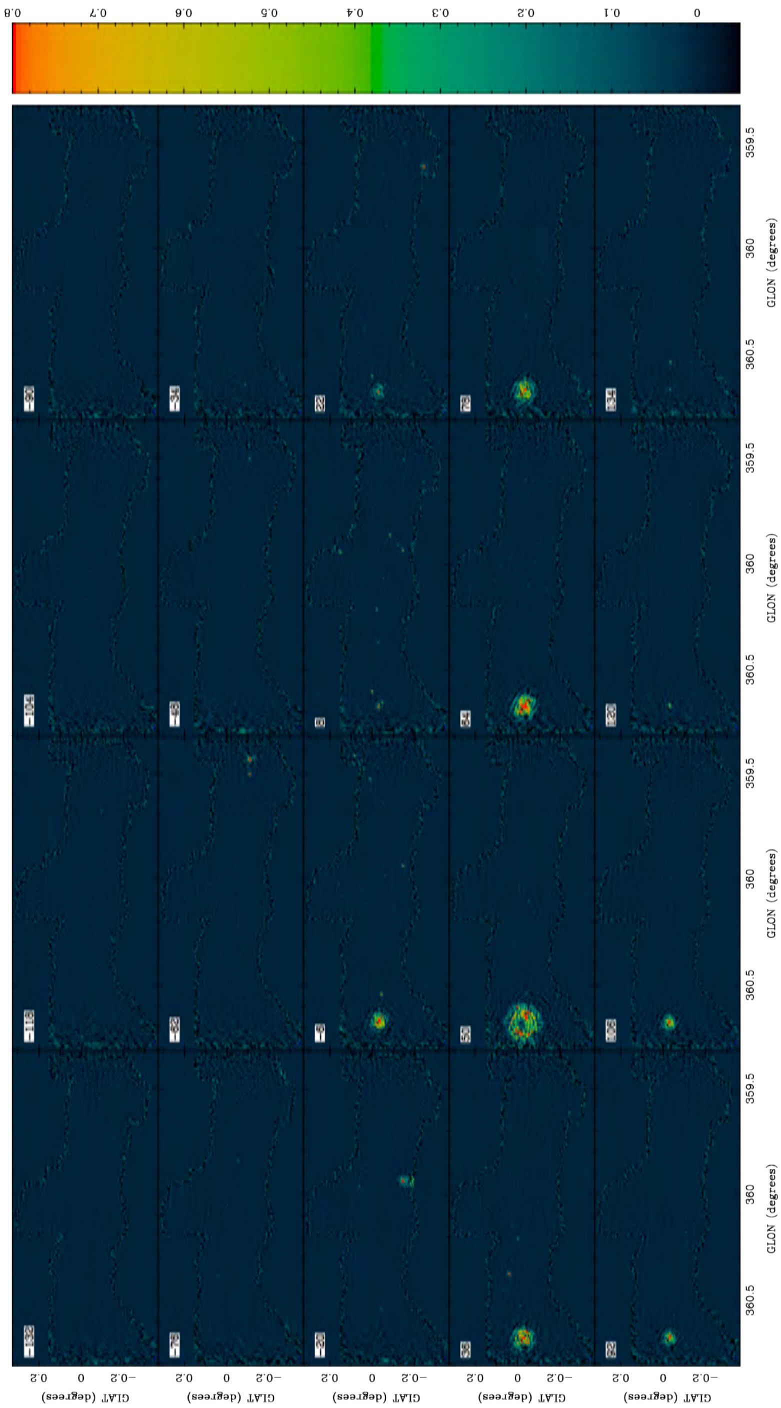

Figure A.33: Channel map of H_2O

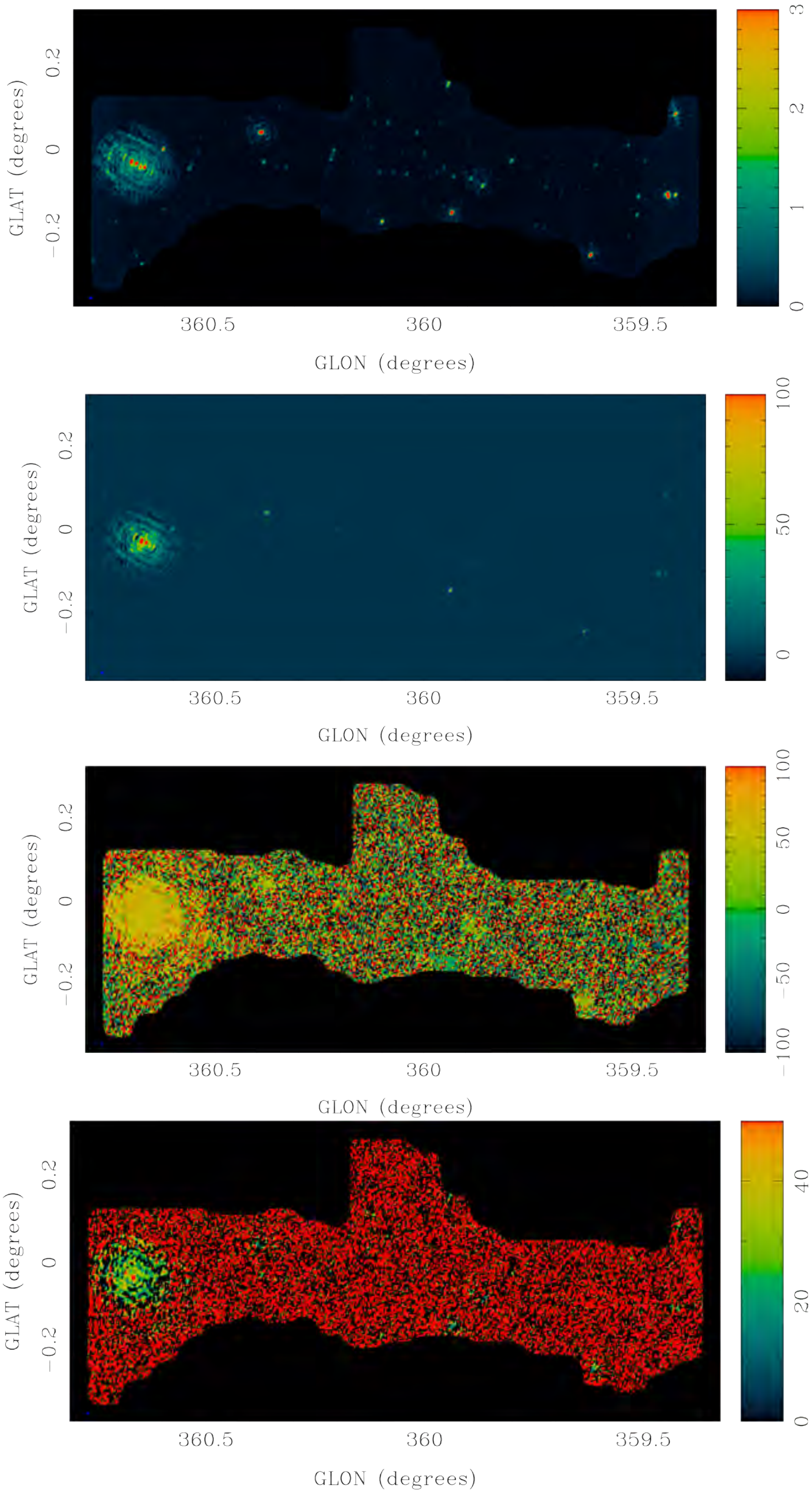

Figure A.34: H_2O moment maps. *top to bottom*: peak intensity (moment -2), integrated intensity (moment 0), velocity (moment 1), velocity dispersion (moment 2)

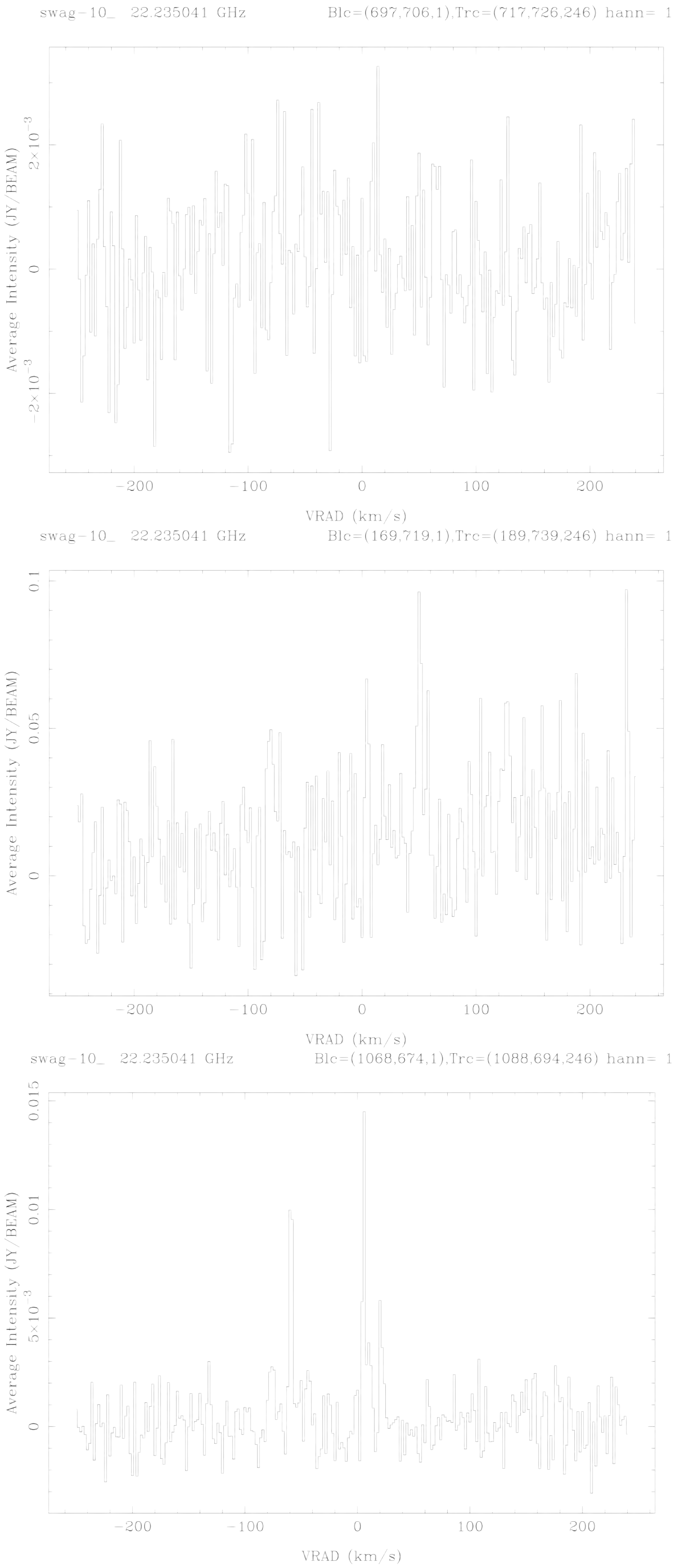

Figure A.35: H_2O spectra. *top to bottom*: Sgr A*, B2, C

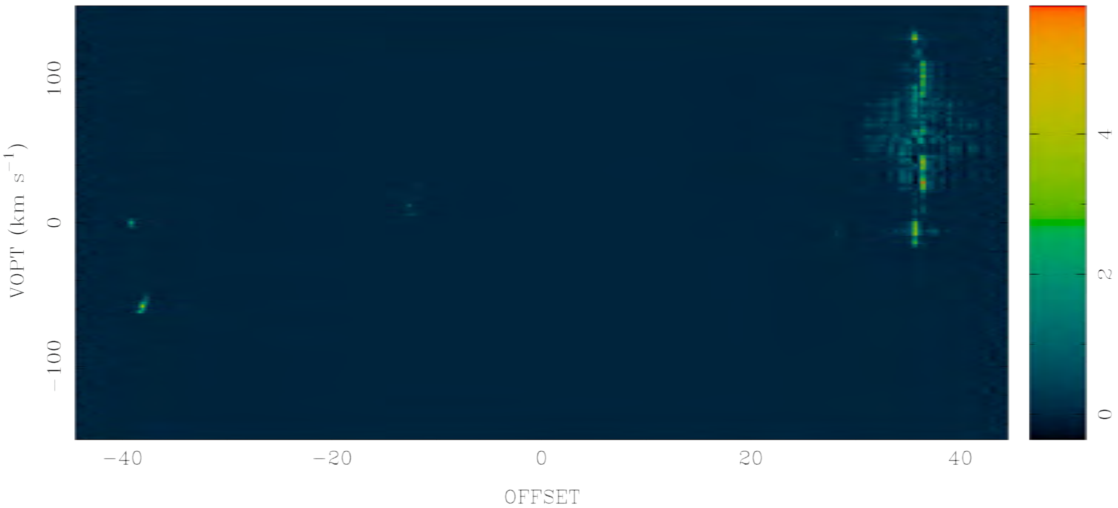

Figure A.36: H_2O position velocity diagram through Sgr B2 ($\sim -30 - -40$") and Sgr C ($\sim +35$")

A.1.0.10 OH

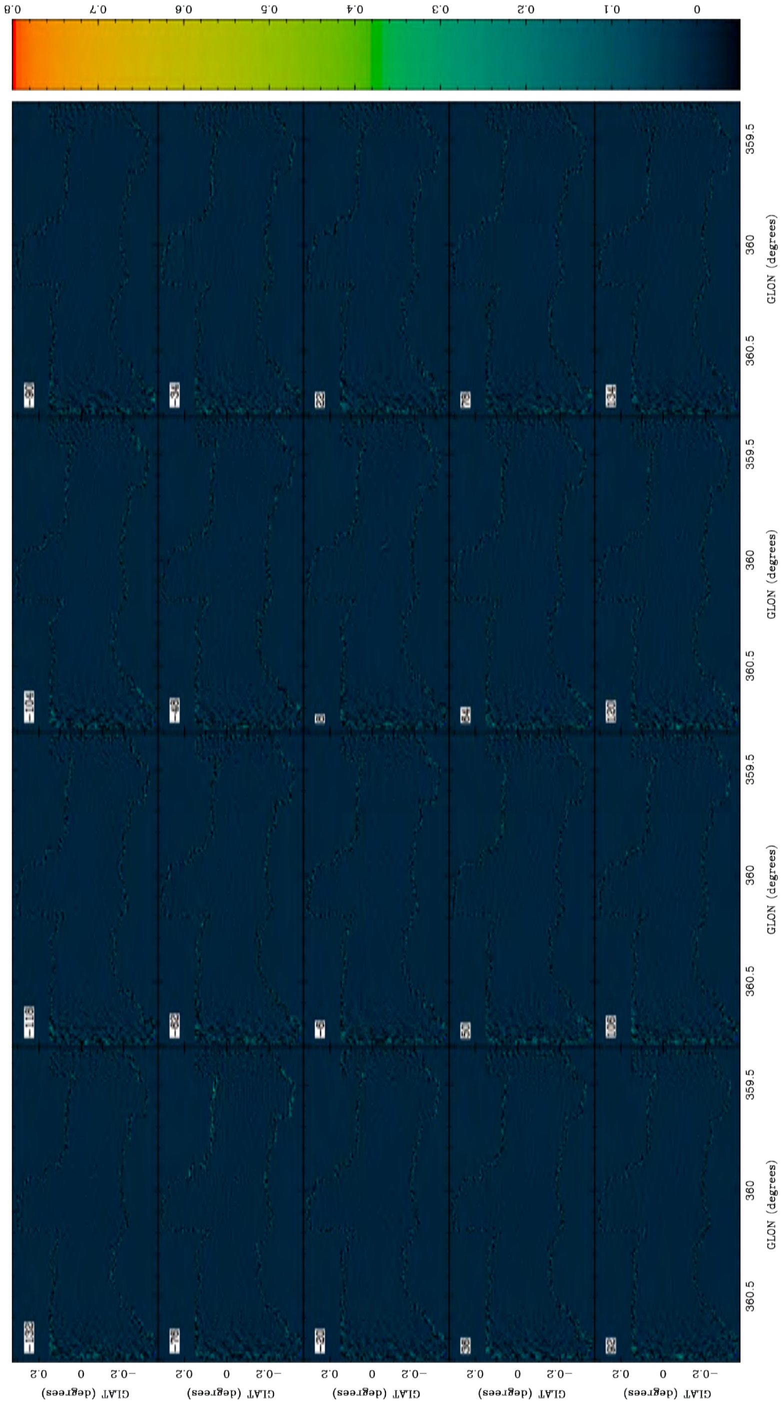

Figure A.37: Channel map of OH

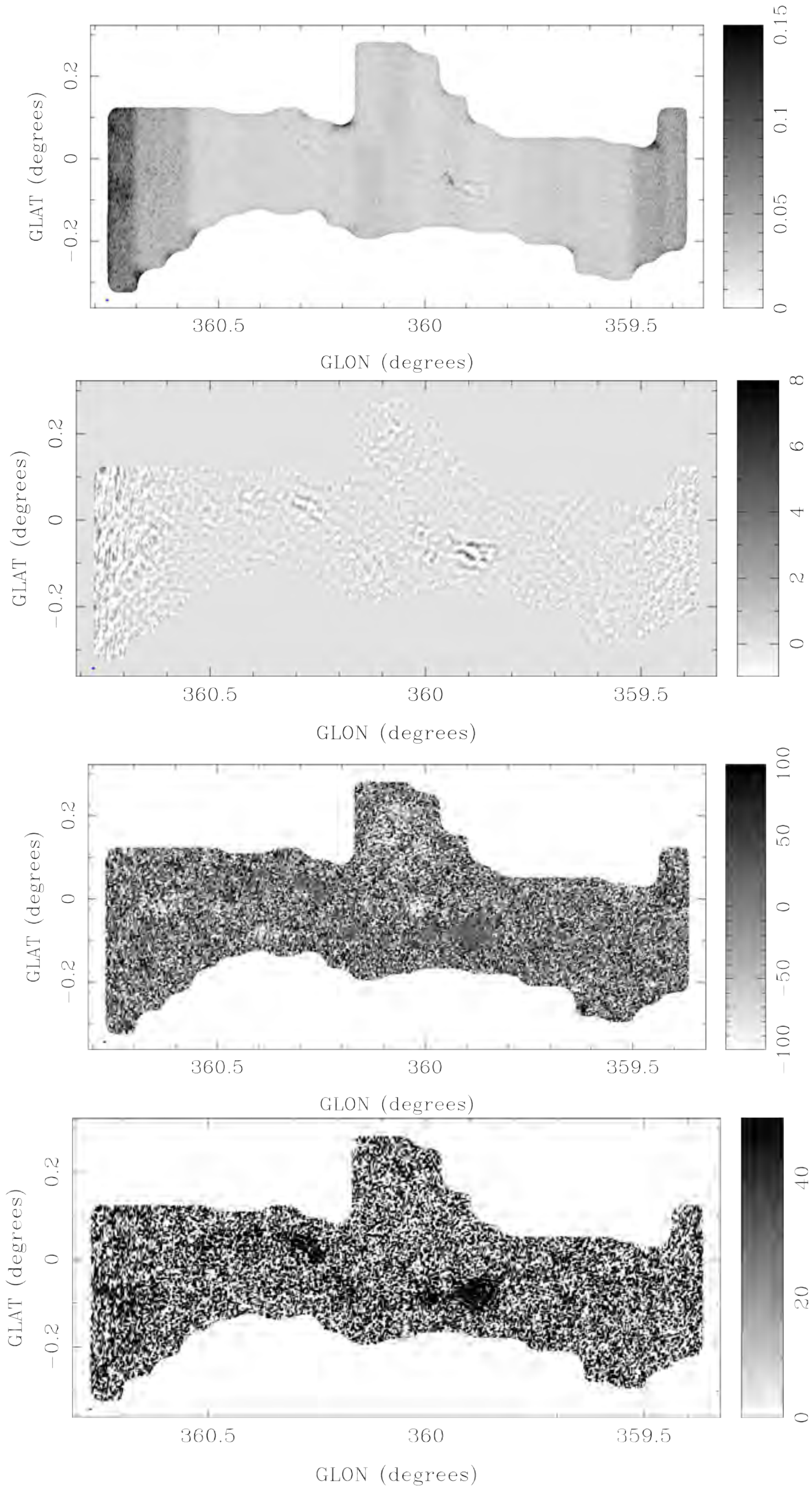

Figure A.38: OH moment maps. *top to bottom*: peak intensity (moment -2), integrated intensity (moment 0), velocity (moment 1), velocity dispersion (moment 2)

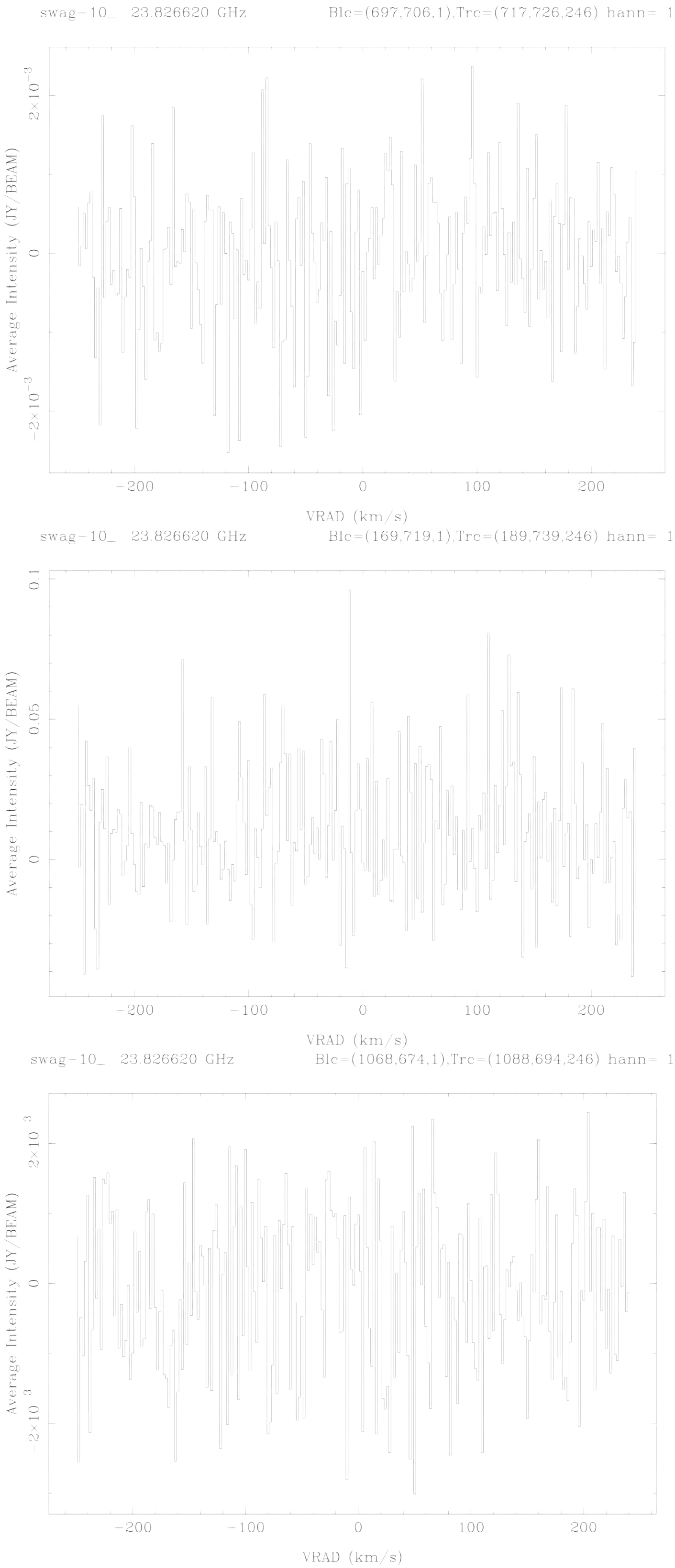

Figure A.39: OH spectra. *top to bottom*: Sgr A*, B2, C

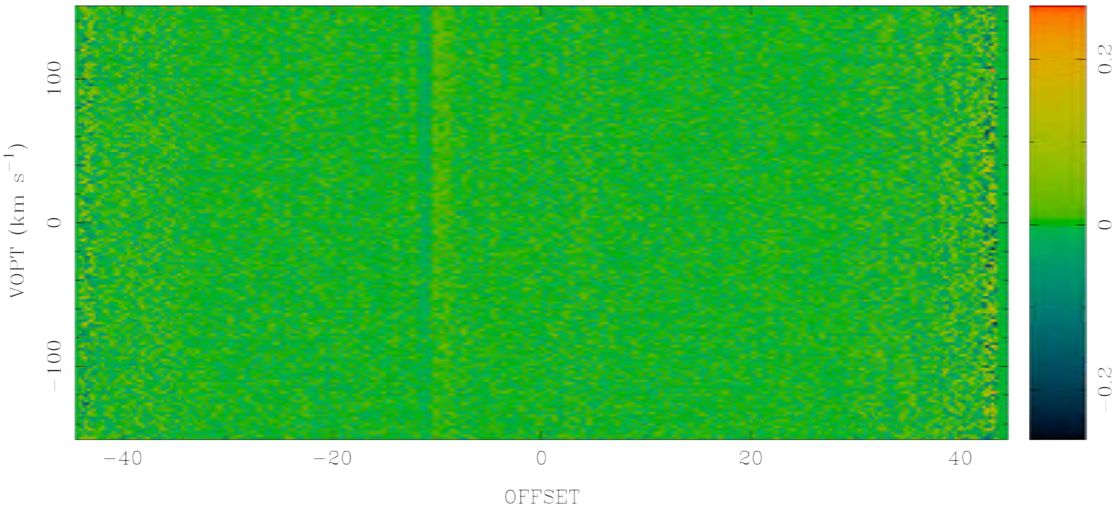

Figure A.40: OH position velocity diagram through Sgr B2 ($\sim -30 - -40$") and Sgr C ($\sim +35$")

A.1.0.11 CH_3OH

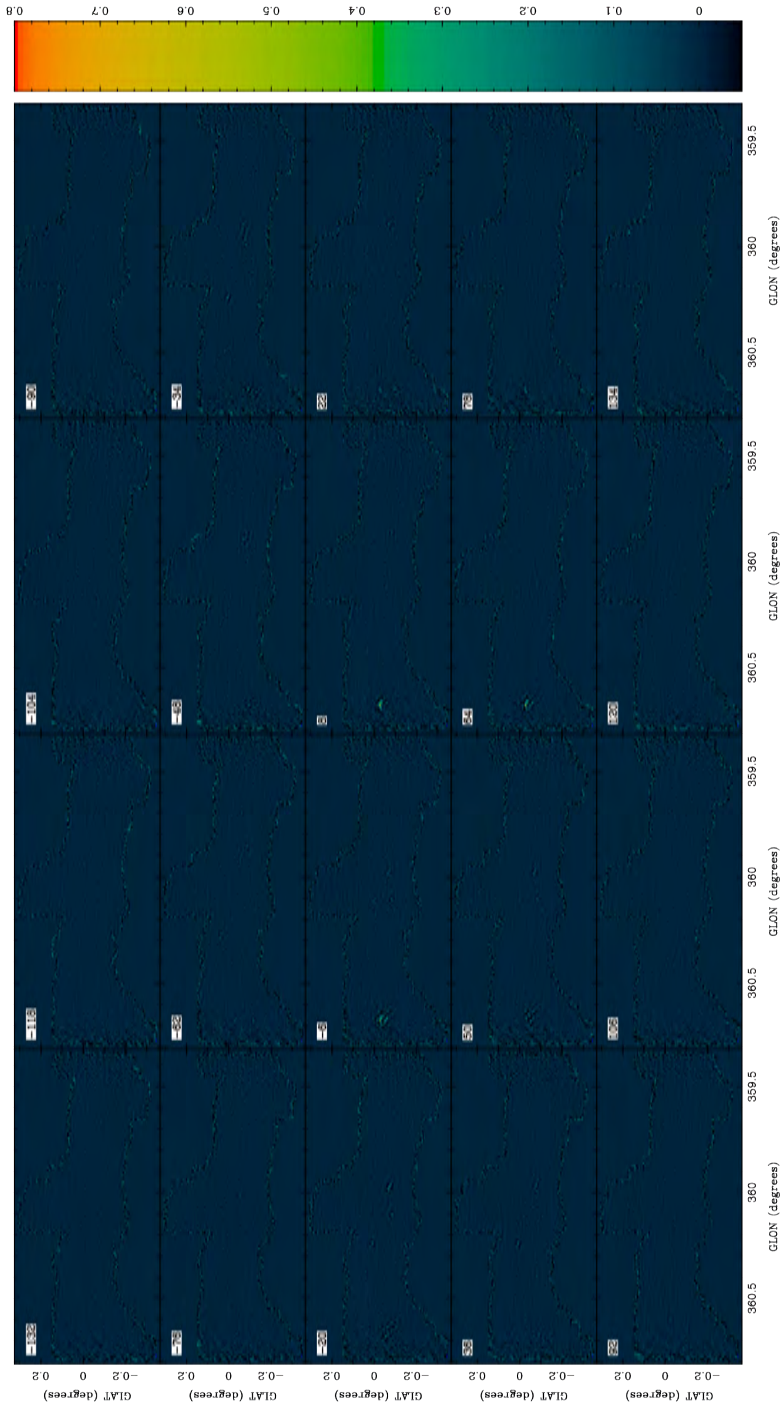

Figure A.41: Channel map of CH_3OH

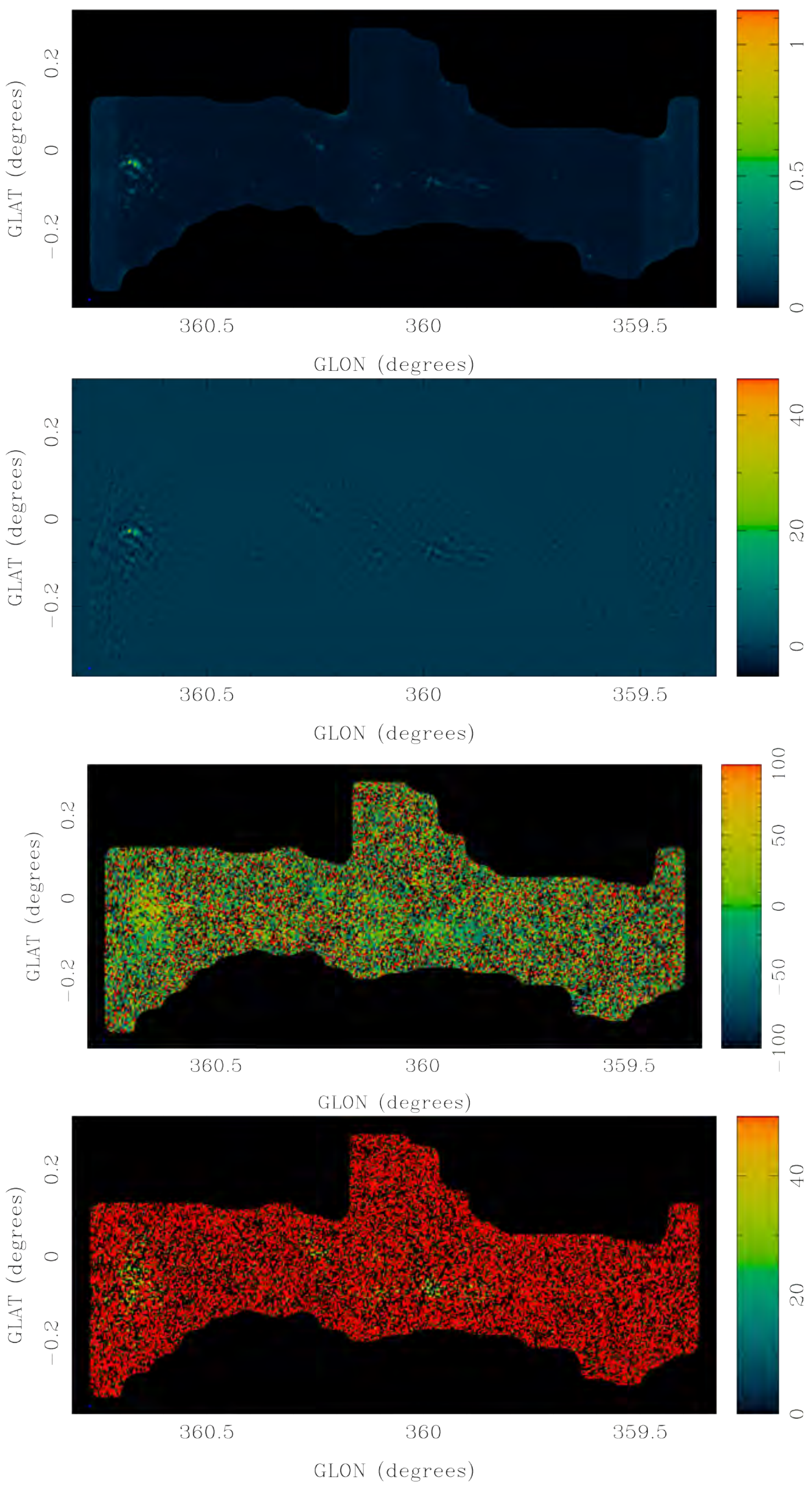

Figure A.42: CH_3OH moment maps. *top to bottom*: peak intensity (moment -2), integrated intensity (moment 0), velocity (moment 1), velocity dispersion (moment 2)

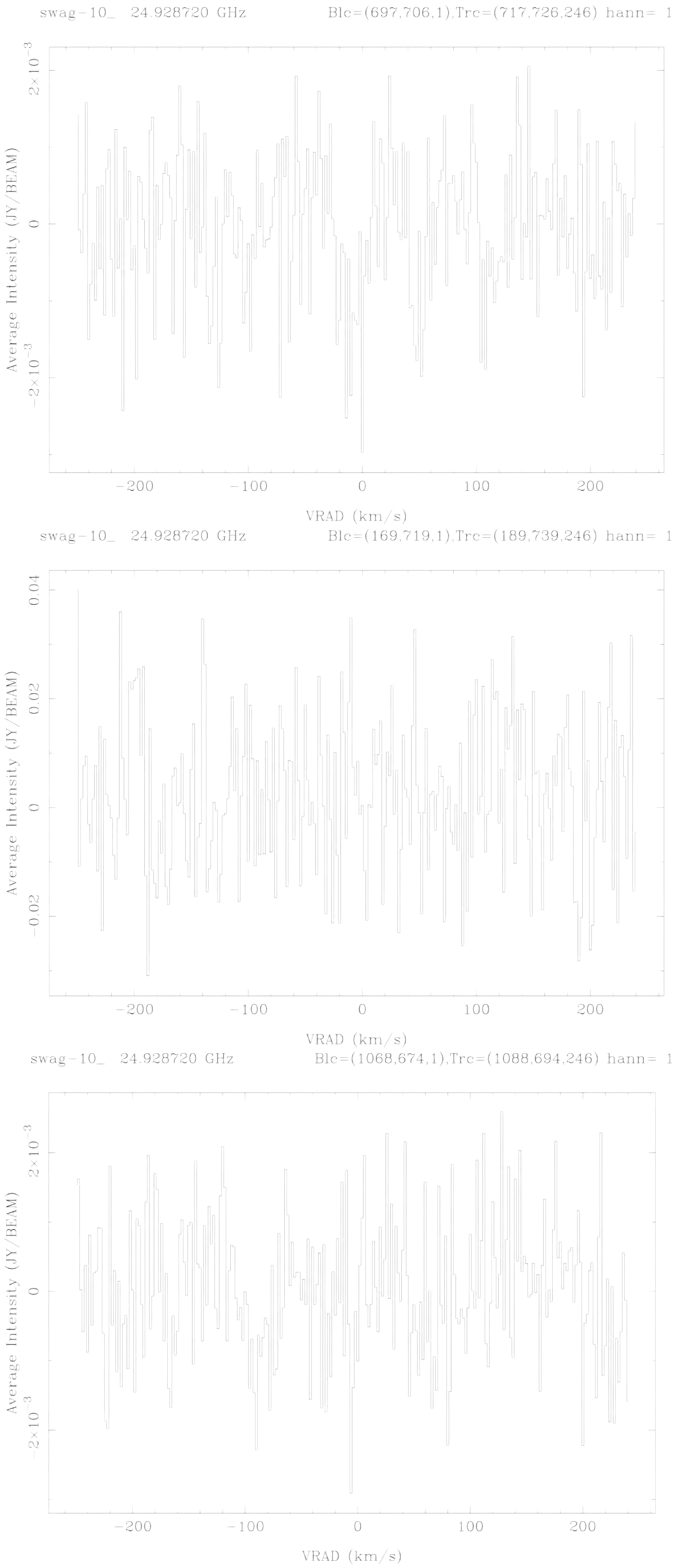

Figure A.43: CH_3OH spectra. *top to bottom*: Sgr A*, B2, C

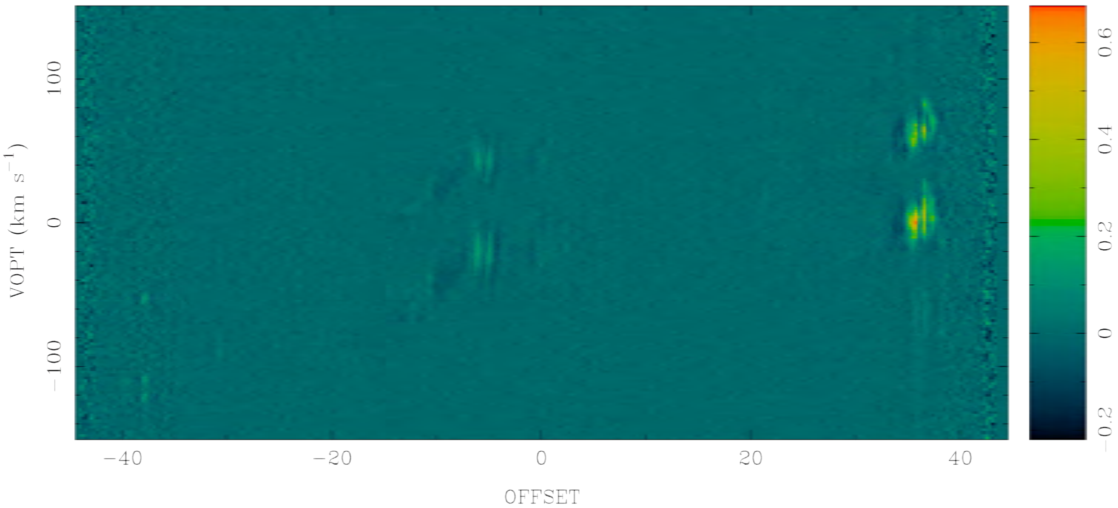

Figure A.44: CH_3OH position velocity diagram through Sgr B2 (∼ −30 − −40") and Sgr C (∼ +35")

A.1.0.12 HNCO

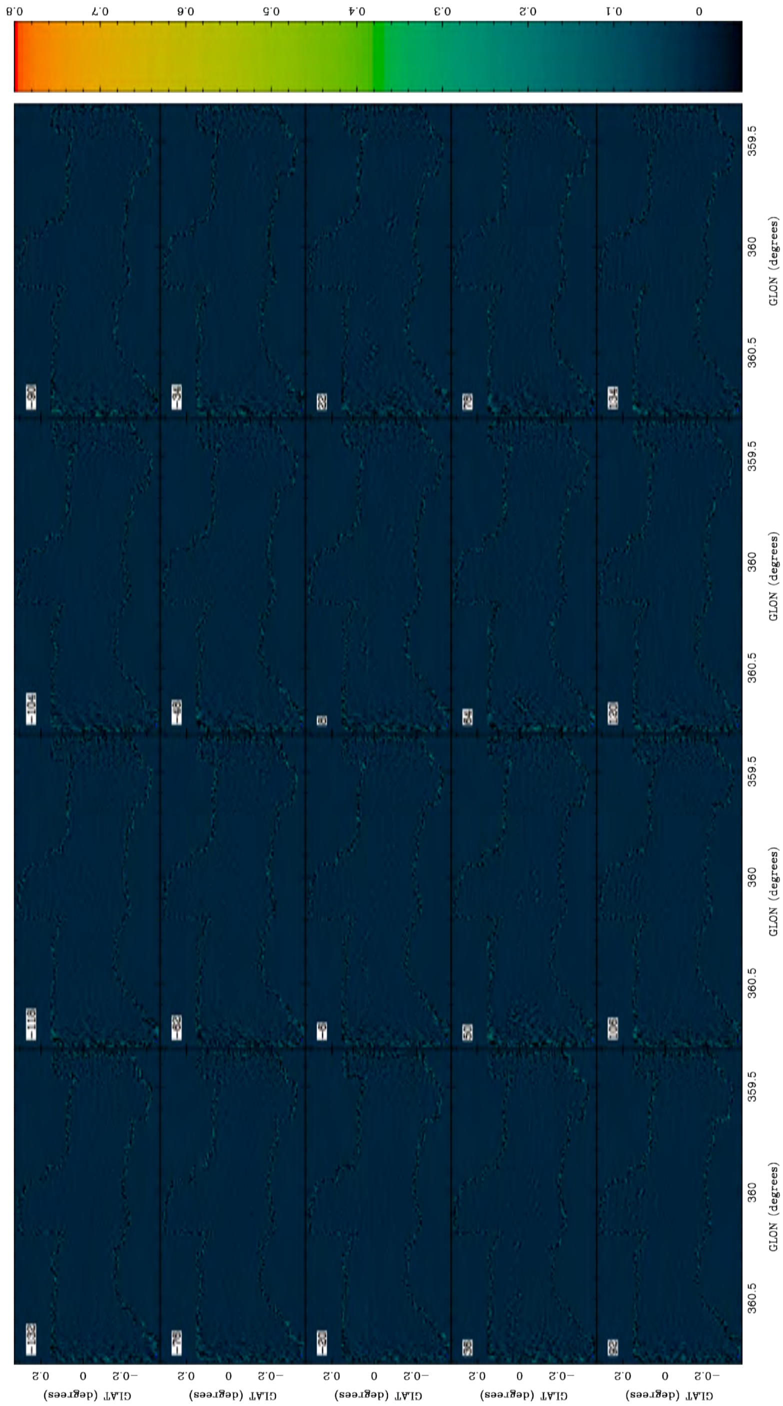

Figure A.45: Channel map of HNCO

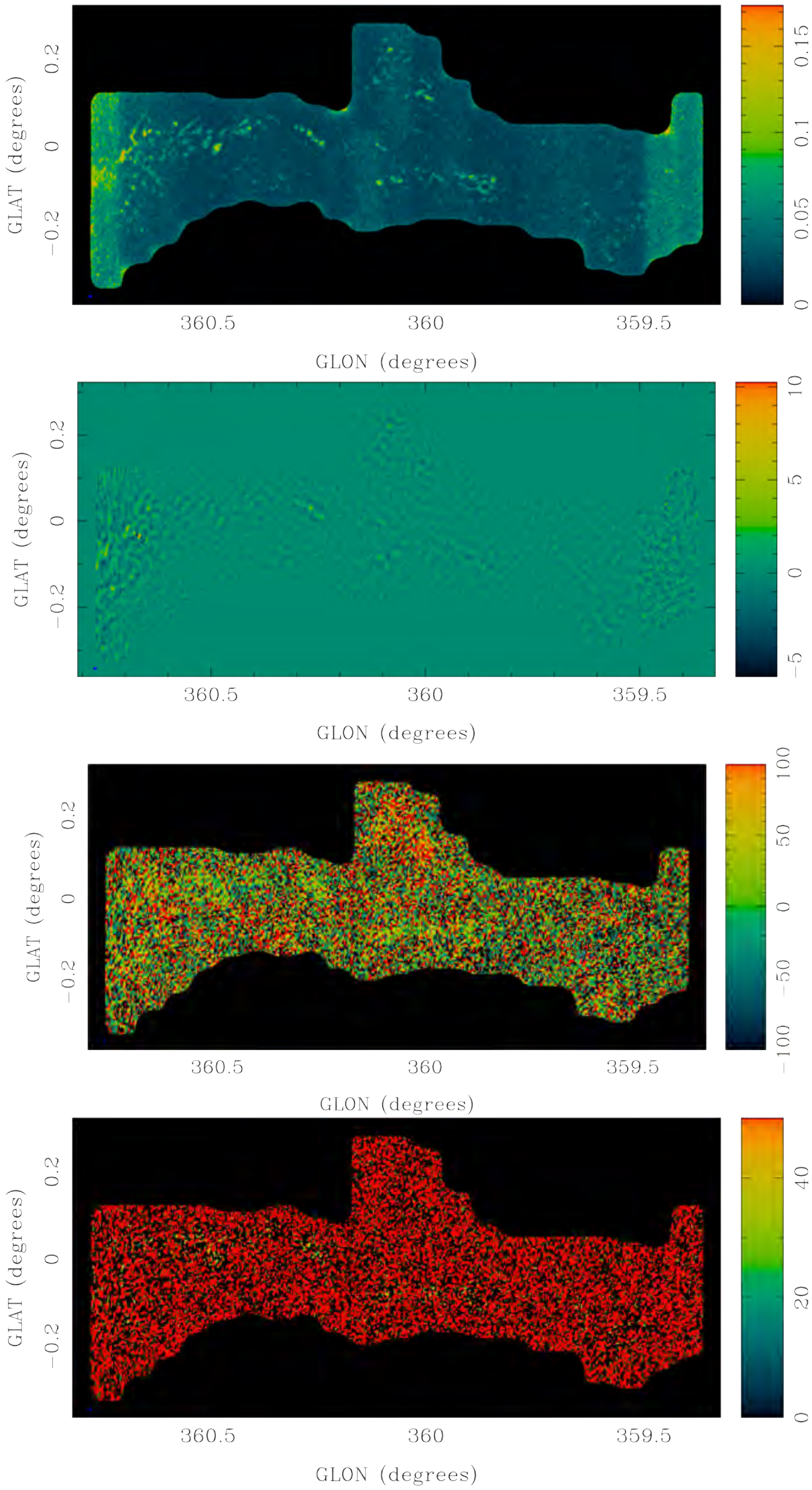

Figure A.46: HNCO moment maps. *top to bottom*: peak intensity (moment -2), integrated intensity (moment 0), velocity (moment 1), velocity dispersion (moment 2)

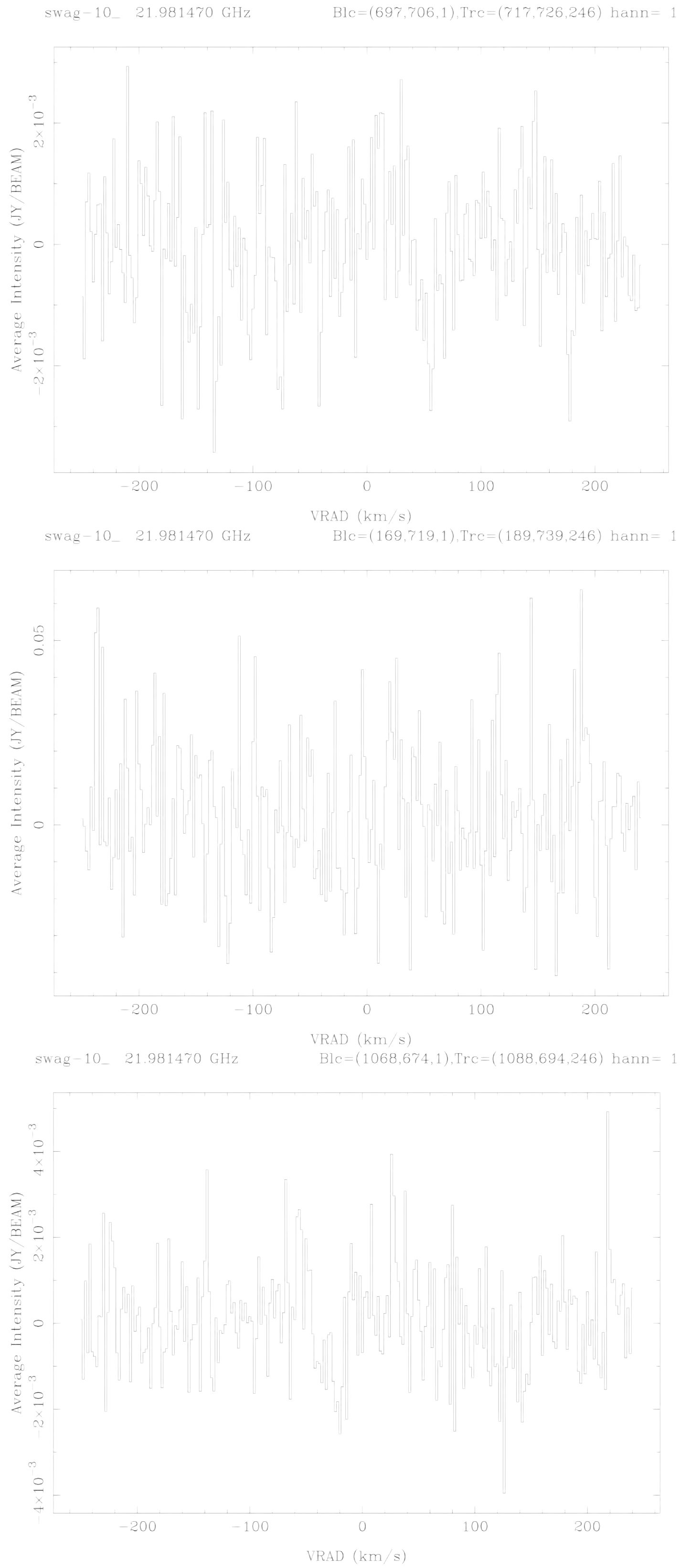

Figure A.47: HNCO spectra. *top to bottom*: Sgr A*, B2, C

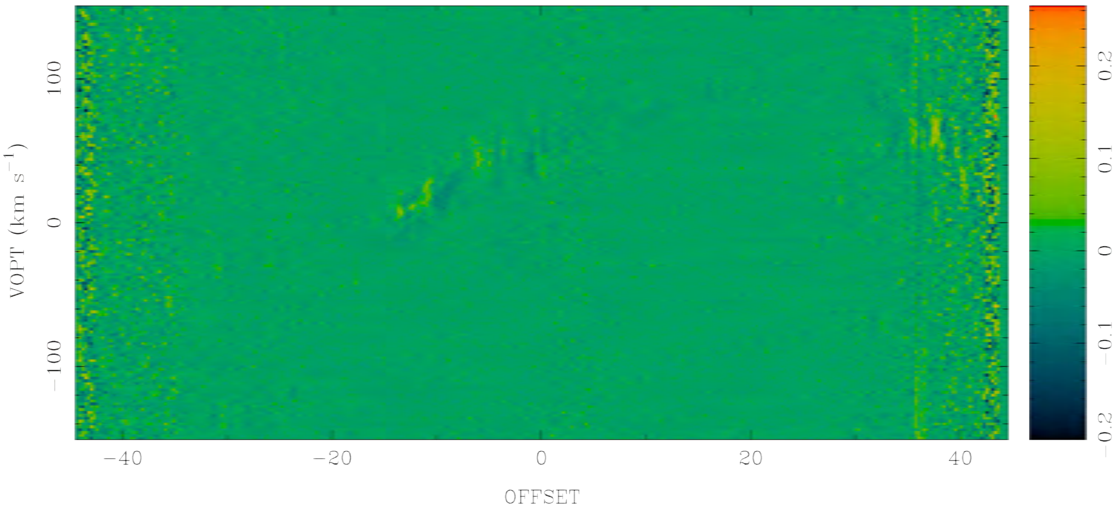

Figure A.48: HNCO position velocity diagram through Sgr B2 (∼ −30 − −40") and Sgr C (∼ +35")

A.1.0.13 HCN

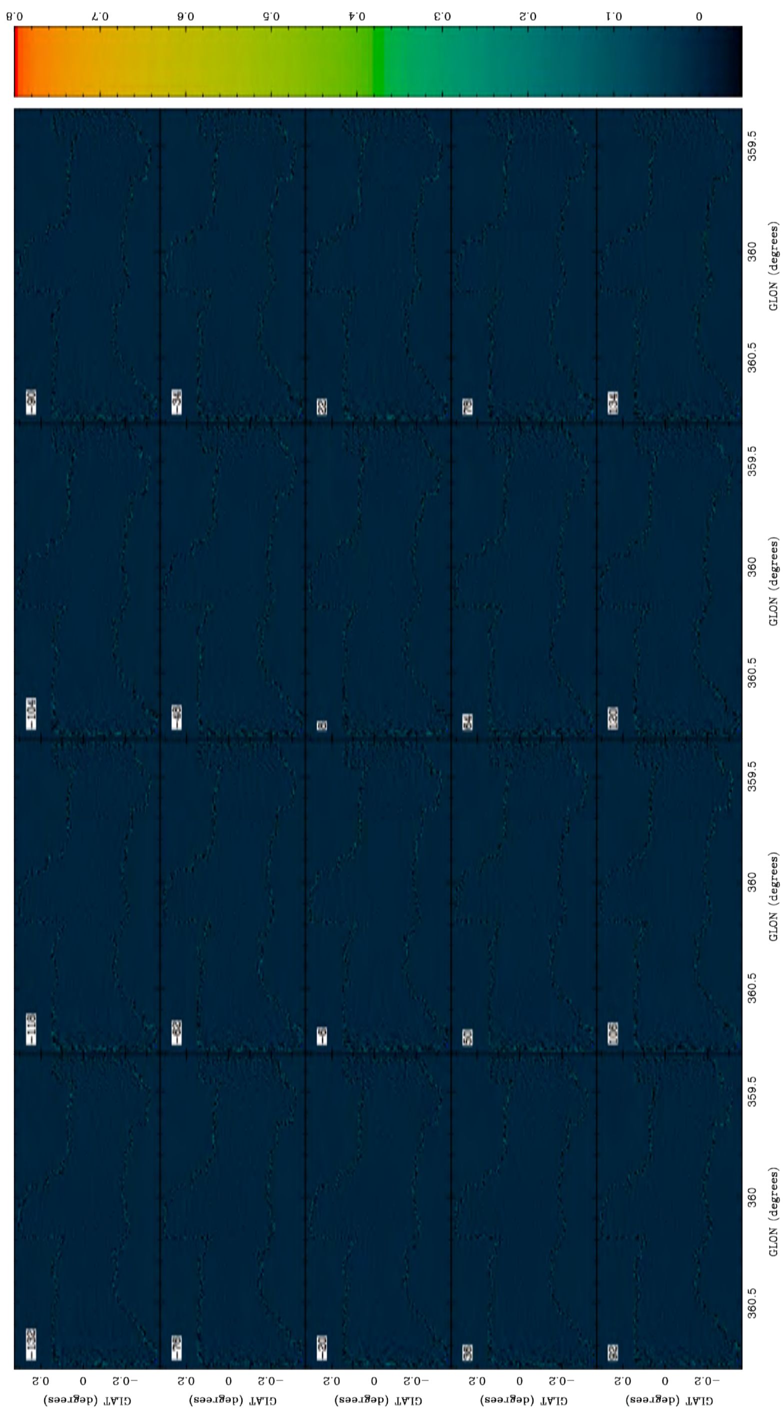

Figure A.49: Channel map of HCN

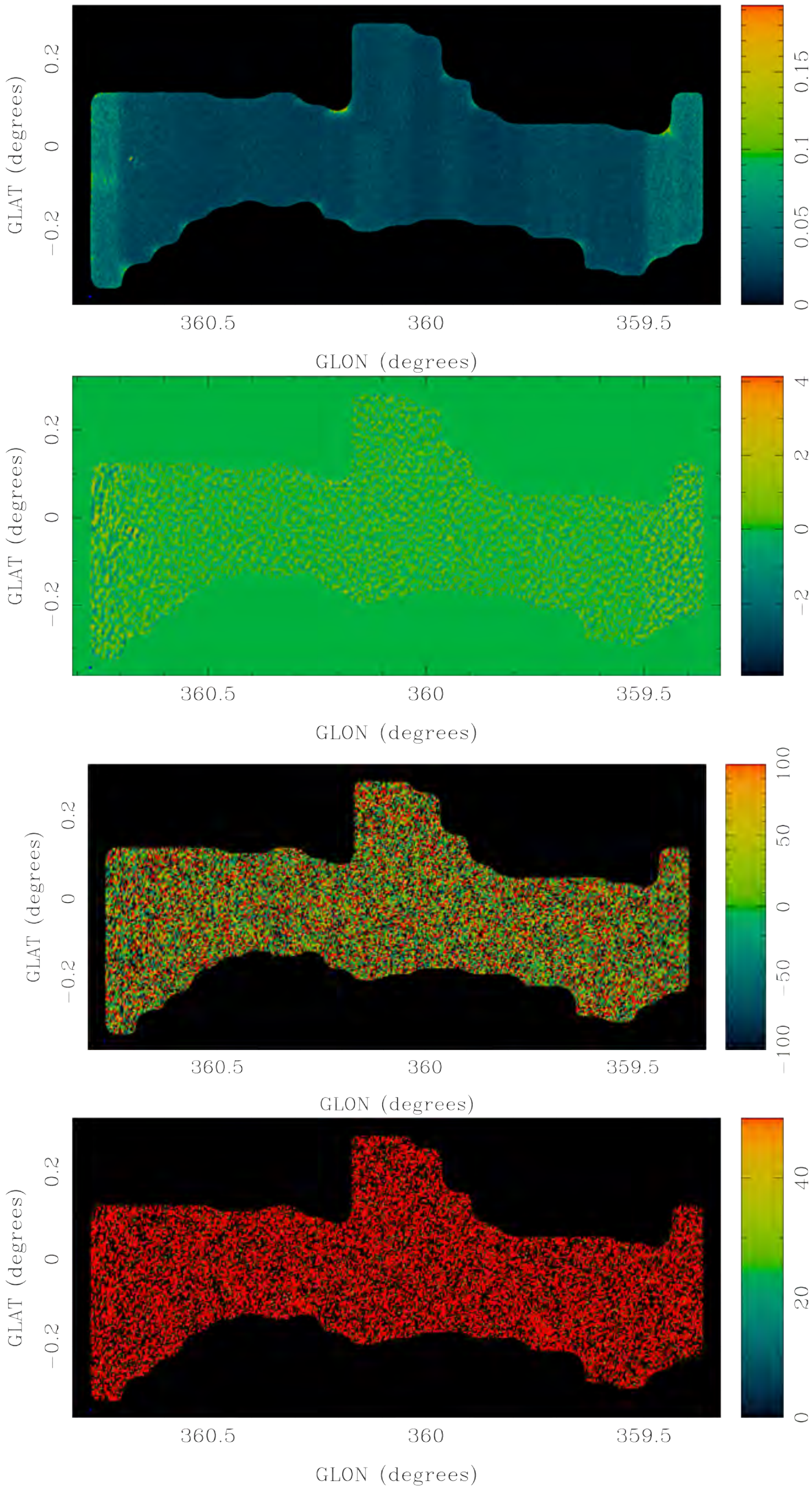

Figure A.50: HCN moment maps. *top to bottom*: peak intensity (moment -2), integrated intensity (moment 0), velocity (moment 1), velocity dispersion (moment 2)

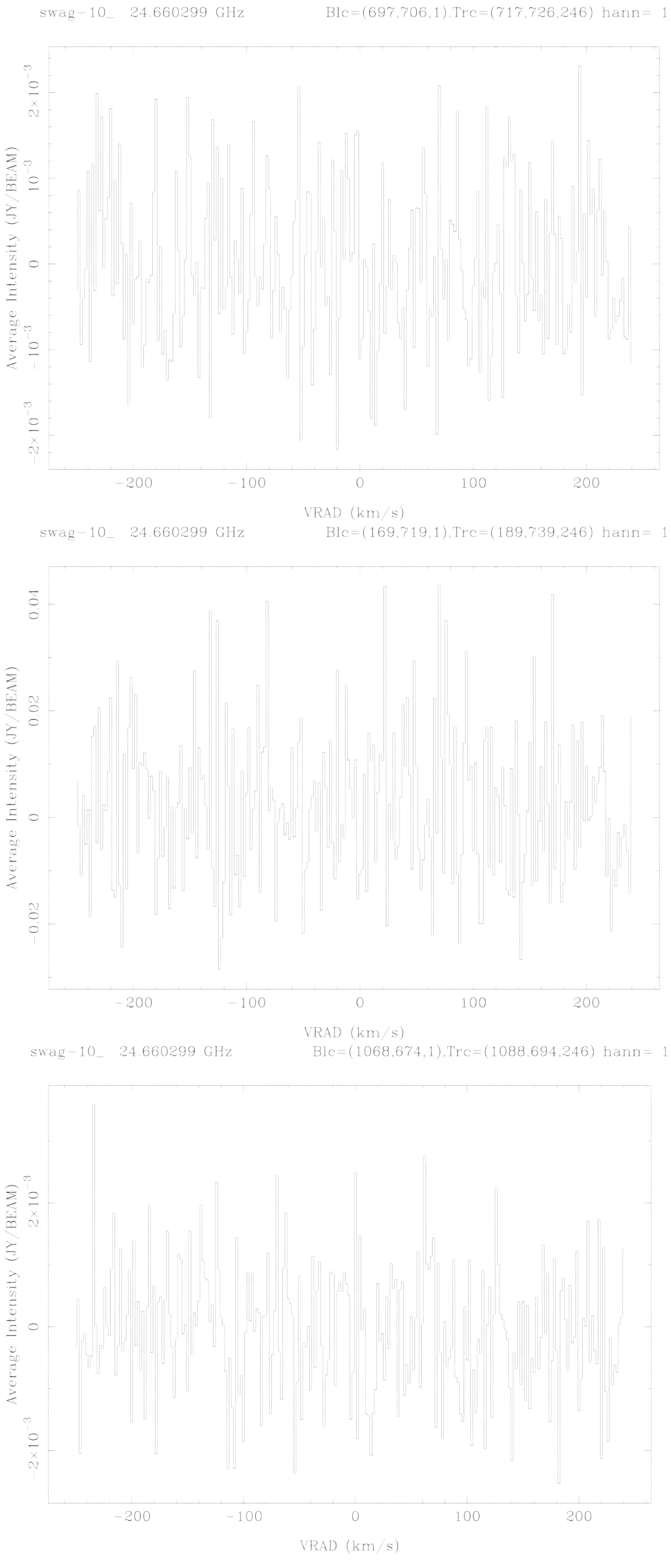

Figure A.51: HCN spectra. *top to bottom*: Sgr A*, B2, C

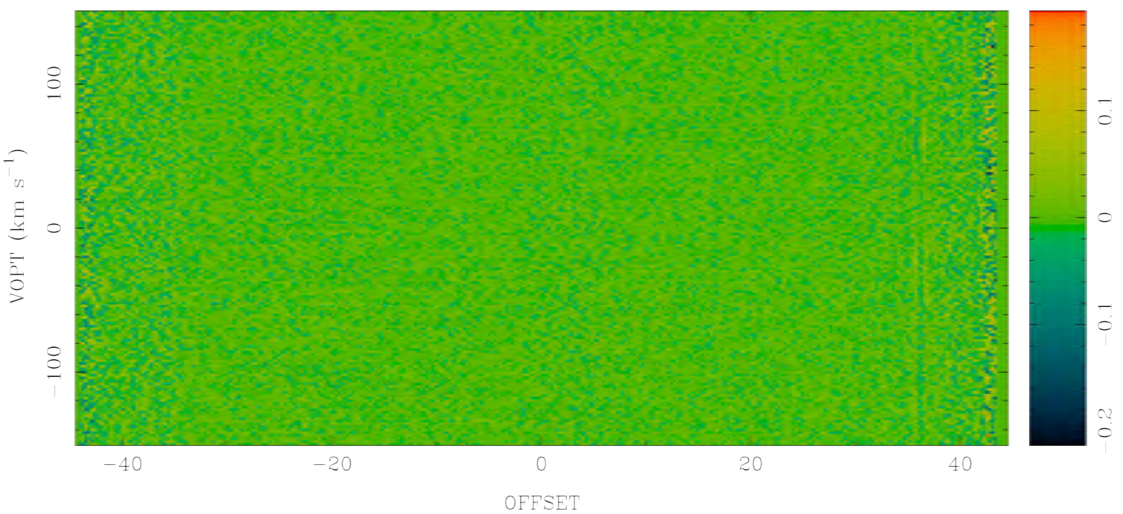

Figure A.52: HCN position velocity diagram through Sgr B2 ($\sim -30 - -40$") and Sgr C ($\sim +35$")

A.1.0.14 SO_2

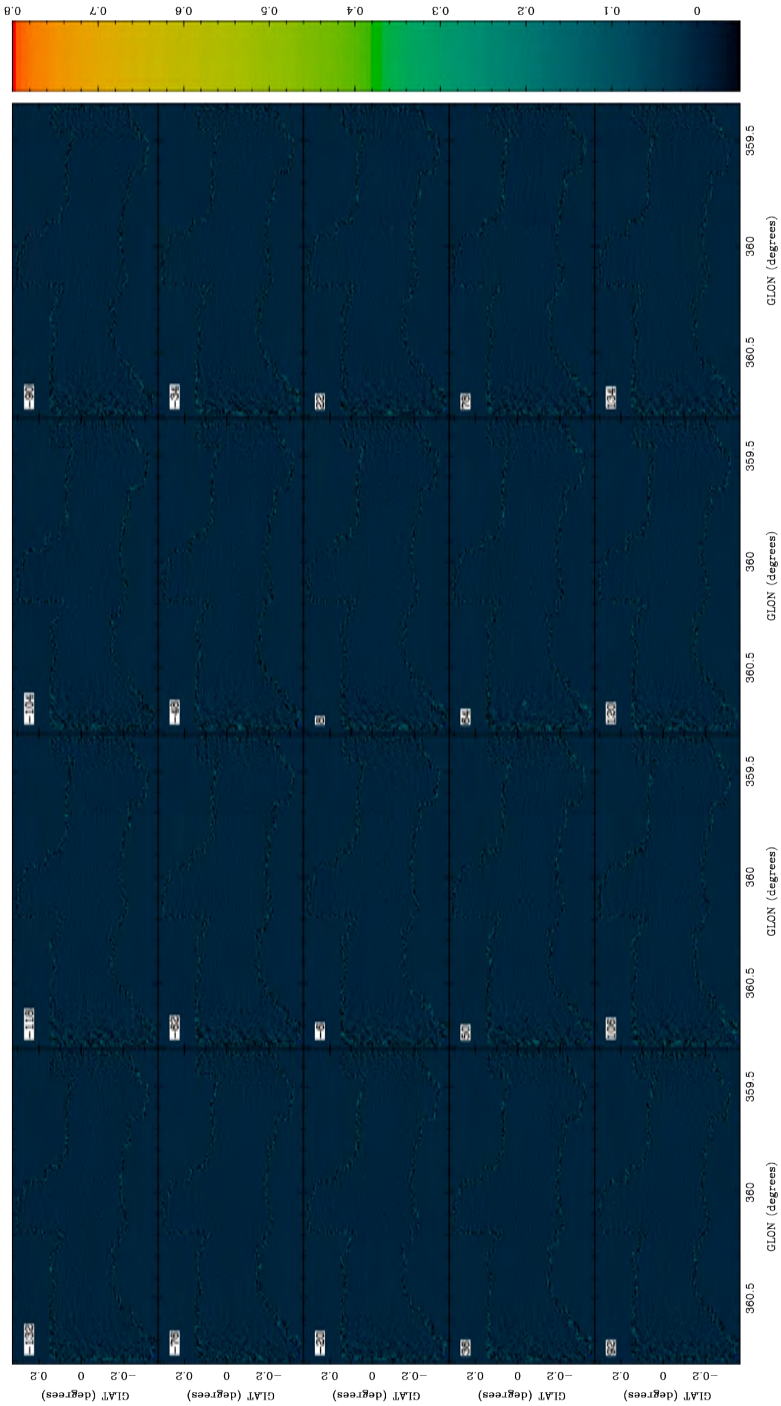

Figure A.53: Channel map of SO_2

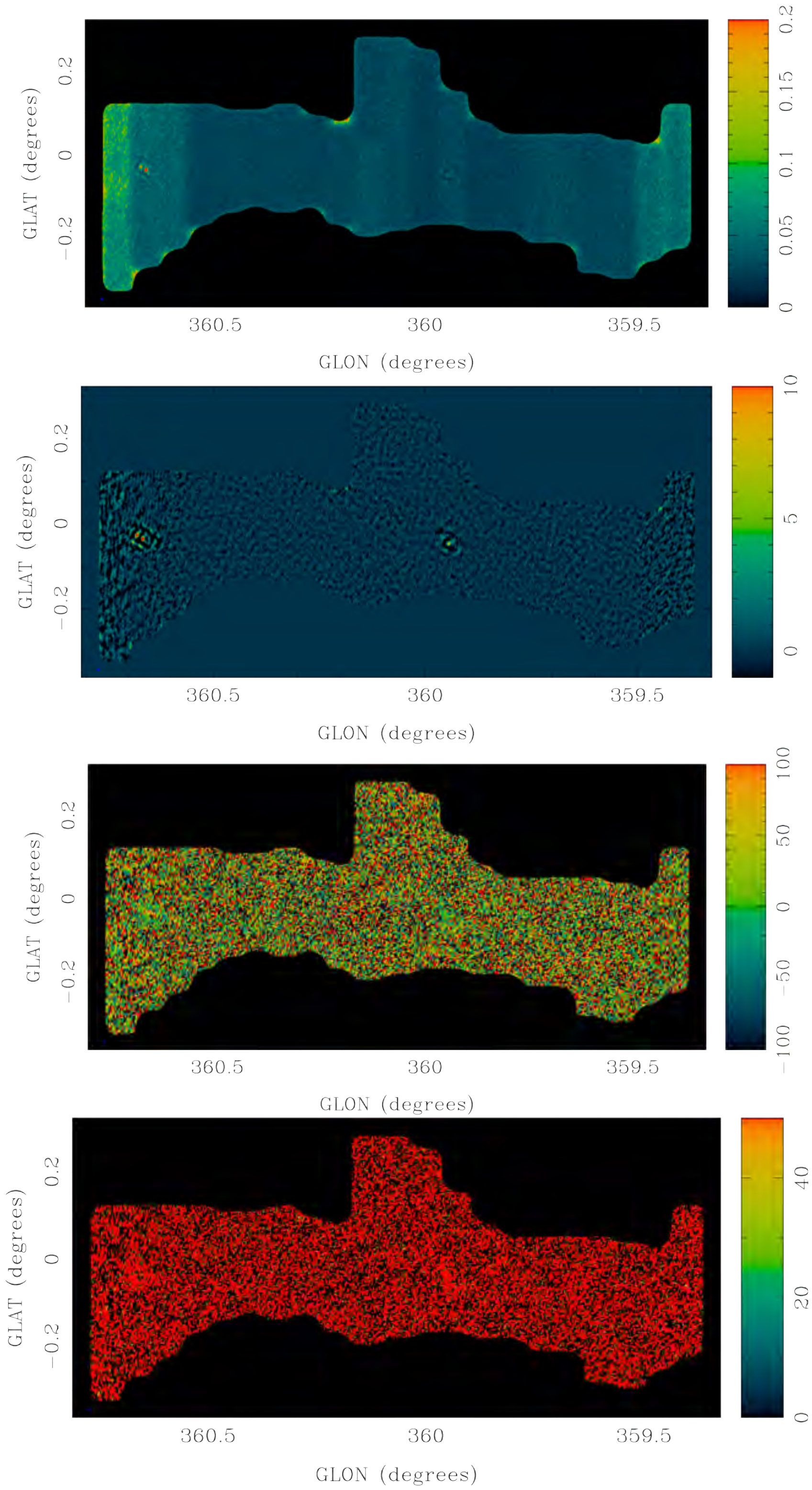

Figure A.54: SO_2 moment maps. *top to bottom*: peak intensity (moment -2), integrated intensity (moment 0), velocity (moment 1), velocity dispersion (moment 2)

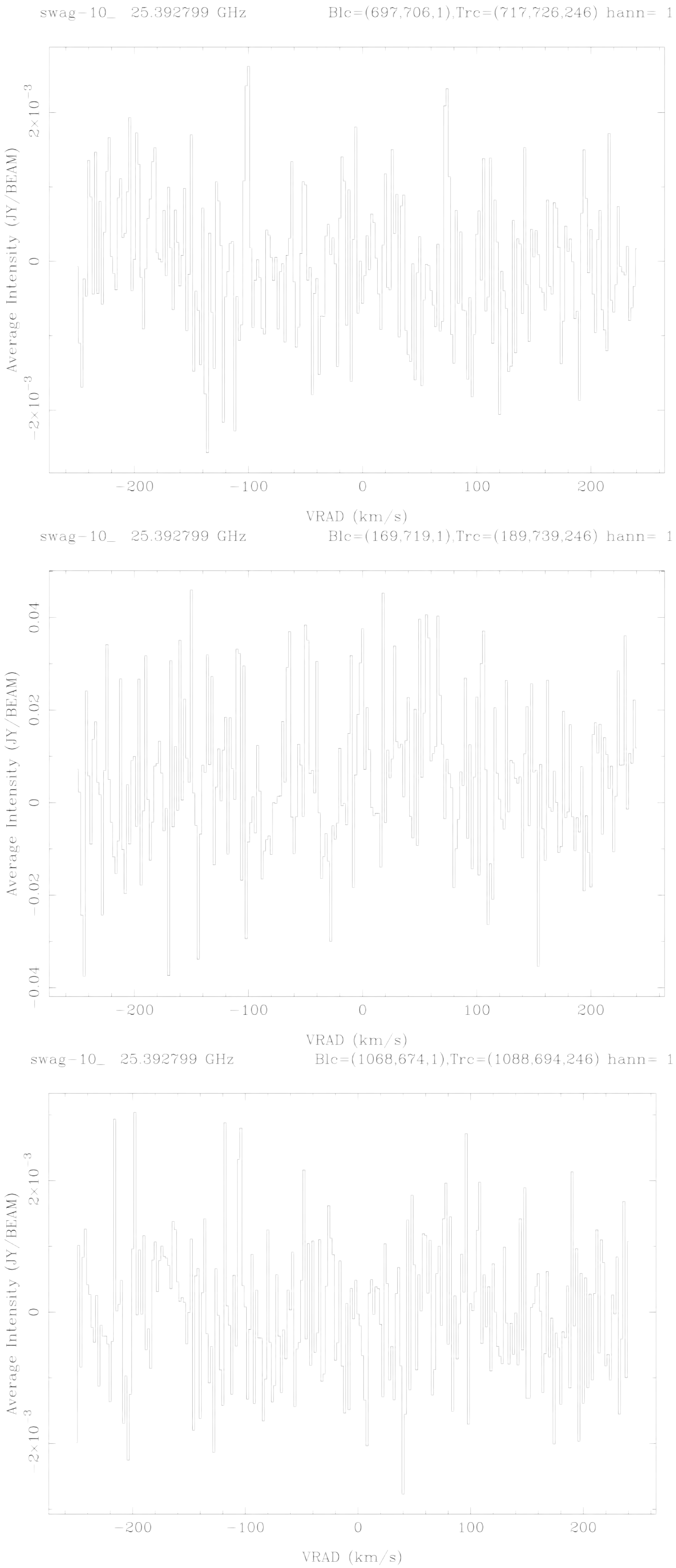

Figure A.55: SO_2 spectra. *top to bottom*: Sgr A*, B2, C

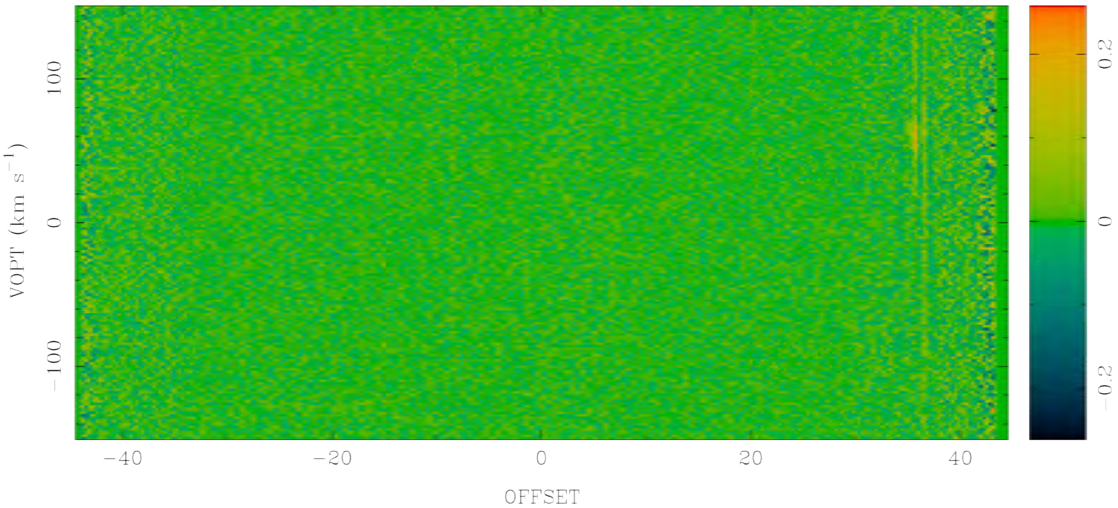

Figure A.56: SO_2 position velocity diagram through Sgr B2 ($\sim -30 - -40$") and Sgr C ($\sim +35$")

A.2 Derived Data Products

This section contains all maps that are derived from pixel-by-pixel fitting, i.e. maps of line-of-sight velocity, line width, column density, opacity and temperature. The creation of these maps is explained in §2.4.

A.2.0.1 Line-of-sight velocity

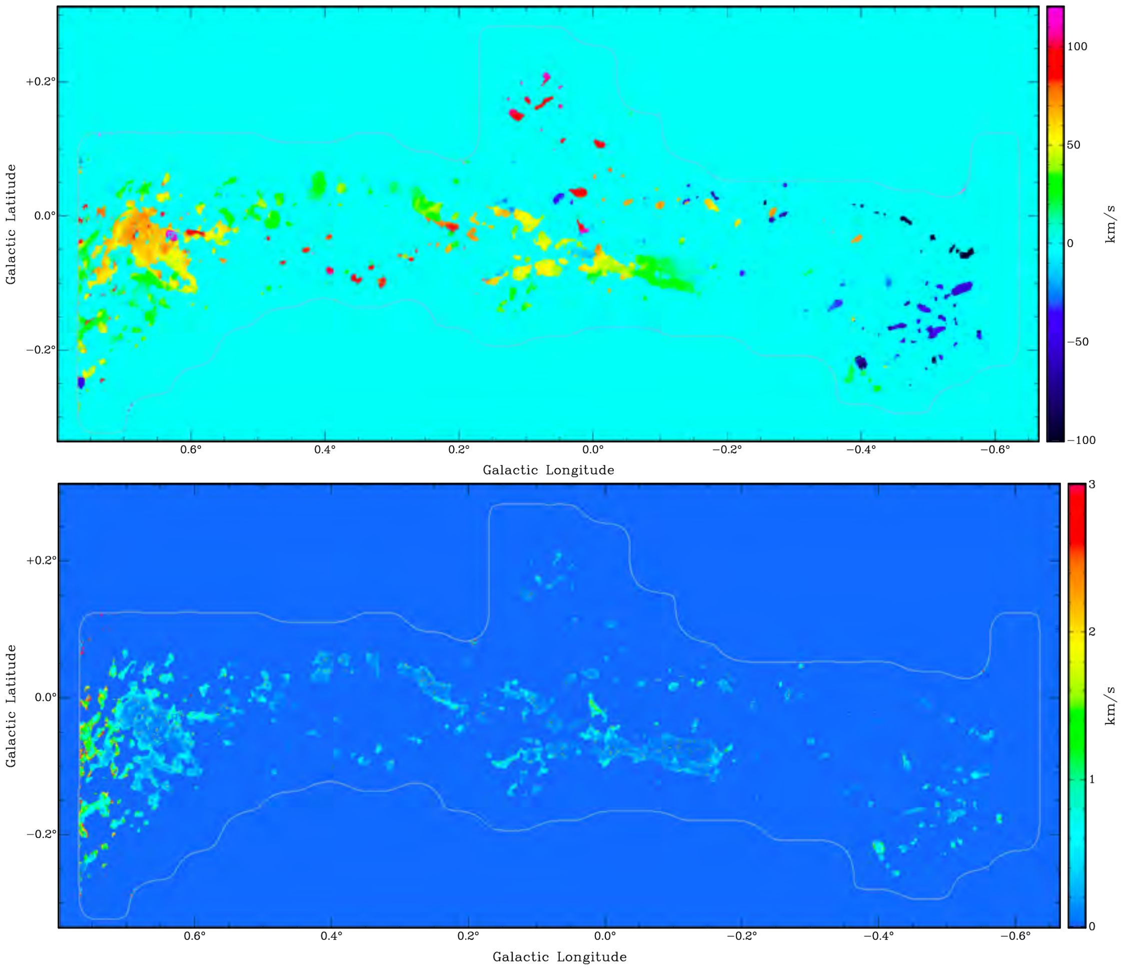

Figure A.57: Line-of-sight velocity map (*top*) and error map (*bottom*) of NH_3 (1,1)

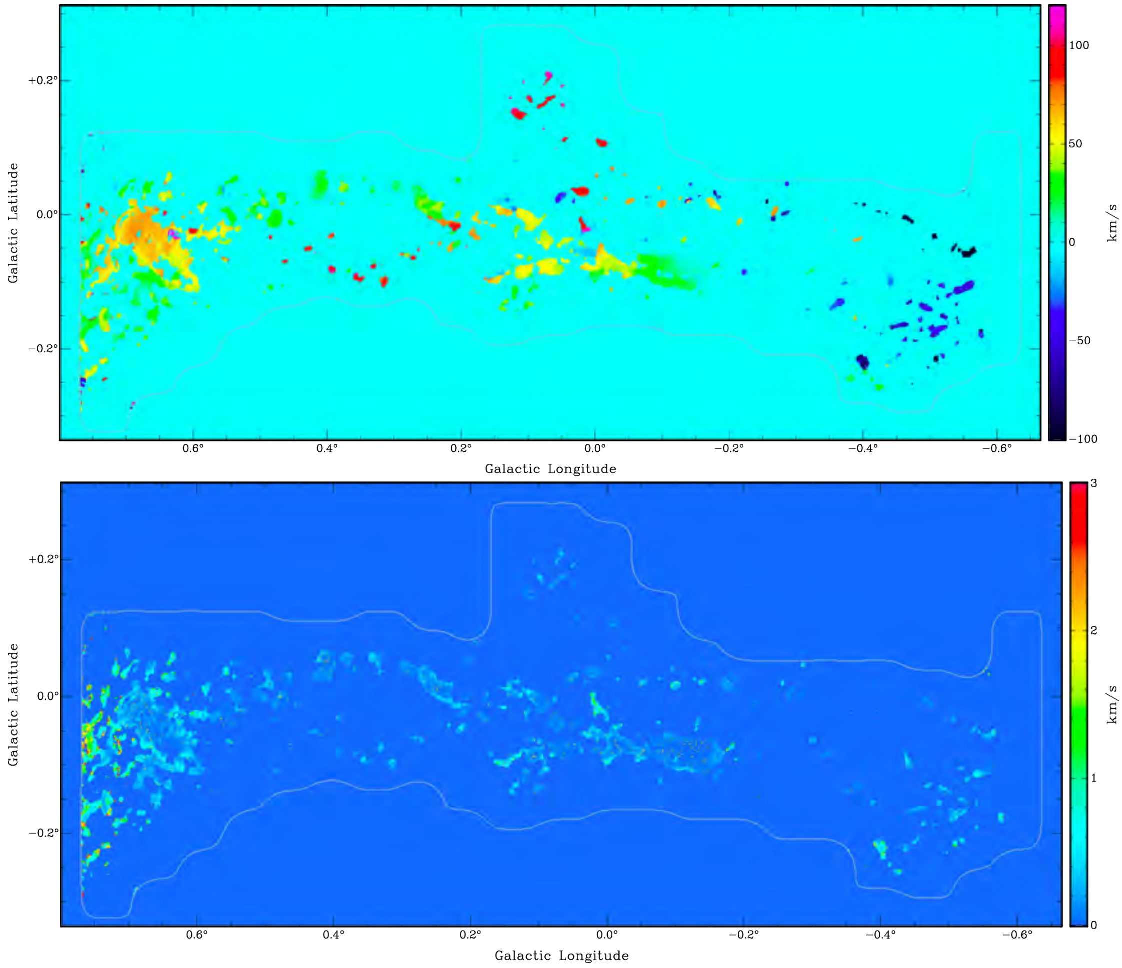

Figure A.58: Line-of-sight velocity map (*top*) and error map (*bottom*) of NH_3 (2,2)

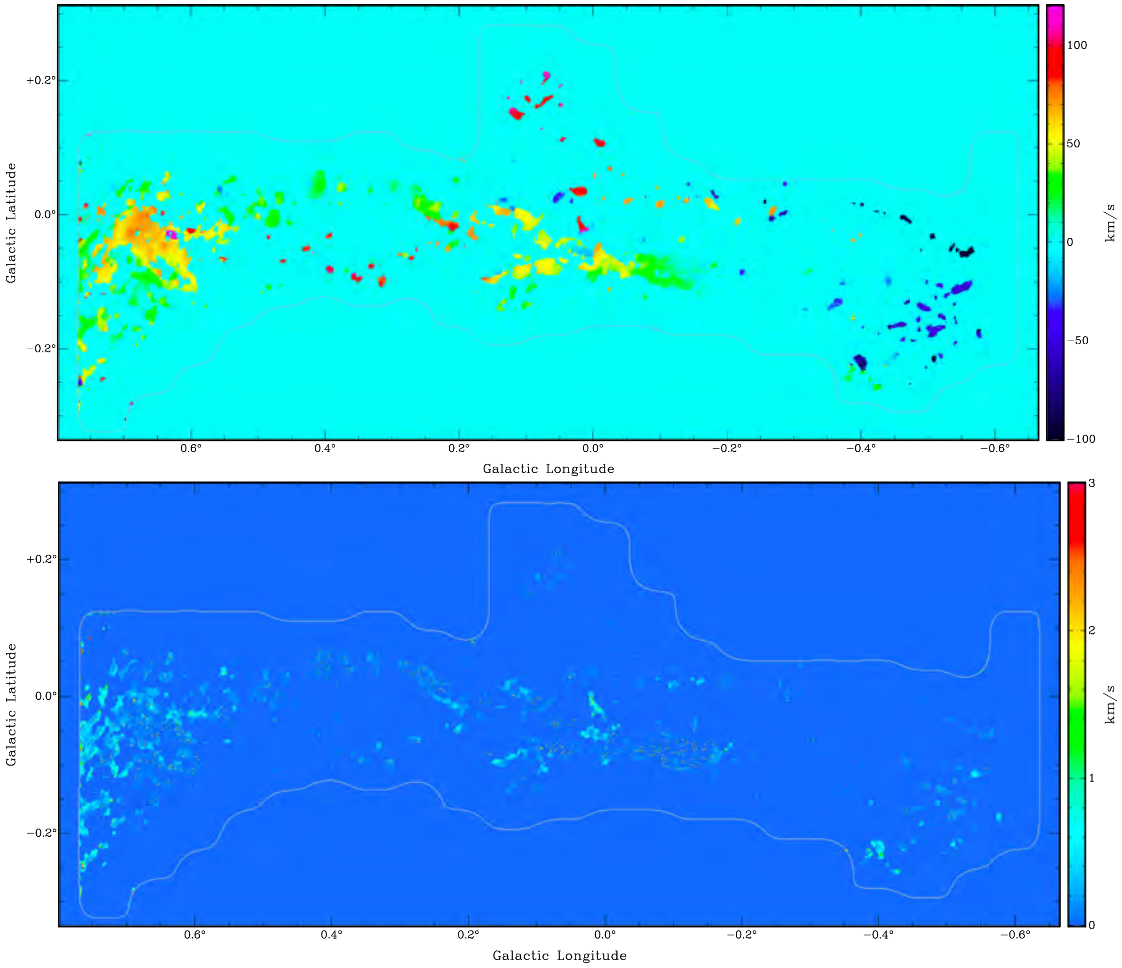

Figure A.59: Line-of-sight velocity map (*top*) and error map (*bottom*) of NH_3 (3,3)

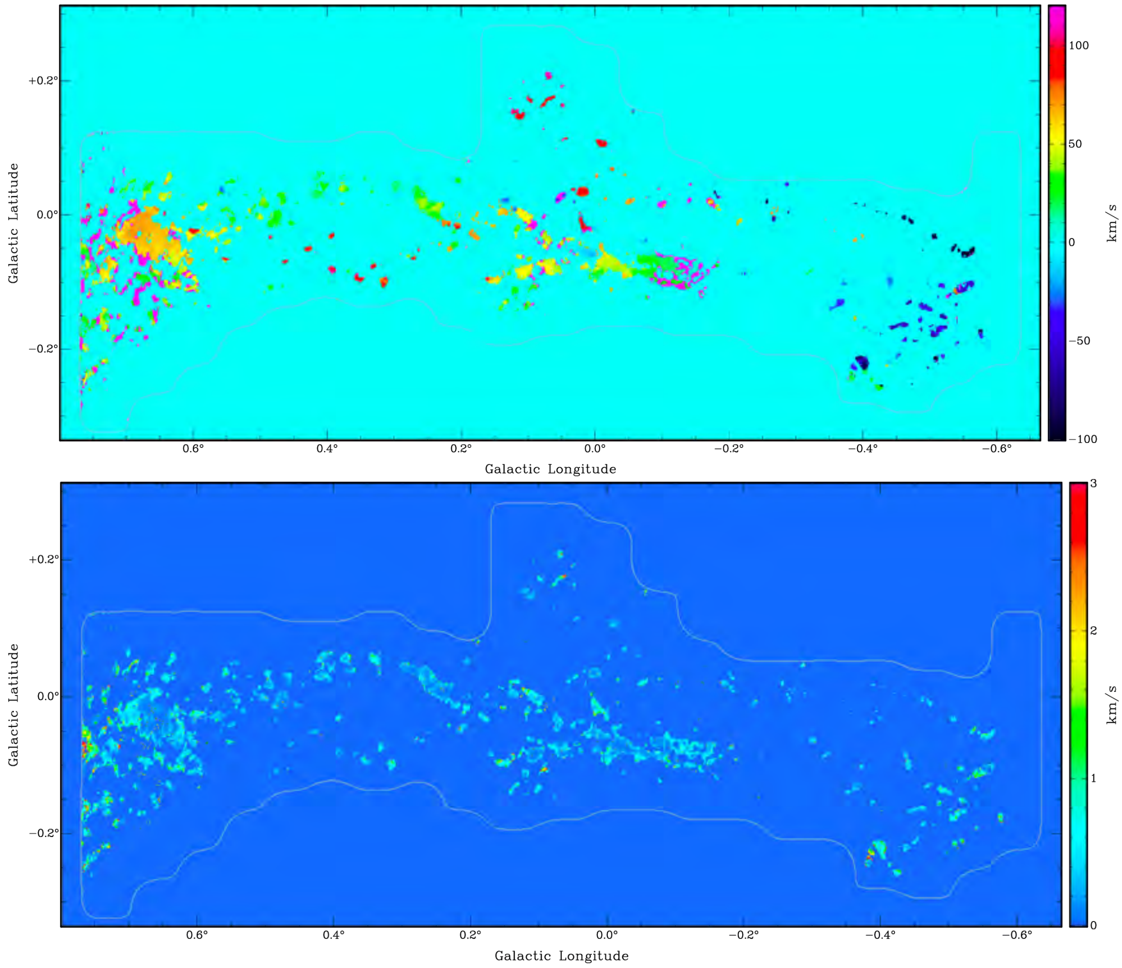

Figure A.60: Line-of-sight velocity map (*top*) and error map (*bottom*) of NH_3 (4,4)

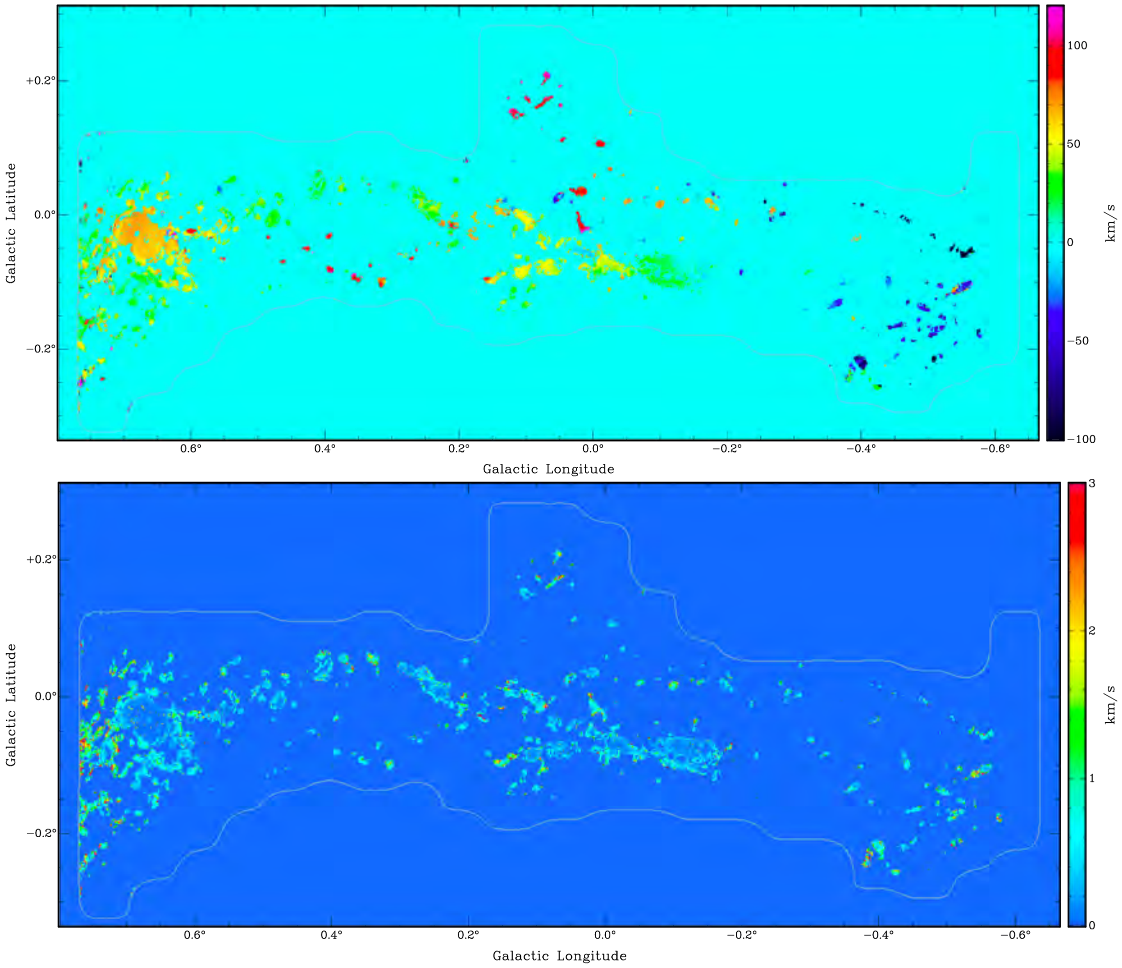

Figure A.61: Line-of-sight velocity map (*top*) and error map (*bottom*) of NH_3 (5,5)

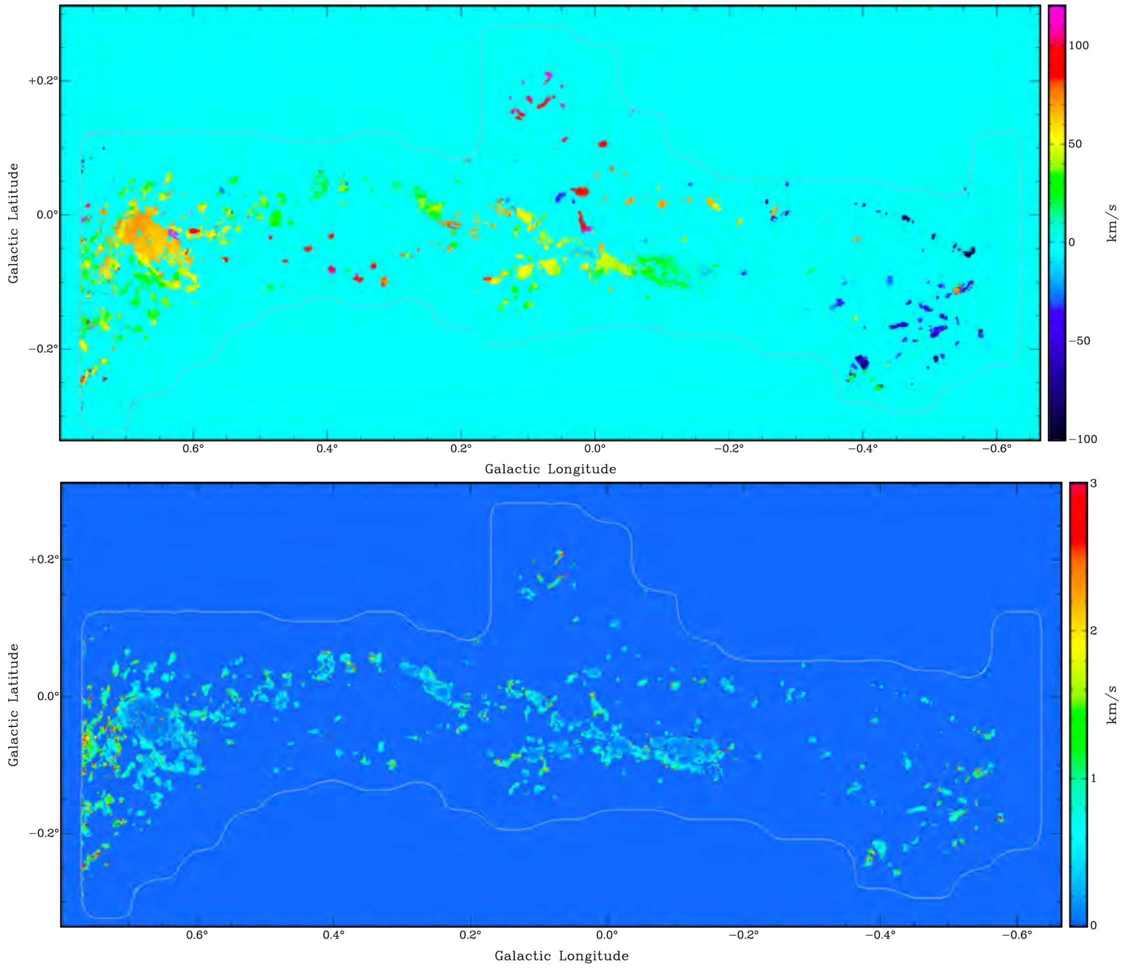

Figure A.62: Line-of-sight velocity map (*top*) and error map (*bottom*) of NH_3 (6,6)

A.2.0.2 Line Width

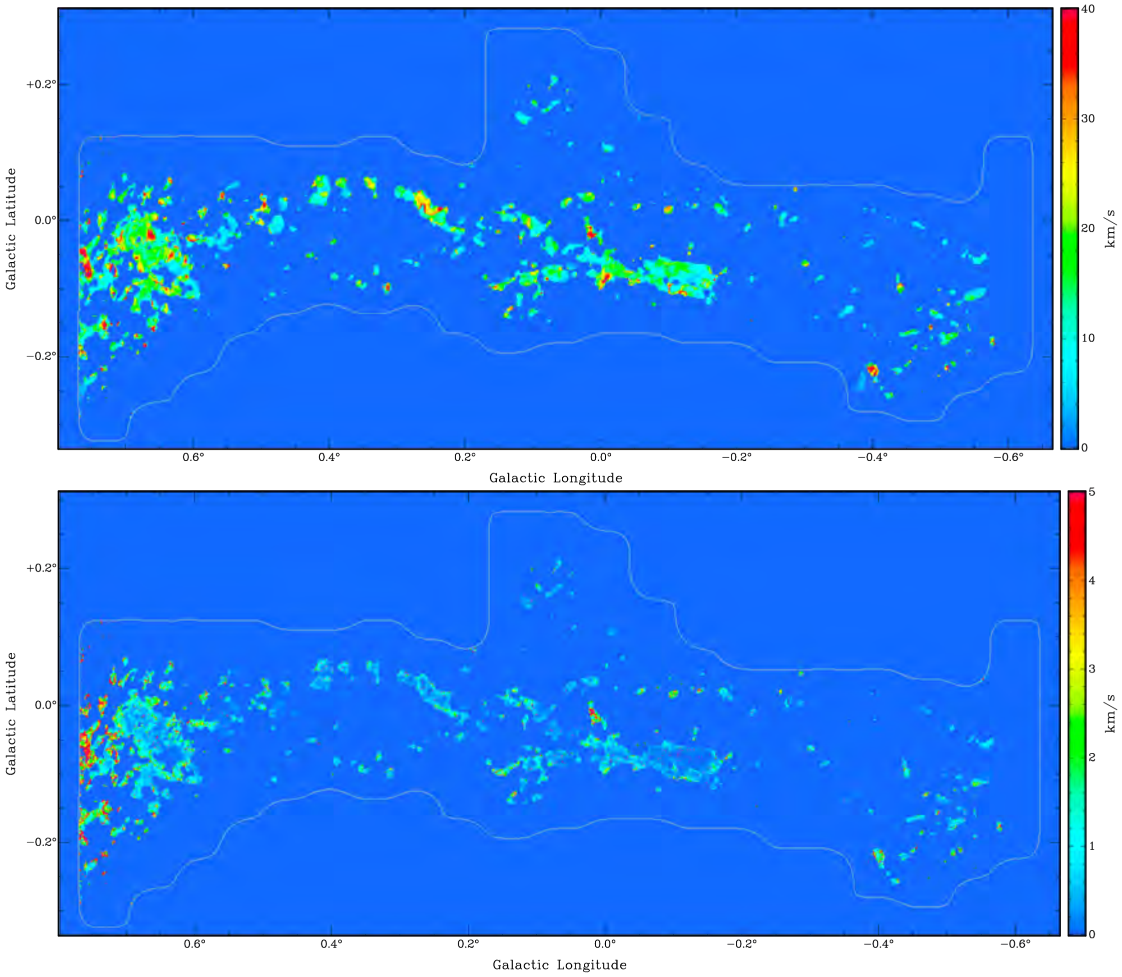

Figure A.63: Line width (FWHM) map (*top*) and error map (*bottom*) of NH_3 (1,1)

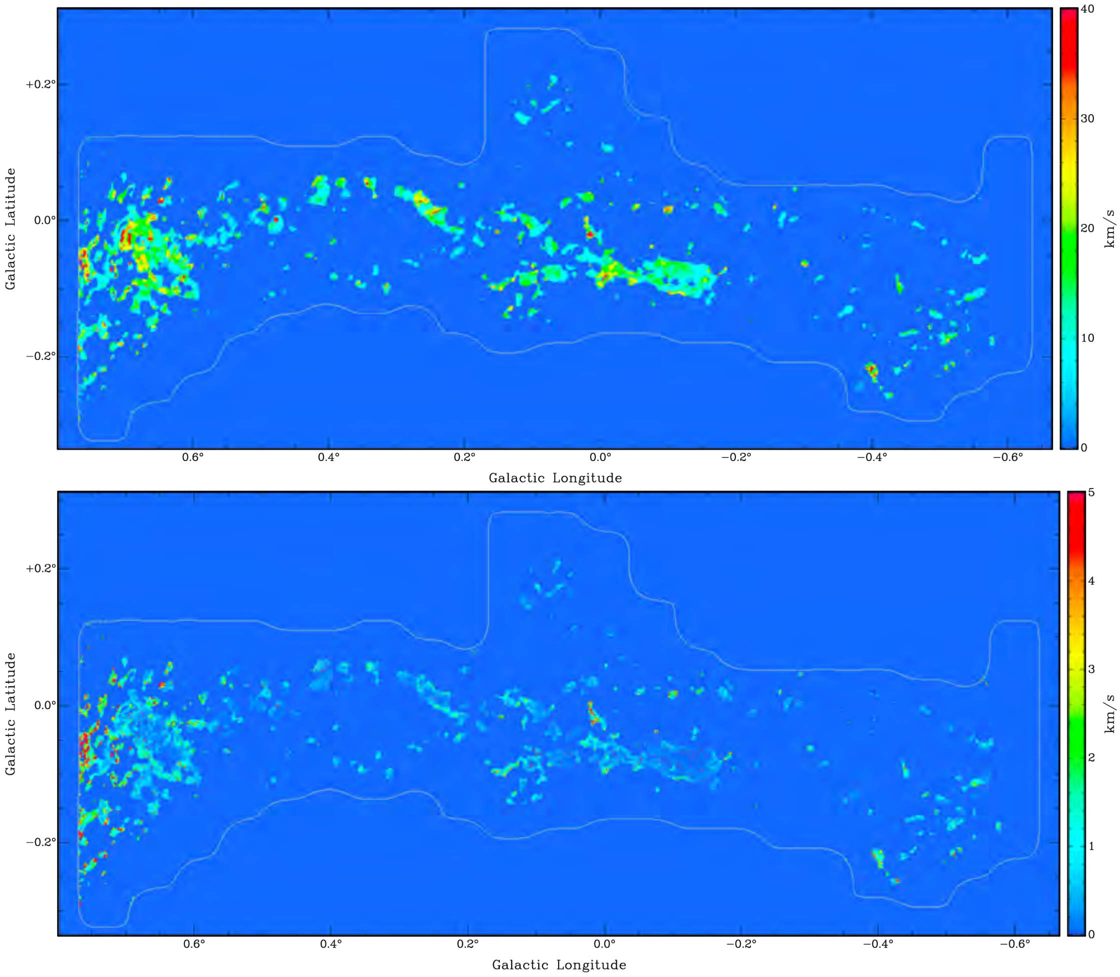

Figure A.64: Line width (FWHM) map (*top*) and error map (*bottom*) of NH_3 (2,2)

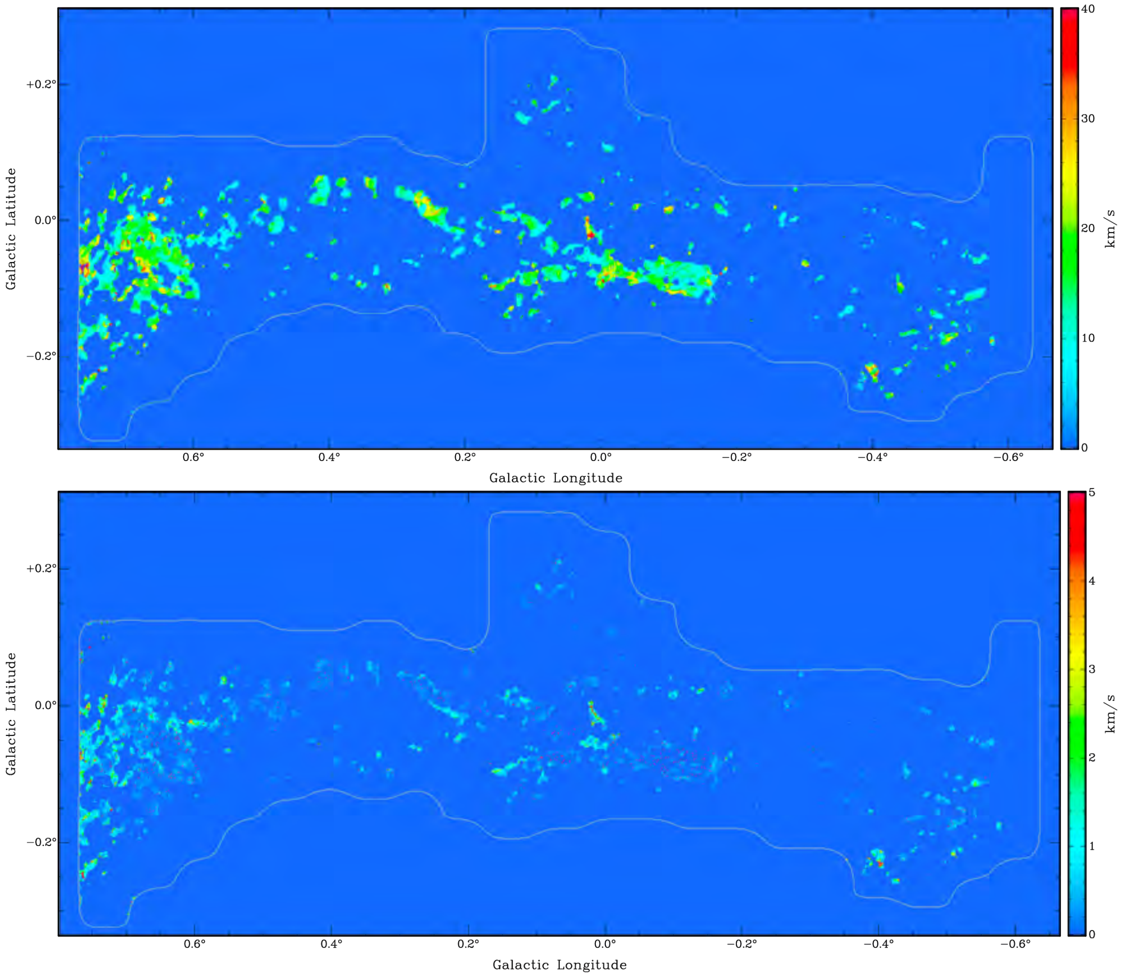

Figure A.65: Line width (FWHM) map (*top*) and error map (*bottom*) of NH_3 (3,3)

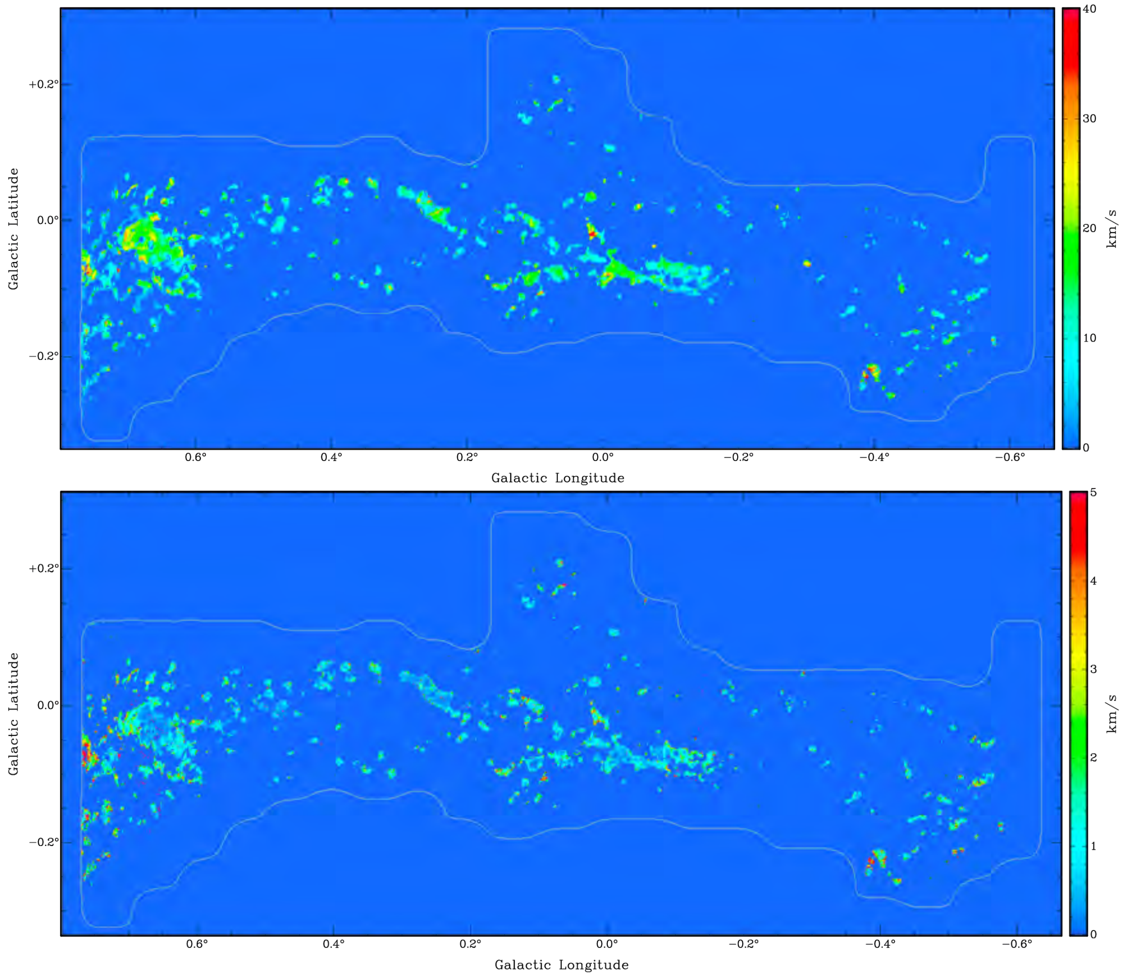

Figure A.66: Line width (FWHM) map (*top*) and error map (*bottom*) of NH_3 (4,4)

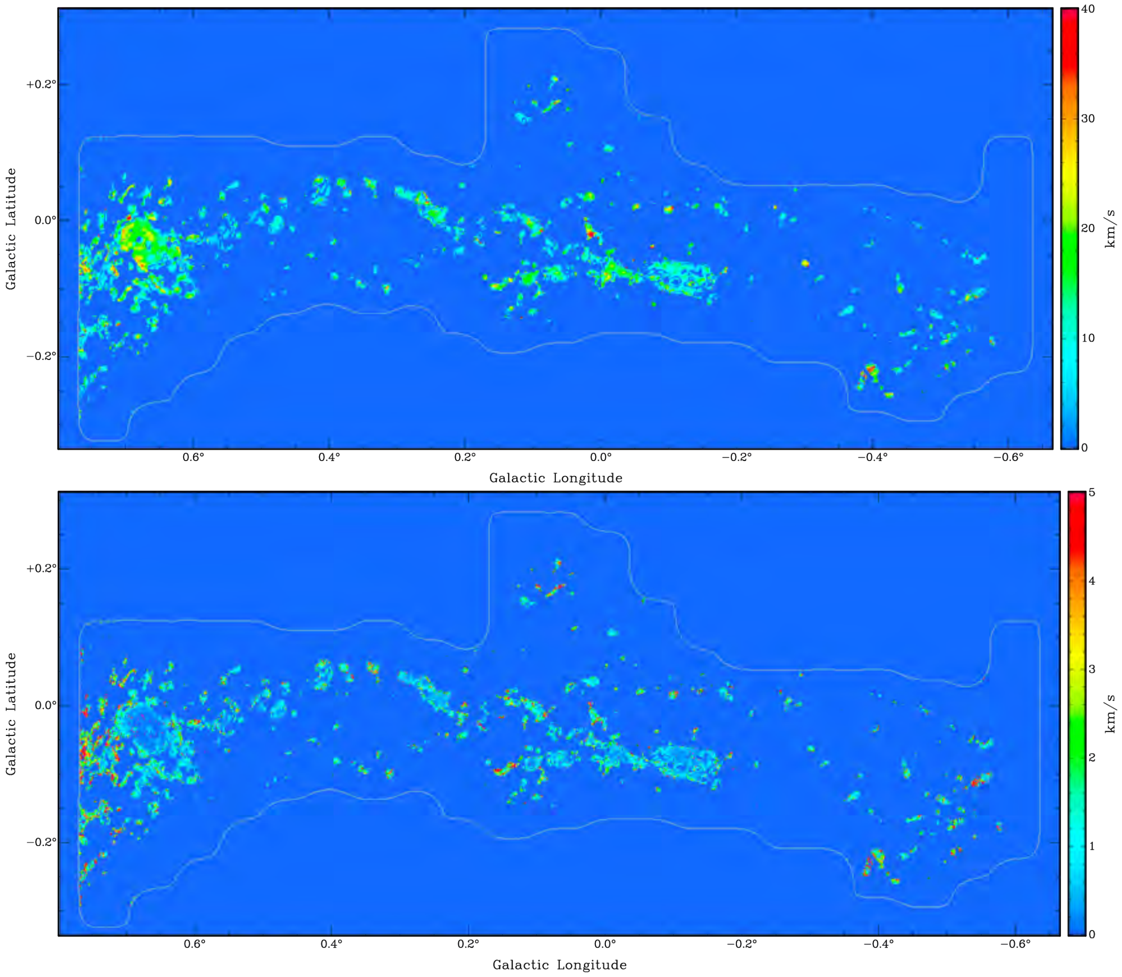

Figure A.67: Line width (FWHM) map (*top*) and error map (*bottom*) of NH_3 (5,5)

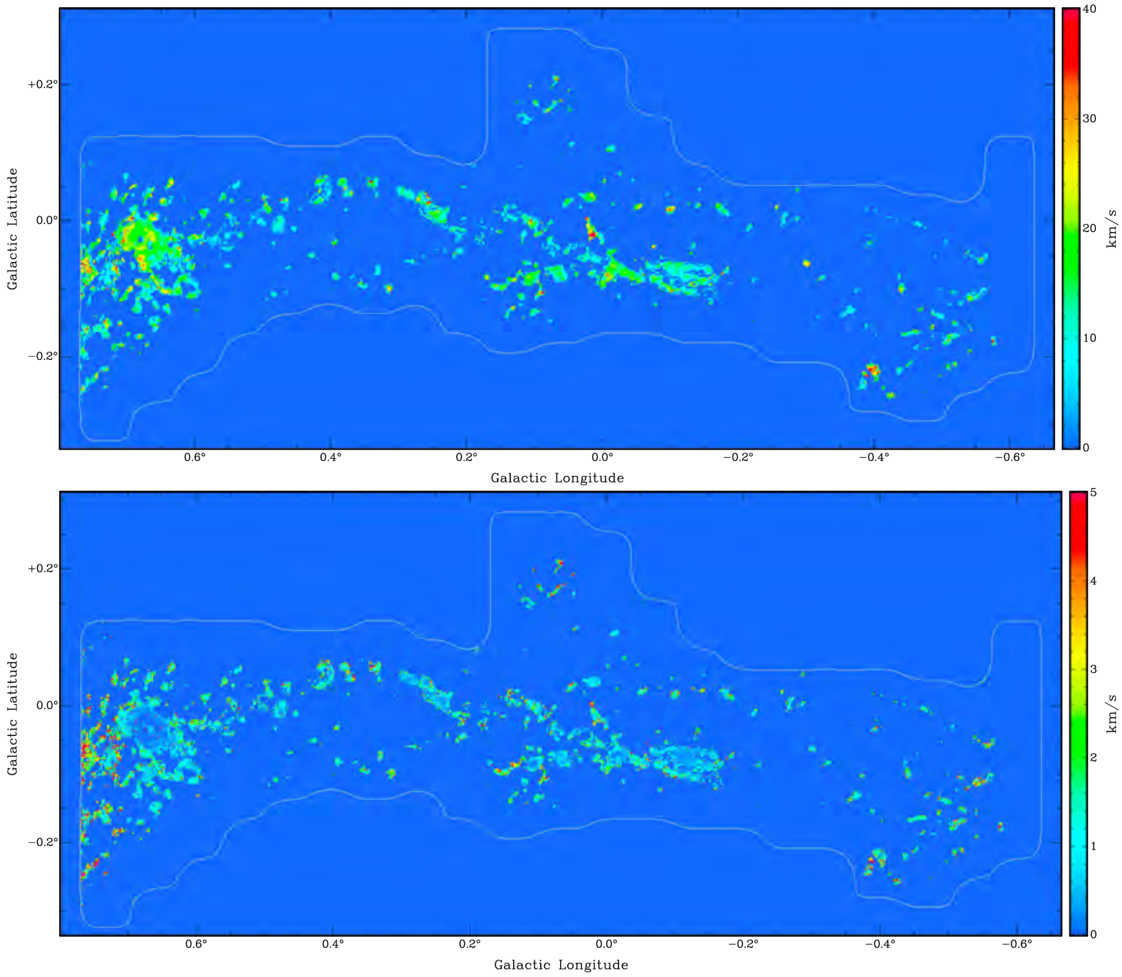

Figure A.68: Line width (FWHM) map (*top*) and error map (*bottom*) of NH_3 (6,6)

A.2.0.3 Column Density

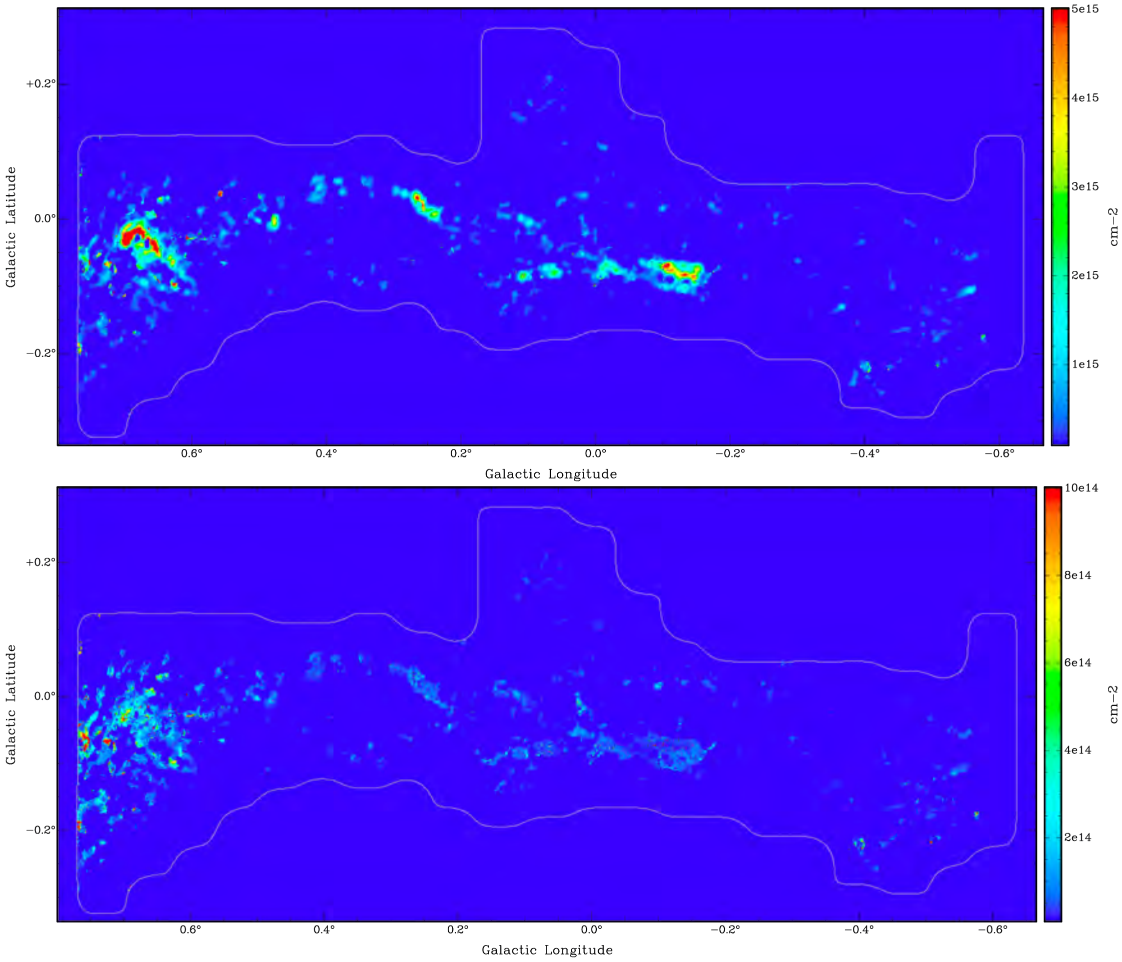

Figure A.69: Column density map (*top*) and error map (*bottom*) of NH_3 (1,1)

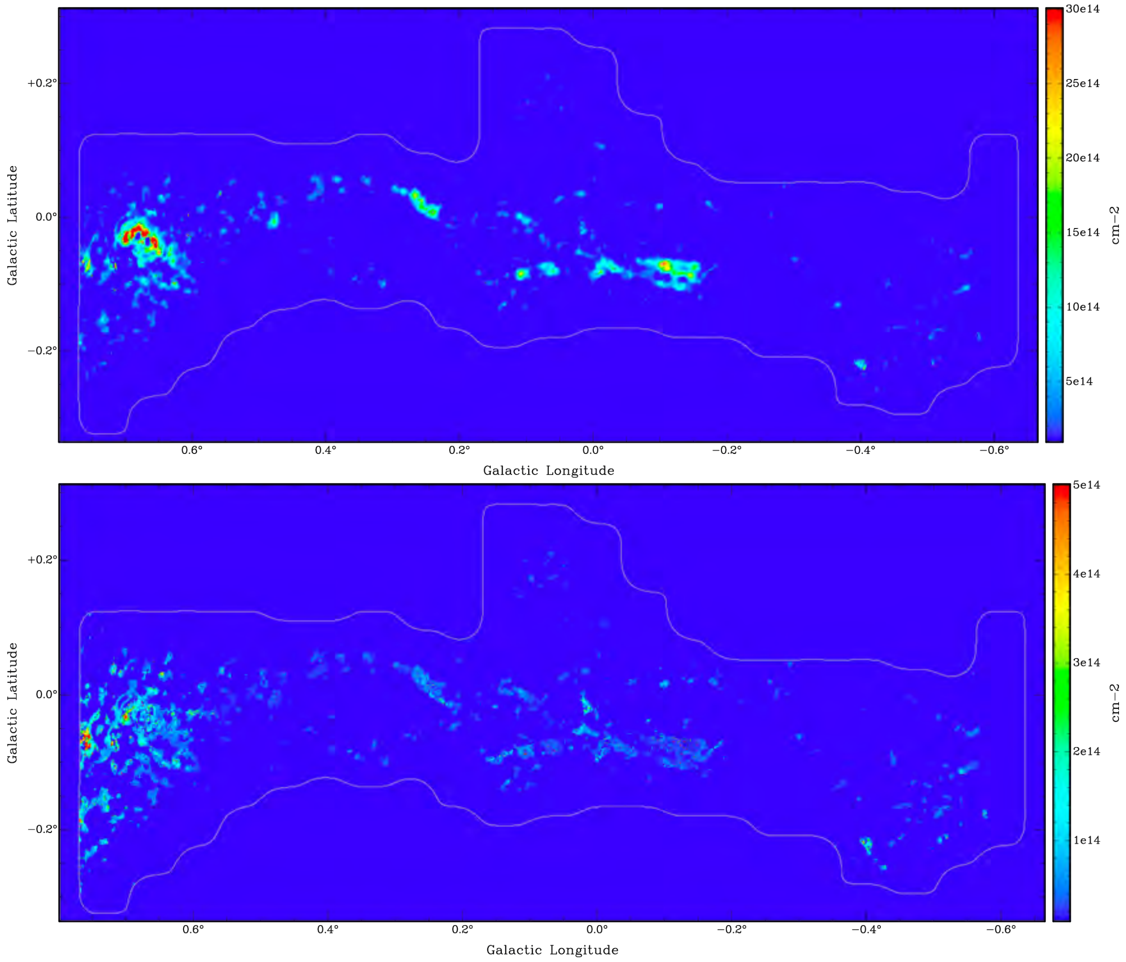

Figure A.70: Column density map (*top*) and error map (*bottom*) of NH_3 (2,2)

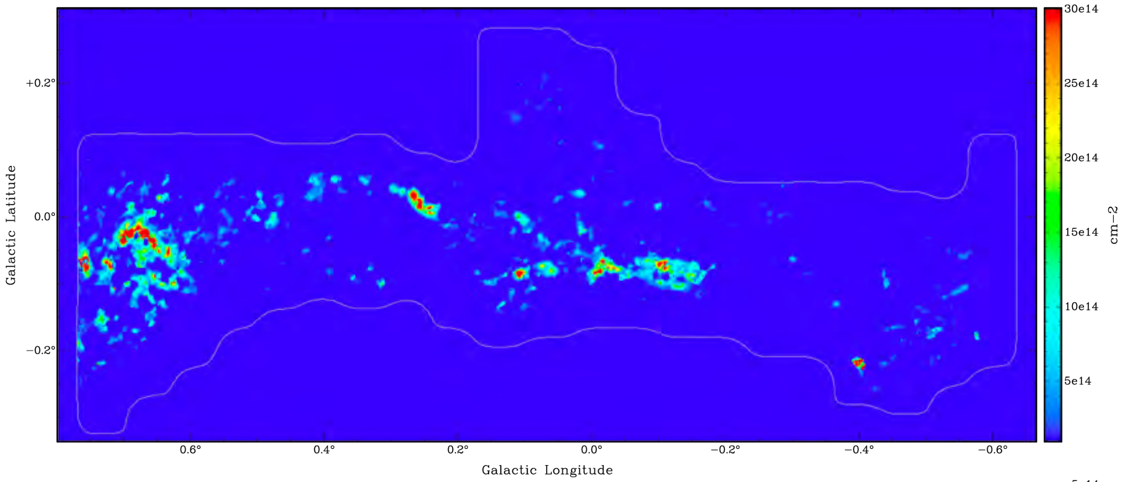

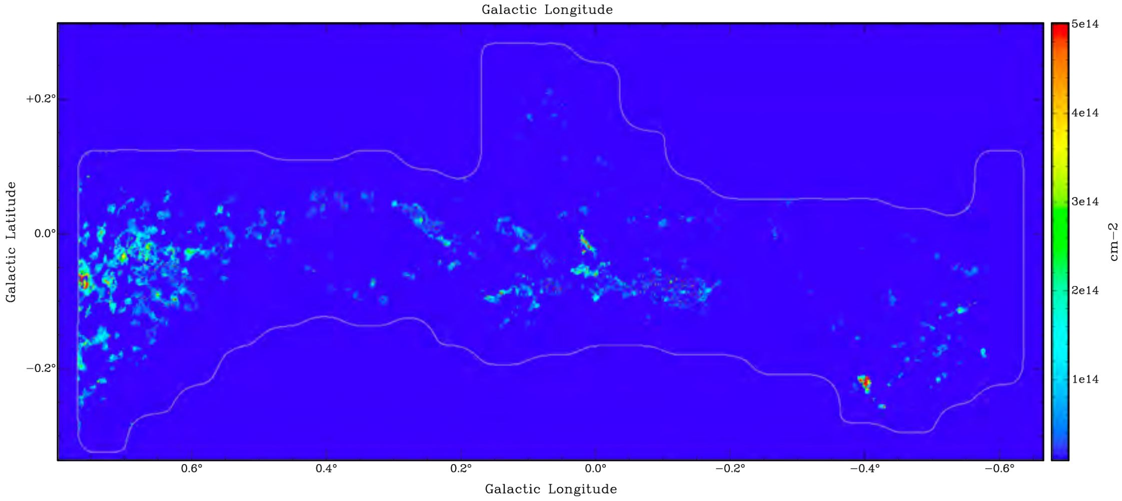

Figure A.71: Column density map (*top*) and error map (*bottom*) of NH_3 (3,3)

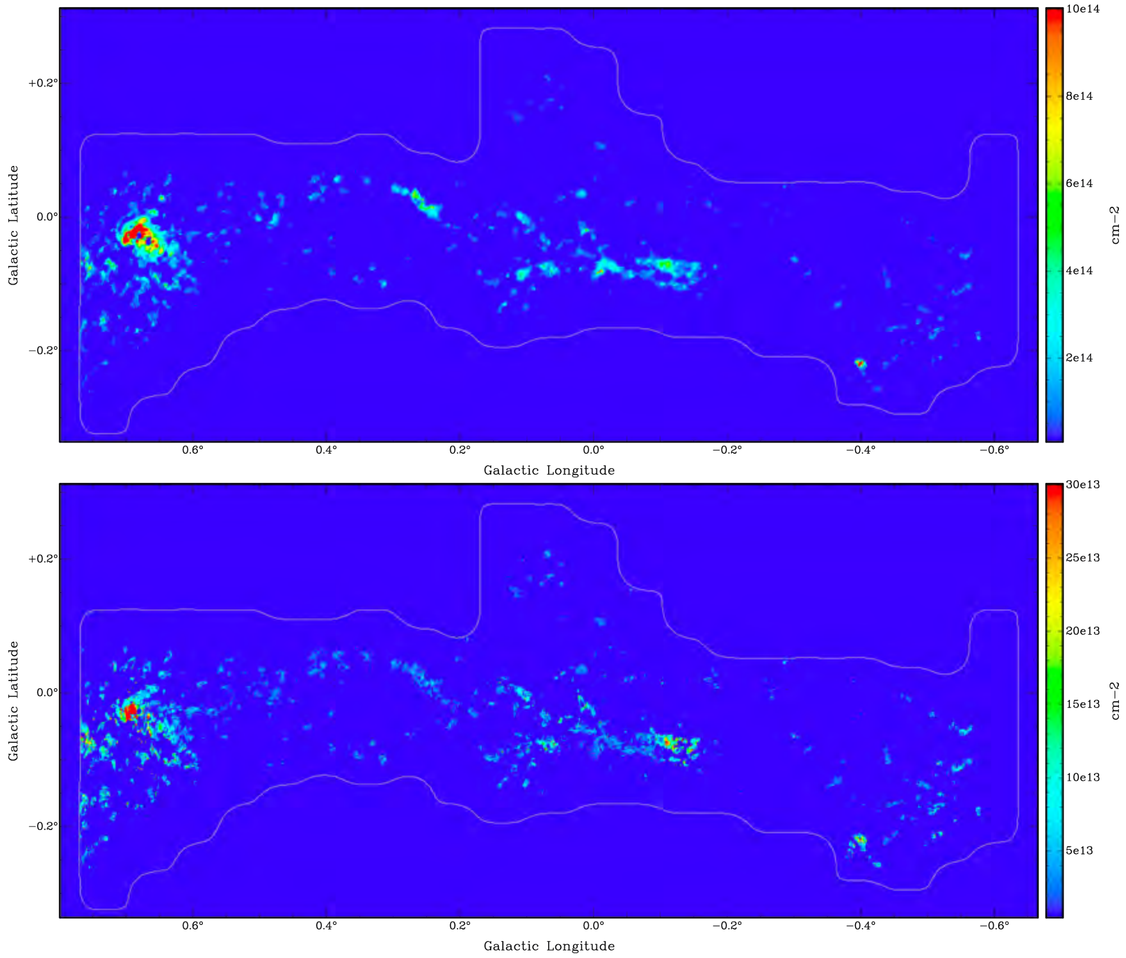

Figure A.72: Column density map (*top*) and error map (*bottom*) of NH_3 (4,4)

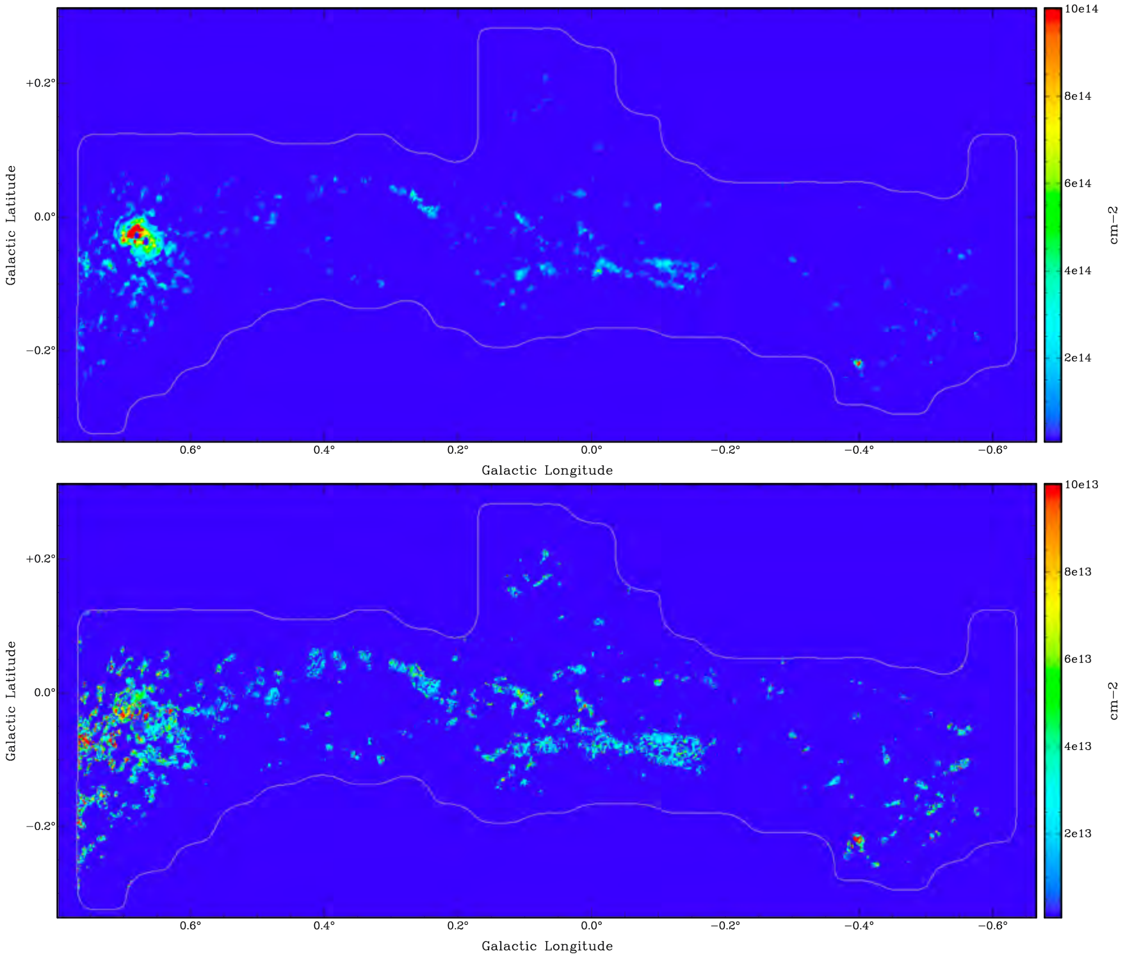

Figure A.73: Column density map (*top*) and error map (*bottom*) of NH_3 (5,5)

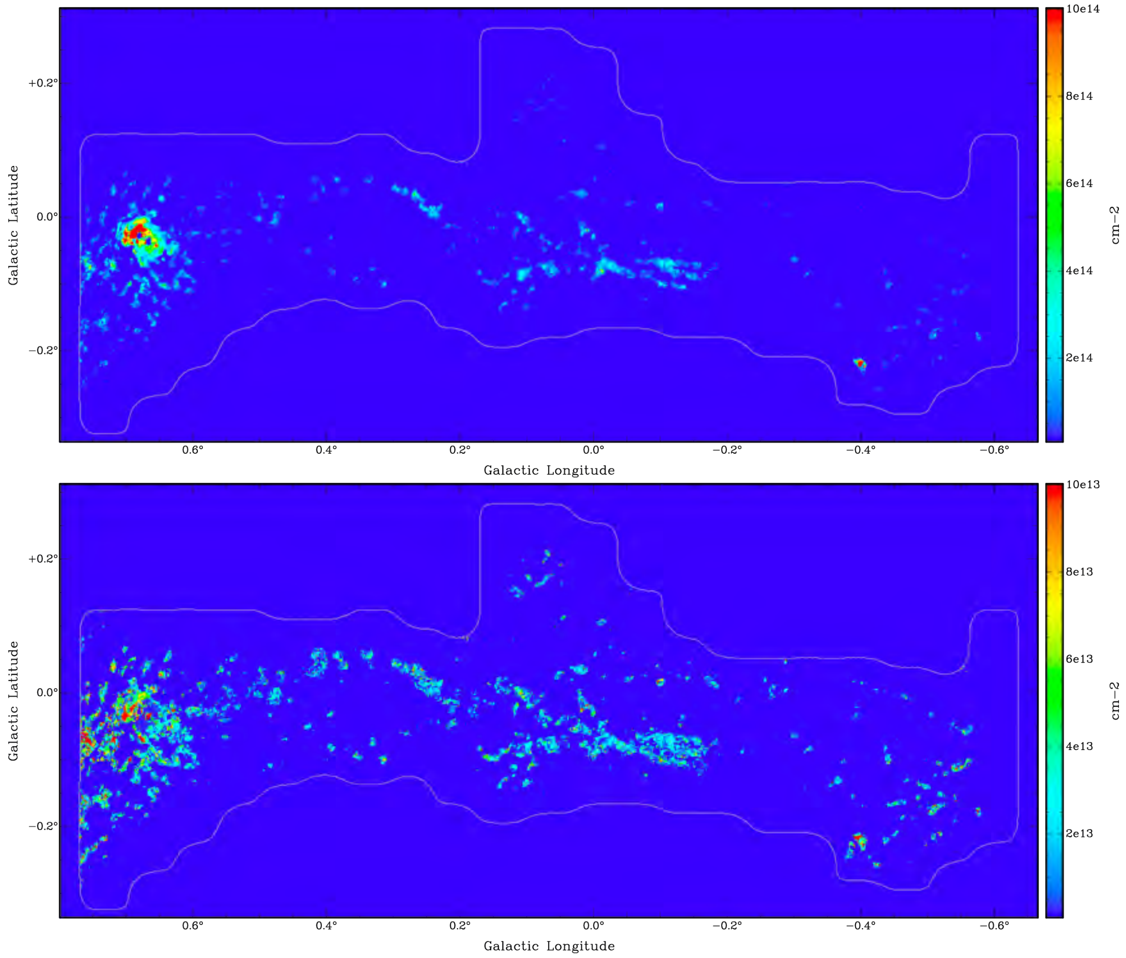

Figure A.74: Column density map (*top*) and error map (*bottom*) of NH_3 (6,6)

A.2.0.4 Opacity

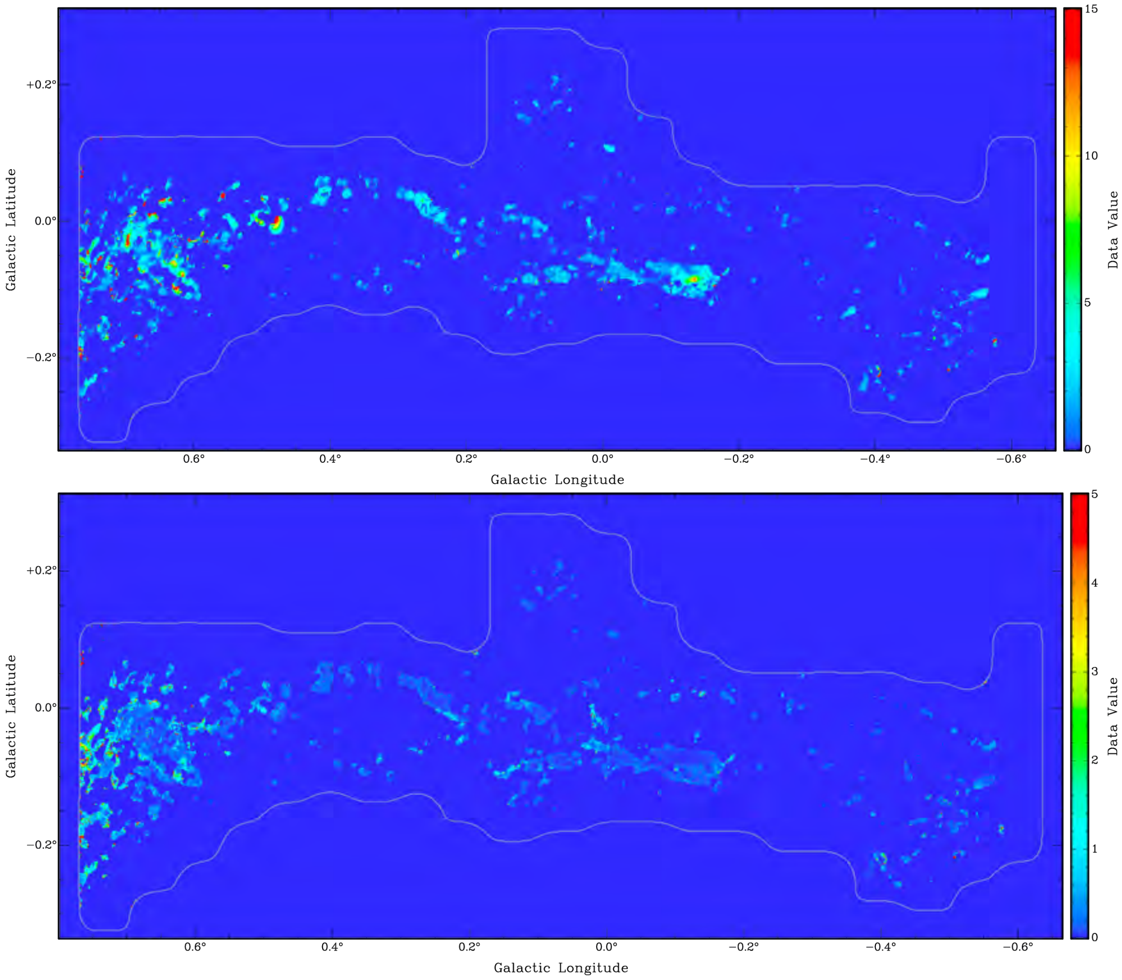

Figure A.75: Opacity map (*top*) and error map (*bottom*) of NH_3 (1,1)

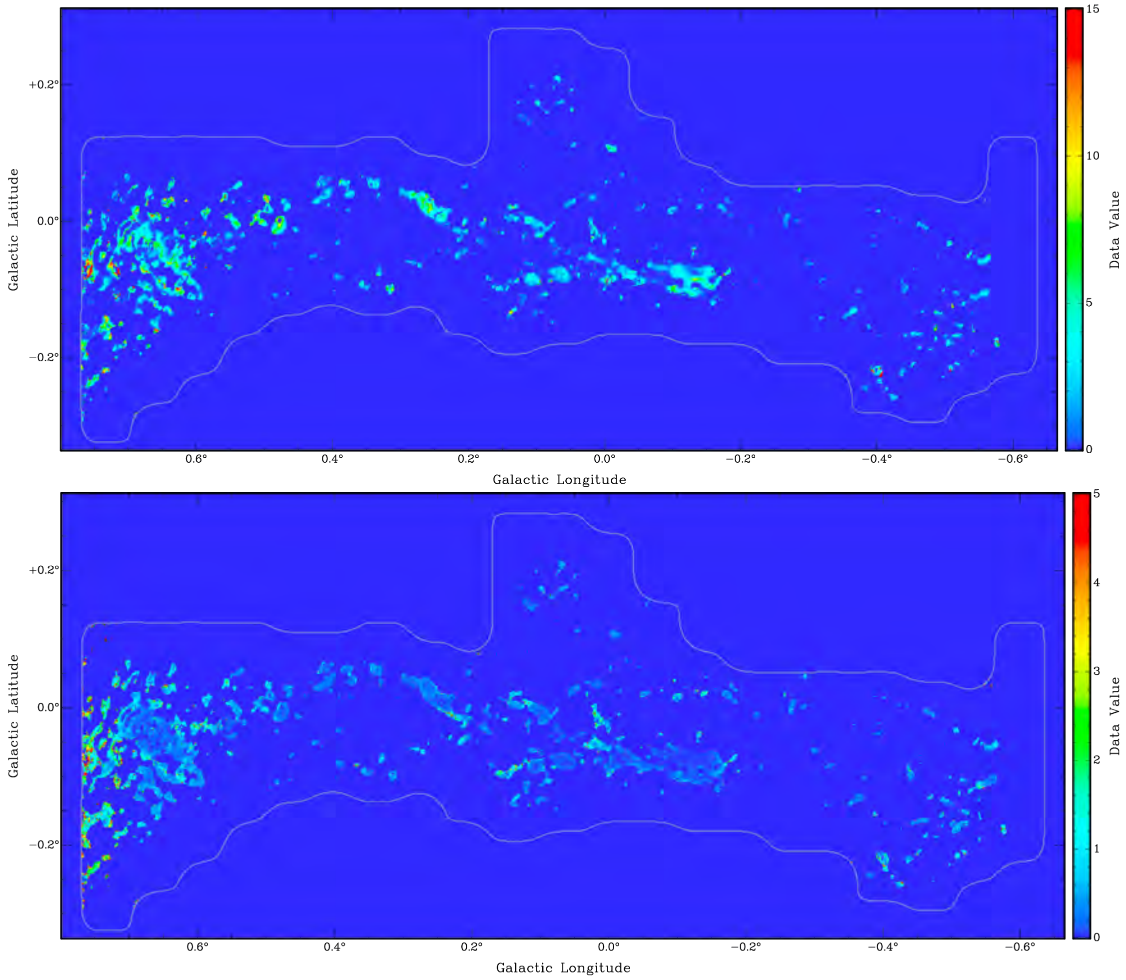

Figure A.76: Opacity map (*top*) and error map (*bottom*) of NH_3 (2,2)

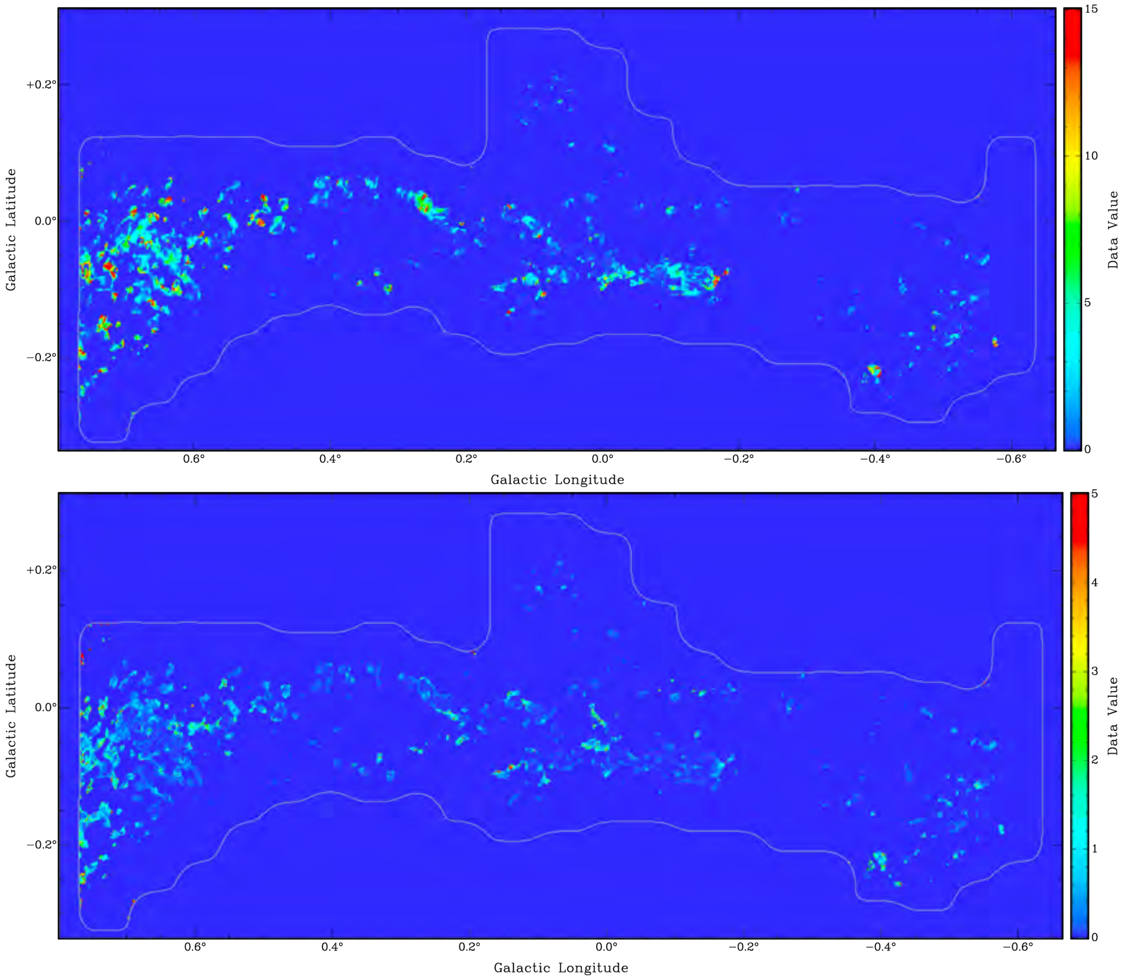

Figure A.77: Opacity map (*top*) and error map (*bottom*) of NH_3 (3,3)

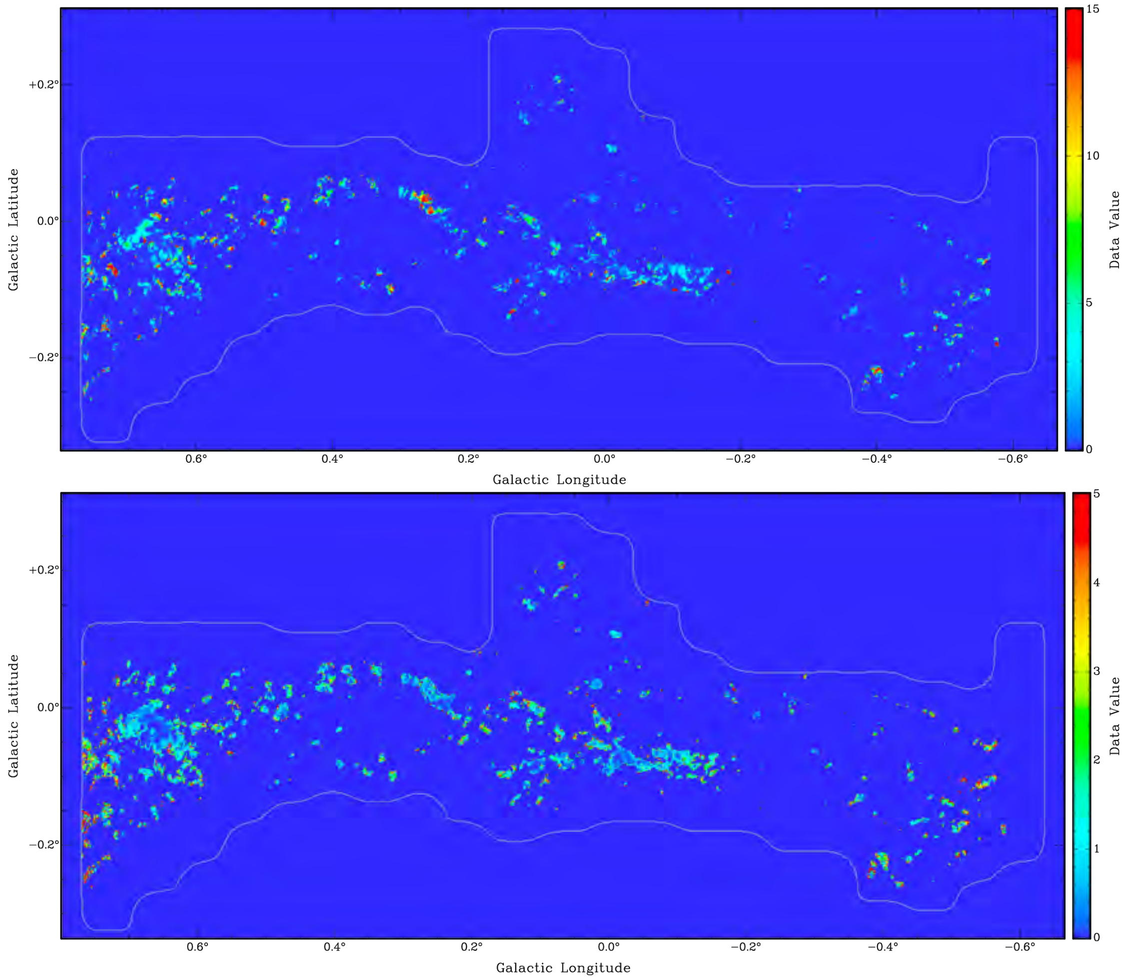

Figure A.78: Opacity map (*top*) and error map (*bottom*) of NH_3 (4,4)

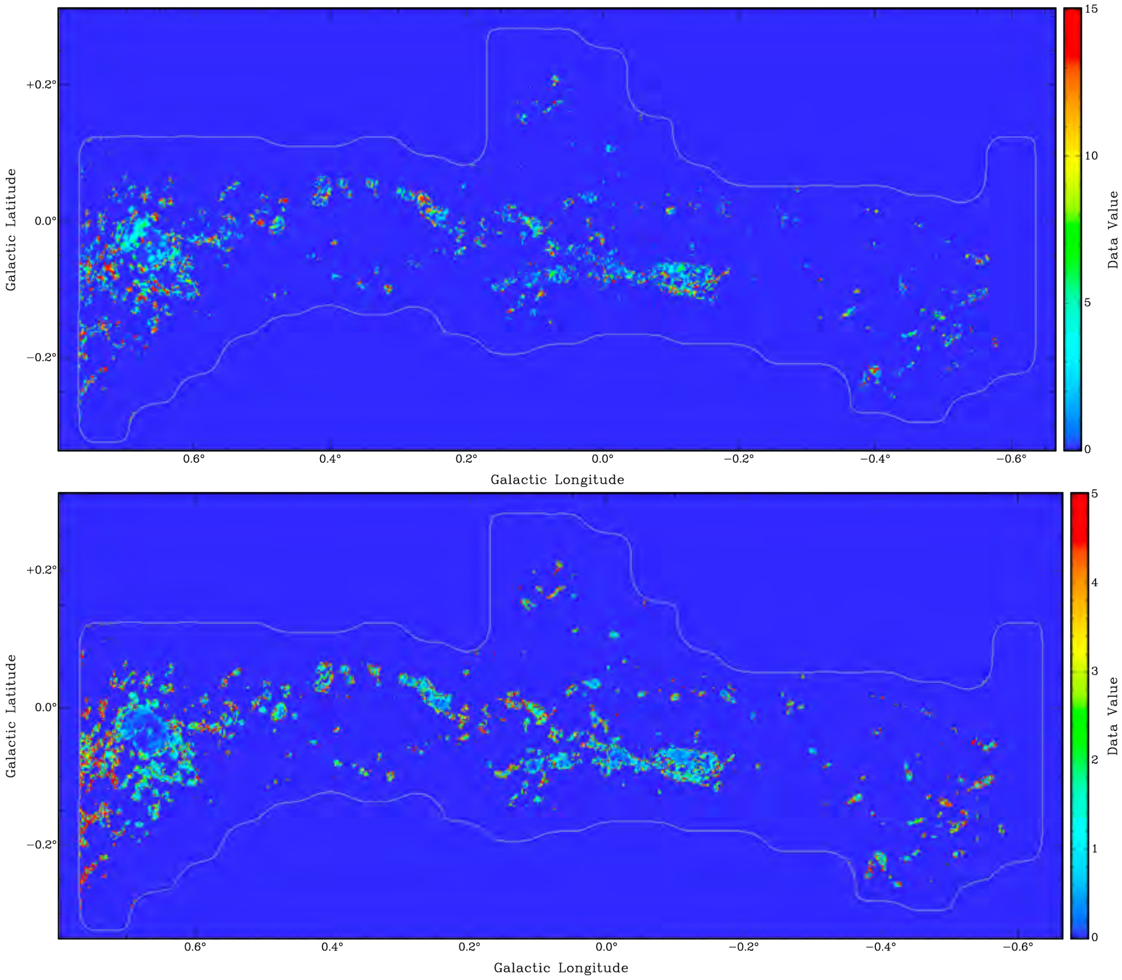

Figure A.79: Opacity map (*top*) and error map (*bottom*) of NH_3 (5,5)

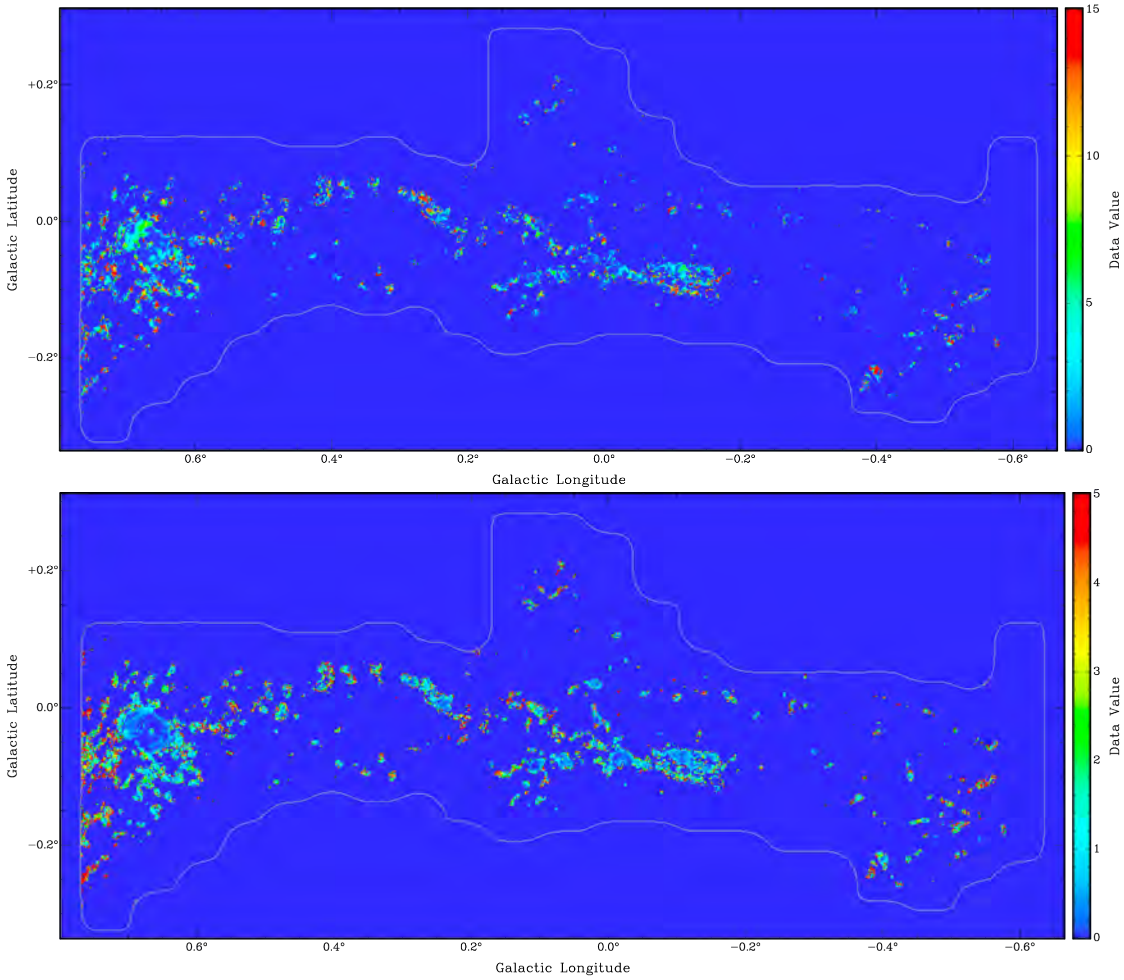

Figure A.80: Opacity map (*top*) and error map (*bottom*) of NH_3 (6,6)

A.2.0.5 Temperature

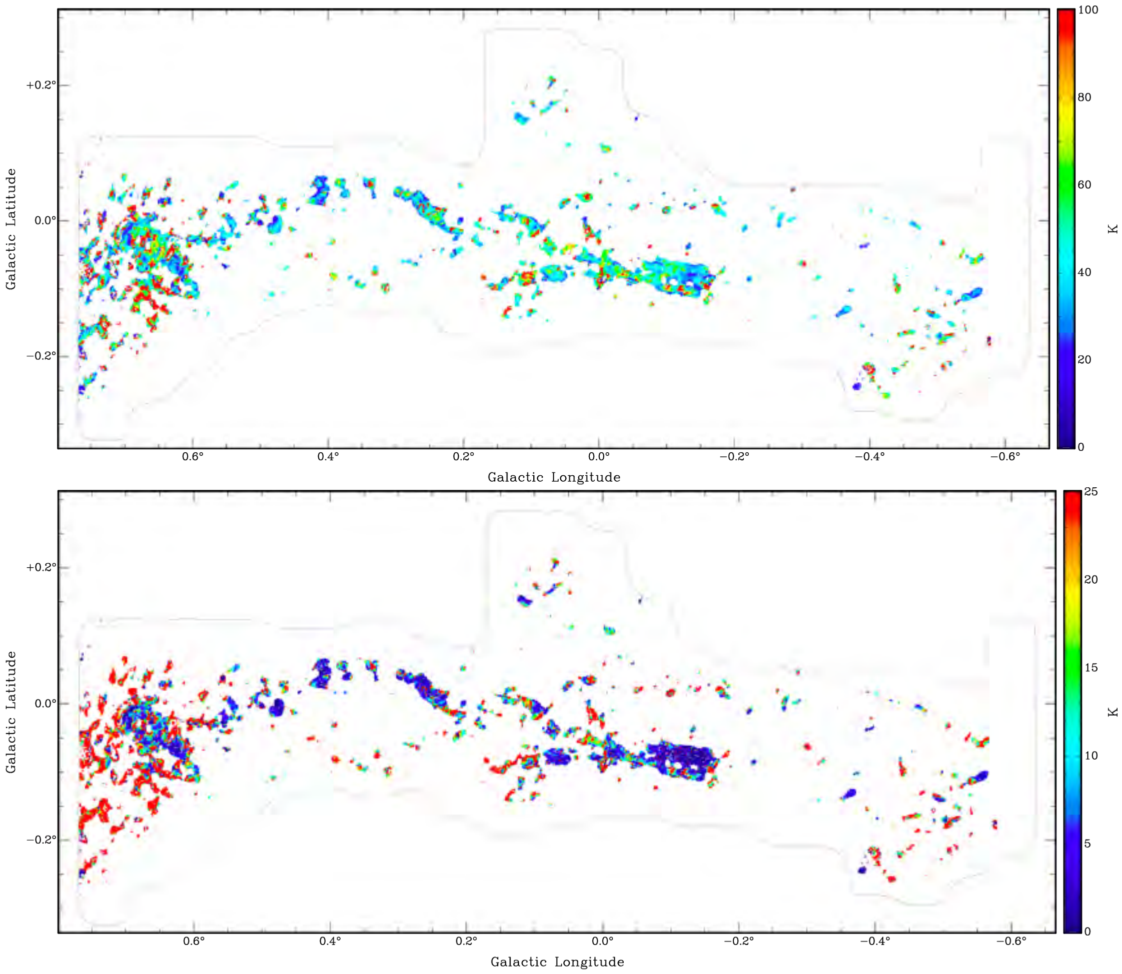

Figure A.81: T_{12} map (*top*) and error map (*bottom*)

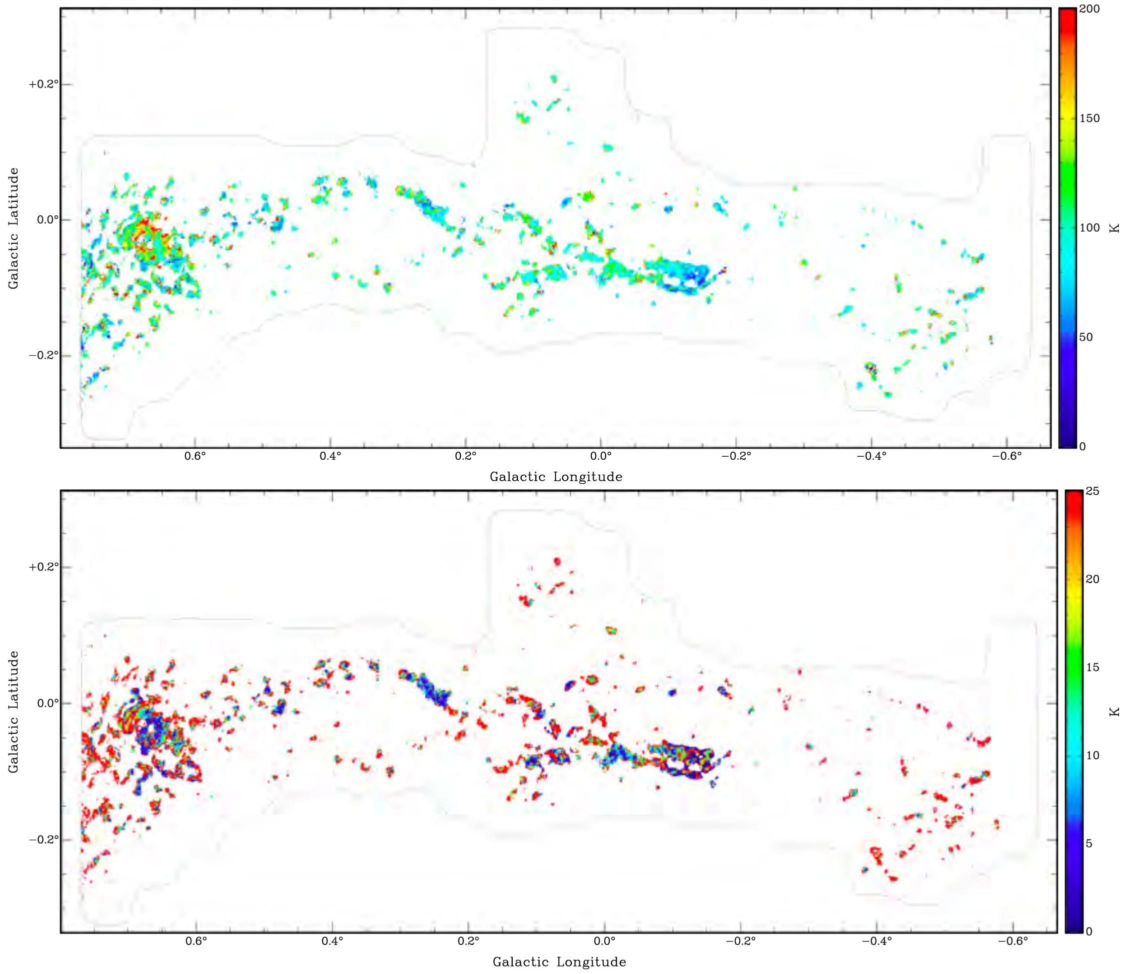

Figure A.82: T_{24} map (*top*) and error map (*bottom*)

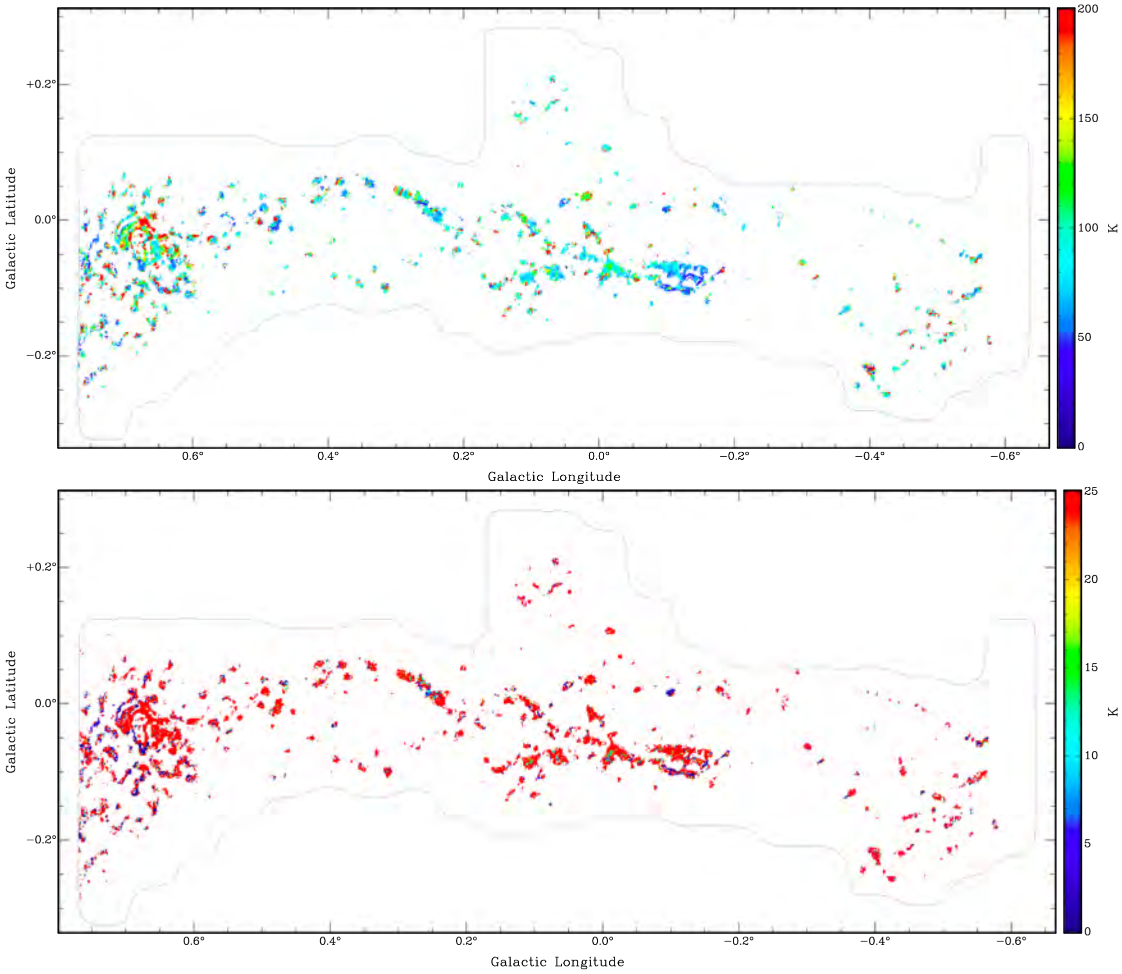

Figure A.83: T_{45} map (*top*) and error map (*bottom*)

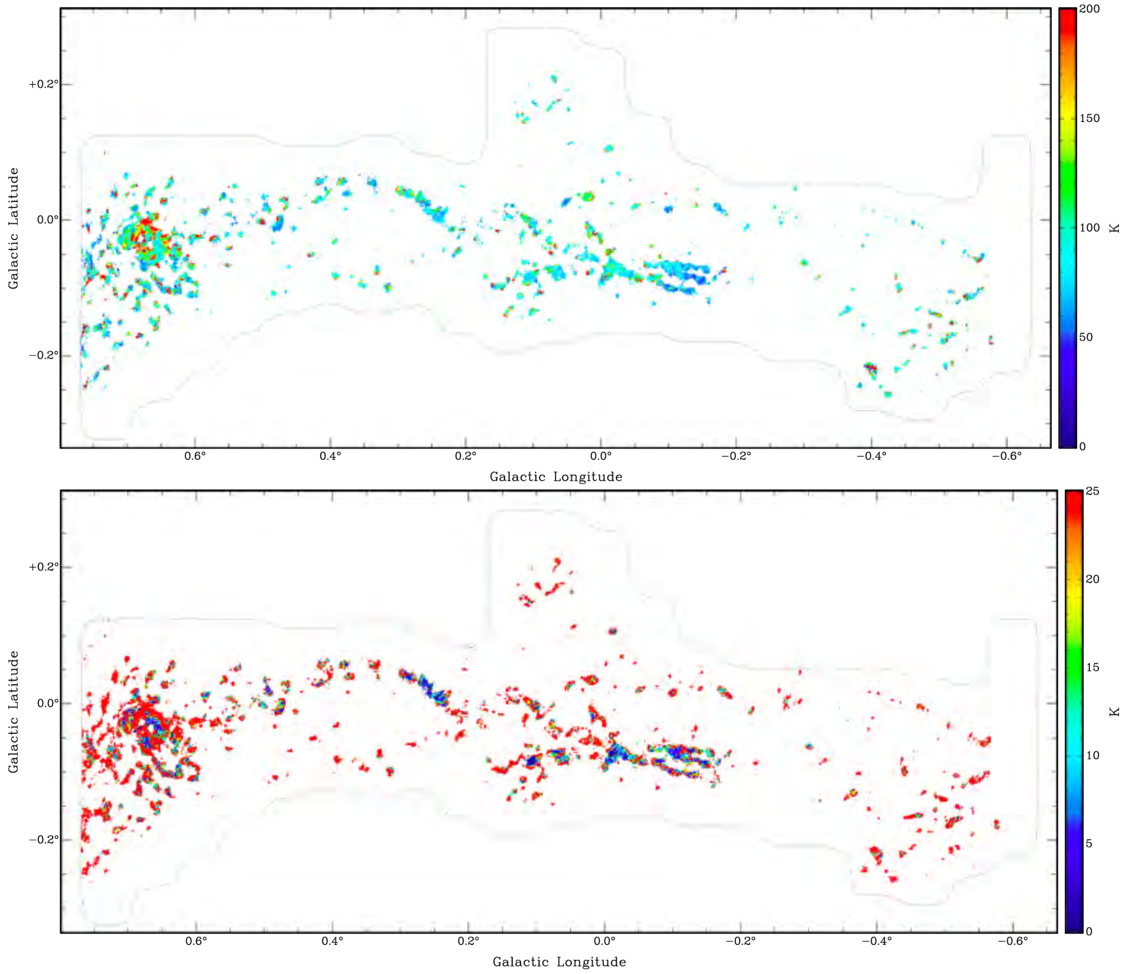

Figure A.84: T_{36} map (*top*) and error map (*bottom*)

B More Plots on the Star Formation Sequence

This appendix contains the plots corresponding chapter 3 for T_{12}, T_{45} and T_{36} and higher ammonia lines (J = 2, ..., 6).

B.1 Time vs. NH_3 Temperature

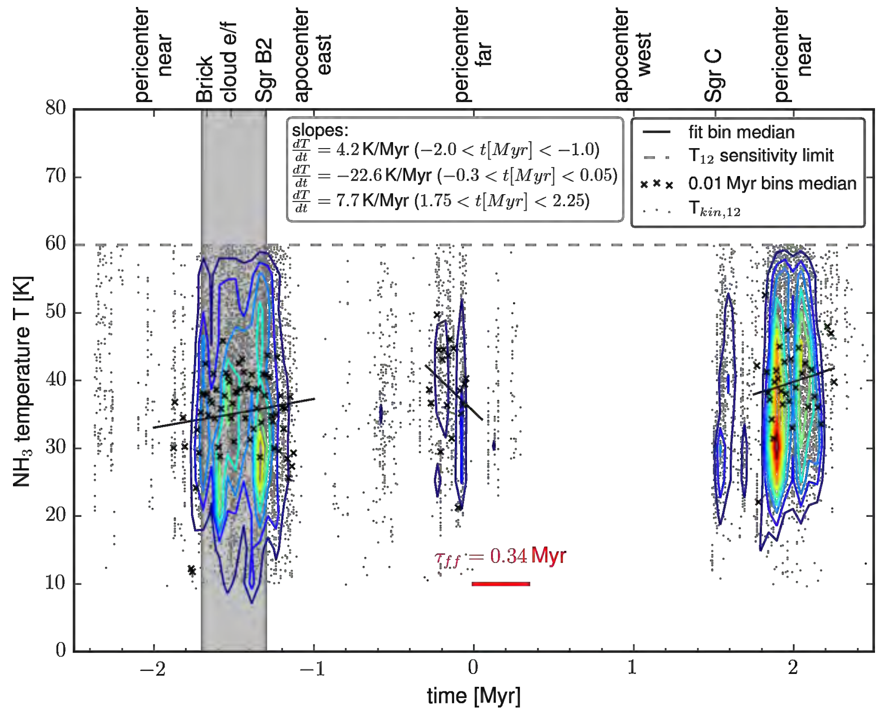

Figure B.1: T_{12} as a function of time since far side pericenter passage.

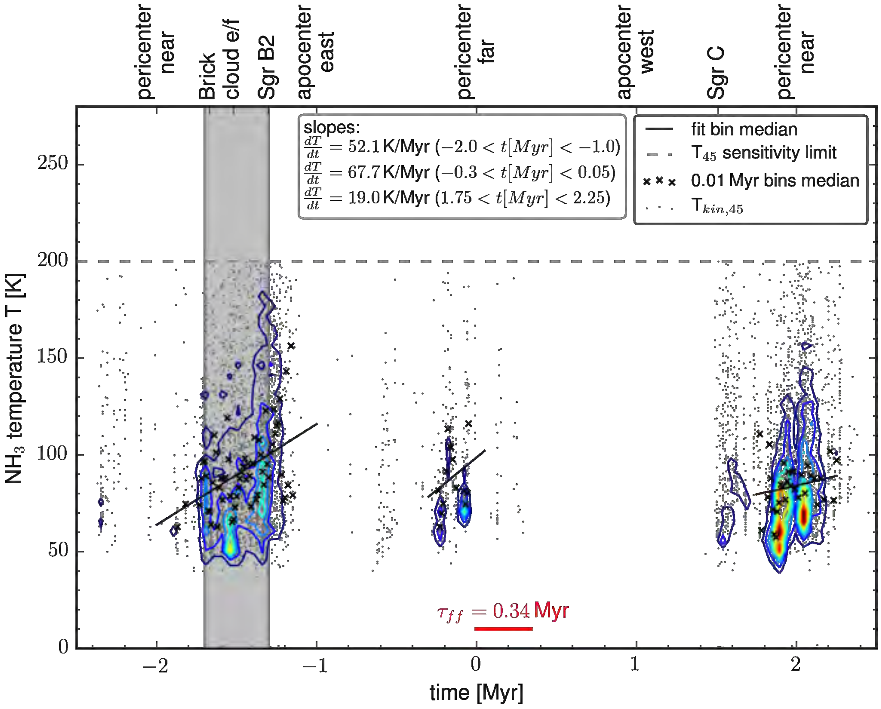

Figure B.2: T_{45} as a function of time since far side pericenter passage.

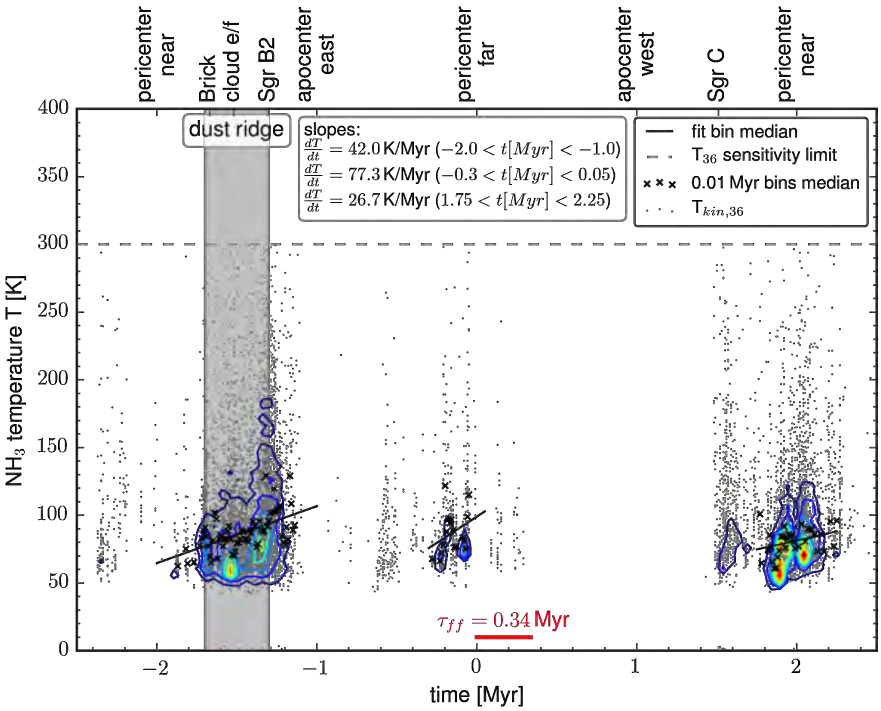

Figure B.3: T_{36} as a function of time since far side pericenter passage.

B.2 Phase vs. NH_3 Temperature

The following plots show ammonia temperature vs. time since last pericenter passage. The respective plot with T_{24} is already shown as fig. 3.21 in §3.3.

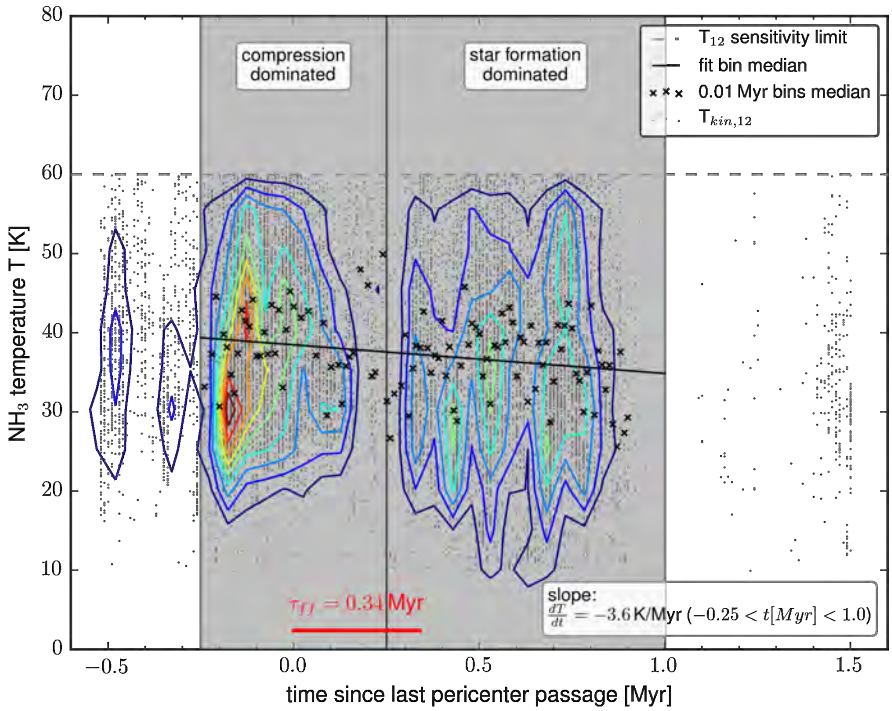

Figure B.4: Ammonia temperature T_{12} evolution along time since the last occurrence of pericenter passage.

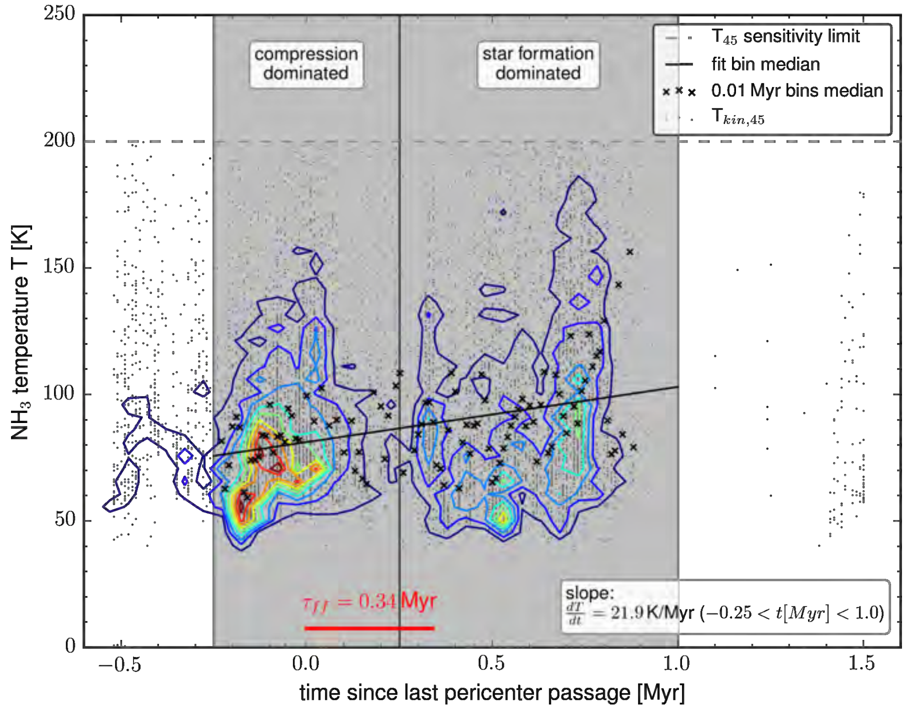

Figure B.5: Ammonia temperature T_{45} evolution along time since the last occurrence of pericenter passage.

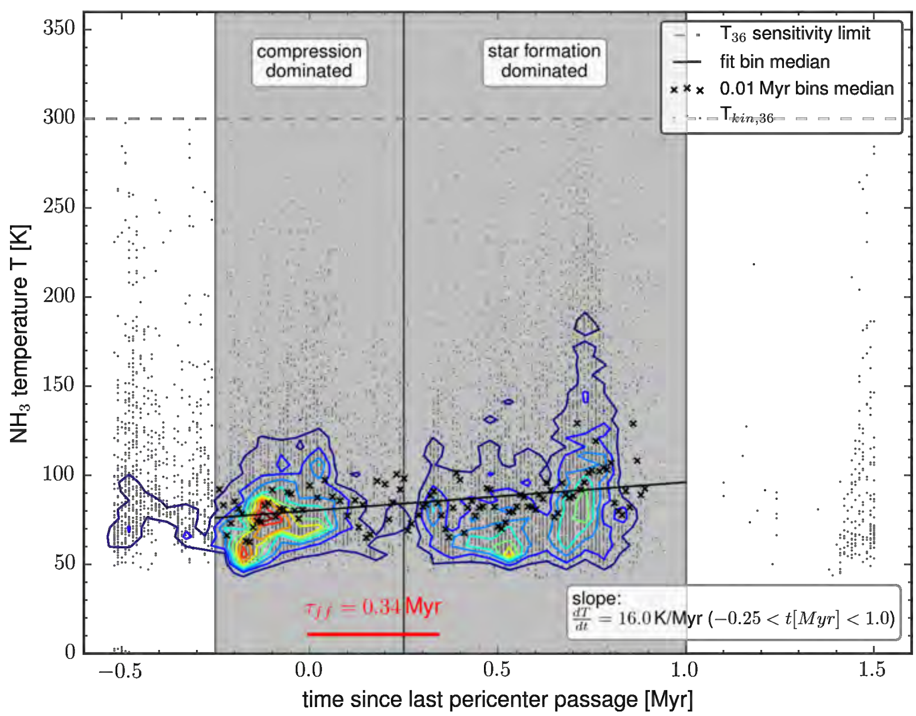

Figure B.6: Ammonia temperature T_{36} evolution along time since the last occurrence of pericenter passage.

B.3 $\mathbf{T}_{dust}$ vs. $\mathbf{T}_{NH3}$

The relation of Hi-GAL dust temperature to T_{24} is shown in §3.3. Corresponding plots for T_{12}, T_{45} and T_{36} can be found on the following pages.

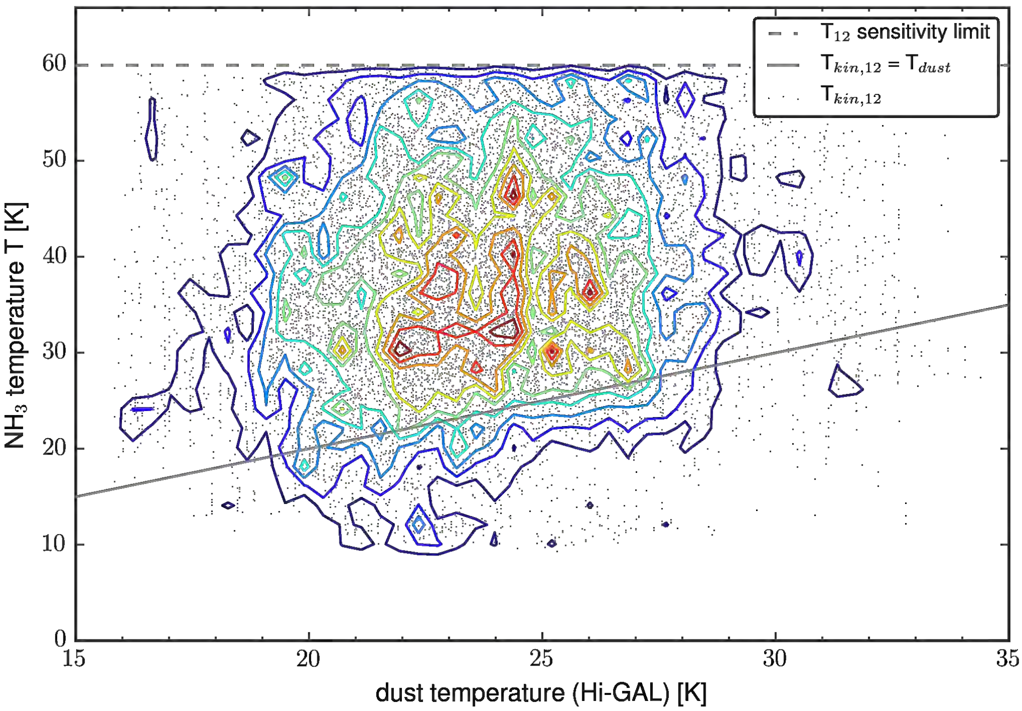

Figure B.7: Dust temperature T_{dust} as a function of NH_3 temperature T_{12}.

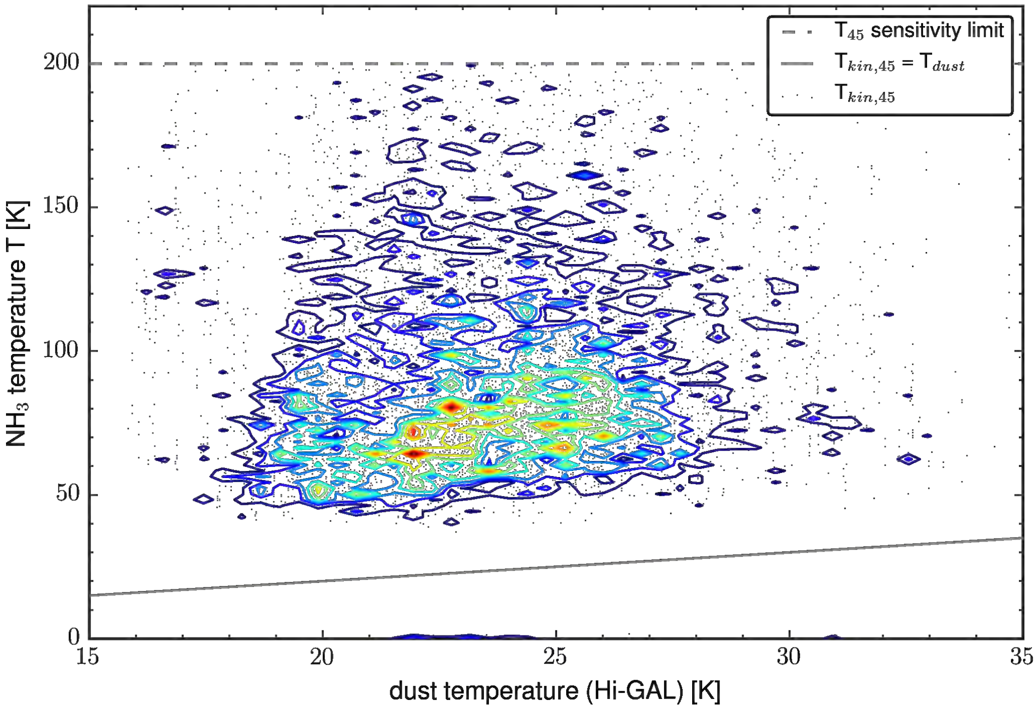

Figure B.8: Dust temperature T_{dust} as a function of NH_3 temperature T_{45}.

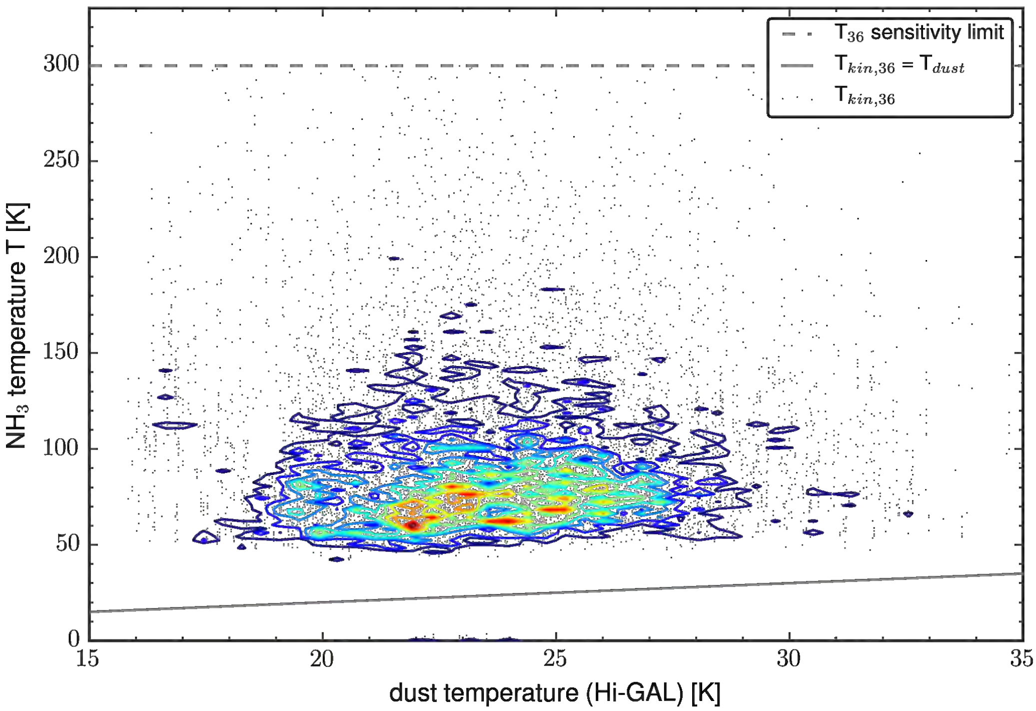

Figure B.9: Dust temperature T_{dust} as a function of NH_3 temperature T_{36}.

B.4 Time vs. NH_3 FWHM

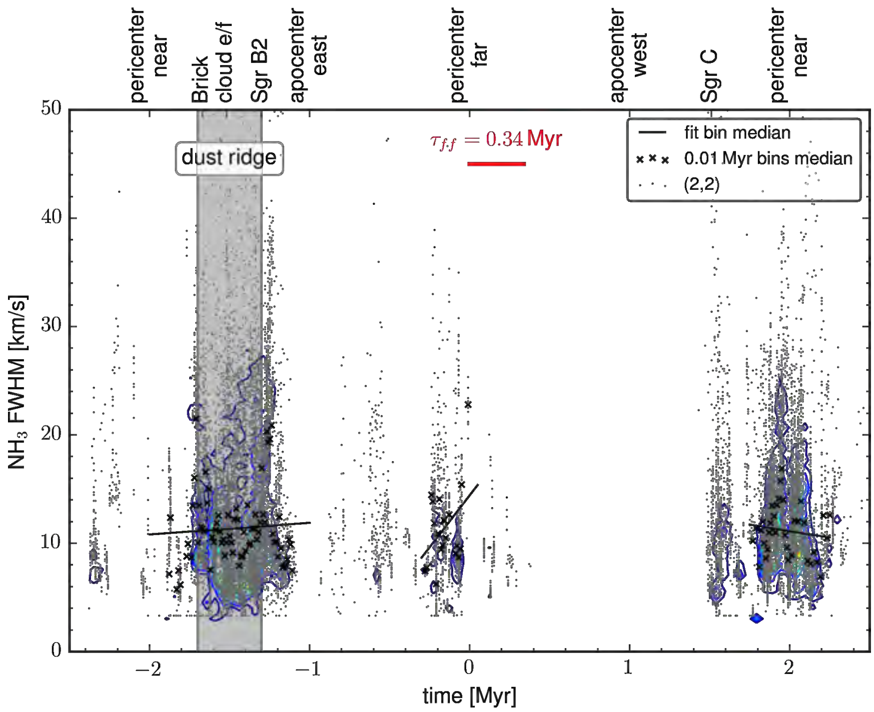

Figure B.10: NH_3 (2,2) FWHM as a function of time since far side pericenter passage.

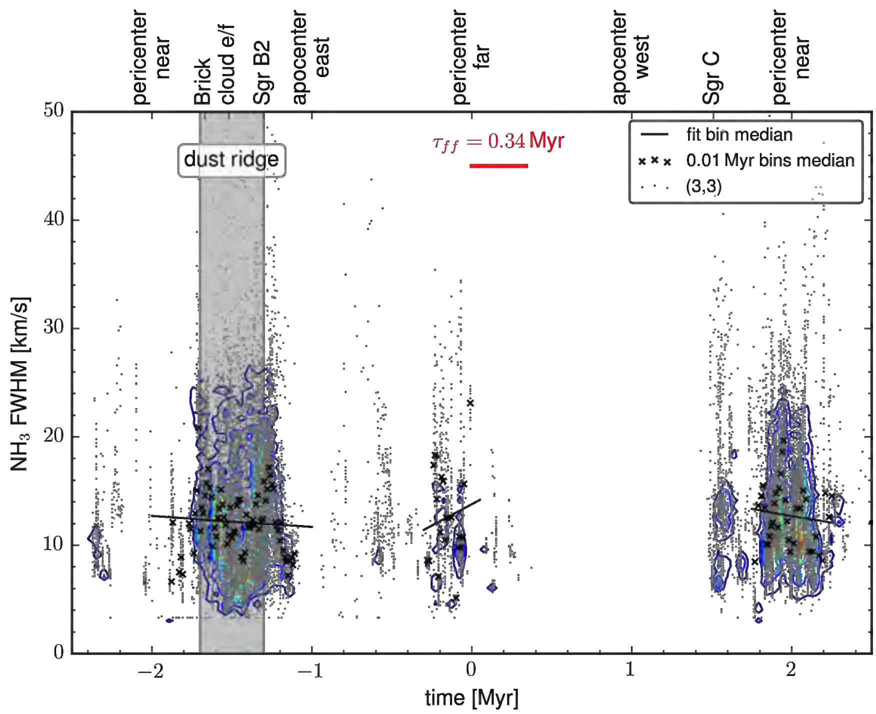

Figure B.11: NH_3 (3,3) FWHM as a function of time since far side pericenter passage.

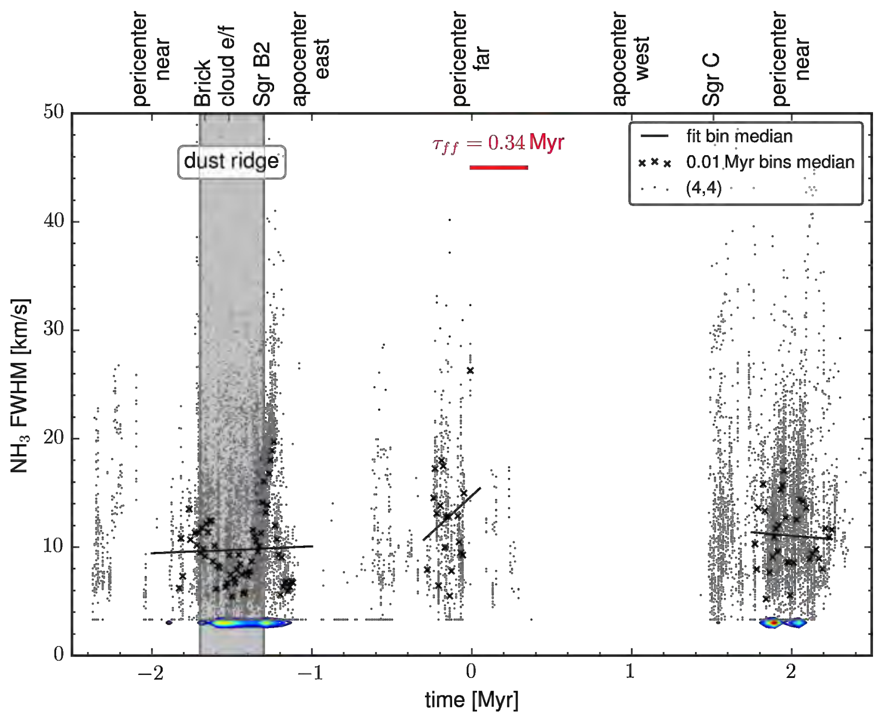

Figure B.12: NH_3 (4,4) FWHM as a function of time since far side pericenter passage.

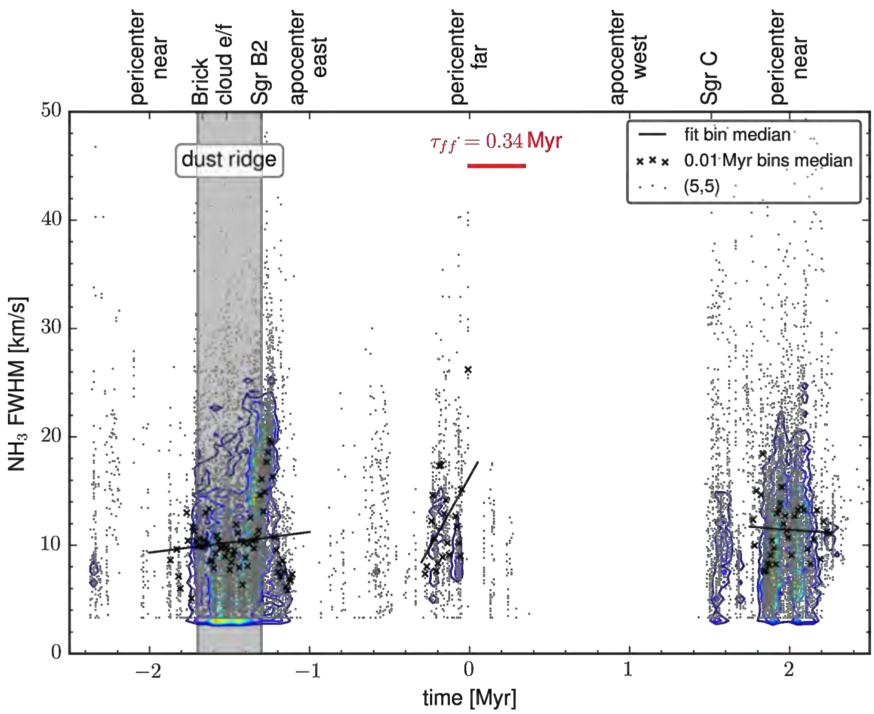

Figure B.13: NH_3 (5,5) FWHM as a function of time since far side pericenter passage.

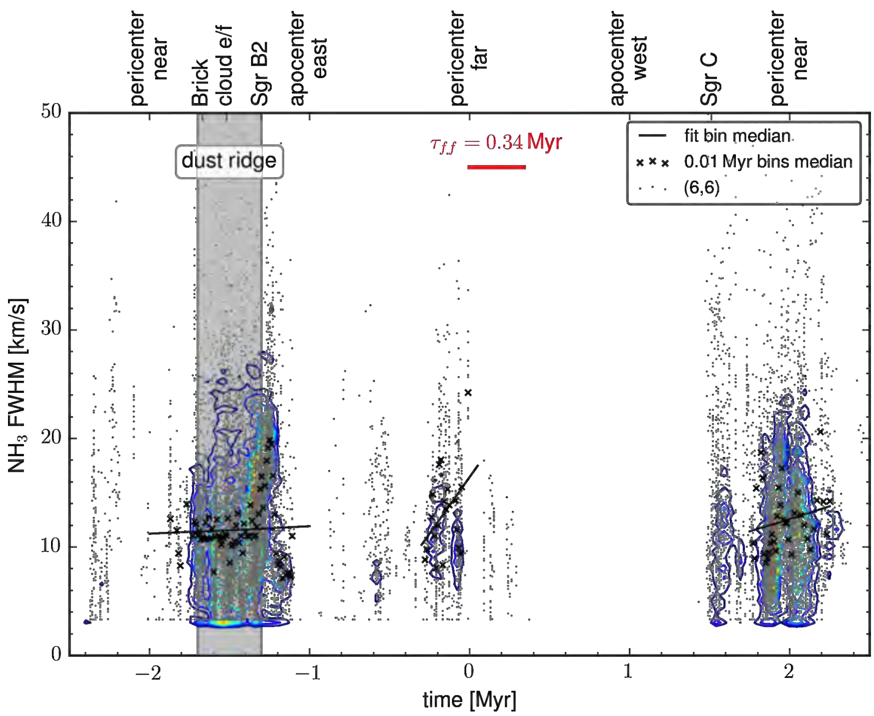

Figure B.14: NH_3 (6,6) FWHM as a function of time since far side pericenter passage.

B.5 Time vs. NH_3 Opacity

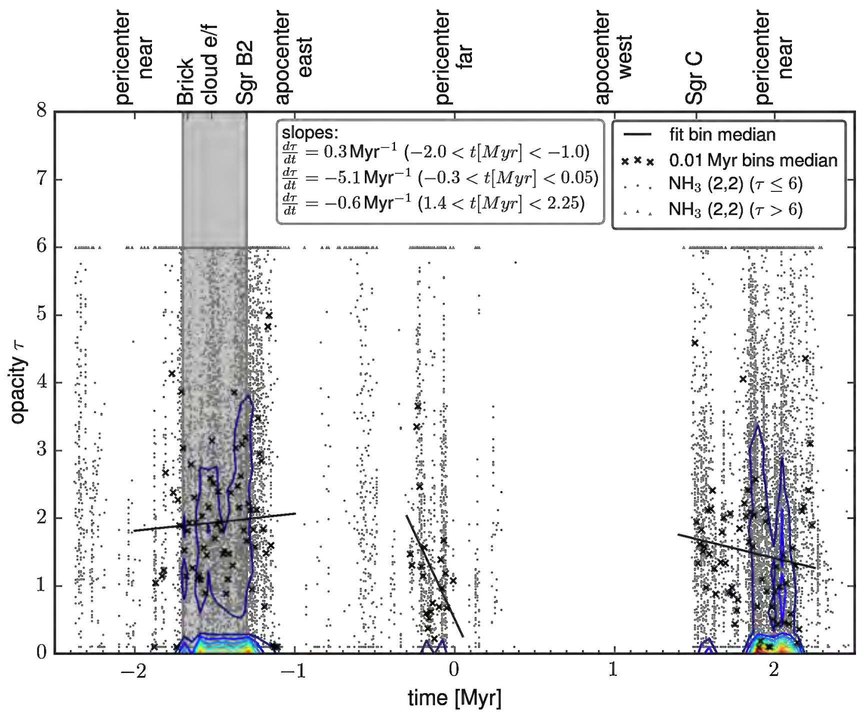

Figure B.15: NH_3 (2,2) opacity as a function of time since far side pericenter passage.

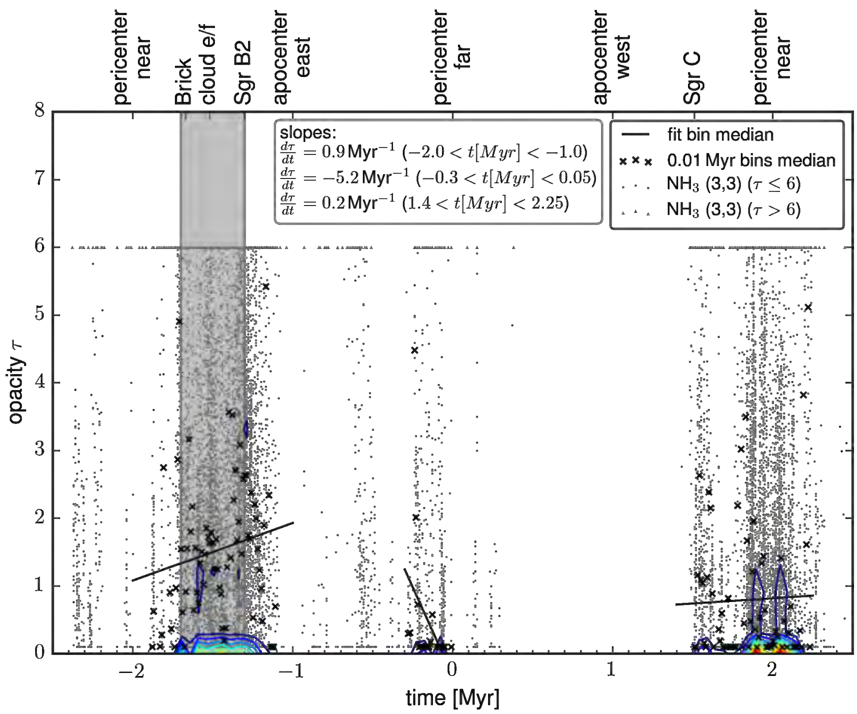

Figure B.16: NH_3 (3,3) opacity as a function of time since far side pericenter passage.

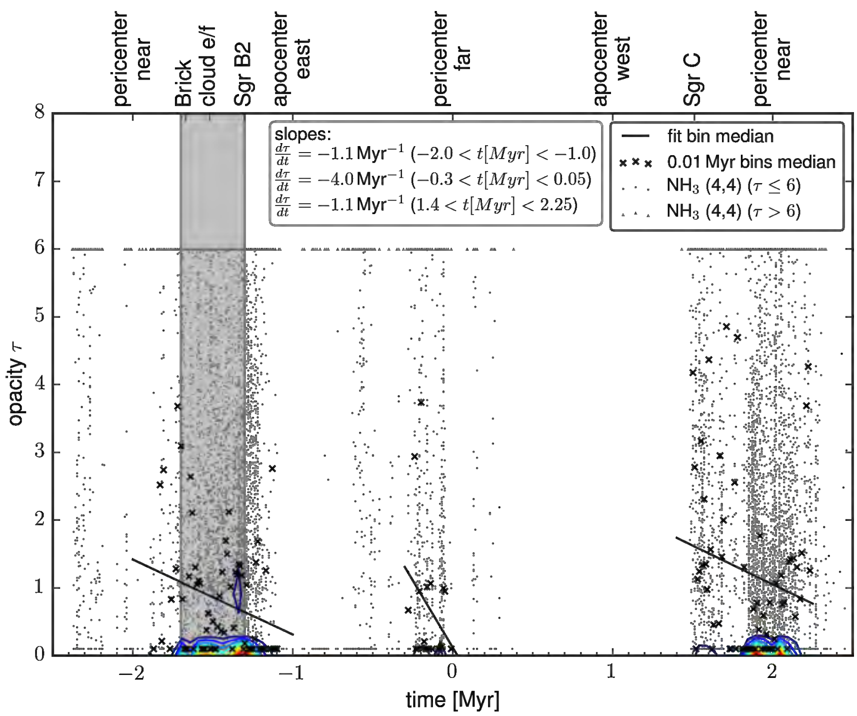

Figure B.17: NH_3 (4,4) opacity as a function of time since far side pericenter passage.

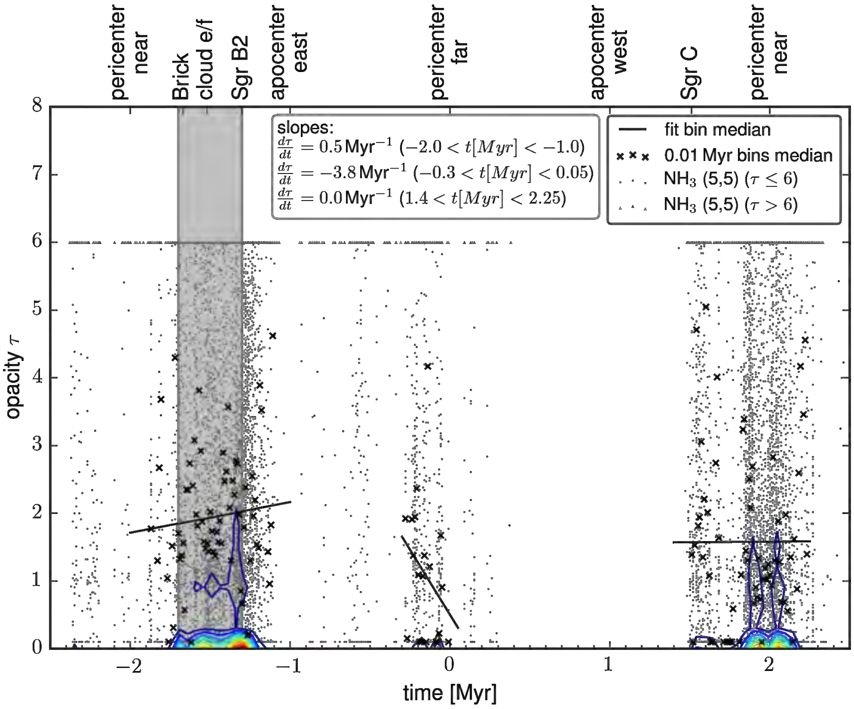

Figure B.18: NH_3 (5,5) opacity as a function of time since far side pericenter passage.

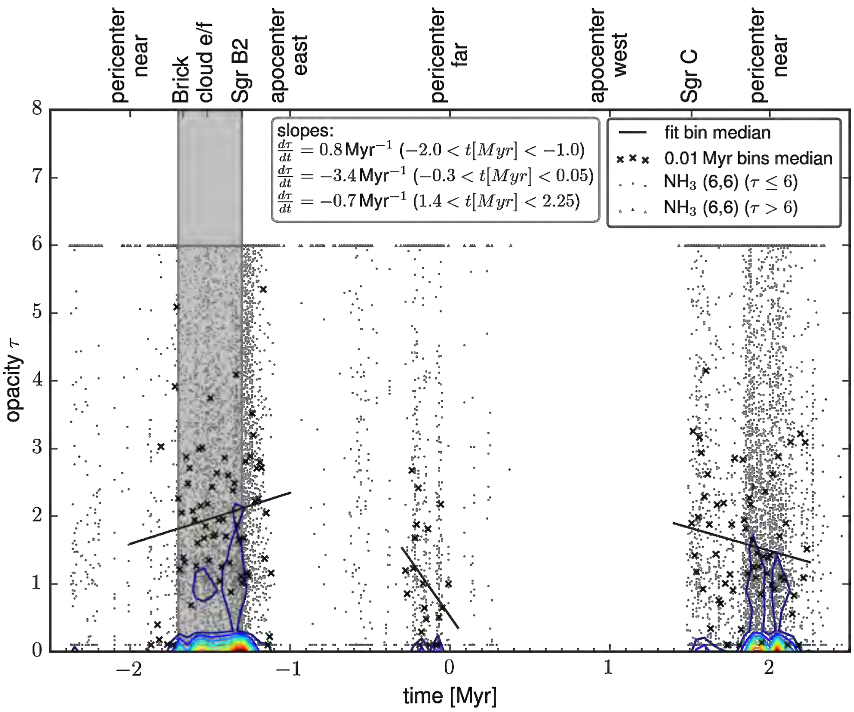

Figure B.19: NH_3 (6,6) opacity as a function of time since far side pericenter passage.

B.6 Time vs. NH_3 Column density

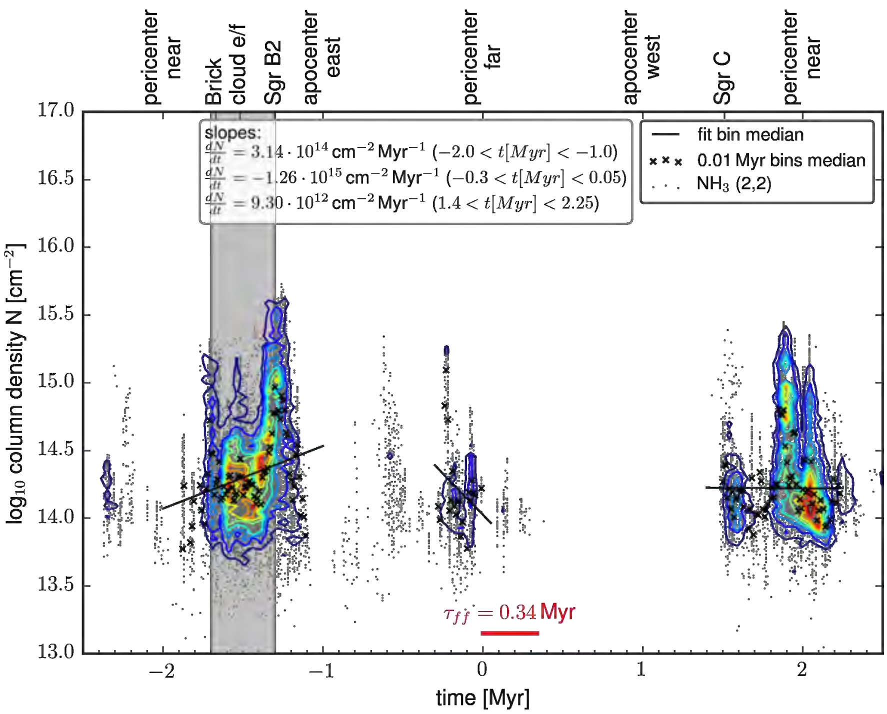

Figure B.20: NH_3 (2,2) column density as a function of time since far side pericenter passage.

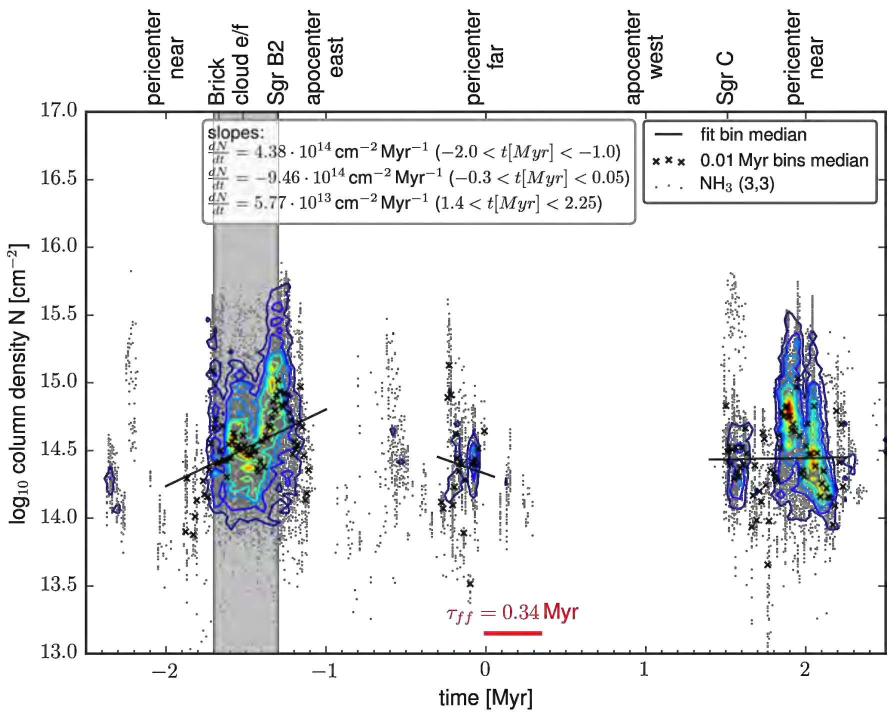

Figure B.21: NH_3 (3,3) column density as a function of time since far side pericenter passage.

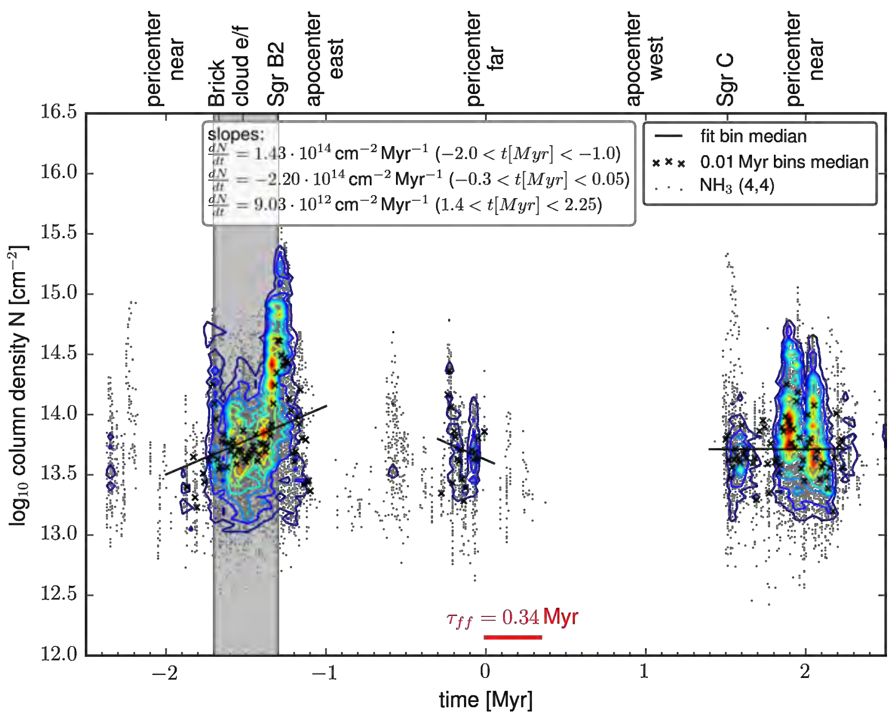

Figure B.22: NH_3 (4,4) column density as a function of time since far side pericenter passage.

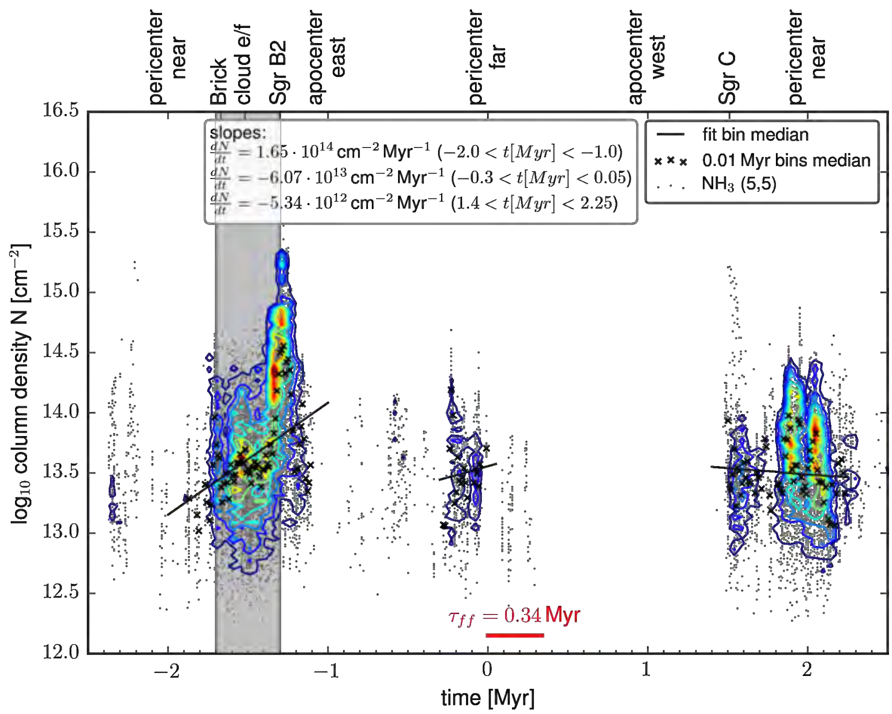

Figure B.23: NH_3 (5,5) column density as a function of time since far side pericenter passage.

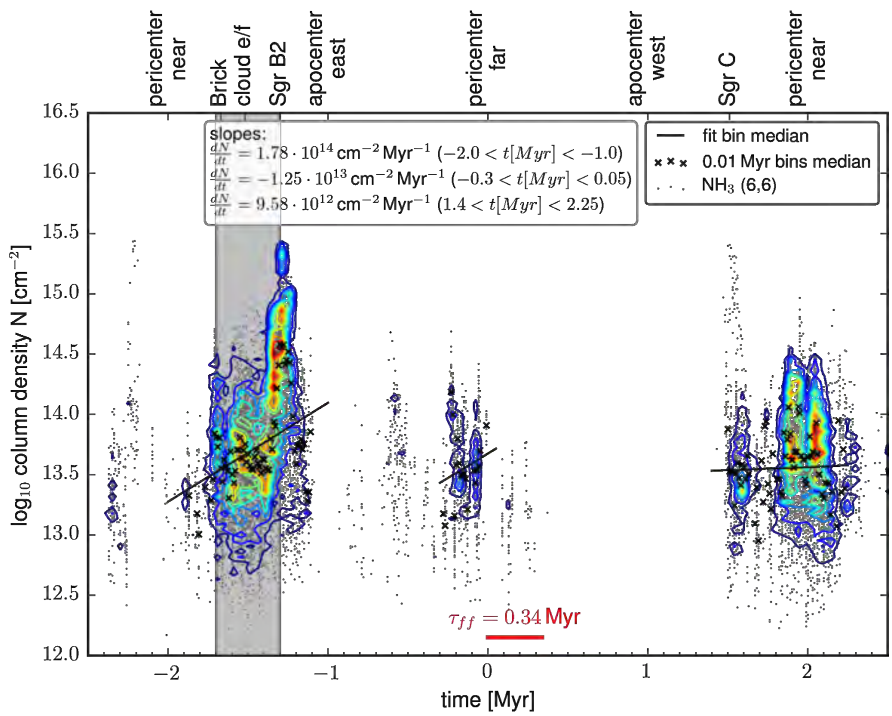

Figure B.24: NH_3 (6,6) column density as a function of time since far side pericenter passage.

List of Figures

List of Tables

Bibliography

Bertoldi, F. & McKee, C. F. 1992, ApJ, 395, 140

Betz, A. L., McLaren, R. A., & Spears, D. L. 1979, ApJ, 229, L97

Beuther, H., Walsh, A., Schilke, P., Sridharan, T. K., Menten, K. M., & Wyrowski, F. 2002, A&A, 390, 289

Binney, J., Gerhard, O. E., Stark, A. A., Bally, J., & Uchida, K. I. 1991, MNRAS, 252, 210

Blitz, L., Fukui, Y., Kawamura, A., Leroy, A., Mizuno, N., & Rosolowsky, E. 2007, Protostars and Planets V, 81

Bolatto, A. D., Leroy, A. K., Rosolowsky, E., Walter, F., & Blitz, L. 2008, ApJ, 686, 948

Bracewell, R. 1978, The Fourier transform and its applications, McGraw-Hill electrical and electronic engineering series (McGraw-Hill)

Briggs, D. S. 1995, PhD thesis, The New Mexico Institute of Mining and Technology

Calzetti, D. 2001, PASP, 113, 1449

Chabrier, G. 2003, PASP, 115, 763

Chira, R.-A., Beuther, H., Linz, H., Schuller, F., Walmsley, C. M., Menten, K. M., & Bronfman, L. 2013, Astron. Astrophys., 552, A40

Compiègne, M., Verstraete, L., Jones, A., Bernard, J.-P., Boulanger, F., Flagey, N., Le Bourlot, J., Paradis, D., & Ysard, N. 2011, A&A, 525, A103

Corby, J. F., Jones, P. a., Cunningham, M. R., Menten, K. M., Belloche, A., Schwab, F. R., Walsh, A. J., Balnozan, E., Bronfman, L., Lo, N., & Remijan, A. J. 2015, Mon. Not. R. Astron. Soc., 30, 1

Cornwell, T. J. 2008, IEEE Journal of Selected Topics in Signal Processing, 2, 793

Cornwell, T. J. & Evans, K. F. 1985, A&A, 143, 77

Crutcher, R. M. 2012, ARA&A, 50, 29

Danby, G., Flower, D. R., Valiron, P., Schilke, P., & Walmsley, C. M. 1988, Mon. Not. R. Astron. Soc., 235, 229

Draine, B. T. 2003, ARA&A, 41, 241

Draine, B. T. 2011, Physics of the Interstellar and Intergalactic Medium (Princeton University Press)

Evans, II, N. J., Dunham, M. M., Jørgensen, J. K., Enoch, M. L., Merín, B., van Dishoeck, E. F., Alcalá, J. M., Myers, P. C., Stapelfeldt, K. R., Huard, T. L., Allen, L. E., Harvey, P. M., van Kempen, T., Blake, G. A., Koerner, D. W., Mundy, L. G., Padgett, D. L., & Sargent, A. I. 2009, ApJS, 181, 321

Faure, A., Hily-Blant, P., Le Gal, R., Rist, C., & Pineau des Forêts, G. 2013, Astrophys. J., 770, L2

Ferrière, K., Gillard, W., & Jean, P. 2007, A&A, 467, 611

Forster, J. R. & Caswell, J. L. 1989, A&A, 213, 339

Genzel, R. & Downes, D. 1977, A&AS, 30, 145

Ginsburg, A., Henkel, C., Ao, Y., Riquelme, D., Kauffmann, J., Pillai, T., Mills, E. A. C., Requena-Torres, M. A., Immer, K., Testi, L., Ott, J., Bally, J., Battersby, C., Darling, J., Aalto, S., Stanke, T., Kendrew, S., Kruijssen, J. M. D., Longmore, S., Dale, J., Guesten, R., & Menten, K. M. 2016, A&A, 586, A50

Ginsburg, A., Walsh, A., Henkel, C., Jones, P. A., Cunningham, M., Kauffmann, J., Pillai, T., Mills, E. A. C., Ott, J., Kruijssen, J. M. D., Menten, K. M., Battersby, C., Rathborne, J., Contreras, Y., Longmore, S., Walker, D., & Dawson, J. 2015, eprint arXiv:1510.06401, 1

Glover, S. C. O. & Clark, P. C. 2012, MNRAS, 421, 9

Gorski, M., Ott, J., Rand, R. J., Meier, D. S., Momjian, E., & Walter, F. 2015, in American Astronomical Society Meeting Abstracts, Vol. 225, American Astronomical Society Meeting Abstracts, 251.02

Gull, S. F. & Daniell, G. J. 1978, Nature, 272, 686

Güsten, R., Walmsley, C. M., & Pauls, T. 1981, A&A, 103, 197

Hartmann, L., Ballesteros-Paredes, J., & Heitsch, F. 2012, MNRAS, 420, 1457

Heyer, M., Krawczyk, C., Duval, J., & Jackson, J. M. 2009, ApJ, 699, 1092

Ho, P. T. P., Barrett, A. H., & Martin, R. N. 1978, ApJ, 221, L117

Ho, P. T. P. & H., C. 1983, Annu. Rev. Astron. Astrophys., 21, 239

Högbom, J. A. 1974, Astronomy and Astrophysics Supplement, 15, 417

Hüttemeister, S., Wilson, T. L., Bania, T. M., & Martin-Pintado, J. 1993, Astron. Astrophys., 280, 255

Hüttemeister, S., Wilson, T. L., Mauersberger, R., Lemme, C., Dahmen, G., & Henkel, C. 1995, Astron. Astrophys., 294, 667

Immer, K., Menten, K. M., Schuller, F., & Lis, D. C. 2012, A&A, 548, A120

Jaynes, E. T. 1957, Physical Review, 106, 620

Jeans, J. H. 1902, Philosophical Transactions of the Royal Society of London Series A, 199, 1

Kauffmann, J., Pillai, T., & Zhang, Q. 2013, ApJ, 765, L35

Kawamura, A., Mizuno, Y., Minamidani, T., Filipović, M. D., Staveley-Smith, L., Kim, S., Mizuno, N., Onishi, T., Mizuno, A., & Fukui, Y. 2009, ApJS, 184, 1

Kennicutt, Jr., R. C. 1998, ApJ, 498, 541

Klessen, R. S. & Glover, S. C. O. 2014, ArXiv e-prints

Krieger, N. 2013, Bachelor theis, University of Heidelberg

Kroupa, P., Weidner, C., Pflamm-Altenburg, J., Thies, I., Dabringhausen, J., Marks, M., & Maschberger, T. 2013, The Stellar and Sub-Stellar Initial Mass Function of Simple and Composite Populations, 115

Kruijssen, J. M. D., Dale, J. E., & Longmore, S. N. 2015, Mon. Not. R. Astron. Soc., 447, 1059

Kruijssen, J. M. D., Longmore, S. N., Elmegreen, B. G., Murray, N., Bally, J., Testi, L., & Kennicutt, R. C. 2014, Mon. Not. R. Astron. Soc., 440, 3370

Krumholz, M. R. 2011, in American Institute of Physics Conference Series, Vol. 1386, XV Special Courses at the National Observatory of Rio de Janeiro, 9–57

Krumholz, M. R. 2014, Phys. Rep., 539, 49

Krumholz, M. R. & Kruijssen, J. M. D. 2015, eprint arXiv:1505.07111, 18, 1

Larson, R. B. 1981, Mon. Not. R. Astron. Soc., 194, 809

Lis, D. C., Li, Y., Dowell, C. D., & Menten, K. M. 1999, in ESA Special Publication, Vol. 427, The Universe as Seen by ISO, 627

Lis, D. C., Serabyn, E., Zylka, R., & Li, Y. 2001, ApJ, 550, 761

Lombardi, M., Alves, J., & Lada, C. J. 2010, A&A, 519, L7

Longmore, S., Barnes, A., Battersby, C., Bally, J., Kruijssen, J. M. D., Dale, J., Henshaw, J., Walker, D., Rathborne, J., Testi, L., Ott, J., & Ginsburg, A. 2016, ArXiv e-prints

Longmore, S. N., Bally, J., Testi, L., Purcell, C. R., Walsh, A. J., Bressert, E., Pestalozzi, M., Molinari, S., Ott, J., Cortese, L., Battersby, C., Murray, N., Lee, E., Kruijssen, J. M. D., Schisano, E., & Elia, D. 2013, MNRAS, 429, 987

Longmore, S. N. & Kruijssen, J. M. D. 2014, Mon. Not. R. Astron. Soc., 439, 3239

Longmore, S. N., Kruijssen, J. M. D., Bally, J., Ott, J., Testi, L., Rathborne, J., Bastian, N., Bressert, E., Molinari, S., Battersby, C., & Walsh, a. J. 2013, Mon. Not. R. Astron. Soc., d, 6

Longmore, S. N., Rathborne, J., Bastian, N., Alves, J., Ascenso, J., Bally, J., Testi, L., Longmore, A., Battersby, C., Bressert, E., Purcell, C., Walsh, A., Jackson, J., Foster, J., Molinari, S., Meingast, S., Amorim, A., Lima, J., Marques, R., Moitinho, A., Pinhao, J., Rebordao, J., & Santos, F. D. 2012, ApJ, 746, 117

Lu, X., Zhang, Q., Kauffmann, J., Pillai, T., Longmore, S. N., Kruijssen, J. M. D., Battersby, C., & Gu, Q. 2015, Astrophys. J. Lett.

Madau, P. & Dickinson, M. 2014, ARA&A, 52, 415

Maret, S., Faure, A., Scifoni, E., & Wiesenfeld, L. 2009, Mon. Not. R. Astron. Soc., 399, 425

Mauersberger, R., Henkel, C., Weiß, A., Peck, A. B., & Hagiwara, Y. 2003, A&A, 403, 561

McKee, C. F. & Ostriker, J. P. 1977, ApJ, 218, 148

Meidt, S. E., Hughes, A., Dobbs, C. L., Pety, J., Thompson, T. A., García-Burillo, S., Leroy, A. K., Schinnerer, E., Colombo, D., Querejeta, M., Kramer, C., Schuster, K. F., & Dumas, G. 2015, ApJ, 806, 72

Meidt, S. E., Schinnerer, E., García-Burillo, S., Hughes, A., Colombo, D., Pety, J., Dobbs, C. L., Schuster, K. F., Kramer, C., Leroy, A. K., Dumas, G., & Thompson, T. A. 2013, ApJ, 779, 45

Mills, E. A. C. & Morris, M. R. 2013, Astrophys. J., 772, 105

Molinari, S., Bally, J., Noriega-Crespo, A., Compiègne, M., Bernard, J. P., Paradis, D., Martin, P., Testi, L., Barlow, M., Moore, T., Plume, R., Swinyard, B., Zavagno, A., Calzoletti, L., Di Giorgio, A. M., Elia, D., Faustini, F., Natoli, P., Pestalozzi, M., Pezzuto, S., Piacentini, F., Polenta, G., Polychroni, D., Schisano, E., Traficante, A., Veneziani, M., Battersby, C., Burton, M., Carey, S., Fukui, Y., Li, J. Z., Lord, S. D., Morgan, L., Motte, F., Schuller, F., Stringfellow, G. S., Tan, J. C., Thompson, M. A., Ward-Thompson, D., White, G., & Umana, G. 2011, ApJ, 735, L33

Molinari, S., Swinyard, B., Bally, J., Barlow, M., Bernard, J.-P., Martin, P., Moore, T., Noriega-Crespo, A., Plume, R., Testi, L., Zavagno, A., Abergel, A., Ali, B., Anderson, L., André, P., Baluteau, J.-P., Battersby, C., Beltrán, M. T., Benedettini, M., Billot, N., Blommaert, J., Bontemps, S., Boulanger, F., Brand, J., Brunt, C., Burton, M., Calzoletti, L., Carey, S., Caselli, P., Cesaroni, R., Cernicharo, J., Chakrabarti, S., Chrysostomou, A., Cohen, M., Compiegne, M., de Bernardis, P., de Gasperis, G., di Giorgio, A. M., Elia, D., Faustini, F., Flagey, N., Fukui, Y., Fuller, G. A., Ganga, K., Garcia-Lario, P., Glenn, J., Goldsmith, P. F., Griffin, M., Hoare, M., Huang, M., Ikhenaode, D., Joblin, C., Joncas, G., Juvela, M., Kirk, J. M., Lagache, G., Li, J. Z., Lim, T. L., Lord, S. D., Marengo, M., Marshall, D. J., Masi, S., Massi, F., Matsuura, M., Minier, V., Miville-Deschênes, M.-A., Montier, L. A., Morgan, L., Motte, F., Mottram, J. C., Müller, T. G., Natoli, P., Neves, J., Olmi, L., Paladini, R., Paradis, D., Parsons, H., Peretto, N., Pestalozzi, M., Pezzuto, S., Piacentini, F., Piazzo, L., Polychroni, D., Pomarès, M., Popescu, C. C., Reach, W. T., Ristorcelli, I., Robitaille, J.-F., Robitaille, T., Rodón, J. A., Roy, A., Royer, P., Russeil, D., Saraceno, P., Sauvage, M., Schilke, P., Schisano, E., Schneider, N., Schuller, F., Schulz, B., Sibthorpe, B., Smith, H. A., Smith, M. D., Spinoglio, L., Stamatellos, D., Strafella, F., Stringfellow, G. S., Sturm, E., Taylor, R., Thompson, M. A., Traficante, A., Tuffs, R. J., Umana, G., Valenziano, L., Vavrek, R., Veneziani, M., Viti, S., Waelkens, C., Ward-Thompson, D., White, G., Wilcock, L. A., Wyrowski, F., Yorke, H. W., & Zhang, Q. 2010a, A&A, 518, L100

Molinari, S., Swinyard, B., Bally, J., Barlow, M., Bernard, J.-P., Martin, P., Moore, T., Noriega-Crespo, A., Plume, R., Testi, L., Zavagno, A., Abergel, A., Ali, B., André, P., Baluteau, J.-P., Benedettini, M., Berné, O., Billot, N. P., Blommaert, J., Bontemps, S., Boulanger, F., Brand, J., Brunt, C., Burton, M., Campeggio, L., Carey, S., Caselli, P., Cesaroni, R., Cernicharo, J., Chakrabarti, S., Chrysostomou, A., Codella, C., Cohen, M., Compiegne, M., Davis, C. J., de Bernardis, P., de Gasperis, G., Di Francesco, J., di Giorgio, A. M., Elia, D., Faustini, F., Fischera, J. F., Fukui, Y., Fuller, G. A., Ganga, K., Garcia-Lario, P., Giard, M., Giardino, G., Glenn, J. ., Goldsmith, P., Griffin, M., Hoare, M., Huang, M., Jiang, B., Joblin, C., Joncas, G., Juvela, M., Kirk, J., Lagache, G., Li, J. Z., Lim, T. L., Lord, S. D., Lucas, P. W., Maiolo, B., Marengo, M., Marshall, D., Masi, S., Massi, F., Matsuura, M., Meny, C., Minier, V., Miville-Deschênes, M.-A., Montier, L., Motte, F., Müller, T. G., Natoli, P., Neves, J., Olmi, L., Paladini, R., Paradis, D., Pestalozzi, M., Pezzuto, S., Piacentini, F., Pomarès, M., Popescu, C. C., Reach, W. T., Richer, J., Ristorcelli, I., Roy, A., Royer, P., Russeil, D., Saraceno, P., Sauvage, M., Schilke, P., Schneider-Bontemps, N., Schuller, F., Schultz, B., Shepherd, D. S., Sibthorpe, B., Smith, H. A., Smith, M. D., Spinoglio, L., Stamatellos, D., Strafella, F., Stringfellow, G., Sturm, E., Taylor, R., Thompson, M. A., Tuffs, R. J., Umana, G., Valenziano, L., Vavrek, R., Viti, S., Waelkens, C., Ward-Thompson, D., White, G., Wyrowski, F., Yorke, H. W., & Zhang, Q. 2010b, PASP, 122, 314

Morris, M. & Serabyn, E. 1996, ARA&A, 34, 645

Nagayama, T., Omodaka, T., Handa, T., Toujima, H., Sofue, Y., Sawada, T., Kobayashi, H., & Koyama, Y. 2009, PASJ, 61, 1023

Ott, J. 1999, Master's thesis, Universitaet Bonn

Ott, J., Burton, M., Jones, P., & Meier, D. S. 2014, in IAU Symposium, Vol. 303, The Galactic Center: Feeding and Feedback in a Normal Galactic Nucleus, 104–105

Ott, J., Henkel, C., Braatz, J. A., & Weiß, A. 2011, ApJ, 742, 95

Ott, J., Weiss, A., Henkel, C., & Walter, F. 2005, ApJ, 629, 767

Ott, J., Weiß, A., Staveley-Smith, L., Henkel, C., & Meier, D. S. 2014, Astrophys. J., 785, 55

Popescu, C. C. & Tuffs, R. J. 2002, MNRAS, 335, L41

Reid, M. J., Menten, K. M., Brunthaler, A., Zheng, X. W., Dame, T. M., Xu, Y., Wu, Y., Zhang, B., Sanna, A., Sato, M., Hachisuka, K., Choi, Y. K., Immer, K., Moscadelli, L., Rygl, K. L. J., & Bartkiewicz, A. 2014, ApJ, 783, 130

Rodríguez, L. F. & Zapata, L. A. 2013, ApJ, 767, L13

Salpeter, E. E. 1955, ApJ, 121, 161

Schilke, P. 1989, dissertation, Universität Bonn

Schmidt, M. 1959, ApJ, 129, 243

Skilling, J. & Bryan, R. K. 1984, MNRAS, 211, 111

Solomon, P. M., Rivolo, A. R., Barrett, J., & Yahil, A. 1987, ApJ, 319, 730

Soutter, W. 2012, AZO

Stahler, S. W. & Palla, F. 2005, The Formation of Stars (Wiley-VCH), 865

Sternberg, A. & Dalgarno, A. 1995, ApJS, 99, 565

Stolte, A., Ghez, A. M., Morris, M., Lu, J. R., Brandner, W., & Matthews, K. 2008, ApJ, 675, 1278

Tackenberg, J., Beuther, H., Henning, T., Schuller, F., Wienen, M., Motte, F., Wyrowski, F., Bontemps, S., Bronfman, L., Menten, K., Testi, L., & Lefloch, B. 2012, A&A, 540, A113

Takano, S. 2002, Publ. Astron. Soc. Japan, 195

Taylor, G. B., Carilli, C. L., & Perley, R. A., eds. 1999, Astronomical Society of the Pacific Conference Series, Vol. 180, Synthesis Imaging in Radio Astronomy II

Townes, C. H. & Schawlow, A. L. 1975, Microwave spectroscopy. (Dover Publications, New York, NY (USA))

Ungerechts, H., Walmsley, C., & Winnewisser, G. 1986, Astron. Astrophys., 157, 207

Walker, D. L., Longmore, S. N., Bastian, N., Kruijssen, J. M. D., Rathborne, J. M., Jackson, J. M., Foster, J. B., & Contreras, Y. 2015, MNRAS, 449, 715

Walmsley, C. & Ungerechts, H. 1983, Astron. Astrophys., 122, 164

Walsh, A. J., Breen, S. L., Britton, T., Brooks, K. J., Burton, M. G., Cunningham, M. R., Green, J. A., Harvey-Smith, L., Hindson, L., Hoare, M. G., Indermuehle, B., Jones, P. A., Lo, N., Longmore, S. N., Lowe, V., Phillips, C. J., Purcell, C. R., Thompson, M. A., Urquhart, J. S., Voronkov, M. A., White, G. L., & Whiting, M. T. 2011, MNRAS, 416, 1764

Walsh, A. J., Thorwirth, S., Beuther, H., & Burton, M. G. 2010, MNRAS, 404, 1396

Walter, F., Brinks, E., de Blok, W. J. G., Bigiel, F., Kennicutt, J. R. C., Thornley, M. D., & Leroy, A. K. 2008, The Astronomical Journal, 136

Wernecke, S. J. & D'Addario, L. R. 1977, IEEE Transactions on Communications, 26, 351

Wilson, T. L., Henkel, C., Huttemeister, S., Dahmen, G., Linhart, A., Lemme, C., & Schmid-Burgk, J. 1993, A&A, 276, L29

Wilson, T. L., Rohlfs, K., & Hüttemeister, S. 2013, Tools of Radio Astronomy

Yusef-Zadeh, F., Hewitt, J. W., Arendt, R. G., Whitney, B., Rieke, G., Wardle, M., Hinz, J. L., Stolovy, S., Lang, C. C., Burton, M. G., & Ramirez, S. 2009, ApJ, 702, 178

Erklärung

Ich versichere, dass ich diese Arbeit selbstständig verfasst habe und keine anderen als die angegebenen Quellen und Hilfsmittel benutzt habe.

Heidelberg, den May 17, 2016 ....